

Functionalization of Fiber Composites with Nanoparticle-Modified Resin Systems

von der Fakultät für Natur und Materialwissenschaften
der Technischen Universität Clausthal
genehmigte Dissertation
zur Erlangung des Grades

Doktor-Ingenieur

vorgelegt von:

Dilmurat Abliz, M.Sc.

Fachgutachter:

Professor Dr. rer. Nat. Albrecht Wolter
Professor Dr.-Ing. Gerhard Ziegmann
Professor Dr. rer. Nat. Alfred Weber
Professor Dr. Dichen Li

Für die Nutzung dieser Dissertation gelten folgende rechtliche Bestimmungen

- Die vorliegende Dissertation darf von der Technischen Universität Clausthal frei im Internet angeboten werden. Eine weitere Verbreitung oder öffentliche Wiedergabe ist nicht gestattet und kann nur mit ausdrücklicher Genehmigung des Autors (Promovierten) geschehen.
- Die Vervielfältigung ist nur im Rahmen des privaten und eigenen wissenschaftlichen Gebrauchs (§ 53 UrhG) erlaubt.
- Die Publikation darf nicht bearbeitet oder in anderer Weise verändert werden.
- Der Autor hat das Recht, sein Werk, auch auszugsweise, anderweitig verfügbar zu machen und zu verbreiten.
- Für den Inhalt des Dokuments ist allein der Autor verantwortlich.

This publication (dissertation) is subject to the following terms of use:

- The Technical University of Clausthal is entitled to give open access to this publication. Further publication or public broadcasting needs explicit authorization of the copyright owner (doctor).
- Copying is permitted only for private or the own scientific purposes of the person who performs copying (according to § 53 of the German Copyright Act). The copyright owner grants production of complete single copies of this publication by means of a print on demand service.
- This publication may not be edited or changed otherwise.
- The copyright owner has got the right to publish or broadcast this publication as a whole or parts thereof elsewhere.
- The author is exclusively responsible for the content of this publication.

My deepest gratitude

To Prof. Dr.-Ing. Gerhard Ziegmann, for his support and guidance in both work and life during the last five years as I worked as a scientific co-worker in the institute, and to be able to finish the thesis. His openness and enthusiasm for ideas and discussions, attention on details, as well as patience have always taught and inspired me a lot. Especially his trust has been always a big encouragement for me to consistently keep trying and developing myself.

To Prof. Dr. rer. nat. Alfred Weber, for being a co-reviewer of the thesis. I had the pleasure of knowing him from the beginning as I started in TU Clausthal. The discussions and exchanges in many areas have been always very informative and insightful.

To Prof. Dr. Dichen Li and Prof. Dr. Yugang Duan, for their valuable guidance and support beginning from my early master study in Xi'an Jiaotong University to the joint PhD program in TU Clausthal. Special thanks again to Prof. Dr. Dichen Li for his constructive suggestions as being the co-supervisor and co-reviewer of the thesis.

To the whole PuK-family, including all the scientific and technical colleagues that showed great willingness to help, especially at the time beginning when I had difficulty by German language. The discussions and even coffee chats have been always a lot of fun. I also would like to specially thank my office partners: Dr.-Ing. Stefan Kirchberg and Dipl.-Ing. Tamara Florian. I had a wonderful time with a lot of fun in the office with them.

To all the members of the German Research Foundation Research-Group Program (DFG-Forschergruppe 2021), the teamwork helped me a lot to achieve fruitful results and to successfully accomplish the thesis. Also special thanks to Dr. Dr.-Ing. Stephan Sprenger from Evonik Nutrition & Care GmbH for providing silica-epoxy resin masterbatch (Nanopox F400).

To the students whom I had the opportunity to supervise and work together with. The teamwork with students from different countries with distinct cultures helped me not just on research but also taught me to share and respect different ideas and values.

Last but not least, to my family and girlfriend who gave me tremendous support and love. Even if we were separated many years by a long distance, I always felt happy and lucky having them beside me. Without their strong support and love, I never could have made it this far.

Kurzfassung

Nanopartikeln (NP) bieten einen vielversprechenden Weg, um effektiv die Eigenschaften von Strukturen aus faserverstärkten Kunststoffen (FVK) zu verbessern und bestimmte Funktionalitäten einzubringen. In dieser Doktorarbeit wurde die Funktionalisierung von FVK-Strukturen mit drei repräsentativen NP-Systemen mit unterschiedlichen chemischen und physikalischen Charakteristika (Böhmite, Siliziumdioxid und Carbon-Nanotube) vergleichend untersucht. Zunächst, aufgrund der Interaktionen zwischen den drei Ausgangskomponenten sowie ihrem Einfluss auf Prozess und finale Eigenschaften, werden die kritischen Materialeigenschaften jeder Komponente und ihre gegenseitigen Beeinflussungen systematisch charakterisiert. Darüber hinaus werden schwerpunktmäßig die bedeutenden Prozessaspekte wie die Aushärtungskinetik, die Rheologie der NP-modifizierten Epoxidharzmatrix sowie das Kompaktierungsverhalten (globaler/lokaler Faservolumengehalt, Makro-/Mikroporosität) und die Permeabilität der Faserpreforms unter Berücksichtigung des Filtereffekts der NP kritisch untersucht und modelliert. Anschließend, in Anbetracht des komplexen Fließ- und Filterverhaltens der mit unterschiedlichen NP-modifizierten Epoxidharzmatrix, werden unterschiedliche Imprägnierungsstrategien – bestehend aus In-Plane- (sequentielle und parallele Injektion) und Out-of-Plane-Methoden – untersucht. Die Prozessentwicklung wird sowohl durch Experimente als auch Simulationen zum Imprägnier- und Aushärteverhalten von NP-modifizierten Epoxidharzsystemen unterstützt. Schließlich, es werden die mechanischen (mit dem Fokus auf kritische, matrixdominierte Eigenschaften, wie z.B. Risszähigkeit, Biege und interlaminar Schereigenschaften), thermisch-mechanischen und elektrischen Eigenschaften der FVKs hinsichtlich der eingesetzten NP-Systeme vergleichend untersucht. Die Ergebnisse zeigen deutliche Verbesserungen dieser Eigenschaften durch die Modifizierung mit NP.

Abstract

Nanoparticles (NPs) provide a promising way to effectively improve the performance of fiber reinforced polymer (FRP) structures or introduce certain functionalities to them. In this thesis, the functionalization of FRPs with three representative NP systems with different chemical and physical characteristics (boehmite, silica and carbon nanotube) is comparatively investigated. Firstly, due to the interactions among the base components (NP, epoxy matrix and fiber reinforcement) and their influence on the process and the final properties, the critical material characteristics of each component and their interactions are systematically investigated. Moreover, the important processing aspects such as cure kinetics and rheology of the NP-modified epoxy matrix as well as the compaction behavior (global/local fiber volume fraction and macro/micro porosity) and permeability of the fiber preform considering the NP retention effect are critically studied and modeled. Furthermore, the NP-modified epoxy matrix systems show complex flow and retention behavior depending on the ratio of the critical particle size to macro/micro porosity of the preform. Therefore, different impregnation strategies – including in-plane (sequential and parallel injection) and out-of-plane methods – are investigated. The process development is supported by both experimental and simulation studies regarding the impregnation, as well as cure behavior of NP-modified epoxy resin systems, so that a faster and more robust process design can be guaranteed. Finally, the mechanical (focusing on critical matrix-dominated properties, i.e. interlaminar fracture toughness, flexural and interlaminar shear strength), thermal-mechanical and electrical properties of the FRPs regarding the different NP-epoxy systems are comparatively investigated. The results show a remarkable enhancement of these properties by the modification with NPs.

Table of contents

1	Introduction.....	1
1.1	Motivation.....	3
1.1.1	Material and final properties	3
1.1.2	Process.....	5
1.2	Research hypothesis.....	8
1.2.1	Functionalization of FRP with nanoparticles	8
1.2.2	Gradient functionalization	9
2	State of the research	12
2.1	Functionalization of FRPs with nanoparticles	12
2.1.1	Why nanoparticles?	12
2.1.2	Multi-scale functional FRPs fabrication strategies.....	13
2.2	Materials	16
2.2.1	Nanoparticle-epoxy matrix	16
2.2.2	Fiber preform.....	21
2.3	Process simulation	28
2.3.1	Flow simulation	28
2.3.2	Cure simulation	32
2.4	Properties	33
2.5	Research focus and dissertation organization.....	35
2.5.1	Key aspect I: Material characterization and modeling	35
2.5.2	Key aspect II: Process development and simulation	36
2.5.3	Key aspect III: Property characterization and concept evaluation	37
3	Materials and methodologies	38
3.1	Materials	38
3.1.1	Fiber textile.....	38
3.1.2	Nanoparticle-epoxy matrix systems	39
3.2	Methodology for key aspect I: Material characterization and modeling	42

3.2.1	Nanoparticle-epoxy masterbatch	42
3.2.2	Nanoparticle-epoxy matrix	43
3.2.3	Fiber reinforcement	52
3.3	Methodology for key aspect II: Process development and simulation	63
3.3.1	Nanoparticle systems flow and retention behavior	63
3.3.2	Flow simulation	64
3.3.3	Cure simulation	68
3.4	Methodology for key aspect III: Property characterization and concept evaluation	70
3.4.1	Mechanical properties	70
3.4.2	Thermal-mechanical properties	72
3.4.3	Electrical properties	72
4	Key aspect I: Material characterization and modeling	73
4.1	Nanoparticle-epoxy matrix	74
4.1.1	Cure characterization and modeling	74
4.1.2	Rheology characterization and modeling	85
4.2	Fiber preform	90
4.2.1	Filament diameter distribution	90
4.2.2	Global/local fiber volume fraction	91
4.2.3	Filament/Roving distance distribution	92
4.2.4	Permeability: DoE studies	95
4.3	Short summary	99
5	Key aspect II: Process development and simulation	101
5.1	Nanoparticle systems flow and retention behavior	102
5.2	Flow simulation	109
5.3	Cure simulation	111
5.4	Impregnation strategies	115
5.5	Short summary	119
6	Key aspect III: Property characterization and concept evaluation	121
6.1	Mechanical properties	122

6.2	Thermal-mechanical properties	127
6.2.1	Dynamic thermal-mechanical analysis (DTMA)	127
6.3	Electrical properties	128
6.4	Short summary	130
7	Summary and outlook	131
7.1	Evaluation of the results	131
7.1.1	Key aspect I: Material characterization and modeling	131
7.1.2	Key aspect II: Process development and simulation.	132
7.1.3	Key aspect III: Property characterization and concept evaluation	133
7.2	Conclusion	133
7.3	Outlook	137
7.3.1	Material characterization and modeling	137
7.3.2	Process development and simulation.....	138
7.3.3	Visualization of the particle-particle and particle-fiber interactions	138
7.3.4	Nano-carrier-fiber: simultaneously binding and functionalization	139
	Appendix: Material datasheets.....	149

1 Introduction

New materials and processing technologies are leading innovations in human history, always being at the forefront of social development. The advancement of society puts enhanced requirements on materials with more and more extreme boundary conditions, which needs interdisciplinary interactions/integrations from different scientific and technological aspects. For material science and technology, this trend is getting more and more urgent, requiring combined – high mechanical, electrical and thermal properties – or even in some cases contradictory property demands, i.e. higher stiffness/strength properties but also high toughness at low weight, etc. A single material can hardly satisfy many such harsh application requirements, which requires the combination of different materials in a synergistic way.

Composite materials are the combination of at least two different material components – often ones that have very different properties – in a synergistic way to combine the advantages of the single components to achieve unique properties. Natural composites exist broadly in both plants and animals, including wood and bone, etc. Engineered composites go back to 1000 BC in the form of cob (a mixture of straw and mud) to form bricks for building construction. (Mud can be easily dried out (molded) into a brick shape to give the required geometry as a building material. It holds quite well by compression load – has a good compressive strength – but breaks quite easily by stretching or bending – indicating a poor tensile strength. On the contrary, straw bears quite well when stretched, but buckles easily when compressed. By mixing mud and straw together, it is possible to make bricks that are stable for diverse application loads, which makes them excellent building blocks. Another example of one of the wide-known composite is concrete, which is based on the similar principle of combining different characteristics of cement with gravel aggregate and even wood/metal rods as reinforcement material.

As one of the modern composite materials, Fiber Reinforced Polymer Composite (FRPC), also known as Fiber Reinforced Plastic/Polymer (FRP) or Advanced Polymer Composite (APC), is a combination of polymeric matrix with fibers as reinforcement. The polymeric matrix (thermoset, thermoplastic or elastomer) acts as a binding material by supporting and bonding the fibers to transfer the load. As the polymers are easy to process, they deliver a superior molding and shaping ability for the FRPs, which remarkably simplifies the fabrication process. However, they are weak in tensile, bending, shear and impact load conditions, these disadvantages can be effectively compensated by strong reinforcing fibers – including mostly carbon, glass and aramid fibers.

1 Introduction

The biggest advantage of FRPs is that they are light in weight but strong. According to studies, the weight-saving potential of FRPs could be up to 60 -70 % compared to steel, and 40 -50 % compared to aluminum with the same performance [1]. Due to these advantages, the FRPs have demonstrated clear-cut advantages with advanced performance at decreased weight over more conventional metallic materials and gained rapid development. From the early application of FRPs around 1940s, which was then just limited to military fields, FRPs are becoming more and more favorable in engineering applications in many demanding aerospace, wind energy, automotive, infrastructure, and consumer industries.

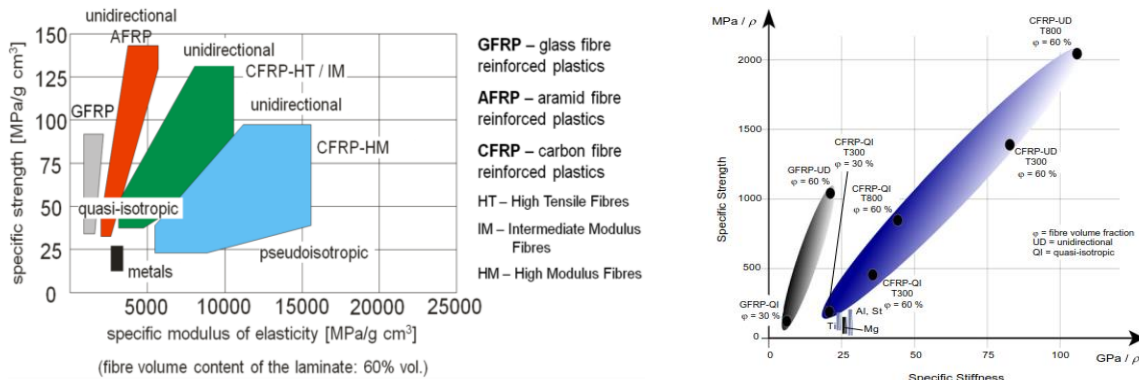


Figure 1.1: FRP stiffness and strength vs. metals [2-4]

In recent years, applications of FRPs for a variety of large and complex structural parts and components in many civil industrial applications are becoming a reality: e.g. airplane bodies and wings, wind turbine blades of more than 70 m, rail cars, automotive bodies, buildings and so on. For instance, the latest Boeing-787 airplane is fabricated with up to 50 % composites by weight, while the Airbus-A350 XWB is fabricated with 53 %. According to several different survey and evaluation reports from the Roland Berger Strategy Consultants [1], Federation of Reinforced Plastics e.V. & Carbon Composites e.V. [5], and Toray Industries, Inc. [6], the world carbon fiber demand is expected to maintain an annual growth rate of 12 - 17 %, breaking at about 100 - 140 Ktons/year by 2020 [1, 5, 6]; while the market demand for the carbon fiber industry is expecting a full-scale expansion in industry applications, including automobile, mechanical engineering, oil and wind energy sectors [6].

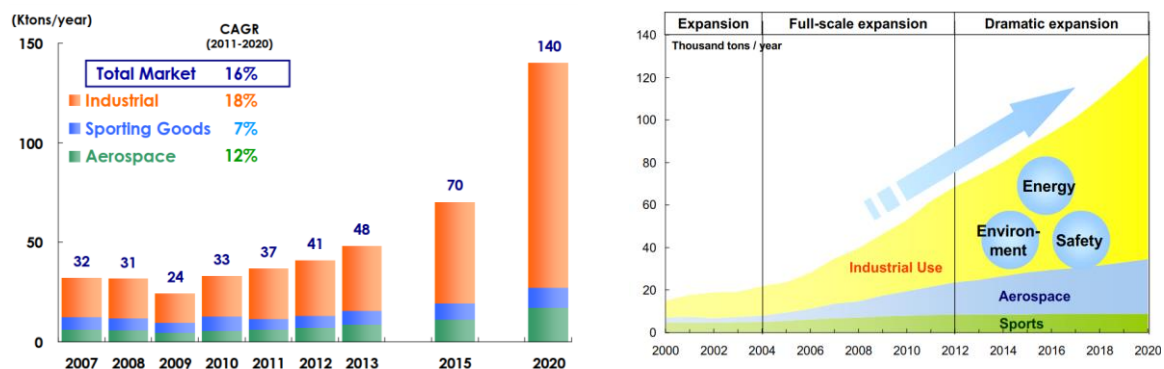


Figure 1.2: Carbon fiber market revolution and forecast [6, 7]

Besides the lightweight advantage, FRPs provide a quite high design and manufacturing flexibility. By choosing an appropriate combination of matrix and reinforcement fiber material and even in compiling its layup stacking sequence, a new material can be adjusted to optimally meet the requirements of particular load conditions, in order to achieve maximum stiffness/strength-to-weight ratio and performance.

1.1 Motivation

The large-scale application of FRPs is determined on one hand by the performance and on the other hand by the cost, which is why it is critical to achieve an optimized balance between the properties and process. Therefore, a synergistic evaluation of all factors – material, process and properties, is necessary to achieve a complete view of the critical aspects in each chain to determine the relationships and provide feasible and practical future development and solution concepts [8].

1.1.1 Material and final properties

Between the two basic components in FRPs, the polymeric matrix has functions of force transmission, shaping, surface condition/quality, chemical resistance, UV-load, heat/electrical deflection resistance and so on. The other reinforcing component is fiber – mostly carbon, glass and aramid. Fiber is responsible for strength, stiffness, drapability, fatigue behavior, energy absorption and so on. The fiber filaments/rovings can be woven, knitted and braided into different textile structures, for accelerating production efficiency and increasing the structural properties [9-11].

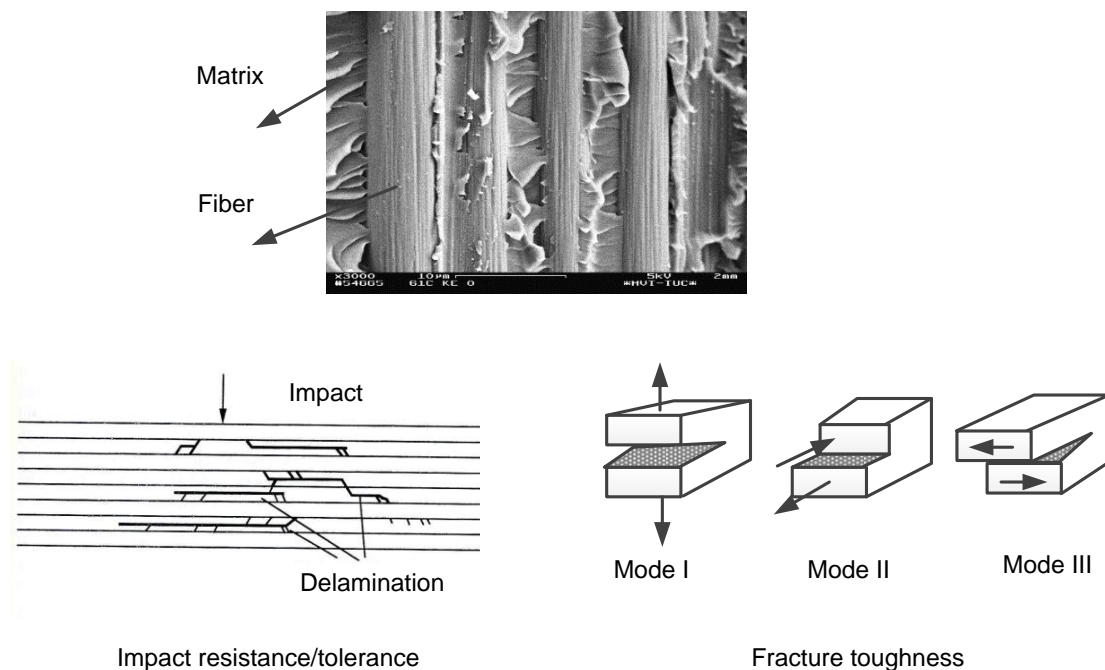


Figure 1.3: Micro structure of FRPs and critical failures due to the low matrix-dominated properties

1 Introduction

The final properties of FRPs are determined by both matrix and fibers, as well as their interphase. Although the FRPs show outstanding performance regarding the fiber-dominated properties, but the **low matrix-dominated properties** e.g. interlaminar shear, fracture toughness, impact and damage tolerance, as shown in the Figure 1.3, are still quite critical in high-performance applications.

In addition, the acting efficiency of the fibers is remarkably compromised due to the comparably much lower properties of the matrix. **According to related studies and reports, the weight-to-stiffness and weight-to-strength of the carbon fibers would be compromised in the composite laminate by about 60% and 30% respectively** [4, 12]. The potential usage degree of fibers could be increasingly brought into play by enhancing the stiffness, strength and the fracture toughness of the resin matrix.

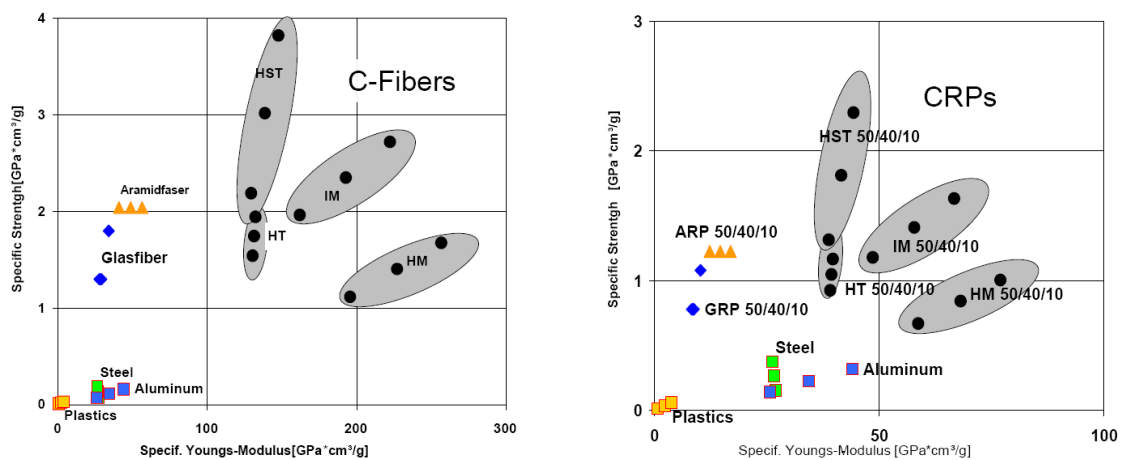


Figure 1.4: Specific fiber (left) and laminate (right) stiffness and strength compared to metal alloys [12]

Besides, the evolution of the final properties of FRP structures is strongly influenced by its cure process during the fabrication process. Due to the large heterogeneity in the thermal and mechanical properties between the matrix and fiber, there is a strong interaction between the thermal and mechanical properties, which makes the **thermal-mechanical properties** quite critical.

Of particular note, high-performance and temperature-stable resin systems tend to be brittle, and show high reaction shrinkage after curing. In addition, due to the large difference in the thermal conductivity and thermal expansion coefficients between the polymer matrix and fiber, there would be a quite heterogeneous volume change between the two components and temperature gradient at the interphase during the curing process. **It could inevitably lead to residual stresses at the fiber/matrix interphase, resulting in spring-in/back, warpage, and other geometric distortions.** These residual stresses and resulted distortions have a significant influence, especially considering large-scale aerospace structures, on the dimensional accuracy, stability and structural performance of the whole structure, as shown in Figure 1.5.

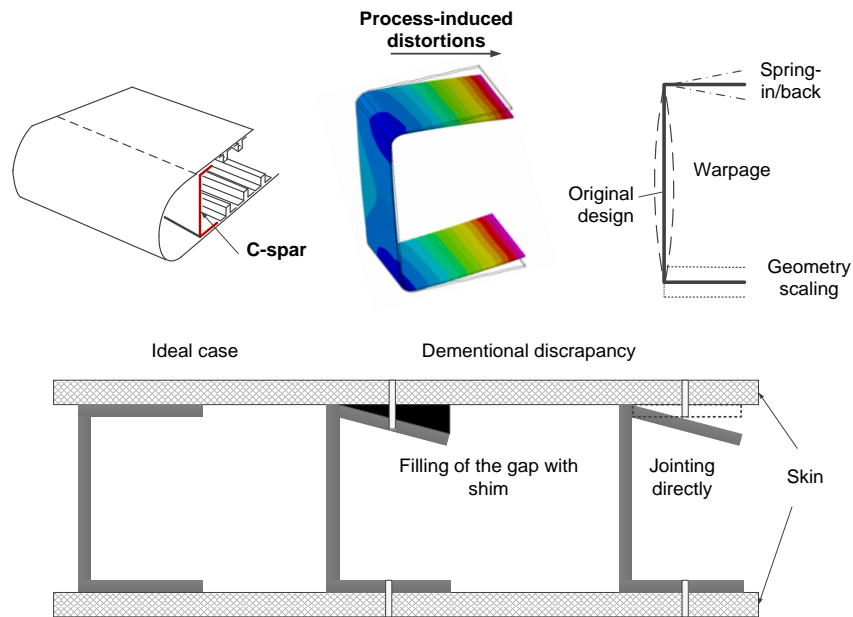


Figure 1.5: Process-induced distortions and potential assembly issues (magnified)

In addition, there are also certain applications where a **high electrical conductivity** of the FRP structures is necessary. For example, most aircraft, large commercial jets and wind turbines are quite vulnerable to lightning strikes [13]. **Composite structures in these applications are inferior to their metal counterparts, as the extreme electrical currents and electromagnetic forces generated by lightning strikes cannot be well conducted and dissipated away.** Composite materials are either not conductive at all (e.g., GFRPs) or are significantly less conductive than metals (e.g., CFRPs). Therefore, currently, the surfaces of airplane wings and fuselage structures need to be electrically conductive in order to dissipate the current flow along the conductive way and protect the structures. The currently available lightning strike protection structures rely on bonded aluminum/copper foils or meshes combined with metallic strips to form an electrical structure network, which inevitably increases the production complexity and final structural weight.



Figure 1.6: Lightning test for wind blade [14]



Figure 1.7: A generic thrust reverser panel with lightning strike damage [15]

1.1.2 Process

There are several different fabrication processes for FRPs, and these are developed considering the material process-ability, process/production complexity, application requirements and cost,

1 Introduction

etc. Figure 1.8 shows an overview of the most representative fabrication technologies that are applied nowadays. **Based on the processing matrix viscosity, they can be principally categorized into liquid composite molding (LCM) technology for low viscous matrices, and prepreg technology for high viscous matrices.**

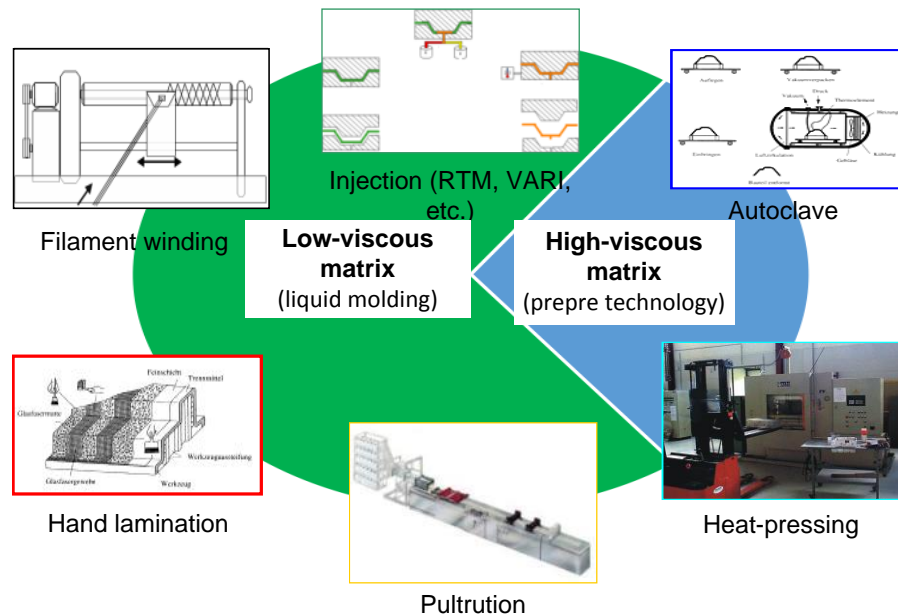
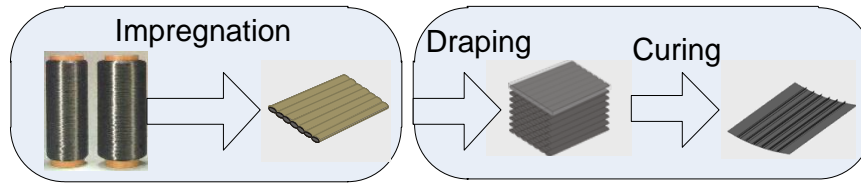


Figure 1.8: Overview and categorization of the manufacturing processes for FRPs

Prepreg technology is based on a prepreg material – a thin semi-finished composite layer in which reinforcement fiber is pre-impregnated with a thermoplastic or thermoset resin matrix in a certain ratio. Generally, the matrix system in a prepreg material is partially cured for ease of handling and is stored at low temperature (normally at -18°C) to prevent further polymerization. The reinforcement in a prepreg is mostly based on unidirectional fibers or woven fabrics. This prepreg material will be laid up on a mold with a certain stacking sequence, as shown in Figure 1.9, and after that, will be cured in an autoclave or oven with high pressure and temperature to achieve full polymerization. The prepreg technology is nowadays often used in aerospace, aircraft and other high-performance applications due to the high quality of the structures that are produced. Unfortunately, the total cost of the composite structures that are produced by the prepreg technology is rather high considering the additional prepreg manufacturing process, excessive cost by storage at low temperature but still limited storage time, as well as high energy and time cost by the harsh curing requirements in autoclave. Moreover, due to the decreased drapability of the prepreg, this technology is only suitable for simple geometrical structures – mostly flat or with slight curvature. This, inevitably, also leads to extra post-assembly steps to produce an integrated structure.

Prepreg technology: multi-step process



LCM technology: single-step process

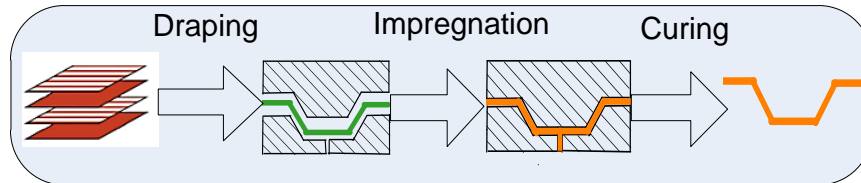


Figure 1.9: Comparison of LCM and prepreg technology process steps

In comparison, LCM technology is based on the impregnation (hand lamination, injection, filament winding, pultrusion and so on) of the dry fibers directly by low-viscous liquid resin matrix and curing simultaneously. By adjusting the impregnation strategies and fabrication parameters, injection pressure, temperature, compaction and so on, the process can be adjusted for highest efficiency and flexibility, making the process more attractive for complex structures in serial production. The reduced and simplified process steps could remarkably reduce the production cost that makes the process quite favorable in many industrial applications.

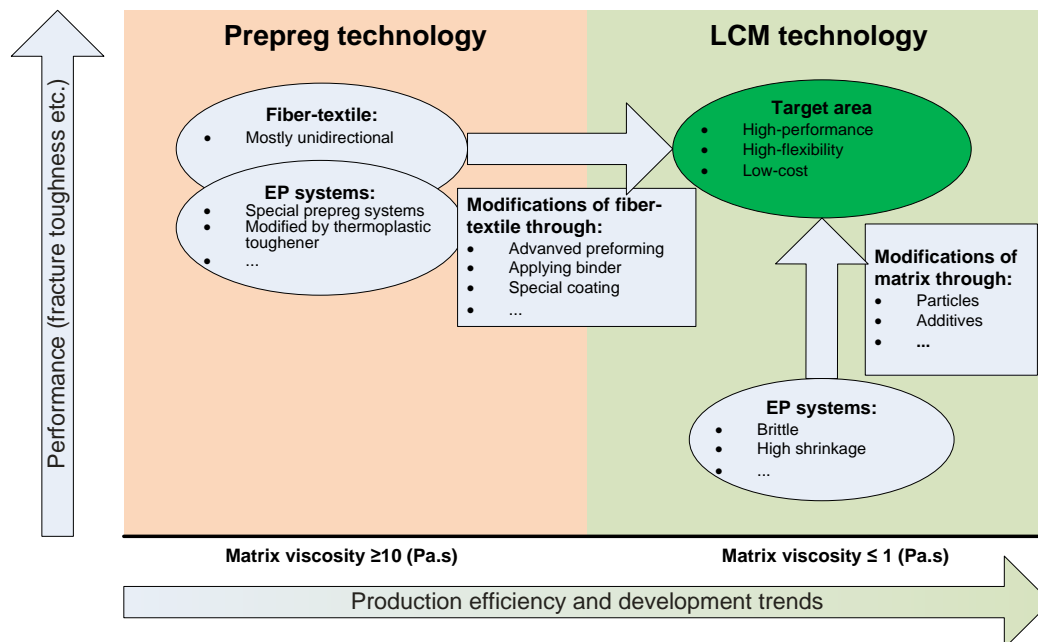


Figure 1.10: Comparison of LCM vs. prepreg methods and potential development trends by the material and processing aspects.

However, as mentioned earlier, liquid epoxy resin systems have mostly small molecule size for the good flowability, which inevitably leads to higher shrinkage after the polymerization process by creating a large single molecule and tend to be more brittle, compared to their

partially cured and even already modified prepreg counterparts. The shrinkage and brittleness of liquid epoxy resin systems is a critical issue, which leads to reduced mechanical properties in matrix-dominated fiber composite properties – particularly compression, and impact properties. In addition, the production introduced residual stress and distortion of the structure increases by the FRP structures that are fabricated by LCM processes. **As matrix is a critical weak point on the whole chain – especially by low-viscous resin for LCM processes, developing new high-performance matrix material is a trend of current development, in which modification of the matrix by nano-scale additives have shown a promising way** [16-18]. Figure 1.10 shows a comparison of the processing and properties of LCM vs. prepreg methods and potential development trends by the material and processing.

1.2 Research hypothesis

1.2.1 Functionalization of FRP with nanoparticles

In the continual quest to improve material properties to match the ever-increasing demands of societal and technological development, new and innovative composite materials with multi-functionalities and higher performance are sought. A promising way for the improvement of properties and for incorporating desired functionalities in FRPs is by the introduction of nano-scale functional fillers – simply called nanoparticles (NPs) – which possess certain qualities that could change or adjust the overall properties of the composite part.

By introducing effective NPs into the composites, a multi-scale hierarchical composite material – synergistic integrated from nano to micro scale components – could be tailored to display multi-functionalities. Multi-scale functional FRPs integrate high structural mechanical performance with a number of functional properties, including high mechanical performance, electrical/thermal conductivity, magnetic properties, frictional and wear performance, self-health-monitoring and even active response capability to outer conditions, as illustrated and listed in the Figure 1.11. The principle mechanism, actual development and potential application of the multi-scale functional FRPs are reported in several papers [18-23].

Modification of the resin matrix with NPs is especially attractive in LCM processes, allowing for a cost-efficient production of high-performance FRPs. The effectiveness of NPs is dependent on the chemical (composition, surface modification) and physical (size, morphology, stiffness and concentration) characteristics. However, depending on these characteristics, NPs may affect the critical impregnation-dominating aspects such as matrix cure kinetics, rheology and fiber-preform permeability. Therefore, “gradient functionalization” with respect to the application requirements is a smart way to synergistically balance the process and performance of the FRP structures, which will be explained in the following subchapter.

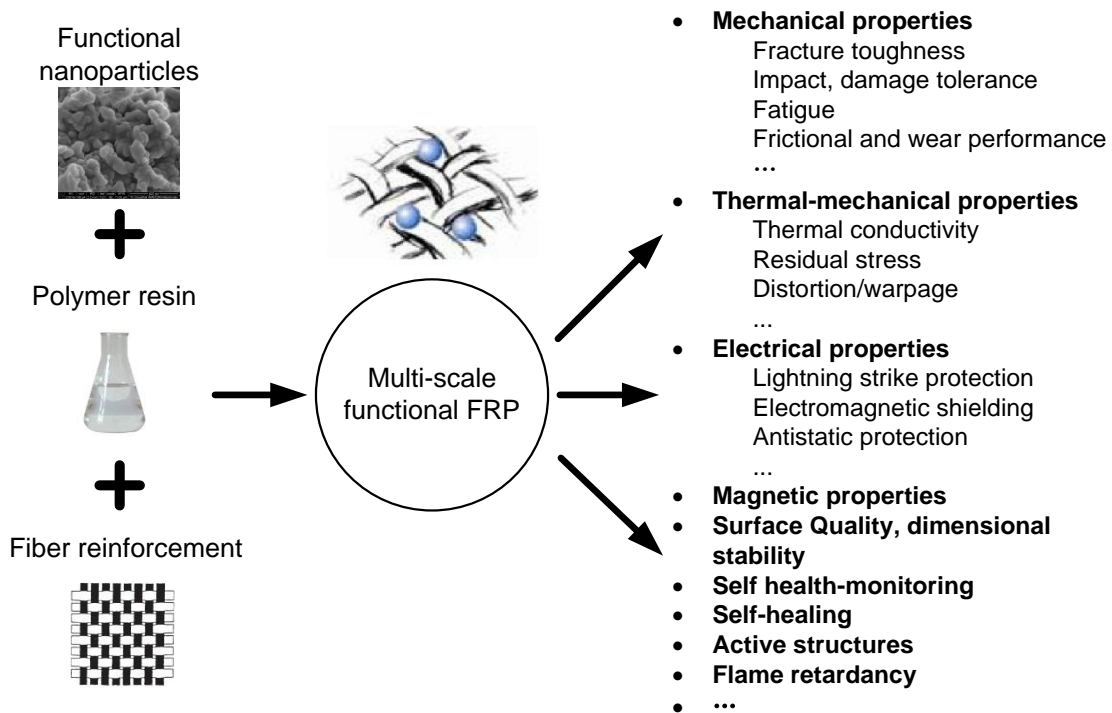


Figure 1.11: Application of multi-scale FRPs that are functionalized with nanoparticles

1.2.2 Gradient functionalization

Functional Gradient Materials (FGMs) or Functional Gradient Composites (FGCs) are characterized by spatial variation in material properties based on their application requirements. The FGMs are advanced materials in the family of engineering composites made of two or more constituent phases with continuous and smoothly varying compositions in a certain defined direction. FGMs are engineered based on different gradients of composition in the preferred material axis orientation according to the application condition. **Composite materials are based on the concept of “proper material combination for the right application” to achieve a new material that’s better than either of the starting materials, while FGMs are based on a one-step-further concept for the optimal combination and distribution of constituents at the right position in the structure.** Due to this characteristic, FGMs are superior to and more efficient than homogeneous single or multi-constituent materials [24-26]. Some representative examples of the FGMs from nature can be found in bone, teeth and bamboo (Figure 1.12). They, after thousands of years of natural evolution, are optimized for maximum structural properties with optimized distribution of each component. The cross section of a bamboo culm shows a functional graded distribution of the cellulose fibers – more fibers near to the outer region, which provides the optimum resistance to bending moment from its own weight and wind load [27-30]. Similarly, a tooth requires a high wear resistance outside (enamel) and a ductile inner structure for reasons of fatigue and brittleness. Furthermore, it requires a translucent outer area and a specific set of color nuances for reasons of aesthetics.

1 Introduction

In technical application, FGMs were first proposed around 1984-85 when Japanese researchers studied advanced materials for aerospace applications while working on a space plane project [31]. The body of the spaceplane will be exposed to a very high temperature environment (up to 2000°C), with a temperature gradient of approximately 1000°C between the outside and inside of the spaceplane. There was no uniform material that able to endure such conditions. Therefore, the researchers devised a new concept to fabricate a material by gradually changing (grading) the material composition (see Figure 1.13), and in this way improve both thermal resistance and mechanical properties [32].

There is a wide application potential for FGMs and it is expected to increase as the cost of material and fabrication processes is reduced by improving these aspects. Therefore, the functional gradient is relatively further developed in application with metallic or ceramic materials [24-26, 33, 34].

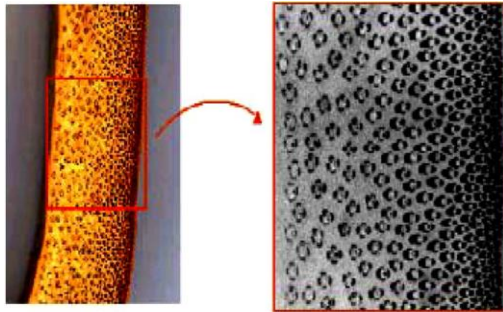


Figure 1.12: Functionally-graded fiber packing in bamboo [27, 30]

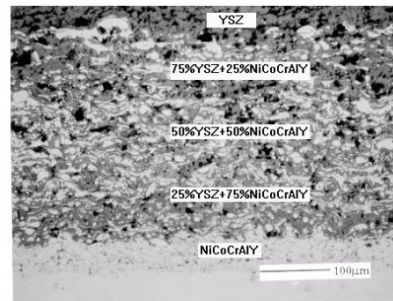


Figure 1.13: Functionally-graded $\text{ZrO}_2/\text{NiCoAlY}$ thermal barrier coating [32]

Considering the application requirements on the properties and functionalities of the FRP structures, it is obvious that the concept of the “functional gradient” could provide a good alternative for enhancing the properties of FRPs with optimized balance between cost, process efficiency and properties.

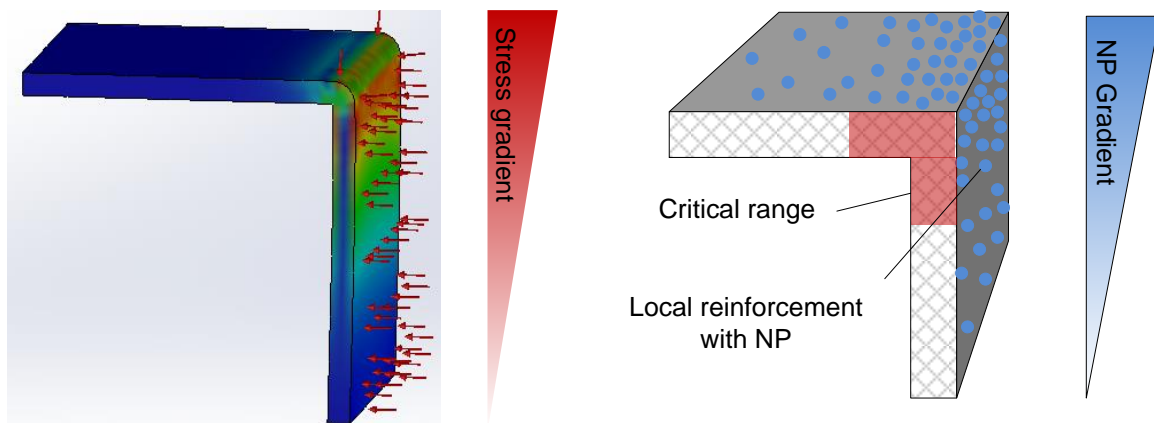


Figure 1.14: Gradient functionalization of FRP structures with NPs according to stress gradient

Impregnation with selective NP-modified epoxy matrix systems (different NP types or concentrations) enables an optimal gradient-functionalized FRP structure corresponding to the stress gradient during application. This improves the performance of FRPs and, at

the same time, guarantees production efficiency by minimizing the negative effects of NPs on the impregnation processes. The concept of multi-scale gradient with NPs in FRPs regarding the stress gradient is illustrated in the Figure 1.14. Accordingly, the impregnation process can be designed with multiple inlet/outlet positions applying matrix systems that are modified with selective NPs to harmonize the process with FRP properties and provide the optimal gradual reinforcement.

Considering the main proposed hypothesis, the focus of the work lies in the critical aspects regarding the interaction and correlation between materials (NP, epoxy matrix and fiber preform), process, and final properties with an emphasis on the functional gradient adjustment, with optimized material and process parameters. The concept of “functional-gradient FRPs” is a synergistic consideration and balance of the critical aspects in the whole FRP production chain – increased material properties, process efficiency and property optimization, with a final goal of efficient production of high-performance FRPs at low cost. This new concept has a great application potential in the future. The critical aspects regarding this hypothesis will be put forward and discussed further in Chapter 2 based on the current state of the field regarding the processing of NP-filled matrix systems and their properties.

2 State of the research

In this chapter, the current state of research and development regarding the critical aspects in the production of functional FRPs is reviewed. Considering the mutual interactions among the materials, process and properties, the literature review is concentrated on the critical material and process aspects that dominate the final properties. The goal is to clarify the current research status and point out the most scientifically and technologically critical challenges regarding material, process and property which are not fully investigated or solved yet.

2.1 Functionalization of FRPs with nanoparticles

2.1.1 Why nanoparticles?

According to the definition in ASTM [35] or ISO [36] standards, NPs are principally defined as a sub-classification of ultrafine particle with lengths in two or three dimensions greater than 1 nanometer and smaller than about 100 nanometers, and which may or may not exhibit a size-related intensive property. For primarily purpose to identify materials for which special provisions might apply, the definition to NP is adopted by the EU-commission and recommended as follows [37]:

»"Nanomaterial" is a natural, incidental or manufactured material containing particles, in an unbound state or as an aggregate or as an agglomerate and where, for 50 % or more of the particles in the number size distribution, one or more external dimensions is in the size range 1 nm - 100 nm.

In specific cases and where warranted by concerns for the environment, health, safety or competitiveness the number size distribution threshold of 50 % may be replaced by a threshold between 1 and 50 %.

By derogation from the above, fullerenes, graphene flakes and single wall carbon nanotubes with one or more external dimensions below 1 nm should be considered as nanomaterials. «

Compared to the standard big particles, the NPs show plenty of fundamental changes in the physical-chemical properties. As the NPs have very high ratio of specific surface area to volume, by application in FRPs, the NPs show an extreme high particle-matrix interphase, by which the functionality – effective load transfer, crack pinning etc. – could be maximized with minimum amount of particles. This is particularly important for final structure property, and also is one of the most important advantages compared to conventional big particles. Especially for the LCM fabrication of FRPs where the viscosity of the matrix is a dominating factor, the influence of the NPs on the rheological behavior of the resin matrix is rather small [16],

compared to the micron particles. Moreover, as the particle-filled matrix will be injected into a porous fiber preform by LCM fabrication, the flow and retention behavior of the particles is a critical aspect for both processing and properties, therefore NPs are more preferable to micron particles for modification of FRPs by LCM processes.

Various types of NPs are investigated or applied in FRPs, including quasi-spherical (all dimensions are similarly in nano size) ceramic NPs, i.e. Al_2O_3 , SiO_2 , SiC , and TiO_2 , fibrous NPs (diameter is in nano size, but length dimension is in micron size) such as single-/multi-walled Carbon Nanotubes (CNT), Carbon Nanofibers (CNF) or layered sheet-structural NPs (only thickness is in nano size, but width and length dimension is in micron size) including graphite, Graphene Nanoplatelets (GNP) and etc. The morphological characteristics and properties would lead to different influence for the process parameters and final properties, as illustrated and summarized in the following Figure 2.1.

Quasi-spherical nanoparticles:
 Al_2O_3 , SiO_2 , SiC etc.



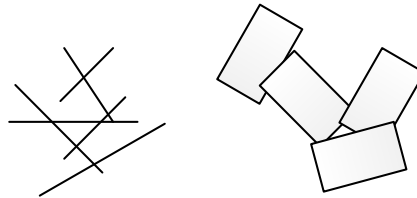
Advantages:

Easier for dispersion;
Lower cost;
Lower adverse effect on processing;
...

Disadvantage:

Low aspect-ratio;
higher density;
high loading;
...

Fibrous or sheet-structural nanoparticles: CNT, GNP etc.



High aspect-ratio;
Lower density;
Lower percolation concentration ;
...

Difficult to disperse;
Higher adverse effects on processing
(viscosity and etc.)
...

Figure 2.1: Illustration and comparison of quasi-spheric and other NPs

2.1.2 Multi-scale functional FRPs fabrication strategies

There are principally three different ways, as illustrated in the Figure 2.2, to introduce NPs into the FRPs: 1) modifying the matrix by mixing or in-situ growing the NPs in the matrix for impregnation; 2) modifying the fibers by coating/grafting or spraying of the NP on the fiber textile; 3) incorporation of the NP intermediate phase in the composites, for example inserting CNT paper as an interlayer into the FRPs or applying carrier-medium with NPs etc. Before evaluating these different methods, it is necessary to differentiate which kind of particles that

2 State of the research

are being considered – quasi-spherical, fibrous or sheet-structural NPs. The selection of the process steps relies, to a large degree, on the material and fabrication efficiency as well as cost, plus process robustness with the NP-filled matrix system.

The introduction of NPs may significantly influence the matrix flow behavior and permeability of the preform due to the increased interaction between the NPs, matrix systems and fibers – even in some cases leading to filtration of the particles along the flow length. The filtration behavior of the particle-filled suspension in the fibrous textile structure is dictated by both particle size and intra-fiber pore size – filament distance. Two main filtration mechanism – cake filtration and deep bed filtration – could be distinguished during LCM processing of particle-filled suspensions. Cake filtration is manifested by the partly physical volume capture due to the larger particle size than the intra-fiber gaps of the textiles – dominated by the physical size difference, while deep bed filtration is characterized by the gradual capture of particles smaller than the pore channels – dominated by surface interaction, electrostatic attraction etc. The ratio between the particle size and pore channels D/d (filter grain/particle diameter) was pointed out to be the most critical factor which governs the flow behavior and filtration mechanism in a granular porous media [38-40].

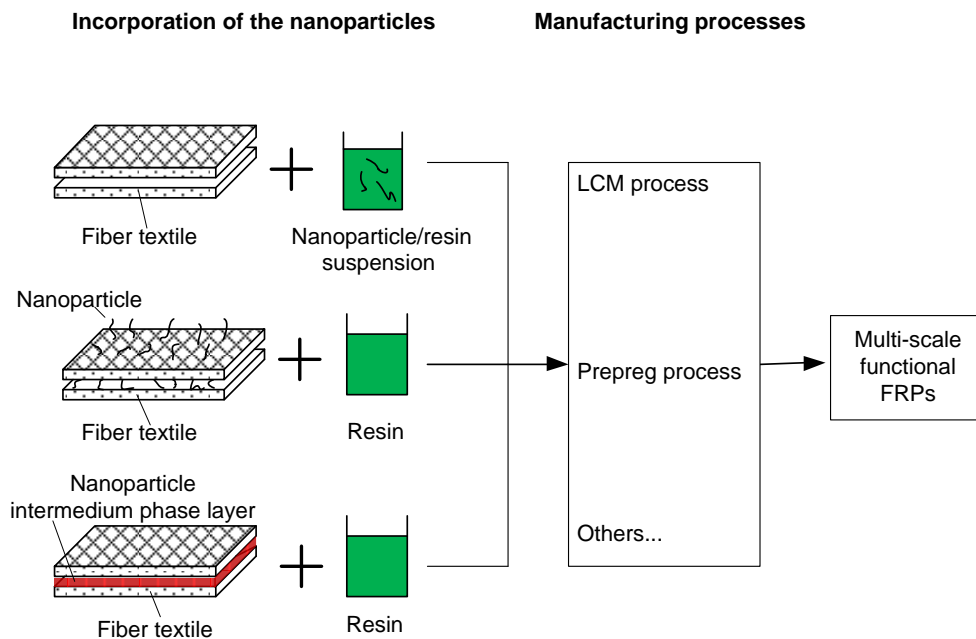


Figure 2.2: Incorporation methods of NPs to manufacture multi-scale functional FRPs

In LCM processes by injecting the NP-modified matrix into the fiber preform, fibrous or sheet-structural carbon NPs – CNT, GNP etc. – could face severe retention which leads to poor impregnation of the preform [41, 42], due to the large size in length or width of these particles which are critical to the filter grain/particle diameter ratio. In the application in LCM processes, cake filtration is manifested by the partly volume capture due to the larger CNT or GNP length than the intra-fiber gaps of the textiles. As long as the particles are captured by the intra-fiber

gaps, the permeability of the porous medium will greatly decrease, and at the same time, the viscosity of the dispersion begins to rise due to the increased concentration of the particles. Therefore, the combined filtering and viscous resistance effect remarkably decrease the impregnation speed, length and quality. Gojny et al [43] investigated a standard RTM technique to produce CNT/glass/epoxy multi-scale composite, and reported that it is a great challenge to manufacture a composite by resin with CNT contents of more than 0.5 wt%, due to the enormous surface area of CNTs and the resulting increase in dispersion viscosity. So, the introduction of these fibrous or sheet-structural NPs are much more preferable by the process 2 and 3 as shown in the Figure 2.2, or only by modified impregnation strategies which is a critical aspect to be investigated in this thesis. For some further information on the process 2 and 3, the readers are redirected to the following papers [22, 44-48].

In comparison, quasi-spherical NPs are much easier to be dispersed in matrix, and also could be much easier processed by impregnation processes – due to the much lower D/d ratio. Therefore, they are much more preferably processed by the method 1. Among the different quasi-spherical ceramic NPs, silica (SiO_2) NP is until now mostly investigated for application in FRPs [17, 49]. There are also some works that studied alumina (Al_2O_3) NP as functional fillers in epoxy [50, 51]. These works on the silica and alumina NPs are mostly concentrated on investigating the influence of the NPs on the final properties, but comparatively very little consideration on the processing aspects – especially particle flow and retention behavior. As a quasi-spherical ceramic NP, boehmite is an aluminum hydroxide (AlOOH), which is often used as a precursor for many aluminum products. Boehmite particle is price-efficient and the hydroxyl groups on the surface could be directly used as functional groups, or easily be modified to different functional groups (amine, acetic acid, lactic acid etc.) to generate a good chemical stability and improved particle-matrix adhesion by possible covalent connection. According to earlier studies, boehmite NPs are shown to be quite efficient for enhancing the mechanical properties of FRPs [52-54].

Even though these advantages, there are hardly any works found that investigate and describe the critical processing aspects and the influence on the FRP properties by application of boehmite NPs. **Therefore, in this thesis boehmite is selected to be the basic reference NP to modify the properties of FRPs by LCM process. At the same time, commercial silica and CNT particles are also selectively investigated to compare some of the critical aspects by the production and final properties of the functional gradient FRPs.**

Considering these aspects, the literature review focuses on the most critical aspects on processing of NP-epoxy suspension and fabrication of multi-scale functional FRPs by LCM process.

2.2 Materials

2.2.1 Nanoparticle-epoxy matrix

2.2.1.1 Cure kinetics

The curing of epoxy is a complex chemical reaction that begins mostly from a liquid state with small monomers to a semi- or solid state, where the small molecules build up a complex 3D network structure. The curing reaction is coupled by both chemical and thermal effects: the reaction is strongly dependent on cure temperature but at the same time, it also generates exothermic thermal energy. Therefore, the identification of the cure kinetics needs synergistic consideration of the chemical and thermal effects.

Most studies by far are concentrated on cure kinetics and rheological characterization and modeling of pure epoxy resin systems [55-59]. With the addition of NPs, the curing process gets more complex due to the possible accelerating or inhibiting effects directly on the curing and rheological behavior. The influence of NPs could be quite complex since both chemical as well as physical effects are involved. According to the earlier studies, both inhibiting and acceleration effects of NPs on the kinetics have been reported. NPs without surface treatment or with hydrophobic surface characteristics – as for the case in mostly investigated silica particles [60, 61] – are reported to be inert to the epoxy reaction with no significant change on the activation energy and the reaction profile [51, 61]. In comparison, NPs with special surface modification or hydrophilic surface characteristics showed mostly an accelerating effect on the reaction kinetics of the original epoxy resin, which is typically the case for alumina NPs [62, 63] or fumed silica [64]. For example, the hydroxyl groups (-OH) can spend hydrogen atoms which are essential for the opening of oxirane rings of the resin or epoxy.

It is to be mentioned that these studies are mostly concentrating on the preliminary investigations on the influence of the silica or alumina NPs on the cure kinetics with very low NP concentrations. There are hardly any reported studies directly relating the modeling of cure kinetics and rheology of these NPs or the reference boehmite NP system with high concentrations – up to 15 wt% as target in this thesis, for the application in LCM processes to fabricate FRP structures. Of course, with the special surface characteristics and higher concentrations of the boehmite NPs concentrations, the interactions could be much more complex with a remarkable influence on the process and final properties.

Differential Scanning Calorimetry (DSC) is a widely used method for analyzing the curing process. However, quite different DSC approaches are available for obtaining this kinetic information, based on the material reaction mechanism, curing speed and curing process. By the curing characterization of the epoxy with DSC, the degree of cure at each point of time

($\alpha(t)$) is determined from the heat released up to that time ($\Delta H(t)$), the heat released during heat-up and equilibration (H_{init}) and the total heat released during the reaction (H_{total}):

$$\alpha(t) = \frac{H_{init} + \Delta H(t)}{H_{total}} \quad \text{where} \quad \begin{array}{l} \alpha(t): \text{degree of cure time } t \\ \Delta H(t): \text{released heat} \\ H_{init}: \text{heat released during} \\ \text{heat-up and equilibration} \\ H_{total}: \text{total heat released} \\ \text{during the reaction} \end{array} \quad \text{Eq. 2.1}$$

Considering that, the heat released during heat-up and equilibration (H_{init}) is normally hard to detect, therefore, the degree of cure is normally determined by the rest enthalpy (H_{rest})

$$\alpha(t) = 1 - \frac{H_{rest}}{H_{total}} \quad \text{where} \quad H_{rest} = H_{total} - (H_{init} + \Delta H(t)) \quad \text{Eq. 2.2}$$

Generally, the kinetic models could be categorized into either phenomenological models or mechanistic models. Mechanistic models are obtained from the balances of reactive species involved in the reaction, which makes it also hard to develop and derive sometimes due to the complexity of cure reactions. In comparison, phenomenological models are simple rate equations without considering the complex details of reactive species and their reaction. Therefore, phenomenological models are much simpler to develop and mostly could also accurately describe and predict the kinetic behavior, which is why it is more preferable in the practice. The difference between these two methodologies are discussed and overviewed elsewhere [65]. Considering this, in this work only phenomenological models are taken into consideration for the modeling.

The reaction rate of a single step process is normally described by a rate function $K(T)$ which is dependent on the temperature (T) and a conversion function $f(\alpha)$ as following:

$$\frac{d\alpha}{dt} = K(T)f(\alpha) \quad \text{where} \quad \begin{array}{l} \alpha: \text{cure} \\ K(T): \text{rate function} \\ f(\alpha): \text{conversion function} \end{array} \quad \text{Eq. 2.3}$$

This function is principally applicable for both isothermal and non-isothermal curing analysis. If a constant heating rate DSC analysis is considered, the above function could be also rearranged as follows:

$$\beta \frac{d\alpha}{dT} = K(T)f(\alpha) \quad \text{where} \quad \beta: \text{heating rate} \quad \text{Eq. 2.4}$$

It needs to be pointed out that Eq. 2.3 and Eq. 2.4 only describe the cure rate of a single-step reaction process. For a multi-step process that includes several parallel reactions, the rate function has a complex form. For example, the overall process rate that involves two parallel reactions could be described as follow [66]:

$$\frac{d\alpha}{dt} = K_1(T)f(\alpha_1) + K_2(T)f(\alpha_2) \quad \text{where} \quad \text{conversion } \alpha = \alpha_1 + \alpha_2 \quad \text{Eq. 2.5}$$

The temperature dependent reaction rate function $K(T)$ can be expressed by an Arrhenius relationship:

2 State of the research

$$K_i(T) = A_i e^{\left(-\frac{E_i}{RT}\right)} \quad \text{where} \quad \begin{array}{l} i = 1, 2 \dots \\ A: \text{pre-exponential factor} \\ E: \text{activation energy} \\ R: \text{ideal gas constant} \\ T: \text{absolute temperature} \end{array} \quad \text{Eq. 2.6}$$

So, based on the rate function, the development of the model is to determine the sets of reaction triplet – A : pre-exponential factor which is the frequency of vibrations of the activated complex [66], E : activation energy for the reaction and $f(\alpha)$: conversion (reaction mechanism) function. The conversion function $f(\alpha)$, however, could vary quite differently depending on the reaction mechanism. Although there are significant numbers of reaction models, they can be principally categorized into two major types: n th order (accelerating or decelerating) and autocatalytic. Normally, the reaction mechanism could be differentiated by the characteristic kinetic curves of the three reaction models, which will be explained in more detail in 3.1.2.

2.2.1.1.1 Dynamic vs. Isothermal DSC analysis

The kinetic model parameters could be estimated by means of both dynamic and isothermal curing DSC experiments. The selection of dynamic or isothermal modeling is firstly dependent on the interested curing process in the practice. For the modeling, it is possible to develop kinetic parameters both by dynamic and isothermal DSC measurements. In theory, a dynamic DSC trace should contain all the kinetic information normally embodied in a series of isothermal experiments [67], which makes the kinetic analysis of non-isothermal DSC more attractive. Moreover, it is also much easier to detect the reaction complexity by dynamic DSC analysis where multiple reaction peaks are easier to be detected and observed.

However, a practical issue in dynamic DSC experiments is that it is more difficult to identify the reaction mechanism – n^{th} order, autocatalytic or even diffusion-dominated reaction – as both time and temperature changes. Without knowing the reaction mechanism, it is hard to select a proper reaction model that is critical to fully describe the curing process. The adequateness of a rational rate equation to describe the process mechanism exceeds far beyond the goodness/quality/accuracy of numerical evaluation: an excellent data fit for a reaction could be achieved with various kinds of mathematical functions, but it does not necessarily fully describe the real reaction mechanism [57]. Therefore, for the investigation of a new reaction where the reaction mechanism and order are not known, the isothermal method is to be suggested, which enables to detect the reaction mechanism quite simply. Although the isothermal experiments may be more time consuming, they often generate more reliable kinetic parameters.

Moreover, by dynamic DSC process, it is not possible to determine and account for the diffusion-controlled reaction, which is often the case in the isothermal curing (will be discussed in the next section). At the same time, it needs to be pointed out that it doesn't exist a "strict"

isothermal curing, due to the practical issue of heating up and calibrating the DSC for the desired isothermal temperature which in the practice takes several minutes. Nevertheless, this issue is only critical by fast curing systems where most of the reactions might be finished directly during the calibration phase. This issue is studied by Javdanitehran et al. [68] who proposed an iterative method to compensate the lost initial enthalpy. By normal or slow reactive systems like investigated in this thesis, the lost information during the heating up is rather small – there is still enough kinetic information available for accurately developing the model data.

For an unknown material system, a combination of both dynamic and isothermal experiments is the best way to evaluate the different methods and establish kinetic models, considering the curing speed, reaction complexity and reaction temperature. A truly good model should be able to simultaneously describe both types of runs with the same kinetic parameters. **In this thesis, the curing behavior is investigated by both dynamic and isothermal curing processes; the model development is based on the isothermal process and cross validated by predicting the dynamic curing behavior of the material.**

2.2.1.1.2 Reaction mechanism and model evaluation

Although there are significant numbers of reaction models, they can be principally categorized into **two major types: n^{th} order (accelerating or decelerating) and autocatalytic**. The first crucial step for the cure kinetics modeling is to find out how the reaction proceeds. These two reaction mechanisms could be differentiated by the time where the maximum rate of heat evolution is reached: materials obeying n^{th} order kinetics will have the maximum rate of heat evolution at time zero (decelerating), while an auto-catalyzed material will have its maximum heat evolution at 30-40% of the reaction time [69, 70]. Nevertheless, various models are reported and available, depending on the complexity of the reaction, as shown in the following Table 2.1.

Table 2.1: Mostly used reaction kinetic models

Description	Formula	Parameters
Accelerating (n^{th} order)	$\frac{d\alpha}{dt} = K n \alpha^{(n-1)/n}$	<i>K: rate function</i> <i>n: reaction order</i>
Decelerating (n^{th} order)	$\frac{d\alpha}{dt} = K(1 - \alpha)^n$	<i>K: rate function</i> <i>n: reaction order</i>
Autocatalytic reaction	$\frac{d\alpha}{dt} = K \alpha^m (1 - \alpha)^n$	<i>m, n: reaction order</i>
Kamal-Sourour model (n^{th} order + autocatalytic)	$\frac{d\alpha}{dt} = (K_1 + K_2 \alpha^m)(1 - \alpha)^n$	<i>K₁, K₂: rate function</i>
Karkanias-Partridge model (n^{th} order + autocatalytic)	$\frac{d\alpha}{dt} = K_1(1 - \alpha)^{n_1} + K_2 \alpha^m (1 - \alpha)^{n_2}$	<i>m, n₁, n₂: reaction order</i>

In addition, during the isothermal curing, the curing reaction initially begins in a liquid phase, where bimolecular combination is the dominant mechanism of curing termination. As the curing goes on and T_g exceeds the curing temperature (T_c), the reaction rate will be reduced by

2 State of the research

orders of magnitude as the “vitrification” effect due to the glass transition exerts a dramatic restriction on bimolecular reactions. **The “vitrification” effect strongly reduces propagation probability of the free reactive groups and changes the reaction mechanism as diffusion controlled.**

Table 2.2: Mostly applied model factors for diffusion-controlled reaction

Description	Formula	Parameters
Fournier et al. [71]	$f_d(\alpha) = \frac{2}{1 + \exp((\alpha - \alpha_c)/C)} - 1$	α_c : critical cure degree C : fit parameter
Cole et al. [72]	$f_d(\alpha) = \frac{1}{1 + \exp(C(\alpha - \alpha_c))}$	α_c : critical cure degree C : fit parameter
Rabinowitch et al. [73]	$k_i = \frac{1}{\frac{1}{k_d} + \frac{1}{k_{c,i}}}$ $k_d = A_d \exp\left(-\frac{E_d}{RT}\right) \exp\left(-\frac{b}{0.00048 \cdot (T - T_g) + 0.025}\right)$	E_d : diffusion-controlled pre-exponential factor E_d : diffusion-controlled activation energy b : fit parameter

The above described n^{th} order or autocatalytic models can just represent the normal chemical reaction without diffusion domination, therefore it needs to be further modified for fully describing the isothermal curing behavior. The mostly applied diffusion controlled reaction models were put forwarded by Fournier [71], Cole [72] and Rabinowitch [73] et al., as listed in the Table 2.2.

2.2.1.2 Rheology

Parallel to the cure kinetics, viscosity is a critical material parameter as it directly dominates the flow behavior and the process boundary conditions – process window and efficiency for fabrication of FRPs. For example, in LCM manufacturing of FRPs, there is a strict criterion on viscosity limit, normally 1 Pa·s even in some cases just 0.5 Pa·s where low permeable fiber preform is to be impregnated, of the applicable epoxy matrix. When the viscosity is higher than this value, it cannot effectively impregnate the fiber beds that have rather small porous channels, especially at high fiber volume fraction for high-performance applications. At the same time, higher viscosity also increases the potential failure due to the decreased impregnation capabilities of the resin.

The development of the viscosity is dominated by the cure kinetics – the increased molecular size due to the curing. Besides, it is also affected by pressure, temperature, time, shear rate and fillers. Extensive works are conducted on this topic and different models were developed: from simple empirical models, Arrhenius models to detailed models based on free volume analyses. The effects of these parameters and models are extensively discussed and overviewed in paper [74]. In this thesis, the pressure and shear rate are approximated to be constant, therefore the viscosity can be considered only as a function of temperature (T), cure (α) and NP content (C).

$$\eta = \eta(T, \alpha, C) \quad \text{where} \quad \begin{array}{l} T: \text{temperature} \\ \alpha: \text{cure} \\ C: \text{filler content} \end{array} \quad \text{Eq. 2.7}$$

Generally, the dependence of viscosity on temperature for uncured resin system is mostly described by William–Landel–Ferry (WLF) equation, derived from the free volume theory [75]. For the change of viscosity due to cure (time and temperature), a modified WLF model [55, 76], Castro-Macosko model [77] or a combined model of the both [55, 78] were studied in several papers.

Table 2.3: mostly used rheological models

Description	Formula	Parameters
WLF	$\eta = \eta_g \exp\left[-\frac{C_1(T - T_{g0})}{C_2 + T - T_{g0}}\right]$	η_g : the viscosity at the glass transition T_{g0} : glass-transition temperature of the uncured system C_1, C_2 : fit parameters
Modified WLF	$\ln \frac{\eta}{\eta_g} = -\frac{C_1(T)(T - T_g(T, t))}{C_2(T) + T - T_g(T, t)}$	$C_1(T), C_2(T)$: temperature dependent parameters
Castro-Macosko model	$\eta = \eta_\infty \exp\left(\frac{E_\eta}{RT}\right) \left(\frac{\alpha_{gel}}{\alpha_{gel} - \alpha}\right)^{(A+B\alpha)}$	E_η : activation energy for flow η_∞ : viscosity at T_∞ α_{gel} : cure degree at gelation A, B : fit parameters
Combined WLF+Castro-Macosko model	$\eta = \eta_g \exp\left[\frac{C_1(T - T_{g0})}{C_2 + T - T_{g0}}\right] \left(\frac{\alpha_{gel}}{\alpha_{gel} - \alpha}\right)^n$	n : fit parameter

2.2.2 Fiber preform

2.2.2.1 Filament distance and preform porosity

The filament distance or porosity in the preform is one of the dominating factors that determine the preform permeability and matrix flow behavior in LCM processes, especially considering the particle-filled suspension. As mentioned earlier, the flow behavior of the particle-filled suspension in the fibrous textile structure is dictated by both particle size and intra-fiber pore size – filament distance. The ratio between the particle size and pore channel is the most critical factor which governs the flow behavior and filtration mechanism [38, 39].

If a standard textile microstructure is considered, two different basic elements at different scales could be differentiated: rovings and filaments. Correspondingly, there are two different scales of pores: macro-scale pores between the rovings and micro-scale pores between the filaments. Both the macro and micro-scale pores are stochastic variables that are strongly dependent on the roving size, textile architecture, surface weight, as well as compaction and draping conditions, as shown in the Figure 2.3 and Figure 2.4.

2 State of the research

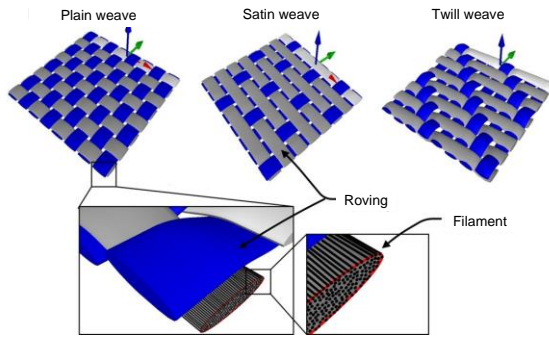


Figure 2.3: Textile structures

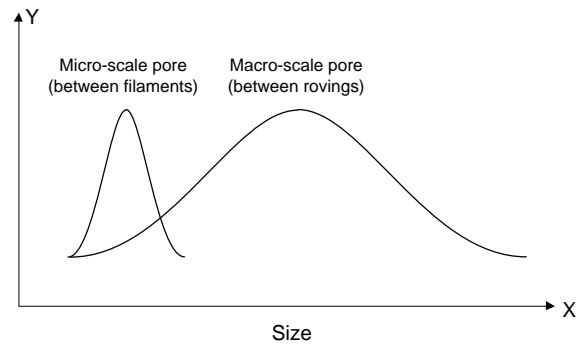


Figure 2.4: Macro-/micro-scale pores in textiles

The challenges in characterizing the porosity lies on one hand on the scale-crossed distribution characteristic of the macro and micro pores, as shown in the Figure 2.4, on the other hand on the stochastic distribution characteristic of both pore geometries. The scale-crossed distribution characteristic of the pore size makes it difficult to be fully characterized by standard picture analysis methods – due to the inevitable restriction in resolution capability. Secondly, the stochastic distribution characteristic of both macro and micro pores makes it quite challenging to be fully described, which demands advanced statistical and mathematical models and methods. For quantifying and modeling the textile or pore geometry, micro-computed tomography (Micro-CT) [79, 80] or optical microscopy [81, 82] are mostly applied, combined with different mathematical statistical models. Even if they showed satisfying results considering the macroscopic tow and spacing – macro pores, however, the micro pores between the filaments were mostly simplified to be homogenous or directly neglected due to resolution limit, experimental or calculation cost and time. **However, the micro pores, in comparison, are presumably much more critical to the particle flow behavior, as they are much smaller and mostly critical for the filtration of the NPs.**

There are also other studies that focused on the characterization of filament distribution [83-85], but concentrating on the mathematical modeling of the stochastic distributed filaments, not really the filament distance – pore size. Most recently, there are also some studies are reported to characterize the apparent dual-scale porosity by industrial porometry [86, 87]. Therefore, **this work focuses on the systematically characterizing of the both macro and micro pores – distance between rovings and filaments – by an improved picture analysis and computation method**, which will be described in the chapter 3.

2.2.2.2 Permeability

Permeability is a critical property of fiber-textile or preform, which determines the flow speed and amount of a fluid in a porous media. The first attempt for explaining the fluid behavior in a porous medium was done by Darcy in 1856, by experimental investigation of water flow velocity through a vertical column of sand with known pressure gradient. Based on his

observation, he derived and put forward an empirical formula to describe the flow of fluids through porous media, which is known as Darcy's law [88, 89]:

$$U = v\varepsilon = -\left(\frac{K}{\eta}\right) \nabla P \quad \text{where} \quad \begin{array}{l} U: \text{darcy velocity} \\ v: \text{apparent velocity} \\ \varepsilon: \text{preform's porosity} \\ K: \text{permeability tensor} \\ \eta: \text{dynamic viscosity} \\ \nabla P: \text{pressure gradient} \end{array} \quad \text{Eq. 2.8}$$

The applicability of Darcy equation is based on following assumptions:

- Fully saturated flow on a *homogenous* porous medium;
- The fluid used in the experiment is *Newtonian* (viscosity independent on the shear rate).
- The flow should be a laminar flow with Reynolds's number: $0 < \text{Re} < 10$

The applicability of Darcy's law to describe the flow in multi-scale porous media has been subject to discussions as it is based on simplification of the dual-scale characteristic of the textile porous structure as homogenous, however, it has been widely accepted as a suitable, yet simple method.

For a single-phase, incompressible flow with full saturation on a stable porous medium without absence of source/sink term, the mass conversation equation for a representative volume element during flow can be described by the well-known continuity equation, as follows:

$$\nabla \cdot U = 0 \quad \text{Eq. 2.9}$$

By combining the continuity equation with the Darcy equation as in Eq. 2.8, the equation for the governing function for pressure gradient is as follows

$$\nabla \cdot \left(-\frac{K}{\eta} \nabla P\right) = 0 \quad \text{Eq. 2.10}$$

It needs to be kept in mind that, the Eq. 2.10 is a simplified description of single-phase flow behavior in a porous media with the assumption of full saturation. Therefore, K is considered a saturated permeability. Based on the saturation behavior of the fluid based on the dual-scale multi-phase flow characteristics based on the fiber preform pore size distribution and interaction between the liquid and gas phases, **it is possible to differentiate the saturation dependent un-saturated permeability from the saturated permeability with a relative permeability factor** [90, 91] $K_r(S) \in [0, 1]$, where $K_{unsat} = K_{sat} * K_r(S)$. Further details regarding the influence of dual-scale and multi-phase flow on the permeability and flow simulation will be further discussed later in the 3.3.2: Flow simulation.

2.2.2.2.1 Analytical solution: 1D linear flow

By the simplified governing equation for pressure gradient as showed in Eq. 2.10, it is possible to solve the flow velocity or flow front dependency on the pressure by analytically. For 1D linear flow studies, the Eq. 2.10 can be written as following:

2 State of the research

$$\frac{\partial}{\partial x} \left(-\frac{K}{\eta} \frac{\partial P}{\partial x} \right) = 0 \quad \text{Eq. 2.11}$$

For a constant textile permeability and fluid viscosity,

$$-\frac{K}{\eta} \left(\frac{\partial^2 P}{\partial x^2} \right) = 0 \quad \text{Eq. 2.12}$$

Which results in a Laplace's equation

$$\frac{\partial^2 P}{\partial x^2} = 0 \quad \text{Eq. 2.13}$$

By integrating the Laplace's equation twice, it can be derived that the pressure is a linear function of flow length

$$P(x) = ax + b \quad \text{Eq. 2.14}$$

Therefore,

$$p(x) = p_0 - \frac{p_0 - p_f}{x_f} x \quad \text{where} \quad \begin{array}{l} p_0: \text{inlet injection pressure} \\ p_f: \text{flow-front pressure} \\ x_f: \text{flow front} \end{array} \quad \text{Eq. 2.15}$$

So the Darcy equation in Eq. 2.8 can be rewritten as

$$v = -\frac{K}{\eta \varepsilon} \frac{p_f - p_0}{x_f} \quad \text{Eq. 2.16}$$

By linear flow studies, *for a constant porosity material with constant injection pressure*, the pressure gradient could be seen as linear decay between the inlet and flow front, so the Eq. 2.16 can be re-written as in differential from:

$$K_{local} = \frac{v \eta \varepsilon x_f}{\Delta p} \quad \text{where} \quad \begin{array}{l} \Delta p = p_0 - p_f: \text{pressure} \\ \text{difference between inlet} \\ \text{and flow front} \end{array} \quad \text{Eq. 2.17}$$

Or in the integral form

$$K_{global} = \frac{\eta \varepsilon x_f^2}{2 t_f \Delta p} \quad \text{where} \quad t_f: \text{flow front time} \quad \text{Eq. 2.18}$$

By the differential and integral form of the Darcy law, two different permeability: local permeability as in Eq. 2.17 and global permeability as in Eq. 2.18 can be differentiated. Among them, local permeability is more sensitive for local fluctuations in flow front and dependent on the time gap Δt by which the velocity is measured. In comparison, global permeability is based on integral evaluation of the whole flow process. Besides, a concurrent permeability measurement procedure (CPMP) was put forward: Ferland et al. [92] applied an interpolation method that based on a least-square fitting of experimental flow front and pressure data to estimate a permeability that is self-corrected to Darcy law. A similar improved method that is based on interpolation, Squared Flow Front method (SFF method), is mentioned more recently in second international benchmarking for permeability measurement [93], as follows:

$$K_{SFF} = \frac{m \cdot \eta \cdot \varepsilon}{2 \Delta p} \quad \text{where} \quad \begin{array}{l} m: \text{least-square-fit slope of} \\ \text{data set } (x_f^2, t) \end{array} \quad \text{Eq. 2.19}$$

The methods that are based on least-square fit of experimental data are more favorably applied for permeability calculation as they are based on statistical approximation by excluding the experimental uncertainty of the local flow front development and provide the permeability data with the lowest errors.

2.2.2.2.2 Analytical solution: 2D radial flow

For a 2D radial flow case in *quasi-isotropic material*, the Eq. 2.10 can be written as:

$$U = v\varepsilon = -\left(\frac{K}{\eta}\right)\frac{\partial p}{\partial r} \quad \text{where } r: \text{flow radius } \sqrt{x^2 + y^2} \quad \text{Eq. 2.20}$$

The isotropic permeability is calculated by solving the Laplace equation in polar coordinates, as following [94, 95]:

$$K = \{r_f^2 [2\ln(r_f/r_0) - 1] + r_0^2\} \frac{1}{t} \frac{\varepsilon\eta}{4\Delta p} \quad \text{where } \begin{array}{l} r_f: \text{flow front radius} \\ r_0: \text{injection radius} \end{array} \quad \text{Eq. 2.21}$$

Similar to the SFF method as in Eq. 2.19 for 1D linear flow case, the isotropic permeability for 2D radial flow can be calculated in the improved form by least-square-fit slope of flow front development as follows:

$$K = F_{iso} \frac{\varepsilon\eta}{4\Delta p} \quad \text{where } \begin{array}{l} F_{iso}: \text{least-square-fit slope} \\ \text{of data set } (\{r_f^2 [2\ln(r_f/r_0) - 1] + r_0^2\}, t) \end{array} \quad \text{Eq. 2.22}$$

For an *anisotropic material*, where the flow front shows an elliptical form, the physical domain should be firstly transferred to an equivalent quasi-isotropic system [95, 96], therefore, the same equation as in the Eq. 2.21 applies for the equivalent radius in the quasi-isotropic system, as follows:

$$K_e = \{\bar{r}_f^2 [2\ln(\bar{r}_f/\bar{r}_0) - 1] + \bar{r}_0^2\} \frac{1}{t} \frac{\varepsilon\eta}{4\Delta p} \quad \text{where } \begin{array}{l} \bar{r}: \text{equivalent radius } \sqrt{ab} \\ a: \text{ellipse semi-major axis} \\ b: \text{ellipse semi-minor axis} \end{array} \quad \text{Eq. 2.23}$$

The permeability in the main axis of the ellipse could be then further calculated by:

$$K_a = \sqrt{\frac{1}{\alpha}} K_e, \quad K_b = \sqrt{\alpha} K_e \quad \text{where } \alpha = \frac{b^2}{a^2} = \frac{K_b}{K_a}: \text{anisotropy factor} \quad \text{Eq. 2.24}$$

For more information regarding the evaluation algorithm of 2D permeability, the readers are redirected to the following benchmarking study as a joint investigation between two institutes with the participation of the author [97]. The same concept of equivalent quasi-isotropic system also applies for 3D ellipsoid flow studies and permeability calculation of the main permeability components [98].

2.2.2.2.3 Experimental determination of permeability

While studies were conducted for predicting the permeability analytically or by simulation, as by Kozeny-Carman [99, 100] or Gebart [101] models, the practical application of these

2 State of the research

methods is still being challenged due to lack of robustness and general applicability. Due to the complexity in the textile porous structure depending on the textile type and compaction behavior, which can significantly influence the permeability and flow behavior. Currently, the most reliable and widest used method for permeability characterization is the conduction of experiments. Experimental permeability measurement methods can be principally categorized into unsaturated (transient) and saturated (stationary) permeability methods for all 1D, 2D and 3D flow studies, as illustrated in the following Figure 2.5. The permeability measurements could be carried out with different boundary conditions – constant injection pressure or volume/mass flow. Different methods could be applied for the flow-front tracking by unsaturated or for volume/mass flow measurement by saturated permeability measurements, as follows [102]:

- Unsaturated (transient) method by flow-front tracking with optical, pressure, capacitive, dielectric, ultrasonic etc. sensors.
- Saturated (stationary) method by volume flow measurement: gravimetric.

By 1D linear-flow experiments, the fluid propagates through the reinforcing fabric in one dimension, therefore, to characterize the full in-plane permeability tensor of the reinforcing material, at least three experiments (0° , 45° and 90°) are required. Moreover, linear flow experiments are also sensitive to experimental errors such as race tracking and so on, which demands proper sealing of the textile's edges to guarantee a good one-dimensional flow. By contrast, the radial-flow experiment is based on injecting the test fluid through a central injection point, resulting in an elliptical shape of the flow front when the fluid propagates through the reinforcing material. Therefore, radial-flow experiments allow, theoretically, for measuring the in-plane permeability tensor with a single experiment without extra effort for sealing and less errors.

Generally, under a stable flow condition – incompressible flow on a stable porous medium with constant porosity – the permeability is a constant value, independent of the measurement condition and parameters. However, in the practical measurements, **due to the simplification of the dual-scale porosity of fiber-textile to be a homogenous porous material, the apparent flow front observed in the experimental condition could deviate from the real flow front – depending on the macro/micro-flow dominated flow mechanism or multi-phase saturation behavior**, as illustrated in the Figure 2.6. Besides, depending on the test fluid and surface interactions between the fiber and fluids, the capillary effect, fiber swelling (mostly by natural fibers), or even particle filtration – which is the case on this work – could all lead to a deviation or change of the permeability along the flow length. Therefore, in this thesis, the interactions and influence of the different test fluids, especially the particle-filled matrix, on the permeability of the preform will be investigated as a critical aspect.

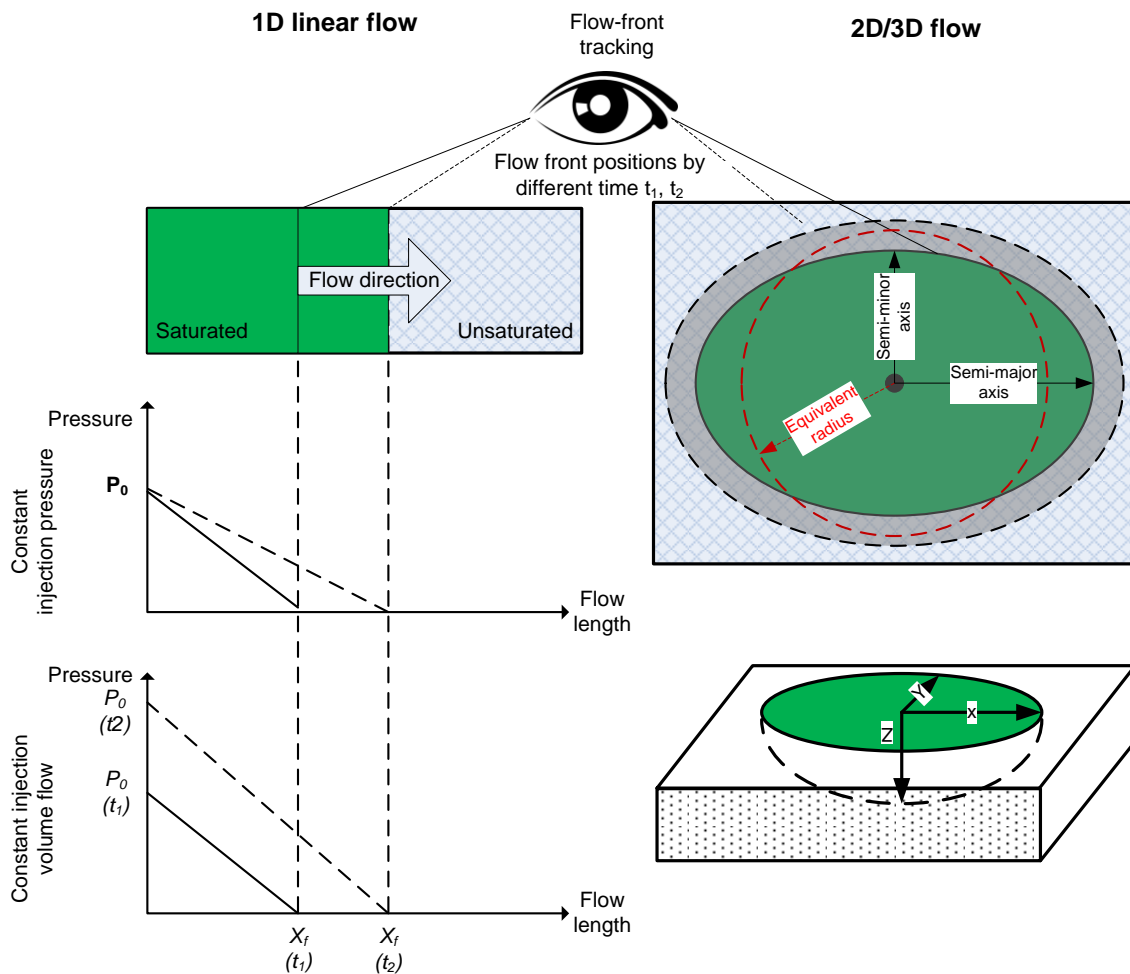


Figure 2.5: Illustration of the flow front propagation and permeability measurements in 1D-3D scenarios

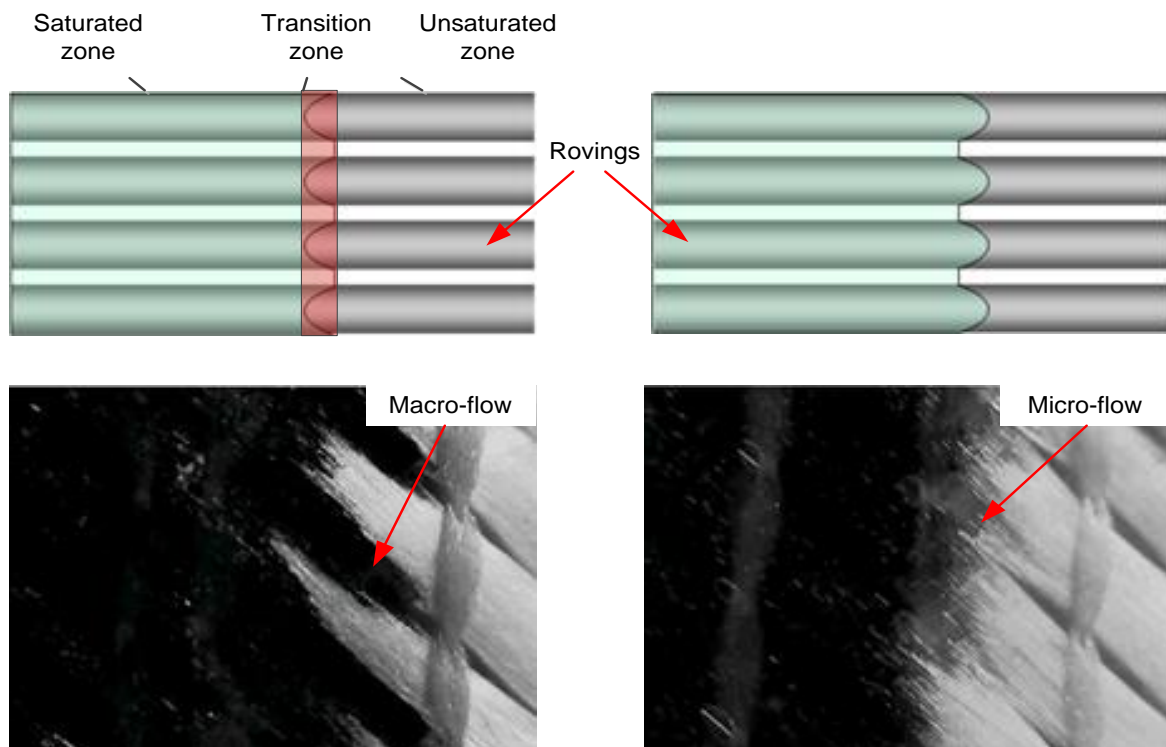


Figure 2.6: Macro-flow (left) or micro-flow (right) dominated impregnation

2.3 Process simulation

2.3.1 Flow simulation

Flow simulation is rather important in LCM processes, considering the high possibility of the potential impregnation failures – dry spots, air bubbles inclusion, which are quite critical for the product qualities but often happens due to the closed nature of the mold where the filling/impregnation state is hard to be observed or controlled manually.

The impregnation process of the dry fibers with fluid is a multiphase flow through porous media. With respect to a fluid flow by a finite control volume (FCV) in a fiber-porous media, as illustrated in the following Figure 2.7, there are normally three phases including solid/fiber, liquid/resin and gas/air, in respective volume fraction of V_s , V_l and V_g , such that

$$V_s + V_l + V_g = 1 \quad \text{Eq. 2.25}$$

With corresponding liquid and gas saturation term being,

$$\begin{aligned} S_l &= V_l / (1 - V_s) \\ S_g &= V_g / (1 - V_s) \end{aligned} \quad \text{Eq. 2.26}$$

Therein, S describes the saturation of the liquid or gas phase in the porosity $(1 - V_s)$, and varies from 0 to 1. The saturation value 0 for the liquid phase means the dry state (filled with air), and the value 1 means the fully saturated state of the porous media.

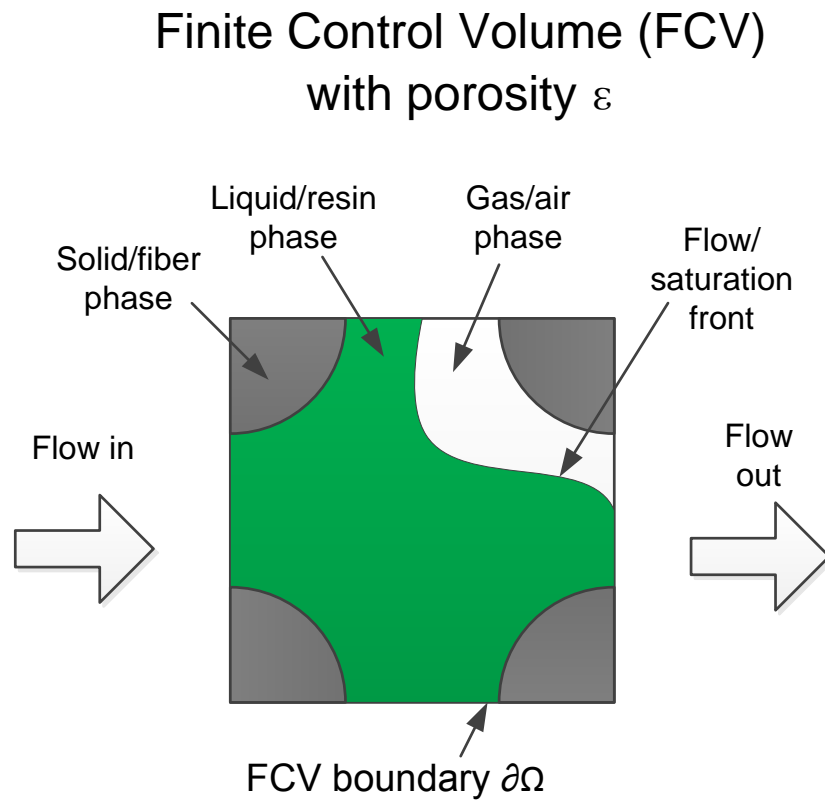


Figure 2.7: Illustration of a fluid flow in FCV by a porous media

Therefore, the mass balance for each phase – liquid or gas – can be derived as following [103-105]:

$$\frac{\partial}{\partial t} \int_{\Omega} \rho S \varepsilon d\Omega = - \oint_{\partial\Omega} \rho U n_{\Omega} d\Omega + \int_{\Omega} F d\Omega \quad \text{where} \quad \text{Eq. 2.27}$$

ρ : liquid/gas density
 S : liquid/gas saturation term
 ε : porosity
 F : liquid/gas source/sink term
 U : liquid/gas velocity vector
 Ω : volume of the FCV
 $\partial\Omega$: boundary of the FCV
 n_{Ω} : unit normal vector to $\partial\Omega$ directed outwards

The timely change in the total mass of a liquid/gas phase inside the FCV is contributed by the total mass flux across the FCV boundary (directed inwards) plus the interior source/sink term. The equation can be transformed to a differential form – which is also known as the Richard's equation – as follows [106]:

$$\frac{\partial(\rho S \varepsilon)}{\partial t} + \nabla \cdot (\rho U) = F \quad \text{where} \quad \text{Eq. 2.28}$$

ρ : fluid/air density
 S : fluid/air saturation term
 ϕ : porosity
 F : fluid/air source/sink term
 U : darcy velocity

The saturation term $S(p)$ describes the relationship between the saturation and pressure, and is also known as capillary model. Mostly used saturation/capillary models are proposed by van Genuchten [107] or Corey-Brooks [108] for simulation of ground water variably saturated flow. Recently, Klunker et al. [109-111] put forward an apparent saturation function for simulating the multi-phase flow in the impregnation process of FRPs and showed promising results with accelerated calculation speed.

In parallel, there are also studies that considered a two-phase flow – resin and air – by a two-phase Darcy law for the impregnation simulation to predict the flow front development and formation, transport and compression of voids in the LCM processes [90, 112, 113]. By these models, the determination of the relationship of the saturation-pressure behavior is critical aspect that are not easy to be directly determined by experiments, as illustrated in the following Figure 2.8 and Figure 2.9.

2 State of the research

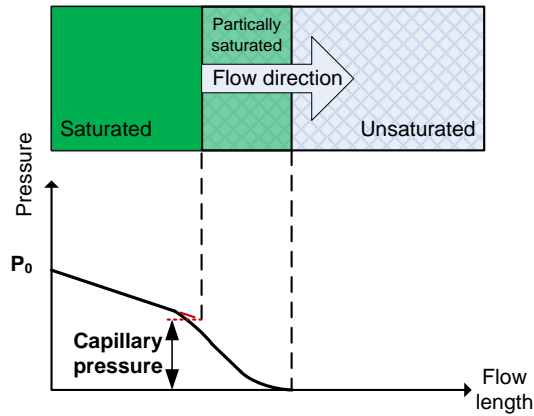


Figure 2.8: Illustration of pressure profile regarding the partially saturated multi-phase flow

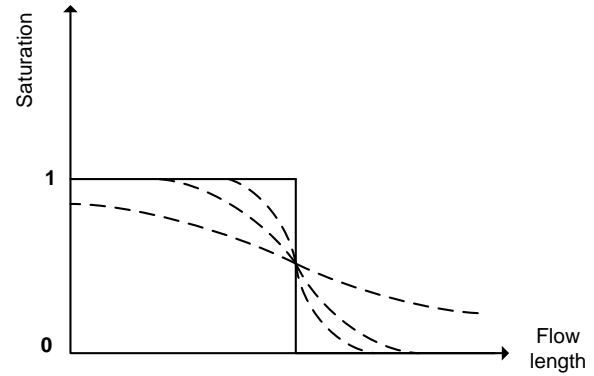


Figure 2.9: Saturation profile depending on the impregnation behavior

By a homogenized model by simplification, the source/sink term in the Eq. 2.28 is zero as there is no extra production or loss of the fluid. However, if the macro and micro flow is to be differentiated with the consideration of void formation, the flow domain needs to be separated to describe the macro flow between the rovings and the micro flow within the rovings. Correspondingly, the permeability should be further differentiated for the macro and micro flows, and the boundary conditions are not necessarily zero regarding the fluid interactions between the two domains [91, 114].

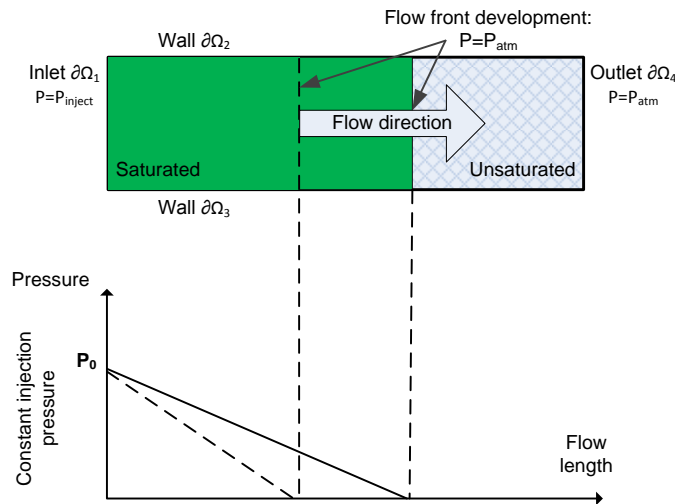


Figure 2.10: Moving pressure boundary condition depending on the development of flow front

For a single-phase, incompressible flow with full saturation on a stable porous medium without absence of source/sink term, the mass conversation equation in Eq. 2.28 can be further simplified to the well-known continuity equation, as shown in Eq. 2.9. Therefore, the flow process by normal RTM processes with standard resin systems without particles, is mostly described by the simplified equation as shown in Eq. 2.10. **However, because the Eq. 2.10 does not include a transient term, a practical issue by the mold filling simulation is the numerical treatment of flow front boundary condition. As the pressure gradient changes with the development of flow front position – where the fluid is displacing the air –**

therefore, the simulation for an un-saturated resin flow needs special moving boundary, transport equation or level-set/phase-field interface methods to obtain a transient solution by successively solving the Eq. 2.10 until the molding filling is complete. Therefore, this equation could be solved numerically by Volume of Fluid (VOF), Finite Element/Control Volumes [115] (FE/CV) techniques or analytically [109, 110]. The techniques and aspects are reviewed in the following review papers [91, 116].

The flow simulation of the particle-filled fluid system is comparably much more critical as the particles may influence the flow behavior of the fluid system, considering the interactions among the particle, fluid and fiber, which could lead to filtration of the particles during the flow. **By the injection of particle-filled matrix systems, if the particles could deposit on the fiber-textile during the flow, it could lead to, on one hand, change of fluid density, cure kinetics and viscosity, and on the other hand textile porosity and permeability.**

There are only limited numbers of works that directly investigate the flow and retention behavior of the particle-filled fluid systems in fiber preform for FRPs manufacturing. Some representative works were done in earlier times from Erdal et al. [117] in which conservation equation and filtration kinetic models for flow of particle-filled systems in porous matrix are proposed. Later, Lefevre et al. [118, 119] put forward improved models coupling the flow and filtration model to simulate the flow behavior. Later Reia da Costa et al. [120] and Haji et al. [121] also worked on to develop and improve the models. Even if these works could show acceptable results for simplified systems or single cases, it needs to be pointed out that most of the works that are related on this topic are based on micro particles where the size distribution and retention behavior comparatively much easier to be characterized and modeled. It is found hardly any work that directly investigates the flow behavior of NP-filled fluid systems in a fibrous preform, which directly related to this thesis. It could be also related to the complexity of this issue due to the following challenges:

- Particle filtration, especially NPs, is a very complex phenomenon that could be influenced by varieties of factors. Among them, the most critical factors are particle size and textile porosity. Regarding to NP size characterization, even if there are plenty of techniques that are available for NP size measurement, it was found in this work that the current procedures and techniques could still be challenged by fully characterizing the agglomeration and even the coarse-particles that might left by the dispersion process (will be discussed in Chapter 5 later).
- Particle agglomeration: NPs might tend to agglomerate due to the increased interfacial interactions. This is also a thorny issue to be fully characterized but with substantial influence on the flow and retention behavior of the NPs.

2 State of the research

- Textile porosity characterization: even though there are several ways to determine the homogenized macro porosity (will be discussed in 3.2.3.2 later), but it is still a quite challenging aspect, due to the complexity as described and discussed earlier in 2.2.2.1, to quantitatively characterize the distribution and change of porosity in textile – especially for the case that NPs deposit on textiles.
- Model development and simulation: as described earlier, for the case of particle retention, each of the parameter in the governing function could change – changing pressure gradient, viscosity, permeability etc. Therefore, the modeling and simulation are rather challenging regarding the complex modeling and numerical implementation.

2.3.2 Cure simulation

Except from the flow behavior, the curing is also a key factor during the impregnation of the FRP structures. The final property of the epoxy resin or the epoxy-based composites is strongly related to its cure process and final cure state. Although some radiation cure technologies (x ray, electron beam, ultraviolet etc.) are proposed [122-125], but the dominant curing processes today for epoxy matrix composites are based on a range of thermal heating processes, as overviewed and summarized by the author in elsewhere [126]. Because the cure reaction is exothermic and epoxy has very low thermal conductivity (thermal conductivity at 25 °C: 0.19 W/m K), **curing process for polymer composites needs to be accurately designed and controlled, especially in the industrial application where thick matrixes or composite laminates with thickness of up to hundreds of millimeters are required – typical in wind turbine blades. Otherwise, the big temperature gradient from the thermal conduction and from the reaction exothermy could lead to a non-homogenous curing of parts with large residual stresses and poor fiber/matrix bonding, even leading to thermal degradation of the matrix due to the temperature overshoot**, as shown in the following Figure 2.11 and Figure 2.12. Therefore, curing is an important process step in most applications, as it is directly determining the process efficiency and final quality of the part.

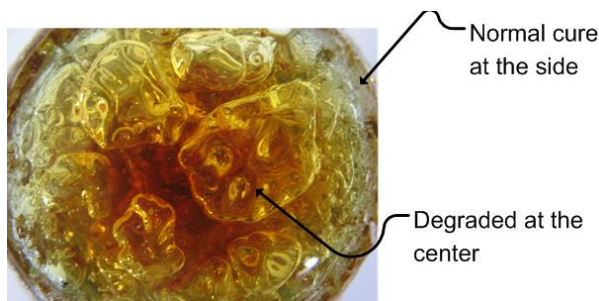


Figure 2.11: Matrix thermal degradation during cure because of temperature overshoot [111]

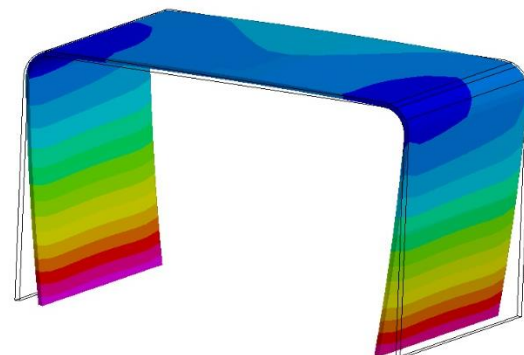


Figure 2.12: Distortion of FRP parts after curing due to thermal induced stress (magnified)

By introduction of ceramic NPs, it is expected that the thermal conductivity of the matrix be increased, with remarkable reduction of thermal expansion, reaction shrinkage of the matrix, which results in decreased cure/temperature gradient, temperature overshooting so that improved final properties [16, 127, 128]. Nevertheless, considering the influence of the NPs on the critical material thermal properties and cure kinetics, the cure process is more complex. Cure simulation provides the basis for, on one hand, investigating the influence of the NPs on the curing and thermal behavior, on the other hand, is critical for designing and controlling the material and process parameters to optimize the process efficiency, robustness and final properties. There are several research works regarding the curing process of the standard impregnation processes with neat resin [129-132], nevertheless the influence of the NPs, especially the reference system – boehmite-epoxy – as in this thesis is not investigated yet.

2.4 Properties

As described in previous chapters, the main goal of introducing NPs is to improve the properties of the FRPs by cost-effective LCM manufacturing. The focus of this work lies principally in on the matrix dominated mechanical properties – fracture toughness, compression, interlaminar shear strength and impact tolerance. Regarding the main goal of this work, the review also focuses on works related on modification of resin systems and FRPs by quasi-spherical NPs by LCM processes.

Among the different quasi-spherical ceramic NPs, silica (SiO_2) NP is until now mostly investigated for application in FRPs [17, 49]. There are also some works that studied alumina (Al_2O_3) NP as functional fillers in epoxy [50, 51]. These studies showed the positive improvement of the matrix properties by introduction of NPs. The elastic-modulus, fracture toughness and thermal conductivity of the matrix increases almost linearly depending on the silica NP content [16, 49, 133], as shown in Figure 2.13 and Figure 2.14. Similar studies for alumina NP also showed linear increase in the fracture toughness – even with better performance compared to silica [51]. On the other hand, other studies [16] with the silica have also showed a linearly decrease in the volume shrinkage and thermal expansion coefficient – the main factor that influence the fiber-matrix interface bonding and leading to increased residual stress, as shown in Figure 2.15 and Figure 2.16. Moreover, significant improvements are also reported for the compressive – both parallel and transvers to fiber direction, damage tolerance and fatigue performance of both matrix and FRPs, whereas it needs to be mentioned that some studies reported a plateau of these performance or even decreasing after some certain critical particle contents [17, 50].

Based on the studies regarding the silica or alumina NPs, it is obvious that the most critical matrix properties that dominate the current challenges in the structural properties could be

2 State of the research

improved in an almost linear way by introduction of the NPs— at least until the critical particle content that is processable in LCM process. NPs can quite effectively improve and modify the performance of the FRPs. Of course, all these changes are dependent on the particle type, size, geometry and even bonding mechanism with matrix – physically or chemically as well as the process parameters. Therefore, in this work, the matrix-dominated properties of the boehmite-filled FRPs will be in focus, which are still white spot in the current research.

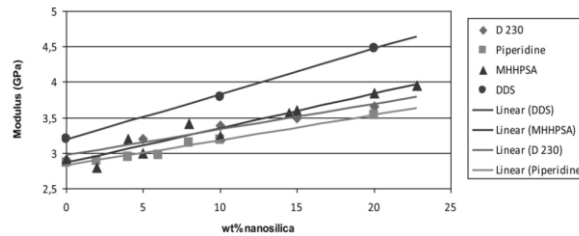


Figure 2.13: E-modulus of epoxy vs. nanosilica content cured with different hardeners [49]

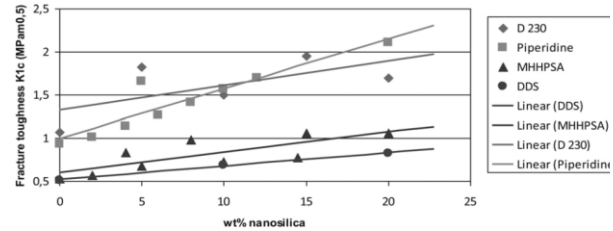


Figure 2.14: K_{IC} of epoxy vs. nanosilica content cured with different hardeners [49]

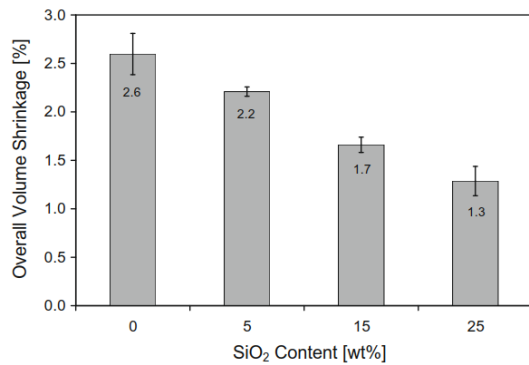


Figure 2.15: Overall volume shrinkage of epoxy-silica nanocomposites at RT [16]

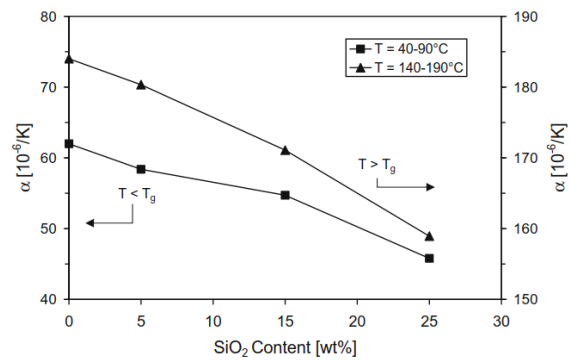


Figure 2.16: Linear coefficient of thermal expansion (CTE) for epoxy-silica nanocomposites [16]

2.5 Research focus and dissertation organization

According to the overview outlining the current state of the art, the following important aspects can be derived which are both scientifically and technically important but not yet well investigated and understood. **Considering the critical aspects in the FRP production chain – material, process and properties – the research focus is categorized into the following three key aspects: 1) Material characterization and modeling; 2) Process development and simulation; 3) Property characterization and concept evaluation.** The three aspects are closely related to each other: material behavior directly determines the process strategy and boundary conditions; process strategy and parameters have a substantial influence on the fabrication efficiency and final properties; and the final property profile regarding the application requirements in turn place certain requirements on the material and processing. Accordingly, the following Figure 2.17 provides an overview of the research key research aspects and organization of the dissertation. Detailed explanations regarding the aspects and logical flow are provided below.

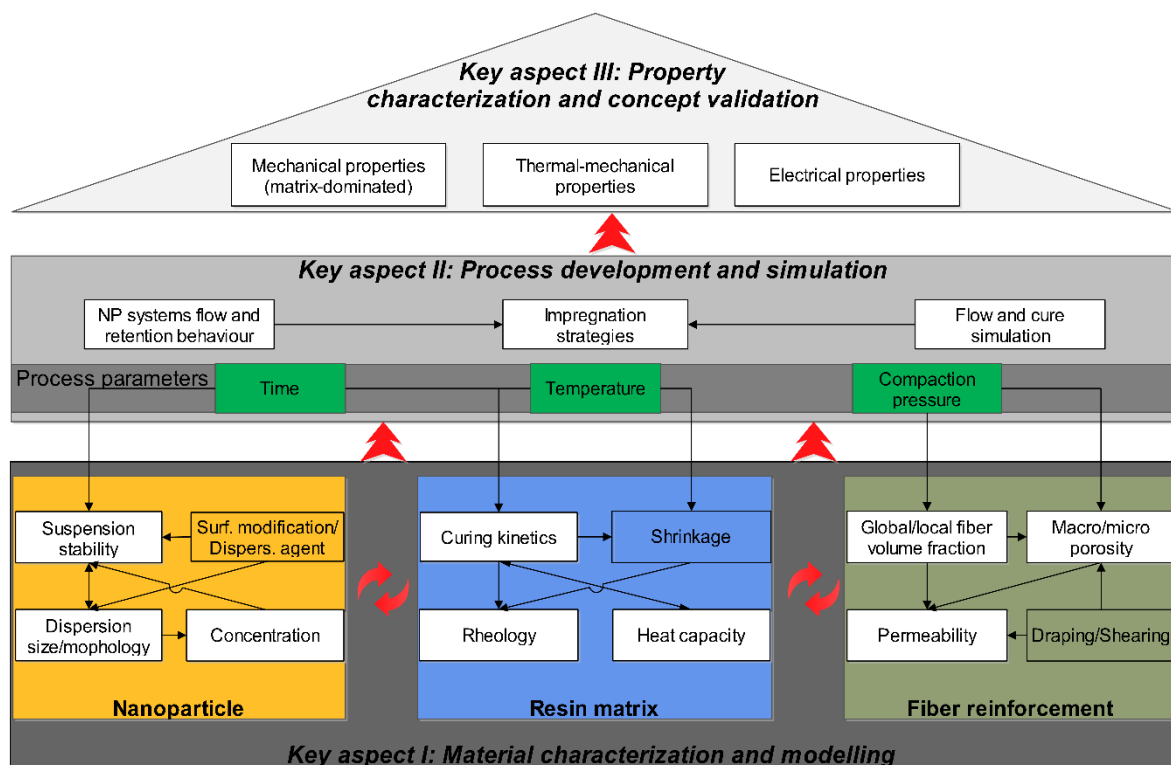


Figure 2.17: Research key aspects and thesis organization

2.5.1 Key aspect I: Material characterization and modeling

There are three basic material components for fabrication of multi-scale functional FRPs: NP, epoxy matrix and fiber reinforcement. They could interact with each other with an influence on both material characteristics and process parameters, as well as the final properties.

2 State of the research

Therefore, it is important to fully understand and characterize each of the basic material component properties and their interactions.

2.5.1.1 Nanoparticle

The focus here lies principally in investigation and characterization of particle size evolution, NP-epoxy suspension stability and particle content. Considering that the process parameters and final FRP properties are influenced by particle morphologies, NP-epoxy masterbatch fabrication methods (dry particle dispersion, in-situ growing), and surface functionalization etc. Therefore, apart from the reference NP – boehmite (AlOOH), there are also two other NPs – silica (SiO_2) and CNT – are considered and critical aspects and interactions to be comparatively investigated.

2.5.1.2 NP-epoxy matrix

The focus on the NP-epoxy matrix characterization lies on the influence of NPs on the matrix cure, rheological behavior and thermal properties (cure degree, glass transition temperature – T_g , specific heat capacity – C_p). These are the most critical aspects for process development and final properties. Furthermore, the cure kinetics and rheological behavior of the NP-epoxy matrix is theoretically investigated and modeled as the fundamental basis for process development, and flow/impregnation as well as cure simulation.

2.5.1.3 Fiber reinforcement

For the LCM process, especially by impregnation with a particle-filled matrix system, the filtration characteristics of the fiber-textile and preform, and the permeability are the most important aspects. These are dominated by the compaction behavior – global/local fiber volume fraction and textile porosity distribution in the structure. Therefore, the focus on fiber-textile and preform lies in characterizing the macro and micro textile porosity –filament distance distribution – and permeability behavior. The permeability behavior is investigated depending on different materials (oil, pure epoxy and NP-epoxy suspension) and process parameters – fiber volume fraction (FVF), temperature (fluid viscosity) and injection pressure. In order to find out the correlations between the parameters regarding permeability and flow behavior, design of experiments (DoE) methodologies are applied by which semi-experimental model regarding the maximum flow length is derived.

2.5.2 Key aspect II: Process development and simulation

Considering the complex flow and retention behavior of NP-filled suspensions, it is important to develop new fabrication concepts. This is characterized in this thesis by investigating and developing impregnation strategies – including both in-plane (sequential and parallel injection)

and out-of-plane methods. The process development is supported on one hand by the flow and retention characterization of different NP-epoxy suspensions, on the other hand, by the flow/impregnation and cure simulations so that the process development can be accelerated and robustness can be enhanced.

2.5.3 Key aspect III: Property characterization and concept evaluation

As the last step, it is important to evaluate the proposed concept and applied impregnation strategies. This is carried out by characterization and comparison of the mechanical, thermal-mechanical and electrical properties of the functional FRP structures by the modification with NPs. The characterization on mechanical properties focuses on the most critical – matrix dominated – properties. As thermal-mechanical properties, thermal conductivities as well as dynamic thermal-mechanical analysis (DTMA) are studied as an important criterion for geometrical accuracy and structural stability. In addition, the surface and volume electrical properties of GFRP laminates that are modified by CNTs are investigated.

3 Materials and methodologies

In this chapter, the materials and methodologies that are applied for the experiments and analysis to achieve the research objectives are introduced. The methodology is divided into three key aspects: 1) material characterization and modeling; 2) process development and simulation; 3) property characterization and concept evaluation.

3.1 Materials

3.1.1 Fiber textile

Two different kinds of fiber reinforcement materials are considered and investigated comparatively. As reference, a quasi-unidirectional aerospace quality carbon fiber (CF) textile (Style 796) from Fa. ECC is used. The textile has an average areal weight of 270 g/m^2 (warp/ 0° direction: 400 tex carbon fiber, weft/ 90° direction: 34 tex glass fiber for stabilization), as shown in Figure 3.1. For comparison, also a quasi-unidirectional glass-fiber (GF) textile (HP-U400E) from HP-Textile is investigated. The GF textile has a total areal weight of 450 g/m^2 (warp/ 0° direction: 400 g/m^2 glass fiber, weft/ 90° direction: 50 g/m^2 glass fiber for stabilization), as shown in Figure 3.2. Further information is provided in Appendix I: material datasheets.

The unidirectional fiber textiles are selected as the fibers are mostly aligned in just one direction, which is optimal to differentiate the influence of the fiber direction on the critical process parameters and final properties. If not explicitly mentioned, the investigations and results are based on the reference CF textile.

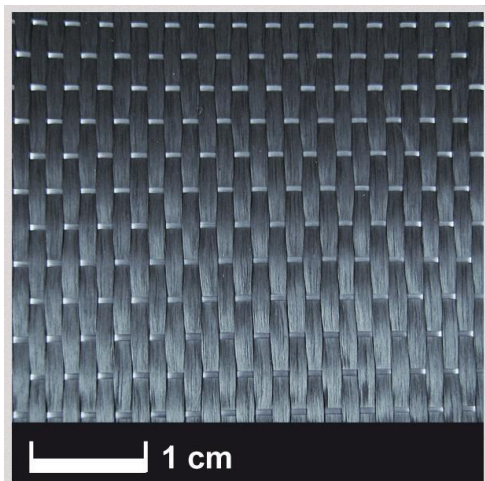


Figure 3.1: Quasi-unidirectional carbon-fiber textile (Fa. ECC, Style 796)

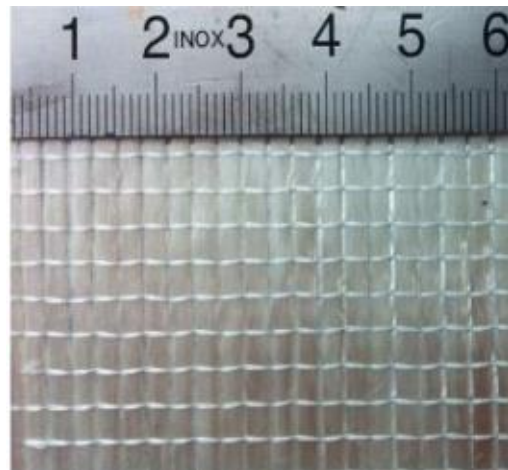


Figure 3.2: Quasi-unidirectional glass-fiber textile (HP-Textile, HP-U400E)

3.1.2 Nanoparticle-epoxy matrix systems

3.1.2.1 Epoxy matrix

The commercial epoxy resin system LY 556 (DGEBA-type epoxy) with corresponding hardener HY917 (methyltetrahydrophthalic anhydride) and accelerator DY070 (1-methyl imidazole) from Huntsman Advanced Materials (Switzerland) GmbH is used. The resin, curing agent and accelerator are mixed at the recommended mass ratio of 100:90:1.

3.1.2.2 Nanoparticles

- **Boehmite:** As a quasi-spherical ceramic NP, boehmite is an aluminum hydroxide oxide – $\text{Al}(\text{OH})\text{O}$, which is often used as a precursor for many aluminum products. Boehmite particle is price-efficient and the hydroxyl groups on the surface could be directly used as functional groups, or easily be modified to different functional groups (amine, acetic acid, lactic acid etc.) to generate a good chemical stability and improved particle-matrix adhesion by possible covalent connection. **In this thesis as the basic reference system, boehmite NPs functionalized with acetic acid (CH_3COOH), as shown in the following Figure 3.3, are investigated.** The acetic acid functionalized boehmite NP is selected because that this specific-functionalized NP showed better flow characteristic regarding viscosity and a higher enhancement of the impact and fracture toughness properties compared to unmodified boehmite NP, based the results of Jux et al [134]. **The special functionalized boehmite NP are called as KE later for the simplification** (*E* is the abbreviation for “*Essigsäure*” in German translation of acetic acid). The boehmite NPs that are used in the study are provided by SASOL (DISPERAL®. HP 14).

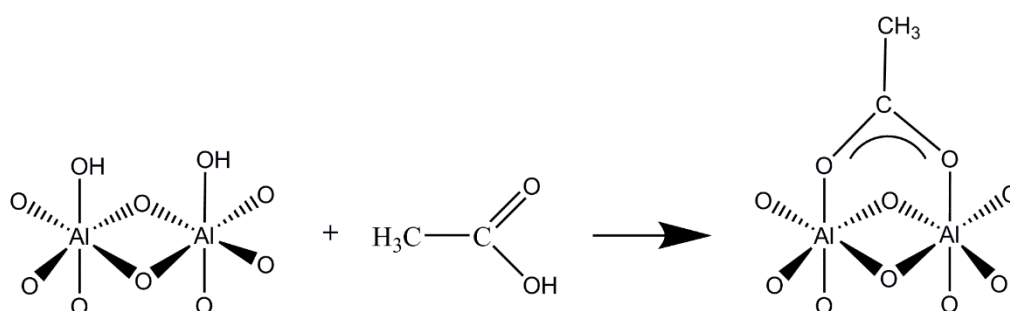


Figure 3.3: Schematic illustration of boehmite NP functionalized with acetic acid (CH_3COOH)

- **Silica:** Compared to the dry boehmite NP, the silica (SiO_2) NPs are directly grown in-situ in a transfer medium. Therefore, information about the silica NPs are directly provided later directly with the silica-epoxy masterbatch/suspension.
- **Carbon nanotubes (CNT):** The multi-wall carbon nanotubes (MWCNT) are from Nanocyl s.a (NC 7000, Belgium). The MWCNT has an average diameter of 9.5 nm and

3 Materials and methodologies

average length of 1.5 μm . CNT NPs are quite different considering the high aspect ratio that shows significant difference on the flow and filtration behavior in the textiles, compared to the above quasi-spherical NP. The density of the MWCNT is reported to be 1.66-1.75 g/cm^3 [135, 136]

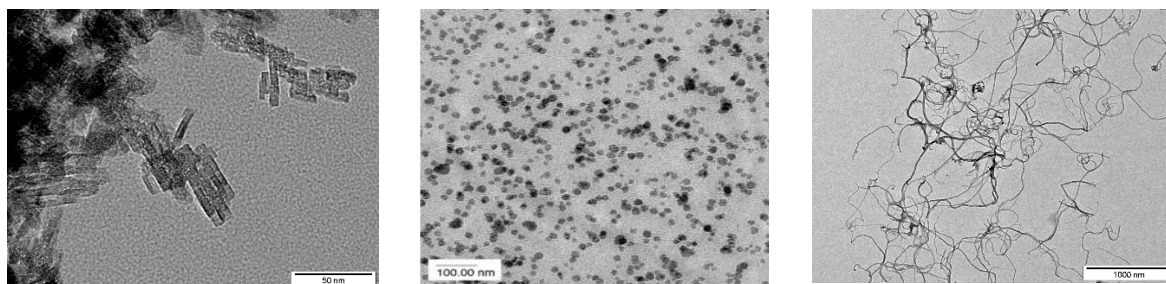


Figure 3.4: Morphology of the investigated NPs. Left: Boehmite (dry aggregate particle structure); Middle: Silica (silica-epoxy after cure [17]); Right: CNT (after dispersed in acetone)

3.1.2.3 Nanoparticle-epoxy matrix

- **Boehmite-epoxy nanosuspension:** as the reference nanosuspension system, boehmite NPs with primary particle size of 14 nm and average agglomerate size of around 30 μm according to the manufacturer (DISPERAL HP14, SASOL Germany) are dispersed into the epoxy matrix a high-performance laboratory kneader HKD-T0.6 (IKA, Germany) to produce masterbatches with 40 wt% boehmite NPs, at the Institute for Particle Technology (IPAT), TU Braunschweig. The particle size within the produced masterbatch is measured by Nanophox (Sympatec, Germany) as described in the paper [54]. The X_{10} , X_{50} and X_{90} values of dispersed particle size within the produced masterbatch are separately 81 nm, 104 nm and 134 nm, as shown in Figure 3.5.
- **Silica-epoxy nanosuspension:** as the second comparative NP system, a commercial diglycidyl ether of bisphenol A (DGEBA) epoxy based silica nanosuspension (NANOPOX F400, 40 wt%, epoxy equivalent weight: 295 g/eq) from Evonik Industries AG is used. Compared to the boehmite nanosuspension, the silica nanosuspension is manufactured in situ directly in the epoxy resin by a modified sol–gel process and has an average particle size of 20 nm and a very narrow particle size distribution.
- **MWCNT-epoxy nanosuspension:** as the third comparative nanosuspension, the CNT-epoxy suspension is prepared in house. The dispersion process is based on the combination of shear mixing with ultrasonic. Considering the extent of the work, regarding the investigations and results about the dispersion and characterization of the MWCNT, the readers are redirected to the following work [137] or thesis [138] that is supervised by the author.

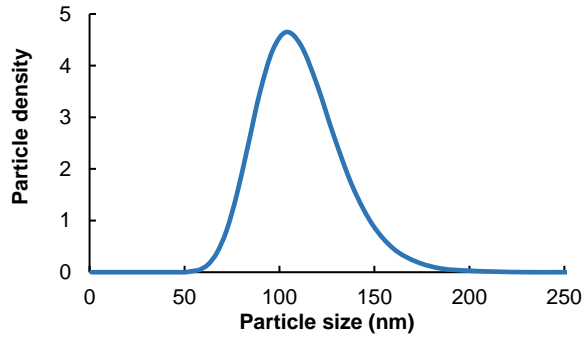


Figure 3.5: Particle size distribution of boehmite nanosuspension

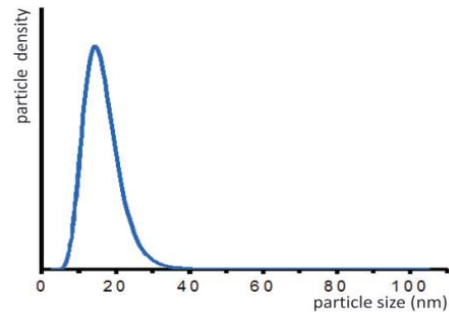
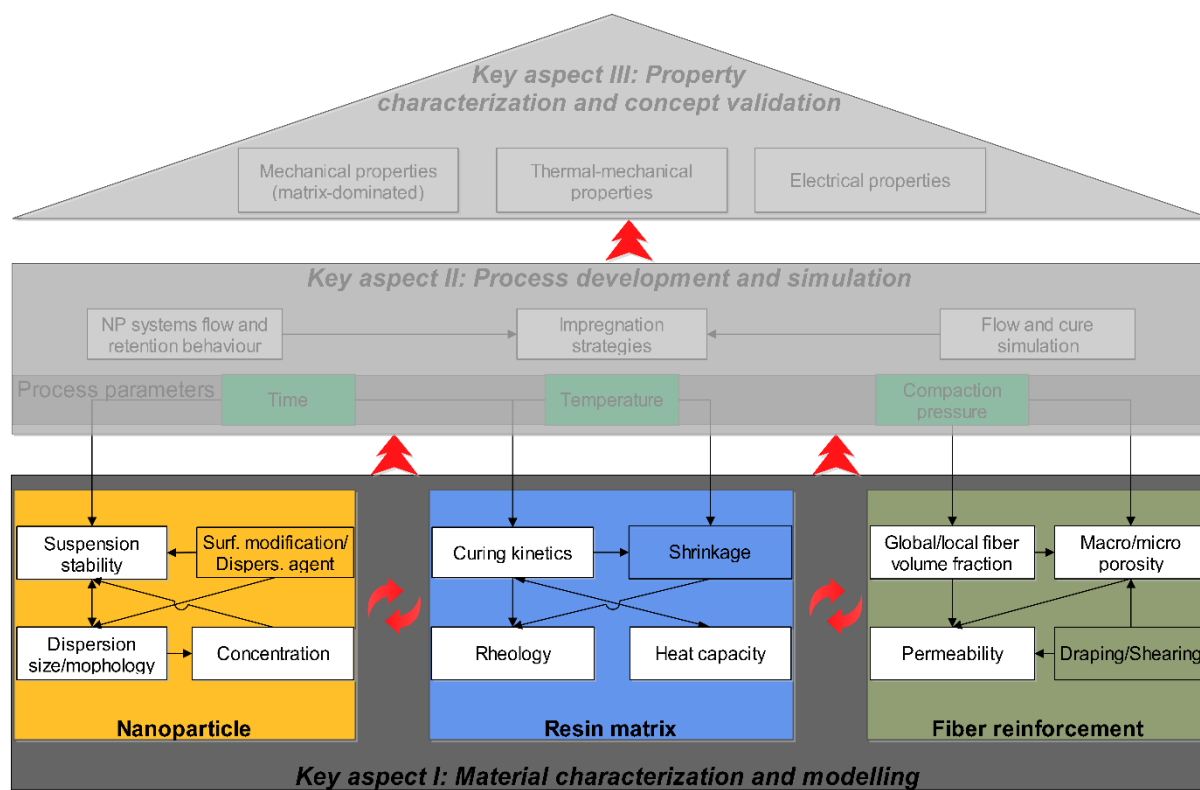


Figure 3.6: Particle size distribution of silica nanosuspension [17]

For the experiments, the masterbatch is diluted to the desired particle concentration with a planetary mixing machine (Thinky Mixer ARV-310) twice with the following parameters: 1) 1.5 minutes at 0 rpm under vacuum of 5 kPa absolute pressure; 2) 1.5 minutes at 1000 rpm under vacuum of 10 kPa absolute pressure; 3) 1.5 minutes at 2000 rpm under vacuum of 1 kPa absolute pressure at room temperature.

Before injection, the NP-epoxy matrix system is filtered with a fine sieve (mesh size approximately 190 μm) to eliminate foreign object or possible leftovers from the masterbatch that are not fully diluted during the dispersion process.

3.2 Methodology for key aspect I: Material characterization and modeling



3.2.1 Nanoparticle-epoxy masterbatch

The critical factors of the NP regarding the processing are the dispersion size, stability and concentration. The dispersion size and stability are effected by the matrix environment and functional groups on the NPs. The dispersion and characterization of the bohmite particles in masterbatch is carried out by project partner – Institute for particle technology (IPAT), TU Braunschweig. Nevertheless, the change in the dispersion and agglomeration during the process is further investigated in the thesis. The dispersion and stability of the NPs are often improved by applying dispersion/stabilization agents, especially in very low-viscous medium (water, ethanol etc.). For the study in this thesis, the resin viscosity is high enough – at least in the masterbatch, so no additional dispersing/stabilization agent is applied. Therefore, this aspect is not under consideration in this work.

3.2.1.1 Boehmite NP size development during the process

In order to investigate the particle size evolution and suspension stability during the process, epoxy suspensions with different boehmite and silica content are prepared and the cryo-fracture surface is investigated in high-resolution scanning electron microscopy (SEM). The particle size distribution is subsequently analyzed by image-processing processes.

3.2.1.2 NP concentration

The NP concentration in the nanosuspensions is measured in both masterbatch and diluted suspensions by TGA measurements on a TGA Q5000 device from TA Instrument (Heat: 30 °C-800 °C, 10K/min, air condition).

3.2.2 Nanoparticle-epoxy matrix

According to the correlation of NP-epoxy suspension and processing parameters, the cure kinetics and rheology is the most important process parameters. Besides, the exothermic energy by curing (cure enthalpy), T_g and specific heat capacity are the important parameters for the cure simulation and final properties. In this thesis, the focus lies in the characterization of these parameters, with an emphasis on modeling the cure kinetics and rheological behavior of the boehmite NP-modified epoxy matrix systems. The following provides an overview on the critical aspects and used methods for investigation.

3.2.2.1 Cure characterization (Cure degree, T_g)

A TA Q-2000 DSC from TA Instrument is used to measure the reaction heat and the glass transition temperature (T_g) of the samples. The attached cooling system RCS90 allows for cooling the samples down quickly to -90 °C. Resin samples of approximately 5–10 mg are placed in aluminum hermetic pans.

Dynamic measurements are performed from -80 °C to 250 °C for the following heating rates: 1, 2, 5 and 10 K/min to characterize the dynamic curing behavior and to obtain the total reaction enthalpy. The cured specimens are checked for the maximum obtainable glass transition temperature ($T_{g\infty}$) using a subsequent dynamic scan from 20 °C to 250 °C. For the isothermal measurements, several samples are prepared in one batch to exclude the potential deviations from the preparation and stored at -18 °C to stop the reaction (proved feasible up to 5 days). The samples are tested isothermally at 100, 110, 120 and 130 °C, respectively. They are cooled firstly down to -20 °C, then heated up quickly to the desired cure temperature and cured at this temperature until the heat flow rate remained constant. At this point, the T_g exceeds the T_{cure} by which the sample vitrifies due to the glass transition, therefore the reaction only proceeds at negligible rate due to the diffusion controlled reaction. The samples are subsequently cooled down to 40 °C and heated up, until it reaches the aging peak (also called as annealing peak) due to the thermal aging effect, directly after the aging peak the samples are quenched again to 40 °C to overcome the disturbance of the aging peak to determine the T_g and rest enthalpy. For the details about the annealing peak and its effect on the reaction peak, the readers are redirected to the other studies [139, 140]. At the third cycle, the samples are heated again using 10 K/min dynamic scans up to 250 °C until the samples are fully cured and the final T_g

3 Materials and methodologies

as well as the residual enthalpy (H_{res}) are measured. The heat flow and temperature are recorded over time. The heat flow data is adjusted using a horizontal baseline, which extends from heat flow values at the end of reaction to initial values.

3.2.2.2 Cure kinetics modeling

As discussed earlier, the first crucial step for the cure kinetics modeling is to find out how the reaction proceeds. There are two main reaction mechanisms: nth order (accelerating or decelerating) and autocatalytic. These two reaction mechanisms could be differentiated by the time where the maximum rate of heat evolution is reached: materials obeying nth order kinetics will have the maximum rate of heat evolution at time zero (decelerating), while an autocatalyzed material will have its maximum heat evolution at 30-40% of the reaction time [69, 70].

DSC provides an easy and quick analysis of the reaction mechanism: when the material is heated at an isothermal temperature and the cure exotherm is recorded, the time where the maximum heat evolution is reached could be detected easily. According to the heat evolution curve versus time as shown in the Figure 3.7, it could be proved that the epoxy resin system in this paper shows an autocatalytic reaction. As shown in Table 1, there are also different models for autocatalytic reactions, among which the Kamal-Sourour model was studied and applied mostly for similar systems, therefore, Kamal-Sourour (nth order + autocatalytic) model from the table was selected for modeling the reaction.

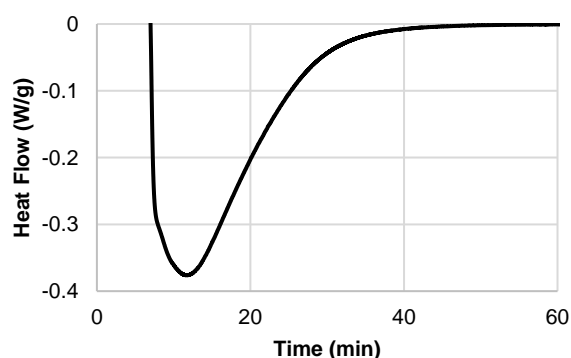


Figure 3.7: Heat evolution at isothermal cure temperature (pure resin, 120°C, Exo down)

Besides, based on the earlier studies, Fournier's model was mostly applied for characterizing the diffusion effect of the similar systems, so the Fournier's model was selected to modify the Kamal-Sourour model as following:

$$\frac{d\alpha}{dt} = (K_1 + K_2\alpha^m)(1 - \alpha)^n f_d(\alpha)$$

$$K_i(T) = A_i e^{\left(-\frac{E_i}{RT}\right)}$$

$$f_d(\alpha) = \frac{2}{1 + \exp(\alpha - \alpha_c)/C)} - 1$$

K(T): rate function
A: pre-exponential factor,
E: activation energy,
R: ideal gas constant and
T: absolute temperature
m, n: reaction order
 α_c : critical cure degree
C: fit parameter

Eq. 3.1

3.2.2.2.1 Estimation of kinetic parameters

According to the selected model as described above, there are eight kinetic parameters (A_1 , A_2 , E_1 , E_2 , m , n , α_c , and C) which need to be determined to describe an isothermal reaction. These parameters are mostly solved numerically by regression analysis on the test data and model. Therefore, it is quite important to properly estimate the initial values of the kinetic parameters, as poor selected initial parameters could lead to instable or poor modeling results, even sometimes without convergence. There are different methods for estimating the initial model parameters which could be categorized into heating rate DSC methods, including Borchardt & Daniels Method [141], Kissinger method [142], Flynn/Wall/Ozawa method [143] & Friedman method [144], or isothermal methods, including Sestak Berggren & Avrami methods [70].

Borchardt and Daniels Method is based on single heating rate DSC measurement, therefore it needs single calibration, works rather fast and simple and provides all three E , A and n estimations. However, it is based on an assumption of n th order well behaved reactions. Kissinger and Ozawa methods are based on at least four variable heating rate DSC methods. The calibration is a little bit time consuming, but it is applicable for complex, multi-staged reactions. However, these methods assume a 1st order reaction, with an estimation of (E and A). Isothermal methods are applicable to both n th order and autocatalytic reactions with an estimation of E , A and reaction orders (m , n , p). However, by isothermal DSC measurements at lower temperatures, the reaction normally does not go to full completion due to the vitrification effect and requires much longer time compared to heating rate DSC measurements. As the heating rate DSC methods are based on either n th or 1st order reactions, for autocatalyzed thermosets, the heating rate methods generally provides an accurate assessment of the activation energy. However, the pre-exponential factor may not be valid since the calculation of A is based on an n th order reaction. A big deviation of the A value between the Kissinger and Prout–Tompkins autocatalytic model estimation was reported by Hardis et al [57]. Therefore, the estimated A values from the heating rate DSC methods needs to be considered quite critically.

The application of these different methods differs depending on the assumption conditions of the models and material curing behavior. They all could, furthermore, be principally categorized into model-free (iso-conversional) and model fitting methods. The assumption conditions and calculation procedures are explained and discussed in the following.

3.2.2.2.1.1 Model-free (iso-conversional) methods

The iso-conversional methods are based on the assumption that the reaction rate at a constant extent of conversion only is a function of temperature. By taking a logarithmic temperature derivative of the Eq. 2.3,

$$\left[\frac{\partial \ln(d\alpha/dt)}{\partial T^{-1}}\right]_{\alpha} = \left[\frac{\partial \ln k(T)}{\partial T^{-1}}\right]_{\alpha} + \left[\frac{\partial \ln f(\alpha)}{\partial T^{-1}}\right]_{\alpha} \quad \text{Eq. 3.2}$$

As α is a iso-conversional constant, the $f(\alpha)$ is also a constant, so the second term in the right hand side of Eq. 3.2 is also zero. Thus:

$$\left[\frac{\partial \ln(d\alpha/dt)}{\partial T^{-1}}\right]_{\alpha} = -\frac{E_{\alpha}}{R} \quad \text{Eq. 3.3}$$

Therefore, the activation energy could be evaluated depending on the conversion, without assuming or determining any reaction model. That is why the iso-conversional methods are also called model-free methods. The iso-conversional methods provide a meaningful analysis and evaluation of the reaction mechanism: a significant change in E_{α} to conversion α (normally the range of 0.1 to 0.9 is considered regarding the experimental deviations) implies that the reaction kinetic is complex, therefore multi-step reaction models need to be considered. However, by the iso-conversional methods, without assuming a reaction model, it is not possible to estimate the other kinetic parameters: pre-exponential factor A and reaction order.

Two most applied iso-conversional methods is Friedman [144] in differential form as in Eq. 3.4, and Ozawa method in integral form [145], as in Eq. 3.5. Both methods could provide the relationship between activation energy and conversion.

➤ **Friedman method:**

$$\ln\left(\frac{d\alpha}{dt}\right)_{\alpha,i} = \ln[f(\alpha)A_{\alpha}] - \frac{E_{\alpha}}{RT_{\alpha,i}} \quad \text{Eq. 3.4}$$

➤ **Ozawa method:**

$$\log \beta_i = -\frac{0.4567E_{\alpha}}{RT_{\alpha,i}} + \log \left[\frac{AE_{\alpha}}{g(\alpha)R} \right] - 2.315 \quad \text{where } \begin{array}{l} \beta: \text{heating rate,} \\ g(\alpha): \text{integral function of} \\ \text{conversion} \end{array} \quad \text{Eq. 3.5}$$

3.2.2.2.1.2 Model-fitting methods

In comparison to the model-free methods that are described above, model-fitting methods are based on derivation of the kinetic parameters by fitting the experimental data for an assumed reaction model. Therefore, the first critical step by this method is to identify and evaluate a suitable reaction model. The determination of the reaction model includes, checking the reaction complexity – the change of the activation energy to conversion, detecting and comparing the reaction curve with the typical kinetic curves from reaction models. Mostly used

model fitting methods include Kissinger method (dynamic DSC process) and Sestak-Berggren & Avrami methods (isothermal DSC process).

➤ **Kissinger method**

As one of the most often used methods in many studies, Kissinger method assumes that the maximum reaction rate occurs at the exothermal peak, the activation energy, E , is related to the heating rate (β), and peak temperature (T_p), as follows:

$$\frac{d^2\alpha}{dt^2} = \left[\frac{E\beta}{RT_p^2} + Af'(\alpha_p) \exp\left(-\frac{E}{RT_p}\right) \right] \left(\frac{d\alpha}{dt}\right)_p = 0 \quad \text{Eq. 3.6}$$

After rearrangement,

$$\ln\left(\frac{\beta}{T_p^2}\right) = \ln\left(-\frac{AR}{E}f'(\alpha_p)\right) - \frac{E}{RT_p} \quad \text{Eq. 3.7}$$

In Kissinger method, $\ln\left(\frac{\beta}{T_p^2}\right)$ is plotted against $1/T_p$, by which the activation energy and pre-exponential factor are decided from the slope and interception. It assumes that the $f'(\alpha_p)$ is independent of the heating rate which holds strictly only for 1st order reaction as $f'(\alpha_p) = -1$. This is, however, reported to be a “reasonable” approximation for nth order and Avrami reactions [70]. Moreover, Kissinger method simplifies the activation energy and pre-exponential factor as being a constant value during the whole reaction, which could be a possible over-simplification for complex reactions. However, this method is applied in many studies for kinetic analysis of epoxy systems and reported to be a feasible estimation of the model starting parameter [58, 59, 146].

➤ **Sestak-Berggren (S-B) method:**

As an important method for kinetic parameters estimation, in S-B method, the conversion function is estimated to be autocatalytic as follows:

$$\frac{d\alpha}{dt} = K\alpha^m(1-\alpha)^n \quad \text{Eq. 3.8}$$

In a logarithmic form

$$\ln\left(\frac{d\alpha}{dt}\right) = \ln(K) + m \cdot \ln(\alpha) + n \cdot \ln(1-\alpha) \quad \text{Eq. 3.9}$$

As the equation has a form of $z = a + bx + cy$, where $x = \ln(\alpha)$, $y = \ln(1-\alpha)$, $z = \ln(d\alpha/dt)$, the kinetic parameters (K , m and n) could be estimated using multiple linear regression analysis. There further estimation of A and E follows the Arrhenius equation as described in Eq. 2.6.

3.2.2.2.2 Heat capacity

Heat capacity of the NP-epoxy suspensions is measured in the same TA Q-2000 DSC from TA Instrument by a modulated form (MDSC). Firstly, the heat capacity of Sapphire – reference material – is measured in the desired temperature range (-90°C – 250°C, 5K/min, ± 1 K, 1 Hz). The test data are compared to the standard value from DIN EN ISO 11357 and a correction factor is determined. Secondly, the heat capacity of the real sample is measured and corrected with the correction factor to get the real heat capacity. In order to separate the dependency of the heat capacity on the curing degree and temperature, firstly the sample is investigated by several quasi-isothermal modulated DSC measurements so that the heat capacity can be obtained by the modulated signal, but the influence of the temperature can be neglected. Secondly, samples with different initial curing states are prepared and heated by MDSC (5K/min) from – 90°C to 250°C, to measure the heat capacity dependent on both cure and temperature.

3.2.2.2.3 Glass transition temperature vs. conversion

The relationship between the glass transition temperature and conversion is modeled by the Dibeneditto equation [147], as follows:

$$\frac{T_g - T_{g0}}{T_{g\infty} - T_{g0}} = \frac{\lambda \cdot \alpha}{1 - (1 - \lambda)\alpha} \quad \text{where} \quad \begin{array}{l} T_{g0}: T_g \text{ of the uncured resin} \\ T_{g\infty}: T_g \text{ of the cured resin} \\ \lambda : \text{model parameter} \end{array} \quad \text{Eq. 3.10}$$

The model parameter λ is mostly determined by data fitting, where plenty of samples with different curing degree need to be prepared and the T_g to be characterized. In comparison, λ could be determined by the equation: $\lambda = \Delta C_{p\infty} / \Delta C_{p0}$, $\Delta C_{p\infty}$ and ΔC_{p0} are isobaric heat capacity change at fully cured and uncured state [148, 149]. In this study, the value for λ is determined by heat capacity ratio method, due to the simplicity.

3.2.2.3 Rheology characterization

The rheological measurements are conducted by a TA AR-2000 instrument from TA Instrument. A 40 mm-diameter aluminum plate geometry is used in plate-plate mode. A platin temperature controller is used as the basic temperature control element to accurately control the temperature. Dynamical viscosity measurement is carried out with 5K/min, from 20 °C to about 140°C, until the viscosity reaches the limit of 1.5 Pa.s. Isothermal viscosity measurements were carried out with a shear rate of 50 1/s, also until the viscosity reaches the limit of 1.5 Pa.s. Besides, oscillation viscosity measurements are also conducted to determine the “gel time” by the point where the storage modulus (G') exceeds the loss modulus (G'').

3.2.2.4 Rheology modeling

Based on the literature review, the Castro-Macosko model was used in several studies for modeling the rheological behavior of epoxy resin systems [150] or films [56] and showed promising results, so in this work the Castro-Macosko model was selected firstly for both pure epoxy and boehmite-filled systems.

$$\eta = \eta_{\infty} \exp\left(\frac{E_{\eta}}{RT}\right) \left(\frac{\alpha_{gel}}{\alpha_{gel} - \alpha}\right)^{(A+B\alpha)} \quad \text{where} \quad \begin{array}{l} E_{\eta}: \text{flow activation energy} \\ \eta_{\infty}: \text{viscosity at } T_{\infty} \\ \alpha_{gel}: \text{cure degree at} \\ \text{gelation} \\ A, B: \text{fit parameters} \end{array} \quad \text{Eq. 3.11}$$

3.2.2.4.1 Estimation of rheological model parameters

Based on the Castro-Macosko model, the temperature dependent viscosity evolution could be predicted by a dynamic rheological analysis. The physical resin parameters (E_{η} and η_{∞}) could be estimated following Arrhenius relationship for viscosity model at zero cure:

$$\ln \eta_0(\alpha = 0) = \ln \eta_{\infty} + \frac{E_{\eta}}{RT} \quad \text{Eq. 3.12}$$

The values of E_{η} and η_{∞} can be obtained from dynamic viscosity plots of $\ln \eta$ versus $1/RT$ at low resin conversion, with the similar calculation as Kissinger plot in cure kinetics.

3.2.2.5 Regression analysis algorithms

The development of the model coefficients is based on linear [58, 61] or non-linear [56, 59] least-square regression analysis to find the optimal coefficients for the models by which the summed square of residuals between the test value and model value. The analysis can be described mathematically as follows:

$$S_r = \sum_{i=1}^n r_i^2 = \sum_{i=1}^n (f(Xdata_i, \Psi) - Ydata_i)^2 \quad \text{where} \quad \begin{array}{l} r_i = \text{residual} \\ n: \text{number of data points} \\ f(Xdata_i, \Psi): \text{model} \\ \Psi: \text{model coefficients} \end{array} \quad \text{Eq. 3.13}$$

Due to the complexity of the model and ill-posedness of the regression analysis, it is found in the later study that, if the regression analysis is based on the single curing curve – single target regression – the developed model data could not necessarily describe the curing behavior by some other curing temperatures. Therefore, a multi-target regression analysis method that considers several curing curves at the same time is implemented, as follows:

$$S_r^m = \sum_{j=1}^N \sum_{i=1}^n r_i^2 = \sum_{j=1}^N \sum_{i=1}^n (f(Xdata_i, \Psi) - Ydata_i)^2 \quad \text{where} \quad N: \text{number of curves} \quad \text{Eq. 3.14}$$

In addition, if the Kamal-Sourour model is rearranged as followed in Eq. 3.15 and the reaction order m is assumed to 1, so at the initial stage of the reaction where the diffusion term $f_d(\alpha)$ is equal to 1, the right side of the equation is a linear function with the slope as K_2 and the

inception as K_1 . The left side of the equation should also show a linear development, by which the reaction order n also could be determined [58, 61].

$$\frac{d\alpha/dt}{(1-\alpha)^n} = (K_1 + K_2\alpha^m)f_d(\alpha) \quad \text{Eq. 3.15}$$

As the linear regression analysis is based on the assumption of the reaction order m as 1, which leads to a decreased freedom of the parameters. On the other side, it is found in the paper the determination of the other reaction order n is mostly based on trial-and-error as it is difficult to quantify the criteria “linear” accurately, which could inevitably compromise the model quality. Therefore, this work is concentrated on the influence of single- and multi-target non-linear regression analysis on the model description and prediction quality. The details will be discussed later in Chapter 4.

Considering the complexity of the determination of the cure kinetics and rheology, a custom-developed software is developed. The operation flow chart and model development processes are shown in the following Figure 3.8 and Figure 3.9.

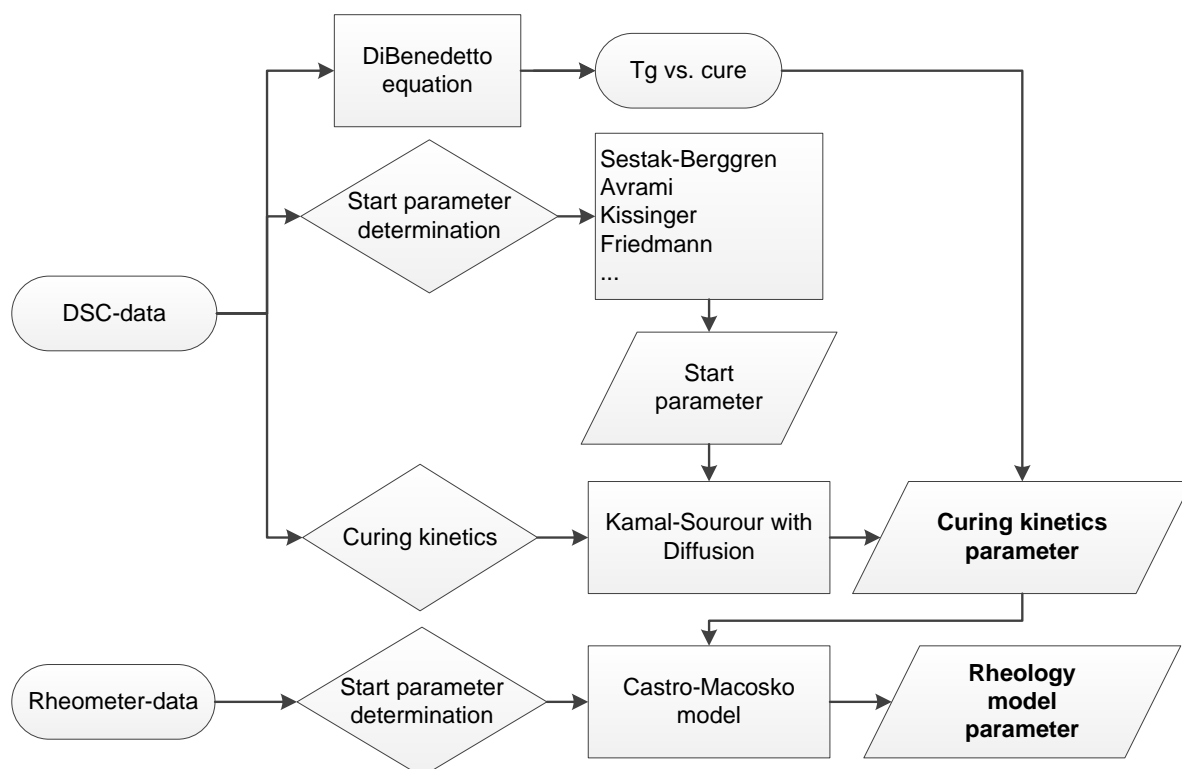


Figure 3.8: Operation flow chart of the custom-developed software for cure kinetics and rheology modeling

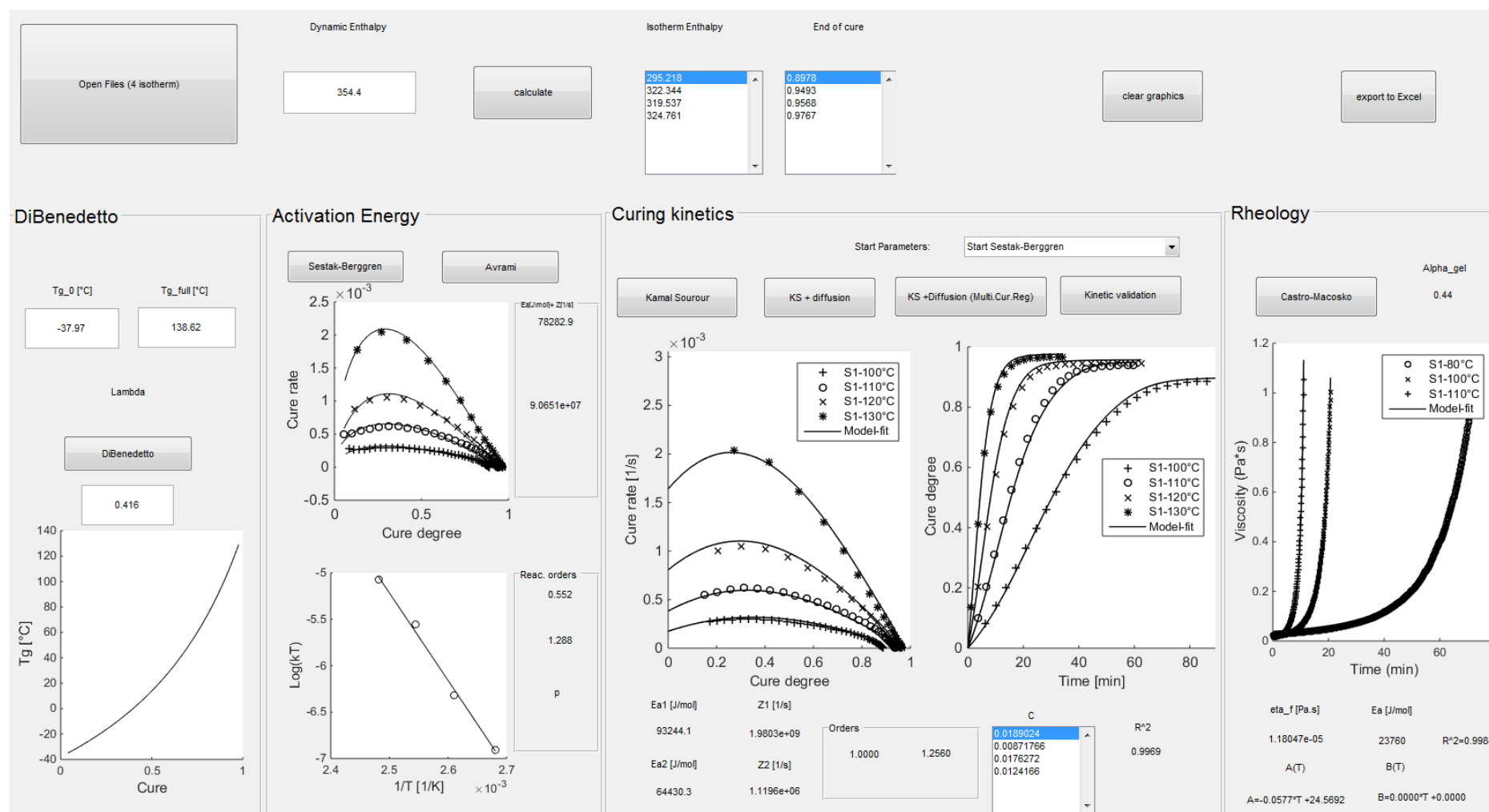


Figure 3.9: User-interface of the custom-developed software for cure kinetics and rheology modeling

3.2.3 Fiber reinforcement

According to the correlation of fiber reinforcement and processing parameters, the fiber volume fraction (FVF), filament distribution and permeability are the most critical parameters in the LCM processes, among which the FVF – dependent on the compression or draping/shearing – is a deciding factor for the filament distance distribution and permeability. Besides, for the particle-filled systems, the NPs could also influence the permeability. Therefore, the compaction behavior, filament distance distribution, permeability and their interaction to each other with consideration of NPs are predominantly investigated and characterized. A shear deformation of the preform by the draping on complex geometries could also influence the permeability and filament distribution, considering the extent of the thesis and specialty of this draping effect, this aspect is not under consideration.

3.2.3.1 Filament diameter characterization

In order to precisely evaluate the fiber volume fraction and filament distance by optical methods, it is critical to accurately detect the boundary and diameter of each filament, which is only possible by high-resolution microscopic methods like scanning electron microscopy (SEM). However, the high local zooming by SEM inevitably leads to a limited view of observable areas in the samples, which could lead to increased loss of statistic information, unless a lot of image collection and analyze. Therefore, three kinds of images with different resolutions are taken by optical microscope (OM) (VK/9710 from KEYENCE) and SEM (DSM Gemini 982 from ZEISS), to compare the influence of resolution on filament recognition and systematical error due to sample size.

3.2.3.2 Global/local fiber volume fraction characterization

Fiber volume fraction (FVF) is one of the dominating factors for the permeability of the fiber preform and the flow behavior of the fluid – especially for particle-filled systems. Therefore, it is quite important and critical to precisely determine the FVF. Due to the heterogeneity of the preform structure, dual-scale macro and micro porous structure, here the FVF at two different scales could be differentiated: global and local FVF. Global FVF is the average value of FVF regarding the whole sample level (in laminate). Yet local FVF shows the FVF within the rovings. Therefore, in this thesis the following different methods are investigated to be able to differentiate the global and local FVF.

3.2.3.2.1 Method 1: laminate thickness

The global FVF in laminate can be calculated with the laminate parameters, by the following equation:

$$V_f = \frac{nW_A}{\rho_f h}$$

where

V_f : fiber volume fraction
 n : number of textile layers
 W_A : areal weight
 ρ_f : fiber density
 h : laminate thickness

Eq. 3.16

3.2.3.2.2 Method 2: Chemical

The global FVF of the laminates is also determined chemically, CF-laminates according to standard “DIN EN 2564:1998, Aerospace series – Carbon fibre laminates – Determination of the fibre-, resin- and void contents” [151] and GF-laminates according to “DIN EN ISO 1172 -1998: Textile-glass-reinforced plastics – Prepregs, moulding compounds and laminates – Determination of the textile-glass and mineral-filler content – Calcination methods” [152].

3.2.3.2.3 Method 3: Optical

Both global and local FVF are calculated optically by filament volume fraction in roving (local_FVF) and roving volume fraction (RVF) in laminate, by the following equation:

$$V_F = local_FVF * RVF$$

where

$local_FVF$: Filament
 volume fraction in roving
 RVF : Roving volume
 fraction

Eq. 3.17

Firstly, several OM images are taken from the rovings so that the filament numbers could be measured by the custom developed software Filpro (will be explained more in detail later). Combining the diameter that is determined by the high-resolution SEM images as described in 3.2.3.1, the local_FVF in roving could be obtained by calculating the percentage of filaments areas in the picture, as shown in the Figure 3.10 left. Secondly, the whole cross section from the laminate is obtained by special image assembling of six separate images, by which the whole cross section could be obtained and the RVF could be determined by special image processing (software ImageJ), as shown in the Figure 3.10 middle and right.

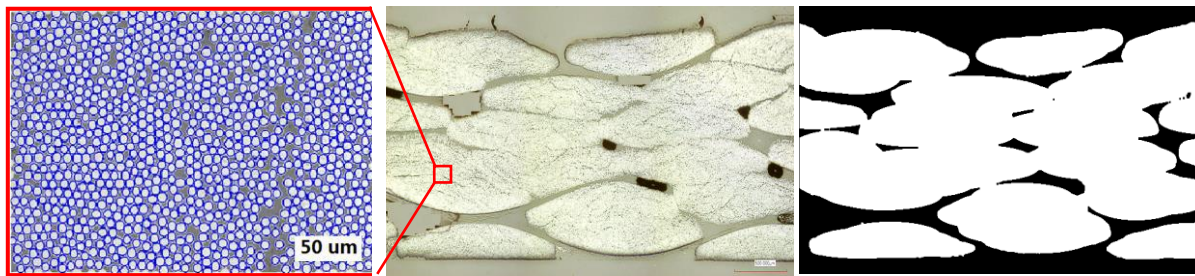


Figure 3.10: Optical determination of FVF (OM images). Left: filament volume fraction in roving; Middle: Laminate cross section (original image); Right: Roving volume fraction (processed image)

3.2.3.3 Roving & Filament distance distribution vs. FVF

Considering the flow behavior of the particle-filled epoxy system in the textile, it is quite important to understand and characterize the porous structure of the fibrous preform to analyze

the particle flow and filtration mechanism in the porous textile structure. As described earlier, if a standard textile microstructure is considered, as shown in Figure 2.3, two different basic elements at distinct levels could be differentiated: rovings and filaments. **Correspondingly, there are two different scales of pores to be differentiated: macro-scale pores that are generated between the rovings and micro-scale pores between the filaments.** Both the macro and micro-scale pores are stochastic variables that are strongly dependent on the roving size, textile architecture and surface weight. The distribution of the two different pore sizes could be illustrated in Figure 2.4. Among them, however, the micro-pores – distance between the filaments in the roving – are expected to be much more important to the particle flow, as they are mostly critical for the filtration of the NPs.

Considering the stochastically distributed filaments in a laminate cross section, as shown in Figure 3.11, several kinds of statistical methods are applied to fully characterize the filament distance distribution in the most representative way: Nearest Neighbor Distance (NND), Neighbor Distance (ND) and Ripley's K function.

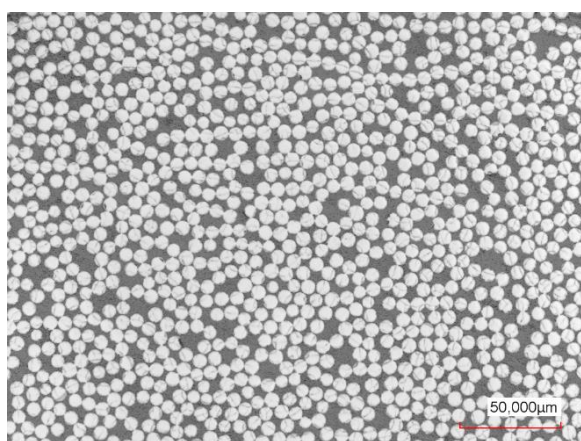


Figure 3.11: Stochastically distributed filaments (typical fiber-laminate cross section)

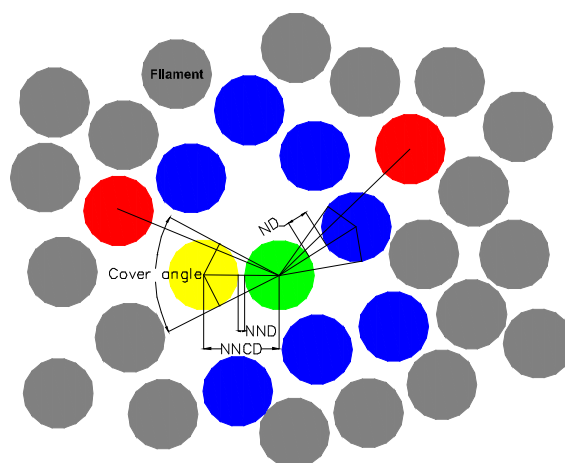


Figure 3.12: Image analyze methods for characterizing the filament distance

The definition of the different statistical characterization methods is explained combining the Figure 3.12 as follows: each filament is a circle with a certain diameter (D); if a certain filament is considered, as the green one as reference in the picture, the nearest neighbor is the one that has the smallest center distance to the reference filament (the yellow one in the Figure 3.12); the distance between the centers of these two are defined as Nearest Neighbor Center Distance (NNCD). To systematically characterize the full distance spectrum – all the neighbor distance – around a filament, the following algorithm is applied: as long as a filament lies outside the cover angles of any other filaments, or a filament can be moved to the reference laminate without interfering with any other filaments, it is considered to be a direct neighbor to the reference filament (the blue ones are the neighbors, but the red ones are not), by which the Neighbor Center Distance (NCD) can be calculated among filaments. The distance of the

filaments is calculated by subtracting the center distance minus radius of the two considered filaments: $NND = NNCD - r_1 - r_2$ or $ND = NCD - r_1 - r_2$.

As mentioned earlier, in order to evaluate the filament distance, it is critical to precisely detect the boundary of each filament, which is only possible by high-resolution microscopic methods like SEM. However, the high local zooming by SEM leads inevitably to a limited view of observable areas in the samples, which could lead to increased loss of statistic information, unless a lot of image collection and analyze. Considering these issues, a combined approach is used to calculate the filament distance: the filament diameter distribution is systematically investigated by SEM pictures in a high resolution with best accuracy, after that optical microscopy is used to detect the cross section with less zooming – bigger view, from which nevertheless the middle points of the filaments can be determined. By combining the filament diameter and filament-center distance information from the two methods, the filament distance can be determined in a rather accurate way.

Laminates with different FVF are fabricated by using Resin Transfer Molding (RTM) process. At least three samples from different positions of the laminates are taken to prepare for the image analyze after grinding and polishing. The cross-section images of composites are investigated both by optical microscope (OM) and SEM. To detect the filaments and obtain the diameter and distance information in laminate cross section, the SEM and OM images of each composite are required to be analyzed by image processing software. As explained earlier, this is quite critical for the accuracy of the analyzed data, especially to analyze the centers of the filaments by OM images. As the edges of the filaments are quite fuzzy due to the low resolution in OM pictures, even sometimes there might be some inevitable filament breakage on the surface due to the grinding and polishing process for sample preparation. So the image processing software is required to be equipped with image fuzzy recognition function.

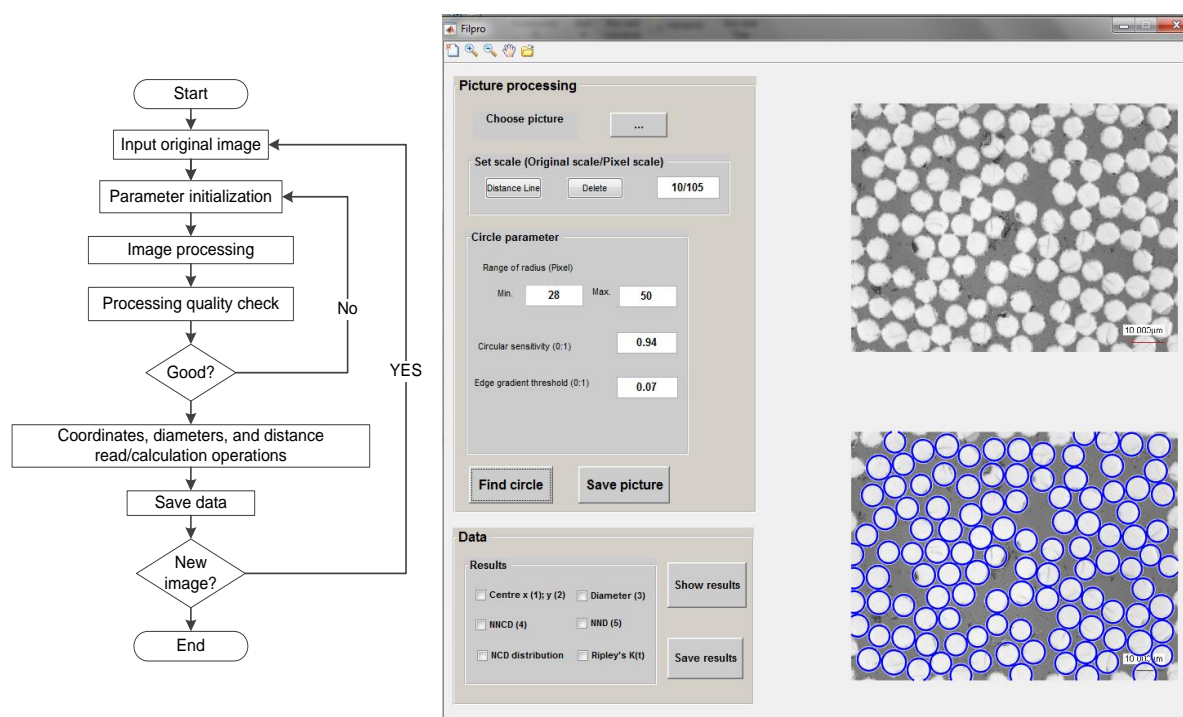
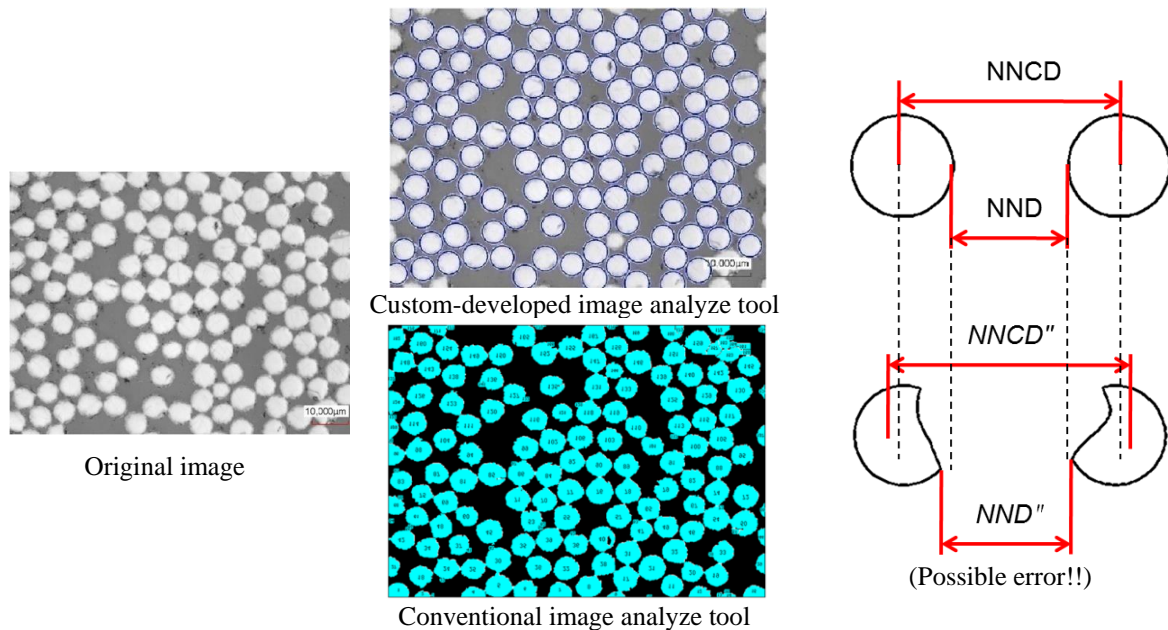
The standard available software cannot meet the requirement. For example, the software ImageJ, which most commonly used for image processing, cannot find a regular outline of the filament from the images, showing distorted shapes in the processed image, as shown in Figure 3.13 (bottom). These all could lead to a higher data error of filament distances because the accurate coordinators and outlines of filament cannot be measured from the irregular filaments images, as shown in Figure 3.13 on the right. Therefore, a custom software tool with image fuzzy recognition function is developed with Matlab to accurately find out and replenish the missing parts of filaments, if necessary, for each filament and their center coordinates in a laminate cross section.

The developed software has the below functions:

- Filament fuzzy recognition;
- Coordinators and diameter of filament measurement;

3 Materials and methodologies

- ND, NND and NNCD operation;
- Ripley's K Function;



3.2.3.4 Permeability tests

3.2.3.4.1 New model for flow front development

As described in the previous chapter in Eq. 2.17 - Eq. 2.19, the timely flow front development – flow velocity – is one of the dominating factors for determining the permeability of the textile. By an injection with standard non-reactive fluids (oil or neat epoxy without curing agent) with constant pressure, the development of squared flow front (x_f^2) versus time (t) shows a linear increase with a constant slope (m), as shown in Figure 3.15 (linear regression). However, for particle-filled systems, if the particles could deposit during the flow, it could lead to change of textile porosity, leading to a gradual deviation of the flow front from linearity, as shown in Figure 3.16. Therefore, in this case, the permeability of the textile could change as a function of time and position.

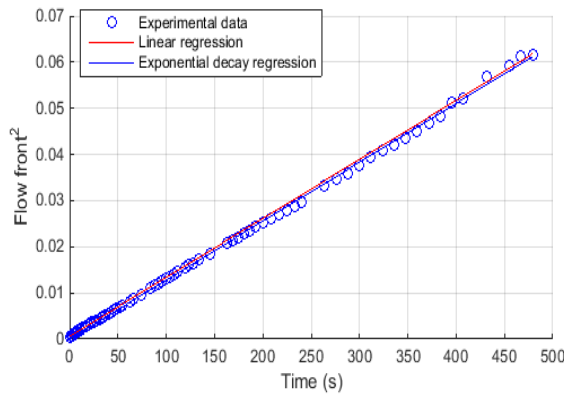


Figure 3.15: Flow front development in a permeability measurement by incompressible flow (oil or pure epoxy)

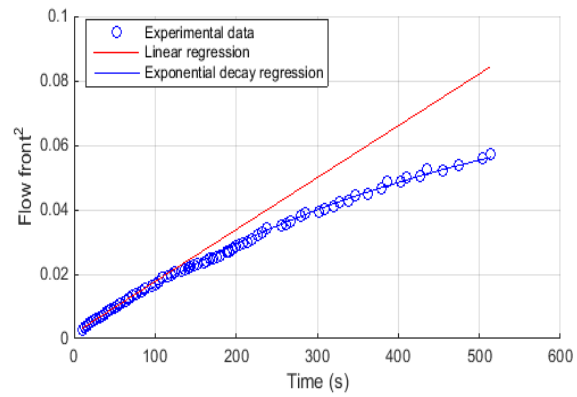


Figure 3.16: Flow front development in a permeability measurement by compressible flow (FVF60%, KE5% suspension)

Nevertheless, after experimental and numerical investigation, it is found out that the development of x_f^2 versus time by a particle-filled fluid could be mathematically well described by an exponential decay function in increasing form as following,

$$y = a(1 - \exp(-bx)) \quad \text{where} \quad \begin{array}{l} a: \text{maximum limit} \\ b: \text{decay factor} \end{array} \quad \text{Eq. 3.18}$$

The exponential decay function curve development regarding the different coefficient values are illustrated in the following Figure 3.17, in comparison with linear development. **In the case of the flow of NP-filled fluid in textiles, the parameter a – maximum limit – represent the maximum squared flow length, and the parameter b – decay factor – represents the NP filtration or gradient factor.**

By this new model, the development of x_f^2 versus t , by a standard non-reactive flow, can be seen as a case where the parameter a tends to infinity and b tends to zero. This shows that the flow behavior of the standard fluids can also be described by the new model, as shown in the

Figure 3.15 (exponential decay regression). **Therefore, the new model can be considered to be more general to be able to describe the timely flow front development of both standard and special – particle-filled fluid – flow cases.**

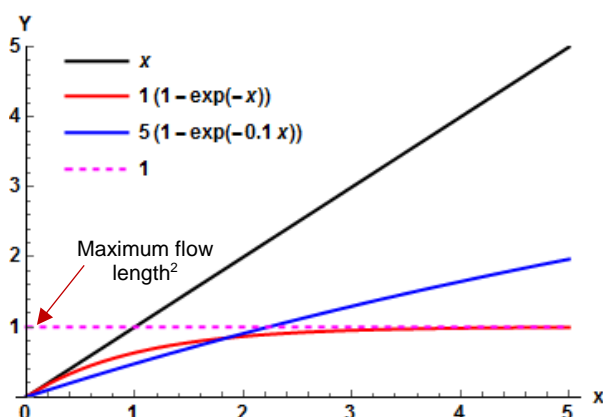


Figure 3.17: The exponential decay function curve development depending on the parameters

To calculate the permeability value, except from the flow front development (x_f^2, t) , the pressure, fluid viscosity (temperature) and pressure gradient values are needed, as discussed in Eq. 2.17 - Eq. 2.19. As the NP retention could influence the permeability, so all the critical manufacturing parameters – FVF, temperature, pressure and NP concentrations – come into play. **It needs to be pointed out that, without knowing the changes in the fluid viscosity and pressure gradient, the proposed model above cannot be directly applied in Eq. 2.17 - Eq. 2.19 for calculation of the permeability value. Nevertheless, it is a semi-experimental model for describing the flow behavior with two characteristic factors – maximum flow front and decay factor, by which the most critical information can be determined without complicated simulations.** To be also able to more precisely determine the flow speed and particle retention, multiphysic-coupled models are needed for the simulation. This aspect will be further described later in 3.3.2: Flow simulation.

3.2.3.4.2 Fluid & viscosity

- **Silicone oil:** silicone oil-AK100 from Wacker is used as the standard fluid for the permeability experiments.
- **NP-epoxy suspension:** For particle-filled suspensions, the KE masterbath that is delivered from IPAT is diluted with the resin (without any curing agent) into 2.5 wt%, 5 wt% and 10 wt%.

Dynamic viscosity measurements are carried out with 5K/min from 20-120 °C, with a shear rate of 50 1/s. It is fitted within the relevant temperature region with a two-term exponential model (see Figure 3.18). This modeled temperature dependence of the viscosity is used to calculate the present viscosity in the permeability measurement.

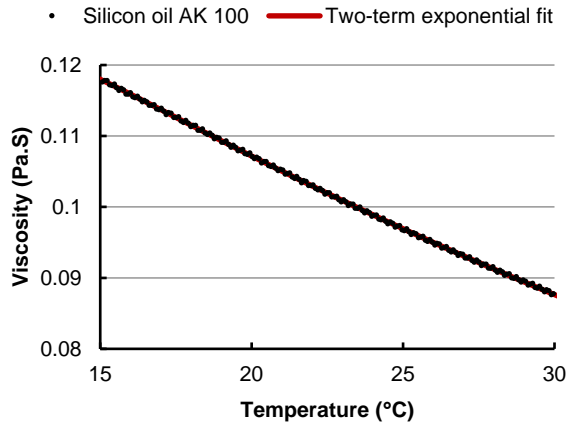


Figure 3.18: Viscosity vs. temperature of the silicon oil test fluids

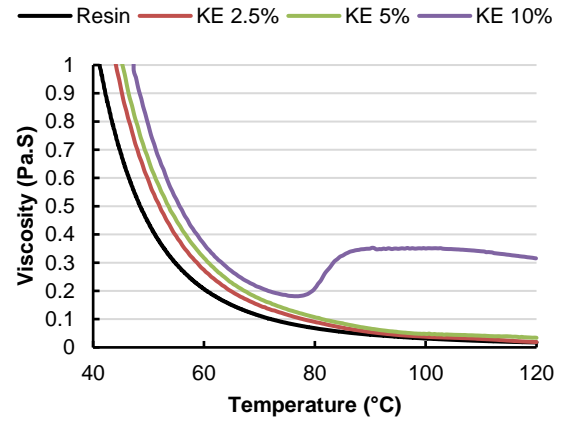


Figure 3.19: Viscosity vs. temperature of the boehmite-epoxy test fluids

The viscosity data are fitted within the relevant injection temperature region (60-100 °C) with a two-term exponential model. This modeled temperature dependence of the viscosity is used to calculate the present viscosity in the permeability measurements. As shown in Figure 3.19, the viscosity of the NP-epoxy suspensions until 5 wt% showed an exponential decrease as the temperature increase. However, at higher particle concentrations, for example KE 10 wt%, there is a sudden change in viscosity by the temperature of about 80 °C. This is proved to be due to irreversible chemical reactions between the particle and epoxy, even without curing agent. Therefore, in order to exclude the possible effect that could be caused due to the reaction, the permeability tests are conducted only with particle up to 5 wt%.

3.2.3.4.3 Flow front tracking

The flow fronts during the permeability tests are tracked by a custom-developed test rig in house [82] (see Figure 3.20). The test rig is mainly devised for optical tracking of the flow front in linear and radial-flow experiments. However, it also allows for linear saturated-flow experiments. In order to prevent tool deformation during textile compaction, it features a stiff upper mold made from a 243 mm high, cross-beam-reinforced steel frame and an 8 mm glass plate and a lower mold made from a steel block. The cavity height is adjustable to any desired value between 1mm and 10 mm by use of spacer plates made from thickness gauge strips. The mold is closed with two hydraulic pistons attached to a manual pump to build up a closing pressure of up to 100 bar. The maximum closing force and the high stiffness of the test rig result in a maximum deflection of less than 0.05 mm (mechanical simulation and measurement). These features allow for an exact definition of the cavity height.

In addition, the cavity height is measured after the experiment with the help of wax pellets, which are placed along the sides of the textile. The pellets are compacted to the cavity height by plastic deformation when the mold is closed. For linear-flow experiments, the sides of the

3 Materials and methodologies

textile are sealed with a hardening fluid to prevent race tracking without causing distortion of the textile. Pressure and temperature data are recorded with sensors located closely to the textile edges at both, the inlet and the outlet for linear-flow experiments, and at the inlet only for radial-flow experiments. Besides, the test rig is also equipped with heating elements from HORN GmbH, the measurement could be carried out also with special high-viscous fluids (NP-filled epoxy etc.) up to 120°C, with an accuracy of $\pm 2^\circ\text{C}$.

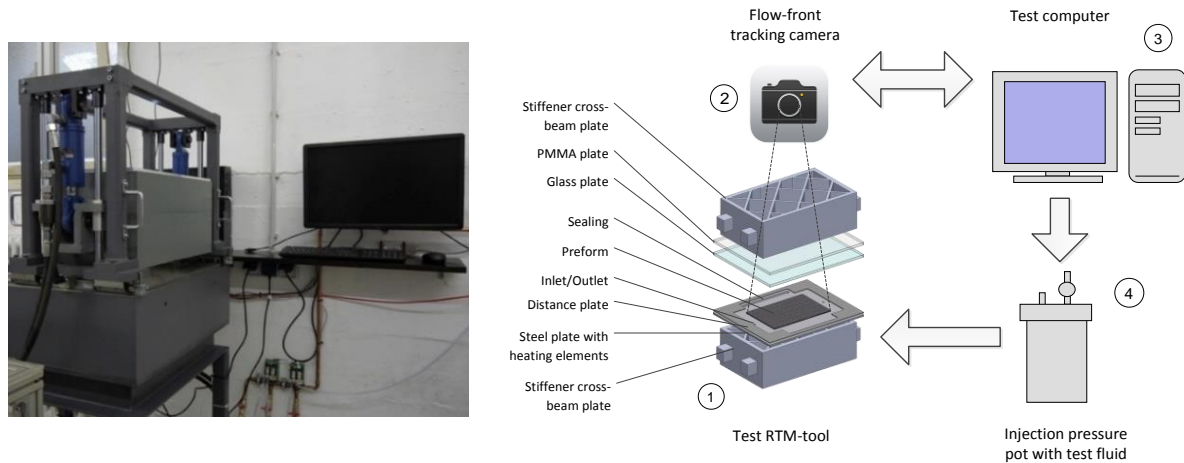


Figure 3.20: Permeability testing rig (left) and functional illustration (right)

A proprietary pressure and temperature recording software and an in-house Matlab script are used to conduct the experiment. The Matlab script provides a graphical user interface to conduct the experiment. It sets the injection pressure (0.5-6 bar) and tracks the flow front by taking photos with a resolution of 2560×1920 pixels and up to 3/fps. The Matlab script also features an algorithm to detect the flow front on-line by using difference images, as shown in the Figure 3.21. Special data evaluation and calculation algorithms are incorporated in the Matlab script considering the flow and filtration behavior of the NP-filled fluids.



Figure 3.21: Example image of a 1D linear flow (top) and 2D radial-flow (bottom) experiment and evaluation steps of the digital image processing algorithm (left to right)

3.2.3.5 Experimental design for permeability: Design of experiment (DoE) methods

In real applications, the textile will be injected with resin, besides the FVF, the other resin and process parameters, including viscosity (temperature) and pressure might affect the dominating dual-scale flow behavior and the measured permeability values. Due to the particle retention during the injection, the permeability could be further influenced by the NP concentration. Therefore, the maximum flow length and filtration factor are important parameters which are critical for injection process and design of injection strategies. Besides the factors above, NP concentration could also influence or determine the response values. The traditional ways of single variable experimental investigation are time-consuming and cost intensive. In order to investigate and find out the relationship between the factors, responses and runs, cost-effective statistical DoE methods could be applied. There are quite a lot of different methods that are applicable based on factor numbers and levels and target. An overview of different methods and selection guideline is provided in the below Table 3.1.

Comparative objective is preferable when there is one or several factors under investigation, but the primary goal of the experiment is to find a conclusion about one a-priori key factor, (in the presence of, and/or in spite of the existence of the other factors), and the question of interest is whether or not that factor is "significant", (i.e., whether or not there is a significant change in the response for different levels of that factor). Screening objective/method is used to select or screen out the few important main effects from the many less important ones. These screening designs are also termed as main effects designs. Response Surface (method) objective is used to estimate interaction and even quadratic effects, and therefore providing an idea of the (local) shape of the response surface that are being investigated. For this reason, they are termed response surface method (RSM) designs. RSM designs are used to: find improved or optimal process settings; troubleshoot process problems and weak points; make a product or process more robust against external and non-controllable influences [153].

Table 3.1: DoE methods and application

DoE methods Number of factors	Comparative Objective	Screening Objective	Response Surface Objective
1	1-factor completely randomized design	-	-
2-4	Randomized block design	Full or fractional factorial	Central composite or Box-Behnken
5 or more	Randomized block design	Fractional factorial or Plackett-Burman	Screen first to reduce number of factors

Two DoE studies based on the response surface method are conducted: firstly, the permeability by neat epoxy without particle as a response, to investigate the effect of FVF, temperature and pressure parameters to the permeability value, as shown in Table 3.2; Secondly, the maximum flow length and filtration factor with particle-filled suspension as response, to further

3 Materials and methodologies

investigate effect of FVF, NP concentration, temperature and pressure to the flow and filtration behavior, as shown in Table 3.3.

The critical factors and their levels are listed below. In order to prevent the evaluation errors due to the deviation in the parameters, the actual measured average values of FVF, temperature and pressure are used for the evaluations. Particle concentration is restricted up to 5 wt% as explained earlier. Other parameters, temperature and pressure, is selected considering the viscosity and commonly used industrial parameters in RTM processes.

Table 3.2: Critical factors and their levels by experimental design for permeability (pure epoxy fluid)

Factors	Level			Response
	1	2	3	
FVF (%)	45	55	65	Permeability
Temperature (°C)	60	80	100	
Pressure (bar)	1	2	3	

Table 3.3: Critical factors and their levels by experimental design for flow length study (NP-epoxy suspension)

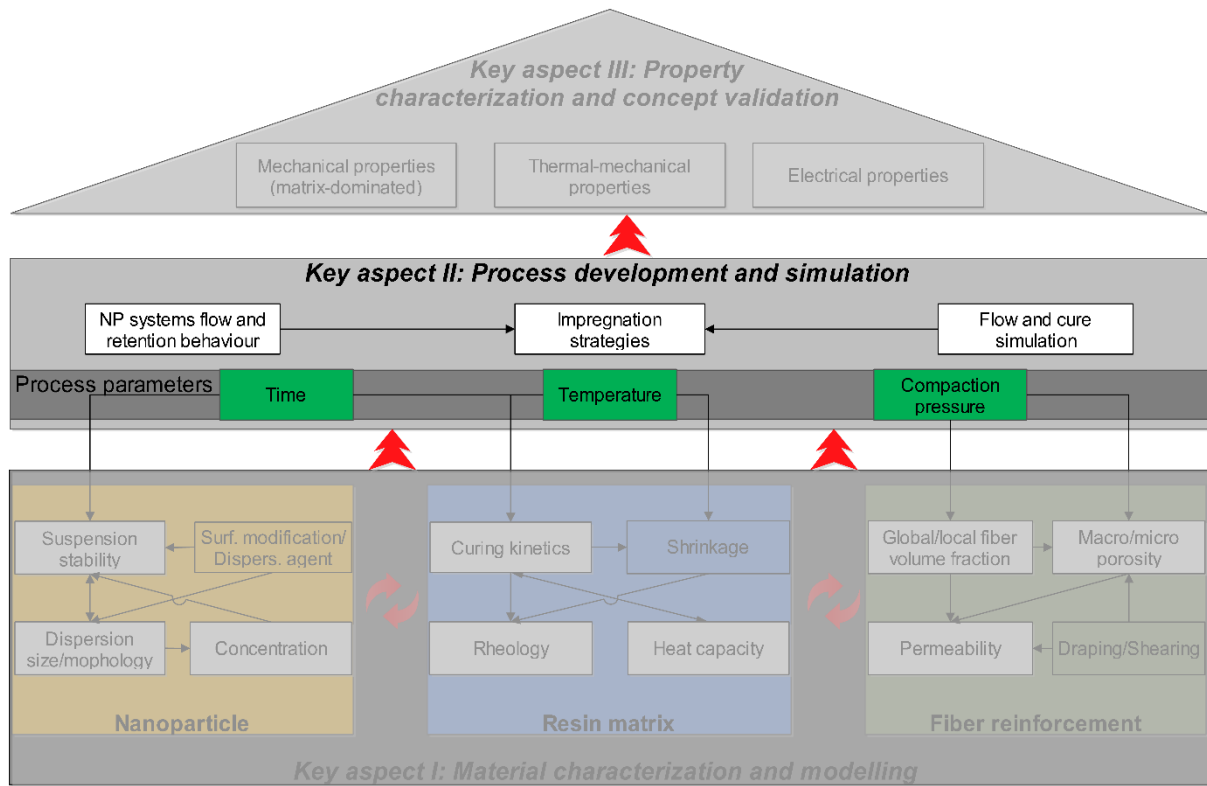
Factors	Level			Response
	1	2	3	
FVF (%)	50	55	60	Flow length & decay factor
NP (wt%)	0	2.5	5	
Temperature (°C)	60	80	100	
Pressure (bar)	1	2	3	

Considering the factors and their possible interactions with each other, a response surface method with 2nd interaction and 2nd power effects is selected for experimental design, as shown in Table 3.4.

Table 3.4: Experimental design using the RSM method with interaction and power effects (NP-epoxy suspension)

Exp. No.	FVF %	NP Wt%	Temperature (°C)	Pressure (bar)	Response	Fit Model	
1	60	5	100	3		Effects(:FVF %, :FVF % * :FVF %, :NP Wt%, :NP Wt% * :NP Wt%, :Temperature, :Temperature * :Temperature, :Pressure, :Pressure * :Pressure,	Single & quadratic effects
2	60	0	60	3			
3	50	0	100	1			
4	60	5	60	3			
5	60	5	60	1			
6	55	0	60	1			
7	60	0	100	2			
8	55	2.5	80	2			
9	50	5	100	1			
10	60	5	100	1		:FVF % * :NP Wt%, :FVF % * :Temperature, :FVF % * :Pressure, :NP Wt% * :Temperature, :NP Wt% * :Pressure, :Temperature * :Pressure)	Second order interactions
11	60	0	80	1			
12	50	5	60	1			
13	50	5	100	3			
14	50	5	60	3			
15	55	0	100	3			
16	50	0	60	2			
17	50	0	80	3		Y(:Permeability)	

3.3 Methodology for key aspect II: Process development and simulation



3.3.1 Nanoparticle systems flow and retention behavior

A special RTM-tool is developed which enables the extraction of fluid samples directly during the injection and observation of flow fronts. Injection experiments are carried out with different FVF and fiber directions. Considering the possible effects of hardeners to the particle dispersion and re-agglomeration behavior, experiments are carried out by diluted NP-epoxy suspensions without hardeners. NP-epoxy fluid samples are taken out directly from the RTM tool by different flow length and time, as shown in the Figure 3.22, and the particle concentration is measured by Thermal Gravimetric Analysis (TGA). In addition, considering that, the FVF is quite critical for the flow and retention of the particles, the cavity height is checked after the experiment with the help of wax pellets, which are placed along the sides of the textile.

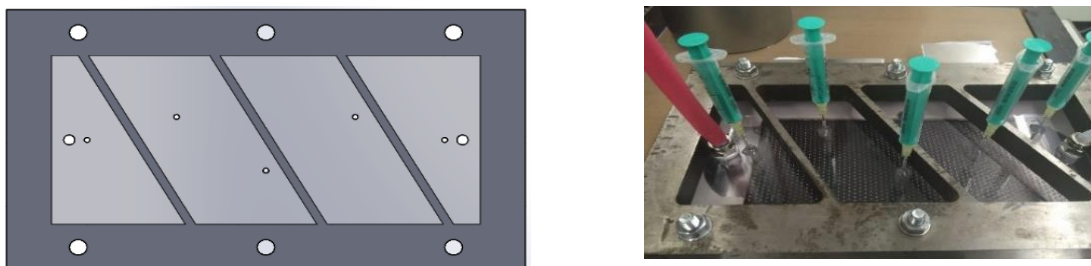


Figure 3.22: Custom-developed RTM tool for NP flow and retention investigation

3.3.2 Flow simulation

As mentioned in the literature review, if the particles could be filtered during the flow, it leads to a change of the fluid density and textile porosity. By separately considering the liquid and particle phases, it is possible to develop the governing mass balance equation for the liquid and NP phase, in a FCV as shown in the following Figure 3.23.

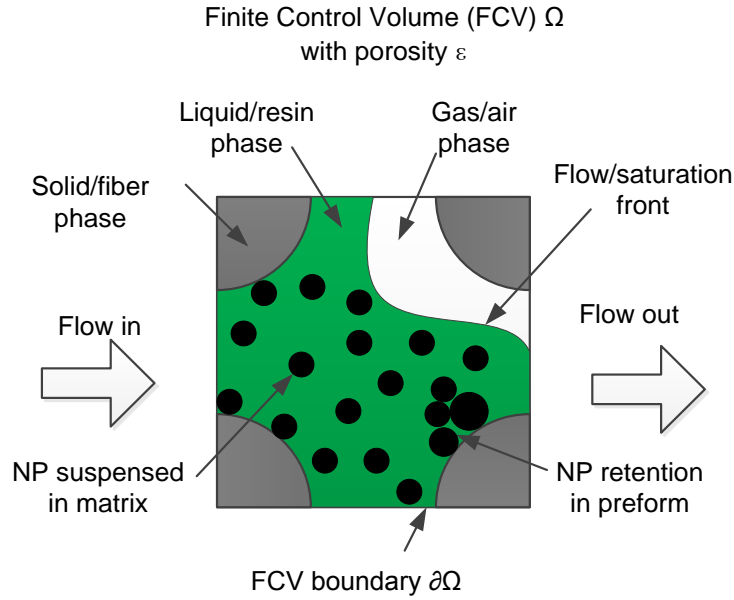


Figure 3.23: Illustration of a NP-filled matrix flow in FCV by a porous media

3.3.2.1 Flow sub-model

For the neat resin matrix, without NPs, the mass balance equation can be derived as follows,

$$\frac{\partial[\rho_l S_l \varepsilon (1 - C)]}{\partial t} + \nabla \cdot [\rho_l v_l \varepsilon (1 - C)] = 0 \quad \text{where} \quad \begin{array}{l} \rho_l: \text{liquid/air density} \\ S_l: \text{liquid saturation term} \\ \varepsilon: \text{porosity} \\ C: \text{concentration of NP in matrix} \\ v_l: \text{liquid velocity} \end{array} \quad \text{Eq. 3.19}$$

Considering the liquid density is to be constant and a full saturation, the equation simplifies to be as following,

$$\frac{\partial[\varepsilon(1 - C)]}{\partial t} + \nabla \cdot [v_l \varepsilon (1 - C)] = 0 \quad \text{Eq. 3.20}$$

For the NPs, the mass balance equation can be derived as follows,

$$\frac{\partial(\rho_p \varepsilon C)}{\partial t} + \nabla \cdot (\rho_p v_p \varepsilon C) = -\frac{\partial(\rho_p \sigma)}{\partial t} \quad \text{where} \quad \begin{array}{l} \rho_p: \text{particle density} \\ \varepsilon: \text{porosity} \\ v_p: \text{particle velocity} \\ \sigma: \text{NP retention} \end{array} \quad \text{Eq. 3.21}$$

Considering that the density of the particle is constant, and the change in the porosity regarding the NP retention can be described as $\varepsilon = \varepsilon_0 - \sigma$, which results in $\partial \varepsilon / \partial t = -\partial \sigma / \partial t$, therefore, the above equation could be rewritten as,

$$-\frac{\partial[\varepsilon(1-C)]}{\partial t} + \nabla \cdot (v_p \varepsilon C) = 0 \quad \text{Eq. 3.22}$$

Combining the equation Eq. 3.20 and Eq. 3.22, the following equation can be derived,

$$\nabla \cdot [v_l \varepsilon(1-C)] + \nabla \cdot (v_p \varepsilon C) = 0 \quad \text{Eq. 3.23}$$

Assuming that by the flow of NPs, the velocity of the liquid and particle is the same, $v_l = v_p$, the equation results in a simple form of continuity equation for suspension as follows,

$$\begin{aligned} \nabla \cdot (v \varepsilon) &= 0 \\ \text{or} \quad \nabla \cdot (U) &= 0 \end{aligned} \quad \begin{array}{l} \text{where} \\ v: \text{apparent velocity} \\ \varepsilon: \text{porosity} \\ U: \text{darcy velocity} \end{array} \quad \text{Eq. 3.24}$$

Therefore, the flow behavior of the suspension can be described by the simple continuity equation as shown in Eq. 3.24 and the Darcy law as in Eq. 2.8.

3.3.2.2 Retention sub-model

The mass balance equation as written in Eq. 3.21 for NPs can be further simplified as following:

$$\frac{\partial(\varepsilon C + \sigma)}{\partial t} + U \frac{\partial C}{\partial x} = 0 \quad \text{Eq. 3.25}$$

The retention kinetic of the NPs is described to be proportional to the volumetric flux, i.e. UC , of the suspended particles by a retention coefficient as follows [119, 154, 155]:

$$\frac{\partial \sigma}{\partial t} = rUC \quad \text{where } r: \text{retention coefficient} \quad \text{Eq. 3.26}$$

3.3.2.3 Material models

3.3.2.3.1 Filter permeability

Regarding the permeability, it is obvious that the filtrated NPs can build up a second porous media that changes the porosity of the fiber preform and overall permeability. It is possible to consider that, the total permeability is a coupled interaction of the textile permeability and the permeability of the second porous media that is created due to the retention of the NPs.

$$\frac{1}{K_{total}} = \frac{1}{K_f} + \frac{1}{K_{NP}} \quad \begin{array}{l} \text{where} \\ K_{total}: \text{total permeability} \\ K_f: \text{fiber textile} \\ \text{permeability} \\ K_{NP}: \text{filtrated NP} \\ \text{permeability} \end{array} \quad \text{Eq. 3.27}$$

Therein, the fiber textile permeability K_f is a constant, but the filtrated NP permeability K_{NP} is dependent on the filtrated NPs. The permeability of the filtrated NPs can be described and modeled by Kozeny-Carman (KC) equation [99, 156]

$$K = \frac{\varepsilon_{NP}^3}{36k(1 - \varepsilon_{NP}^2)} d^2 \quad \begin{array}{l} \text{where} \\ k: \text{KC constant} \\ \varepsilon_{NP}: \text{deposit porosity} \\ d: \text{average diameter} \end{array} \quad \text{Eq. 3.28}$$

The KC constant is dependent on the geometry and porosity of the media. For a well-defined media, it can be determined by numeric or experimental methods. According to the literature review [119, 121, 156], for spherical/granular media with a porosity around 0.5, the values is about 5. The deposit porosity is directly related to the retention of the NPs, and can be written as $\varepsilon_{NP} = 1 - \sigma$. **For a well-defined porous media, the average diameter is easy to determine. Nevertheless, the filtrated NPs are an unknown media that changes due to time and position. Considering the challenge to characterize the average diameter of the filtrated NPs by experiment, a reverse calculation is carried out based on a flow experiment to determine the average diameter from the simulation.**

3.3.2.3.2 NP-epoxy suspension viscosity

The modeling of the viscosity of reactive NP-filled matrix is already discussed earlier in 3.2.2.4 Rheology modeling. Regarding the possible influence of the cure reaction on the particle-particle and particle-matrix interaction with the increased reagglomeration effects during the injection, as the first step a non-reactive NP-epoxy matrix without hardener is considered, so that only the interaction between the flow and retention based on the masterbatch dispersion quality is to be considered. This simplification helps to evaluate the model quality and numerical methods more accurately. Several different models are proposed and applied to model the viscosity of the non-reactive NP-epoxy matrix [119-121], among which the model as follows is selected for the modeling [117, 157],

$$\eta = \eta_0 \left(1 - \frac{C}{A}\right)^{-2} \quad \text{where} \quad \begin{array}{l} \eta_0: \text{viscosity of polymer} \\ A: \text{empirical constant} \end{array} \quad \text{Eq. 3.29}$$

3.3.2.4 Numerical implementation

The flow and retention behaviors of the nanosuspension are coupled by the viscosity of the matrix and the permeability of the textile, as shown in the following Figure 3.24.

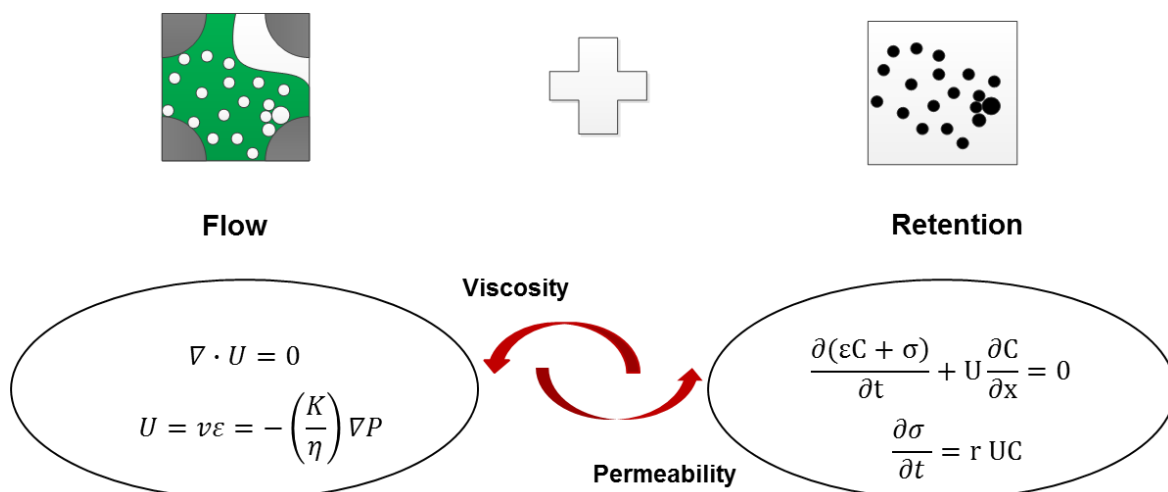


Figure 3.24: Flow and retention coupling during the impregnation process

The flow front tracking is achieved by an extra level-set model that is coupled to the flow and retention models. In standard level set methods, the level-set function Φ_{sd} is defined to be a signed distance function from the interface Γ , by a volume Ω :

$$\Phi_{sd}(x, t) = d(\vec{x}) = \min_{x \in \Gamma} (|\vec{x} - \vec{x}_r|) \quad \text{Eq. 3.30}$$

The level set function is positive on one side of the interface, zero at the interface and negative at the other side of the interface.

$$\Phi_{sd}(x, t) = \begin{cases} -d(x, t) & x \in \Omega^- \\ 0 & x \in \Gamma \\ +d(x, t) & x \in \Omega^+ \end{cases} \quad \text{Eq. 3.31}$$

In addition, in order to represent the density and viscosity discontinuities over the interface, an extra Heaviside function is to be defined from 0 to 1. In numerical simulations, the abrupt jump in the fields from 0 to 1 will cause instabilities, therefore a smeared-out Heaviside function is mostly applied, as follows:

$$H_{sm}(\Phi_{sd}) = \begin{cases} 0 & \Phi_{sd} < -\varepsilon_{ls} \\ \frac{1}{2} + \frac{\Phi_{sd}}{2\varepsilon_{ls}} + \frac{1}{2\pi} \sin\left(\frac{\pi\Phi_{sd}}{\varepsilon_{ls}}\right) & -\varepsilon_{ls} \leq \Phi_{sd} \leq \varepsilon_{ls} \\ 1 & \Phi_{sd} > \varepsilon_{ls} \end{cases} \quad \text{Eq. 3.32}$$

Where, ε_{ls} corresponds to half the thickness of the interface.

If the smeared-out Heaviside function is directly defined as a new level set function $\Phi = H_{sm}(\Phi_{sd})$, it is not necessary to calculate H_{sm} from Φ_{sd} and the new level set function Φ can be directly used to represent the changes and transition between the two different phases by the scalar field of the new level set function:

$$\begin{aligned} \rho &= \rho_{air} + \bar{\Phi}(\rho_{liquid} - \rho_{air}) \\ \eta &= \eta_{air} + \bar{\Phi}(\eta_{liquid} - \eta_{air}) \end{aligned} \quad \text{where } \bar{\Phi}: \text{ scalar of level-set function} \quad \text{Eq. 3.33}$$

The application of the new level-set function is also known as conservative methods [158, 159], and it defines the interface between the two sum-domains: impregnated region and dry region – filled with air. By the interface transition from wetted to dry region, the level-set function value Φ changes from 1 to 0.

The advection of the level-set parameter is governed by a transport equation based on the flow velocity of the matrix. So, the tracking of the flow front can be achieved by tracking the level-set function value of $\Phi = 0.5$. For further information regarding the level-set methods and its implementation, the readers are redirected to the following literatures [160-162].

$$\frac{\partial \Phi}{\partial t} + U \cdot \nabla \Phi = \gamma \nabla \cdot (\varepsilon_{ls} \nabla \Phi - \Phi(1 - \Phi) \frac{\nabla \Phi}{|\nabla \Phi|}) \quad \text{where } \begin{array}{l} \varepsilon_{ls}: \text{ interface thickness} \\ \text{parameter} \\ \gamma: \text{ reinitialization} \\ \text{parameter} \end{array} \quad \text{Eq. 3.34}$$

There are varieties of different software tools available to simulate the mold filling during a LCM process, including commercial PAM-RTM and RTM-Worx tools [163] that are specially tailored to simulate RTM processes. Besides, there are also certain CFD packages, e.g. Ansys

3 Materials and methodologies

Fluent/CFX or Comsol Multiphysics etc. There are also plenty of development in the simulation methods or tool and some of them are made public free of access, for instance OpenFOAM [164], MyRTM [165, 166] etc. Some information about the tools and comparison between OpenFOAM and PAM-RTM tools for simulation of the RTM process can be found here [113]. The flow simulation in this work is carried out by the FEM-software Comsol Multiphysics, due to the flexibility especially regarding multi-physical coupling applications.

3.3.3 Cure simulation

The cure simulation is based on a complex synergistic consideration of coupled thermal, chemical and flow effects during the injection. Considering the slow reaction rate during the injection, the following assumptions are reasonably supposed:

- The injection process is finished.
- The whole textile is filled completely with resin, without any porosity.
- The length of the laminate is much bigger than the thickness and width, so the heat transfer in the length direction could be neglected.
- The thermal transfer due to the convection and radiation is much smaller than the conduction, so could be neglected.

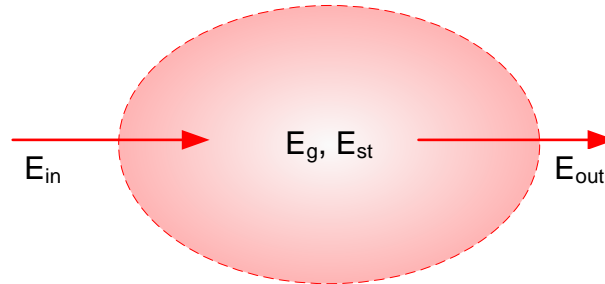


Figure 3.25: Control volume element for heat conduction

If an infinite small control volume is considered, as shown in Figure 3.25, the energy that is transferred into the volume plus the energy generated in the volume (due to the chemical exothermic reaction) is equal to the energy stored plus the energy that is transferred out from the volume. The general heat conduction could be described as

$$E_{in} + E_g = \Delta E_{st} + E_{out} \quad \text{where} \quad \begin{array}{l} E_{in}: \text{income energy} \\ E_g: \text{generated energy} \\ \Delta E_{st}: \text{stored energy} \\ E_{out}: \text{outcome energy} \end{array} \quad \text{Eq. 3.35}$$

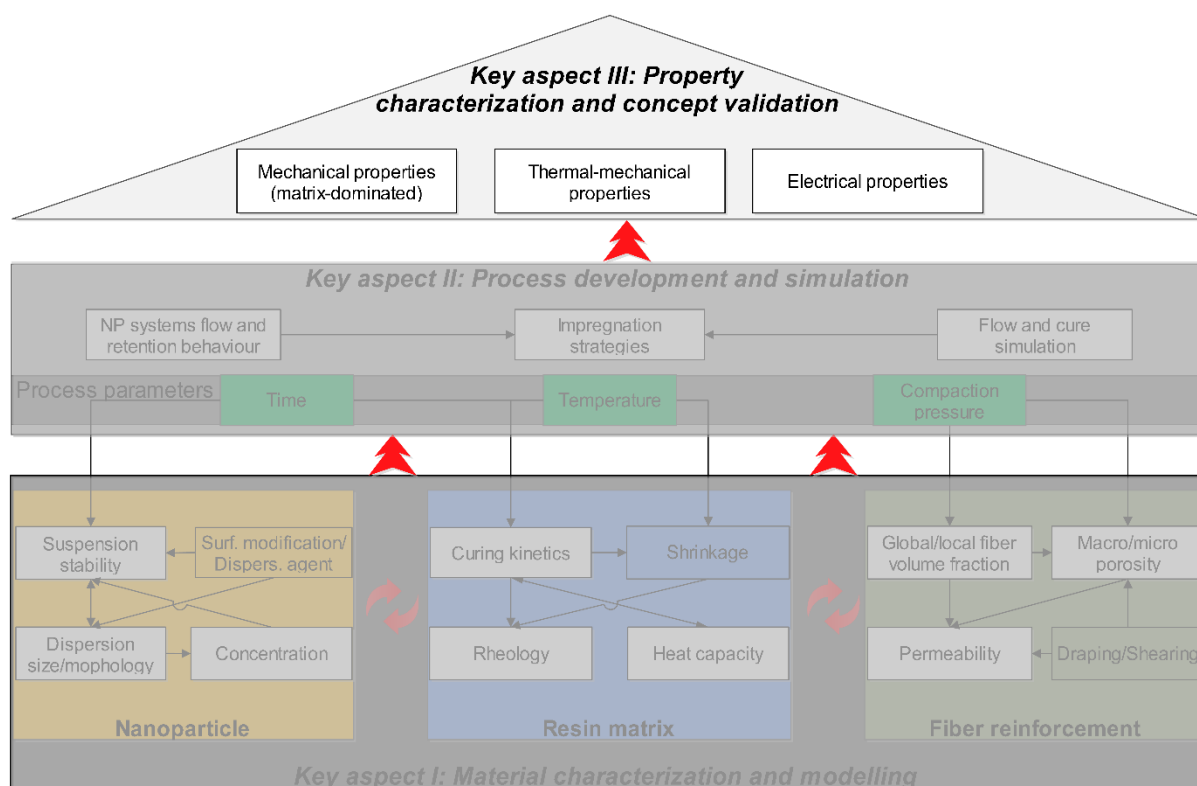
Which could be re-written as follows,

$$\nabla(\lambda \nabla T) + \dot{Q} = \frac{\partial(\rho C_p T)}{\partial t} \quad \text{where} \quad \begin{array}{l} \lambda: \text{heat conductivity} \\ \dot{Q}: \text{generated heat due to the reaction} \\ C_p: \text{specific heat capacity} \end{array} \quad \text{Eq. 3.36}$$

Therefore, each of the material parameters above needs to be characterized. The measurement of heat conductivity and heat capacity is described in 3.2.2.2.2. The generated heat due to reaction \dot{Q} is calculated according to the cure kinetics model.

Because all the critical material parameters and the generated heat by the reaction are dependent on the material composition, so that these parameters are not just dependent on time and temperature, as well as NP concentration. The cure simulation for such a gradient NP distributed FRP is quite complex regarding the material properties and numerical implementation. Therefore, the cure simulations are carried out on the presumption that the particle distribution in the whole laminate is homogenous, by which the critical cure and temperature development states within the laminate are compared depending on the particle concentrations. This is a reasonable simplification as by this method the extreme cases – from no NP to the maximum concentrations of NPs – are still being considered. The cases by the gradient NP distributed FRP structure is assumed to be within the range of the extreme cases. Based on these assumptions, the cure simulation is carried out by the FEM-software Comsol Multiphysics.

3.4 Methodology for key aspect III: Property characterization and concept evaluation



3.4.1 Mechanical properties

For the mechanical properties, mainly the matrix-dominated properties – interlaminar fracture toughness (G_{IC} , G_{IIC}), three-point-bending (transverse to fiber direction) and interlaminar shear strength (ILSS) tests – are considered.

3.4.1.1 Interlaminar fracture toughness

Interlaminar fracture is a critical failure mode for laminated composite structures, which occurs due to high out-of-plane loads where no fibers are present to resist loading. Delamination can occur due to tensile (mode I, G_{IC}), shear load condition (mode II, G_{IIC}), or a combination of the both (mode III, G_{IIIC}). In this work, the interlaminar fracture toughness of functional FRPs is investigated under mode I and mode II deformation. The tests are conducted according to the Airbus Industry Test Methods (AITM) “AITM 1-0005 / EN 6033 Fibre reinforced plastics - Determination of interlaminar fracture toughness energy - Mode I – G_{IC} [167]” and “AITM 1-0006 / EN 6034 Fibre reinforced plastics - Determination of interlaminar fracture toughness energy - Mode II - G_{IIC} [168]”.

The related testing specimens and procedure and the results evaluation involved in the two deformation modes are hereby described as follows: Double Cantilever Beam (DCB) specimen

and End Notch Flexure (ENF) specimen are employed for interlaminar fracture under mode I and mode II deformation, respectively. The specifications and dimensions of the DCB and ENF specimens are shown in Figure 3.26 and Figure 3.27. The initial crack length of 25 mm formed in the middle plane of the laminate is made by inserting a teflon film with a thickness of 25 μm into the stacking process of the laminate. Furthermore, the DCB samples are preloaded to introduce a further crack of about 15 mm to exclude the influence of the teflon film and other adhesive on the measurement. A universal material-testing machine ZWICK is applied for the DCB and ENF test with a load cell of 2.5 KN to measure the applied load.

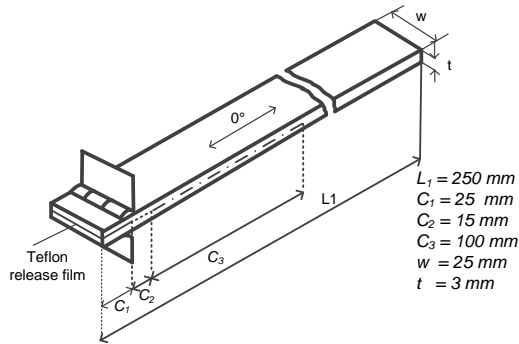


Figure 3.26: Schematic illustration of DCB specimens for G_{IC} test

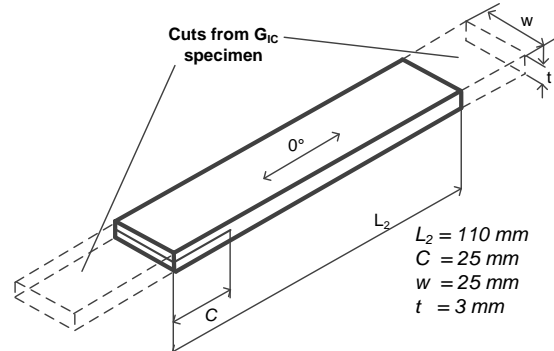


Figure 3.27: Schematic illustration of ENF specimens for G_{IIIc} test

The fracture surface after fracture tests is analyzed by high-resolution SEM to investigate the fracture mechanism of crack propagation in the functional FRPs. Samples are cut from the fracture surface in size of 10 mm \times 5 mm. After cleaning with pressurized air, the samples are mounted on aluminum stubs. The fracture surfaces of the samples are then sputter coated with a thin layer of platinum (Pt) to avoid electrical charging.

3.4.1.2 Three-Point-Bending

The bending properties of the multi-scale FRPs are measured by three-point-bending. The test samples are prepared transverse to fiber direction. The test is conducted according to the standard DIN EN ISO 14125 [169]: “Fibre-reinforced plastic composites: Determination of flexural properties”. The tests are carried out with a velocity of 1 mm/min.

3.4.1.3 Interlaminar shear strength (ILSS)

The ILSS of the FRPs is also an important aspect, as there is no effective reinforcement in the thickness direction. Therefore, the ILSS properties of the multi-scale FRPs are tested by a short-beam-shear test according to DIN EN ISO 14130 [170]: “Fibre-reinforced plastic composites -- Determination of apparent interlaminar shear strength by short-beam method”. The tests are carried out with a velocity of 1 mm/min.

3.4.2 Thermal-mechanical properties

3.4.2.1 Thermal conductivity

The thermal conductivity of the cured NP-epoxy and CFRP samples with different NPs are measured by a Hot-Disk-method by TCA-Netzsch, from 30 – 180 °C.

3.4.2.2 Dynamic thermal-mechanical properties

The dynamic thermal-mechanical analysis (DTMA) is also simply called as dynamic mechanical analysis (DMA). DTMA measurements are performed on DMA Q800 device from TA Instrument. Experiments are run with samples that have a size of about 35 mm × 10 mm × 3 mm (single cantilever). The aim of the measurements is to study the effect of the NPs on the dynamic mechanical properties of functional FRPs. The samples are subjected to a temperature scan from 30 °C to 180 °C with a ramp of 2 °C /min. A fixed strain of 10 µm and frequency of 1 Hz are used in the measurement.

3.4.3 Electrical properties

The surface and the through-thickness volume resistivity measurements are conducted with the Keithley 6517A electrometer and Keithley 8009 resistivity test fixture. The test conforms to the ASTM D-257 standard [171]: “Standard Test Methods for DC Resistance or Conductance of Insulating Materials”. The basic setup and parameters for the surface and through-thickness volume resistivity measurement is shown in Figure 3.28.

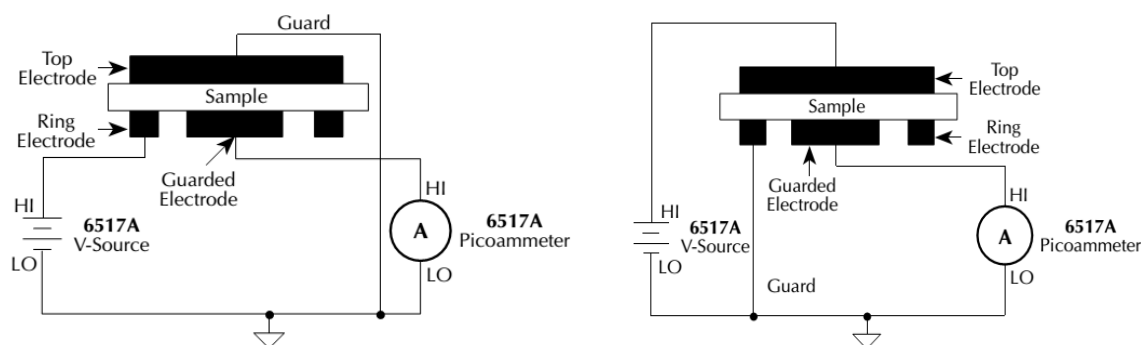
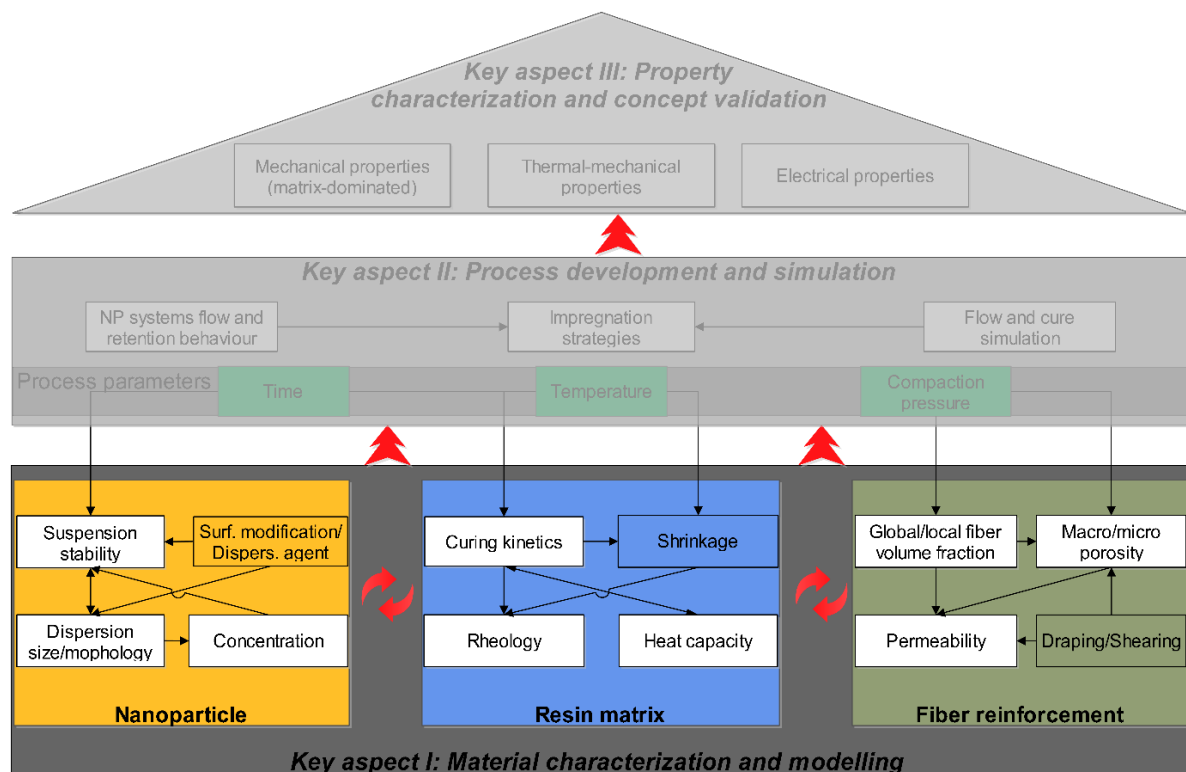


Figure 3.28: Principle of surface (left) and volume (right) resistivity measurement setup

The surface resistivity is measured from the ring electrode to the guarded electrode along the lower surface of the sample. The through-thickness volume resistivity is measured from the top electrode to the guarded electrode through the thickness of the sample. The electrodes in the 8009 resistivity test fixture are covered with conductive rubber to reduce the contact resistance by a better surface contact with the rigid sample. For each sample, five measurements are conducted with a constant voltage of 100V and electrification time of 60 s.

4 Key aspect I: Material characterization and modeling

The focus of this chapter is to discuss the results regarding the key aspect I: material characterization and modeling. The critical aspects and their interactions among the three basic components – NP, epoxy matrix and fiber reinforcement, as shown in the figure below are investigated. Furthermore, the cure kinetics, rheology of the NP-epoxy matrix as well as the permeability of the fiber preform considering the NP retention behavior are modeled.



4.1 Nanoparticle-epoxy matrix

4.1.1 Cure characterization and modeling

4.1.1.1 Dynamic DSC

Dynamic DSC studies are carried out to characterize the dynamic cure, total reaction enthalpy and T_g . As the first step, pure resin system is investigated with 1, 2, 3, 5, 10 K/min. Considering that the DSC tests are rather reproducible, therefore the total enthalpy of the subsequent boehmite NP filled epoxy matrix systems are determined by the average values by two different heating rate DSC tests: 2 K/min and 10 K/min. The glass transition temperature of other mixtures is measured with the heating rate of 10 K/min, as shown in the following Table 4.1.

As the total enthalpy is dependent on the unit mass of the sample, with the increase of the boehmite NP concentration, the proportion of the reactive resin and curing agent will be decreased, which could inevitably lead to the decrease of the total enthalpy. Therefore, the total enthalpy is normalized by the by subtracting the weight concentration of the boehmite NP on the enthalpy.

Table 4.1: Total reaction enthalpy and T_g by different mixtures

Mixture	Average enthalpy (J/g)	Normalized average enthalpy (J/g)	T_{g0} (°C): uncured sample	T_g (°C): cured sample
0% (Pure resin)	354.4 ± 3.9	354.4 ± 3.9	-37.99 ± 0.08	136.32 ± 3.48
KE wt5%	313.4 ± 3.65	329.8 ± 3.84	-35.99 ± 1.13	127.18 ± 0.89
KE wt10%	293.4 ± 1.65	325.9 ± 1.83	-34.87 ± 1.71	121.83 ± 4.61
KE wt15%	266.3 ± 1.2	313.3 ± 1.41	-34.43 ± 0.74	118.68 ± 0.17

According to the normalized average enthalpy, it could be seen that there is a gradual decrease in the total enthalpy. The glass transition temperature before the reaction – T_{g0} – showed a slight increase, which is presumably because that the increased amount of boehmite NPs could restrict the mobility of the epoxy molecules, so that a higher energy is needed for the glass transition. Conversely, the glass transition temperature after the full reaction – T_g – showed a remarkable decrease, indicating a reduced crosslinking density of the epoxy chains due to the NPs.

Figure 4.1 shows the normalized heat flow for different mixtures by the dynamic DSC process (10 K/min). It could be seen that the reaction peak-position temperature is almost the same, indicating no substantial influence of the boehmite NPs on the dynamic reaction behavior. At the same time, dynamic DSC investigations on just boehmite-epoxy suspensions (without any curing agent) as in the Figure 4.2 showed a remarkable reaction peak by the first heating cycle and a shift at the glass transition temperature at the second heating (heat-cool-heat). This shows a clear reactivity of the boehmite NP with the epoxy, even without curing agent. Therefore, it is reasonable to assume that the reactivity of the epoxy with boehmite NP is much smaller than

that with the curing agent, which is why there is not any remarkable change in the curing reaction peak in the dynamic curing. The influence of the boehmite NPs will be further analyzed and discussed later combining the cure kinetics.

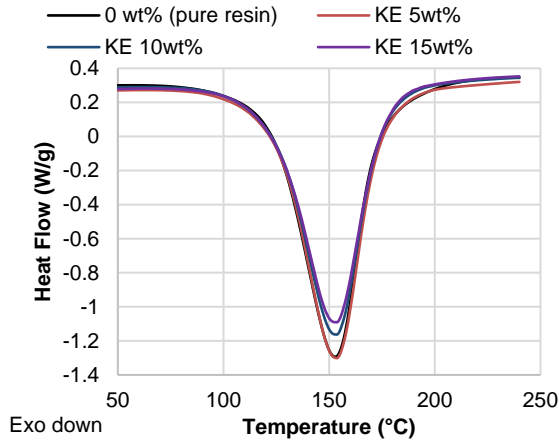


Figure 4.1: Normalized heat flow for KE-suspension by dynamic DSC

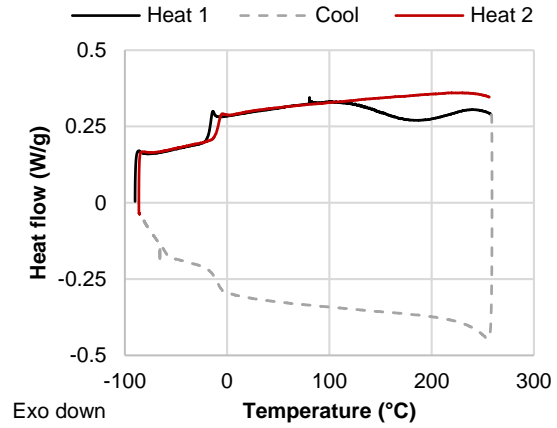


Figure 4.2: Dynamic DSC measurement on 15wt% boehmite-epoxy suspension without curing agent

4.1.1.2 Estimation of kinetic parameters and their influence on model regression analysis

As discussed in Chapter 3, the kinetic parameters are estimated by different methods that are described earlier: model-free (iso-conversional) and model-fitting methods. As model-free method, Friedman's method is selected, as shown in Figure 4.3, and the devolution of activation energy is calculated as shown in Figure 4.4. As model-fitting methods, Kissinger and Sestak-Berggren (S-K) methods are applied, as shown in Figure 4.5 and Figure 4.6.

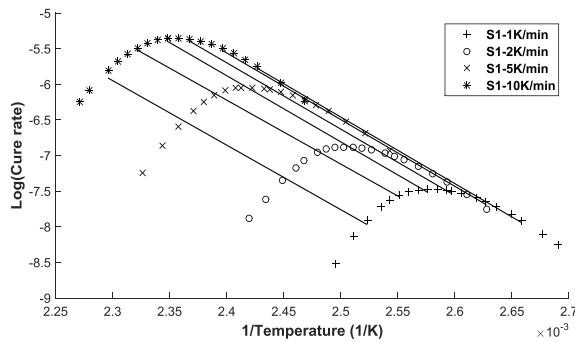


Figure 4.3: Friedman plot

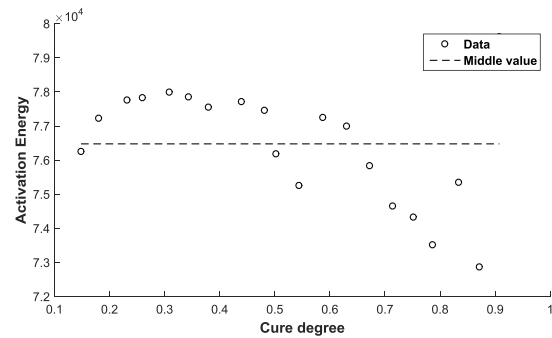


Figure 4.4: The overall activation energy vs. conversion by Friedman method

4 Key aspect I: Material characterization and modeling

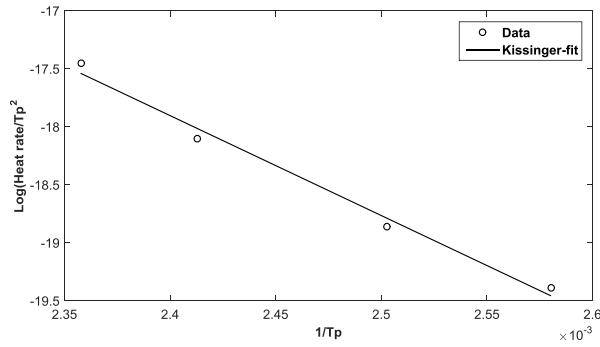


Figure 4.5: Kissinger plot

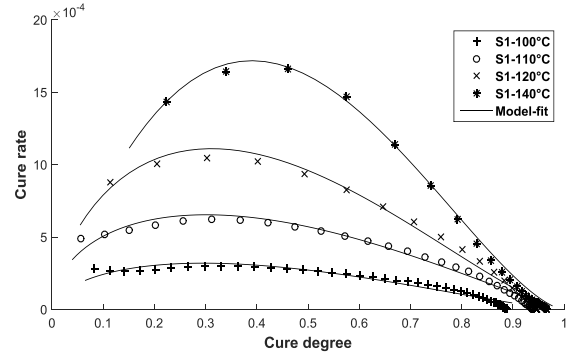


Figure 4.6: Sestak-Berggren plot

The following Table 4.2 shows the different start values that are calculated by the estimation methods described above. The start values within bracket are taken from the other methods or literature, as they could not be directly evaluated. Among them, as explained earlier, the estimation by Friedman and Kissinger methods are based on four variable heating rate DSC processes, while S-B method is based on four isothermal DSC processes.

According to the model-free Friedman method, the change of activation energy E depending on the cure evolution is shown in the Figure 4.4. The changing activation energy as a function of cure degree indicates a multi-step reaction that could be well described by the selected Kamal-Sourour model. By the model evaluation, however, a changing activation energy as a function of cure degree makes the evaluation and kinetic model very complicated. If the average activation energy from Friedman's method is compared to that from the Kissinger method, it could be seen that they are quite close to each other; therefore, the average value is used as start value. However, due to the lack of model estimation in Friedman's method, it is not possible to evaluate pre-exponential factor A and reaction order m and n . In comparison, Kissinger and S-B methods provide an estimation of all the model triplets, by assuming a 1st order and autocatalytic reaction, separately.

Table 4.2: Estimated kinetic parameter start values by different methods for neat epoxy matrix

Kinetic parameters	A_1/A_2 (1/sec)	E_1/E_2 (J/mol)	m	n
Estimation methods				
Model-free: Friedman method	- (from Kissinger)	76793.6 (Average)	(0.5)	(1)
Model-fitting: Kissinger method	1.06E+05	70744.6	(0.5)	(1)
Model-fitting: S-B method	1.47E+07	72857.9	0.52	1.12

It can be seen from the estimated values that, the estimated activation energy values from all the three methods are different, nevertheless similar in the same of orders of magnitude. However, the pre-exponential factor that is estimated from the Kissinger and S-B method deviates by two orders of magnitude. As the Kissinger method is based on 1st order reactions, for autocatalyzed thermosets like the target system in the thesis, the estimated pre-exponential factor may not be valid since the calculation of A is based on a 1st order reaction. A big deviation of the A value between the Kissinger and Prout–Tompkins autocatalytic model estimation was

reported by Hardis et al [57]. Therefore, the estimated A values from the heating rate DSC methods need to be considered quite critically.

Considering that, the S-B method provides proper estimation of all the parameters directly by the isothermal DSC process, therefore, the kinetic parameters estimation of boehmite-filled epoxy suspensions are also carried out by the S-B method, as follows:

Table 4.3: Estimated kinetic parameter start values S-B method for different mixtures

Kinetic parameter Mixture	A_1 / A_2 (1/sec)	E_2 / E_1 (J/mol)	m	n
0% (neat resin)	1.47E+07	72857.9	0.52	1.12
KE 5wt%	6.86E+07	77481.4	0.57	1.07
KE 10wt%	3.74E+07	76019.6	0.48	1.05
KE 15wt%	2.46E+05	59419.3	0.63	1.12

According to the estimated model parameters, both pre-exponential factor and activation energy parameters showed a generally decreasing trend, indicating an acceleration trend of the reaction, which will be further discussed later. In comparison, the reaction order m and n stayed around 0.5 and 1, separately.

4.1.1.3 Cure modeling

The final values for the model coefficients are determined by the regression analysis based on the non-linear least-square fitting of the cure curves – cure rate versus cure degree. It is, therefore, theoretically possible to develop the model values by regression analysis on just a single curing process. By analyzing several different curing curves separately – in this case four isothermal curing, it can be seen that the developed model can well predict each curing process separately as shown in the Figure 4.7 and Figure 4.8. However, it is inevitable that different model values from each curing curves could be developed as shown in the Table 4.4. This is because the regression analysis that based on non-linear least square fitting is an ill-posed optimization that does not have a unique solution. The ill-posed problem regarding the least-square fit analysis is discussed mathematically by the study of Krämer et al [172], and similar phenomenon by the determination of cure kinetics model coefficients was also reported in other studies [59].

Therefore, the model data that is separately developed by each curing process could not necessarily describe the curing behavior of the material by other temperatures, which leads to a curing temperature dependent model. This, on one side, makes the model quite complex, on the other side is logically suspicious even if mathematically right. In earlier studies, the average values from the developed data sets from each cure curves are taken as a general model [59]. However, the model based on the average value seems to predict the curing behavior poorly, as shown in the Figure 4.7 and Figure 4.8. It can be seen that, even if the model data by each separate regression analysis could quite well describe each curing behavior separately, but the

4 Key aspect I: Material characterization and modeling

general model based on the average value seems to be rather poor. The developed model data by separate regression analysis and middle value is provided in the following Table 4.4.

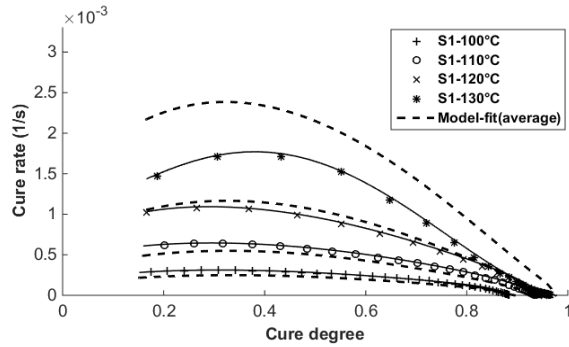


Figure 4.7: Cure rate vs. cure degree (Kamal-Sourour model with diffusion, separate regression)

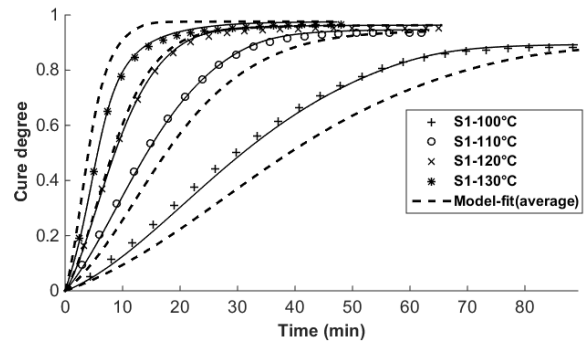


Figure 4.8: Cure degree vs. Time (Kamal-Sourour model without diffusion, separate regression)

Table 4.4: Cure kinetics model parameter by single-target regression analysis and their average values

Kinetic parameter	A_1 (1/sec)	A_2 (1/sec)	E_1 (J/mol)	E_2 (J/mol)	m	n
Temperature (°C)						
100	6.61E+09	6.61E+09	98366.6	90298.3	1.00	1.58
110	6.59E+09	6.62E+09	97434.7	91189.6	1.00	1.38
120	6.58E+09	6.62E+09	98374.4	91706.4	1.00	1.44
130	6.55E+09	6.63E+09	105095.8	91194.5	1.00	1.66
Middle value	6.58E+09	6.62E+09	99817.9	91097.2	1.00	1.52

In comparison to the single-target regression considering each curing curve separately, multiple target regression considers all the data from the different curing curves are simultaneously, by setting the quadratic deviations of the values in all curves as the optimization target to be minimized. Therefore, the regression analysis determines a set of model parameters that describes all the cure curves at the same time. Similar applications and examples regarding multi-curve simulation regression analysis could also be found in the following study [173]. By the multi-target simultaneous analysis, unique model parameters considering all the cure curves could be developed which could describe different curing behaviors at different temperatures, as shown in the following Figure 4.9 and Figure 4.10. The model parameters by the simultaneous regression are provided in the Table 4.5.

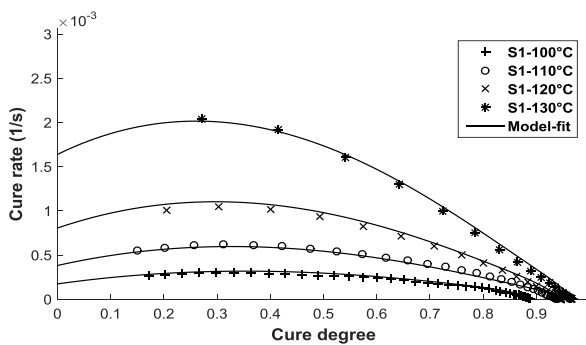


Figure 4.9: Cure rate vs. cure degree (Kamal-Sourour model with diffusion, simultaneous regression)

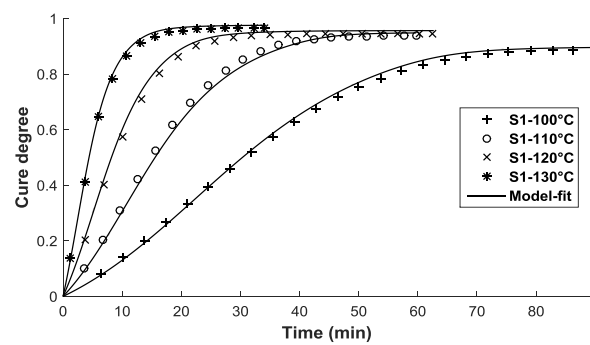


Figure 4.10: Cure degree vs. Time (Kamal-Sourour model without diffusion, simultaneous regression)

Based on the multi-target simultaneous regression analysis, the influence of the different starting values that are based on the model-free and model-fitting methods is investigated, as shown in the Table 4.5. The coefficient of determination (R^2) helps to evaluate the regression quality, as it provides a measure of how well the model corresponds to the underlying experimental data. The closer the value of R^2 is to 1, the better the fit can be considered. It could be seen that even if the quite different start and end values after regression, the R^2 of the kinetic model seems rather good from all the estimations. This can be explained by the ill-posed characteristic of the least-square fit analysis as already discussed where there could be different combinations of solutions based on the estimated start value, without a unique solution.

Table 4.5: Cure kinetics model parameters by multiple-target regression analysis with different start values for neat epoxy matrix

Kinetic parameter	A_1 (1/sec)	A_2 (1/sec)	E_1 (J/mol)	E_2 (J/mol)	m	n	R^2
Estimation methods							
Friedman start parameters	1.00E+04	6.70E+06	90536.5	71076.1	0.43	0.93	0.995
Kissinger start parameters	2.12E+05	6.14E+06	65281.9	70884.6	0.68	1.02	0.997
S-B start parameters	1.99E+09	1.11E+06	93264.2	64411.6	1.00	1.26	0.997
Diffusion factors	α_c : 100°C: 0.8978; 110°C: 0.9493; 120°C: 0.9568; 130°C: 0.9767; C: 100°C: 0.0189; 110°C: 0.0087; 120°C: 0.0176; 130°C: 0.0124;						

As discussed earlier, the vitrification effect that inevitably exists in the isothermal curing process – compared to the dynamic curing – exerts a dramatic restriction on bimolecular reactions, strongly reducing propagation probability of the free reactive groups and changing the reaction as diffusion controlled. The following Figure 4.11 shows the kinetic modeling by pure Kamal-Sourour model. It can be seen that the curing behavior at the beginning could be quite well described; however, the model begins to deviate from certain stages at the end. It is also obvious that the deviation is much bigger at lower curing temperature, for example, the 100 °C curve in the figures.

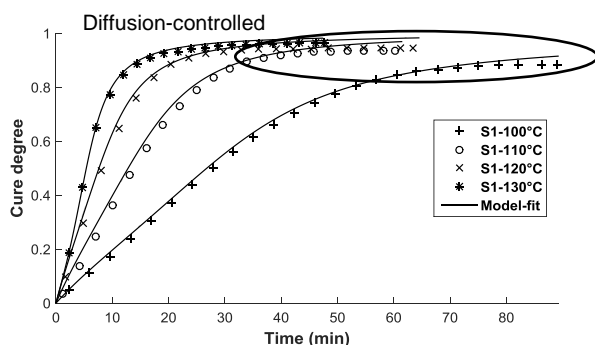


Figure 4.11: Cure degree vs. Time (Kamal-Sourour model without diffusion factor)

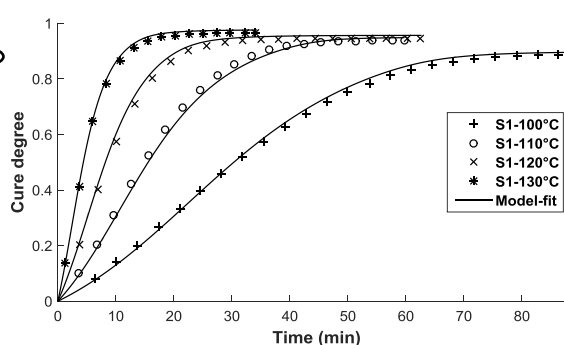


Figure 4.12: Cure degree vs. Time (Kamal-Sourour model with diffusion factor)

By regression analysis of the Kamal-Sourour model with Fournier's model as diffusion factor, the parameters in the Kamal-Sourour model are analyzed simultaneously as shared parameters,

4 Key aspect I: Material characterization and modeling

while the factors in the diffusion factor are analyzed separately. It could be shown that the model could rather good describe the complete curing process, as shown in the Figure 4.12. The final developed model parameters for the resin system based on the model with S-B start value and simultaneous regression is provided in the Table 4.5.

Moreover, it can also be shown that **the curing behavior of boehmite NP modified epoxy matrix can also be well described by the modified Kamal-Sourour model with Fournier's model as diffusion factor**, as shown in Figure 4.13. Therefore, the boehmite NP-filled epoxy suspensions are also modeled with the same model based on the multi-target simultaneous regression analysis, and the model parameters are provided in the following table.

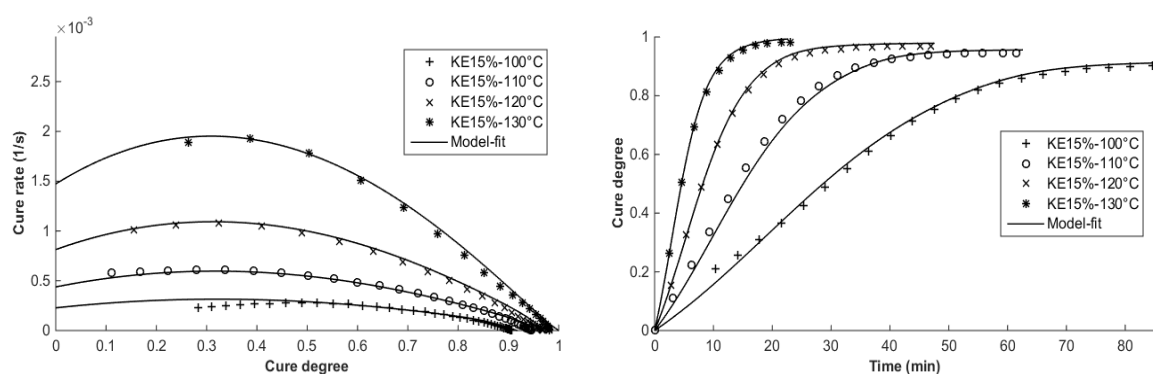


Figure 4.13: 15 wt% boehmite-epoxy matrix cure kinetics modeling;
left: cure rate vs. cure degree; right: cure degree vs. time

Table 4.6: Model parameters by Kamal-Sourour model modified with diffusion factor for different mixtures

Kinetic parameter	A_1 (1/sec)	A_2 (1/sec)	E_1 (J/mol)	E_2 (J/mol)	m	n	R^2
Mixture							
0 wt% (Pure resin)	1.99E+09	1.11E+06	93264.2	64411.6	1.00	1.26	0.997
KE 5wt%	1.96E+09	1.33E+06	93619.1	64435.1	1.00	1.21	0.998
KE 10wt%	1.98E+09	1.49E+06	93262.2	57994.2	1.00	1.18	0.995
KE 15wt%	1.05E+08	3.97E+06	83655.8	68785.4	1.00	1.17	0.992

With the increase of the boehmite NPs, reaction orders m and n stayed around 1 and 1.2, indicating that the boehmite NPs don't change the reaction mechanism dramatically. If the change of pre-exponential factor (A_1 , A_2) and activation energy (E_1 , E_2) is plotted against the NP concentration, as shown in the Figure 4.14, **it can be shown that there is an apparent influence of the boehmite NPs on the model parameters. Nevertheless, it is not possible to determine a clear correlation of the model parameters with respect to the NP concentration.**

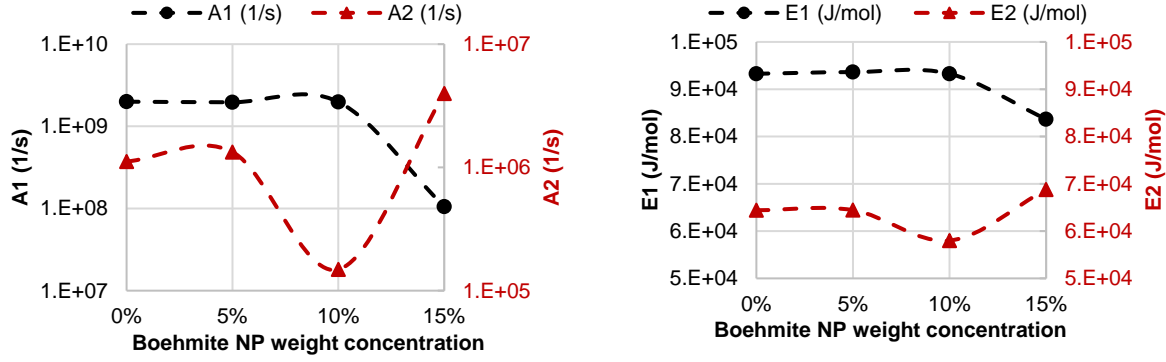


Figure 4.14: Change of pre-exponential factor (A_1 , A_2) and activation energy (E_1 , E_2) regarding the NP concentration

As explained earlier, the Kamal-Sourour model shows an ill-posed characteristic – it was not possible to develop a unique set of model parameters to describe the cure behavior based on the experimental data. This can well explain why it is not possible to determine a clear model parameter correlation regarding the influence of NPs. **It seems that the selected Kamal-Sourour model over describes the curing behavior and R^2 may not suffice as the only criterion to characterize the quality of the model function where further investigations relating the parameter sensitivity and correlation would be necessary to be able to determine that influence of the NP on the model parameters.**

The Kamal-Sourour model, when the cure degree is set to zero, describes an initial cure rate at the very beginning which is determined by rate function K_I as follows,

$$\frac{d\alpha}{dt} = K_I$$

$$K_I(T) = A_i e^{\left(-\frac{E_i}{RT}\right)}$$

Eq. 4.1

The rate function K_I describes secondary reactions that could be initiated by some side aspect, e.g., moisture, in certain systems, which is mostly the case for amine cured epoxy systems [174]. As the target system in this paper is an anhydride cured epoxy resin, by which the influence of moisture on the cure kinetics can be reasonably assumed much smaller than compared to the main reaction, so that the two parameters could be set to zero. However, from the numerical point of view, the Kamal-Sourour model describes only the dependency of cure rate to cure degree, in order to develop the dependency of cure degree to time, an integral calculation based on Euler method is applied. If the initial cure rate – K_I – is set to zero, it leads to a dead cycle by which the calculation could not be initiated. By combining the two aspects, it is reasonable to assume that the K_I is a number that satisfies: $0 < K_I < \exp(-\infty)$. Therefore, it can physically be considered as zero, nevertheless it is bigger than zero so that the integral calculation can be initiated. Based on the assumption, the model parameter could be determined new as follows,

4 Key aspect I: Material characterization and modeling

Table 4.7: New model parameters by Kamal-Sourour model for different mixtures

Kinetic parameter Mixture	A_1 (1/sec)	E_1 (J/mol)	A_2 (1/sec)	E_2 (J/mol)	m	n	R^2
0% (Pure resin)	2.20E-14	1.00E-10	6.30E+06	70272.35	0.45	1.10	0.99
KE 5wt%	2.20E-14	1.00E-10	1.22E+06	64369.72	0.55	1.08	0.99
KE 10wt%	2.20E-14	1.00E-10	6.51E+05	63000.98	0.42	1.03	0.99
KE 15wt%	2.20E-14	1.00E-10	9.54E+04	56684.48	0.44	1.00	0.95

According to the new model parameters, with the increase of the boehmite NPs, reaction orders m and n stayed around 0.5 and 1. The pre-exponential factor A_1 and activation energy E_1 that describes the initial cure rate could be kept constant at 2.20E-14 and 1.00E-10, respectively. The A_2 and E_2 showed a very good correlation – exponential and linear decrease – with respect to the NP concentration, as shown in the following Figure 4.15.

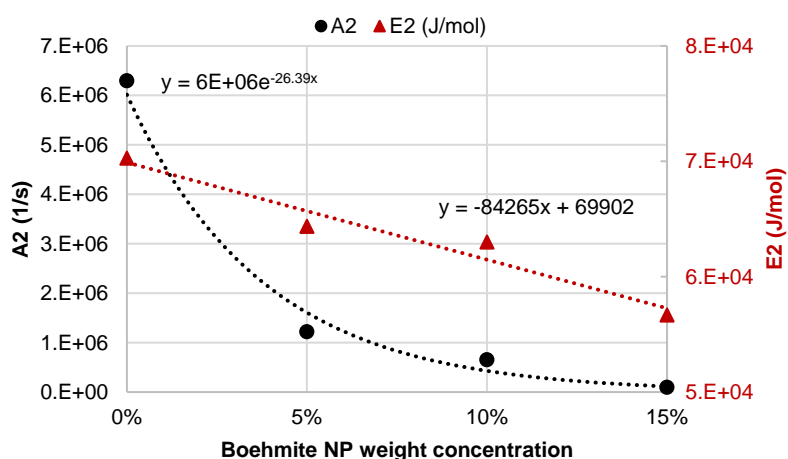


Figure 4.15: Change of A_2 and E_2 regarding the NP concentration by the new modeling

Based on the new modeling assumption and methods, the cure kinetics model for the NP-epoxy matrix can be generalized against NP weight concentration (x wt%), to enable to describe and predict the change in the cure kinetics with respect to different NP concentrations.

Table 4.8: Generalized Kamal-Sourour model parameters against NP concentration

Kinetic parameter	A_1 (1/sec)	E_1 (J/mol)	A_2 (1/sec)	E_2 (J/mol)	m	n
Model parameters regarding NP concentration wt% (x)	2.2E-14	1.00E-10	$6E+6\exp(-26.39x)$	$-84265x+69902$	0.47	1.05

4.1.1.4 Kinetic model validation

Considering the different start values depending on the model-free or model-fitting methods and the variability of regression algorithm as well as the ill-posdness of the regression analysis, which lead to different model values, it is important to prove that the developed model data

could predict all the curing behavior on different processes. Therefore, the model values that are developed by the multi-target non-linear regression analysis of isothermal curing curves are used to predict dynamic curing behavior and is validated by the dynamic curing data from dynamic DSC.

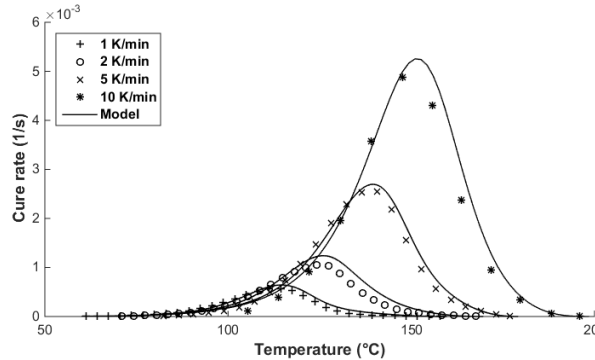


Figure 4.16: Isothermal cure kinetic model validation by dynamic cure rate vs. temperature

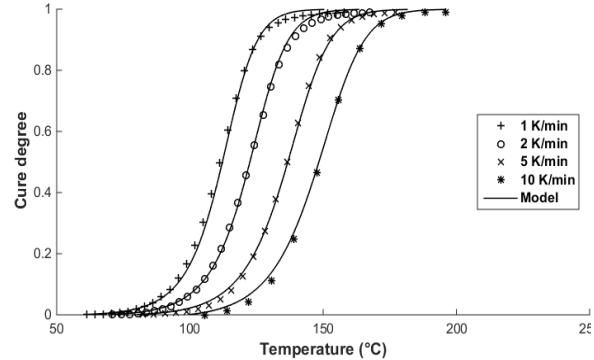


Figure 4.17: Isothermal cure kinetic model validation by dynamic cure vs. temperature

According to the predicted curve and DSC test data, it can be shown that the model predicted curing degree versus temperature is in good agreement with that from the test data. This can prove that the quality and accuracy of the model is rather good so that it could also precisely predict the curing behavior under different processes.

4.1.1.5 Influence of NP on the cure kinetics

Based on the change of model parameters as discussed earlier, the activation energy and pre-exponential factor showed a linear and exponential decrease with respect to the increase in NP concentrations – indicating an acceleration effect of the boehmite NPs. If the curing curve depending on the concentration of the boehmite NP is to be compared, as shown Figure 4.18 below, it also seems that the boehmite NPs show a slight catalytic effect. Nevertheless, considering that the cure degree based on DSC heat flow is calculated regarding to the total enthalpy from the dynamic curing – based on the assumption that the material can be fully cured to achieve 100 % by dynamic heating. Nevertheless, it was shown earlier that with the increase of the boehmite concentration, the total enthalpy and final T_g of the matrix decreases – indicating a decreased total polymerization network density. Therefore, the comparison of the cure development that is based on DSC data is susceptible as the final state of polymerization is changing with increase of NPs.

Except from the curing degree that is calculated by the reaction exothermy in DSC, T_g is also often used as an important criterion for characterizing the cure degree as it is more sensitive, especially at higher curing degree, to the polymerization network than the reaction exothermy as measured in DSC. According to the Figure 4.19 where the correlation between the T_g and cure degree is shown, it can be found that at the initial stage of curing, the T_{g0} value is increasing

4 Key aspect I: Material characterization and modeling

depending on the increase of boehmite concentration. As the reaction proceeds, the T_g also increases. It is obvious that, with the increase of boehmite NP concentration, the T_g of the nanosuspension also increases at the same cure degree up to a cure degree of about 0.8, indicating an increased network stability. This can be explained by the fact that as the boehmite NPs are also partly reactive, it inevitably accelerates the reaction resulting in a more stable structure at the beginning. However, after this crossing point at a cure degree of about 0.8, the T_g of the reference system becomes higher than that of nanosuspensions, indicating an inhibiting effect of the NP on the cure and thus a negative effect on T_g . The final $T_{g\infty}$ value showed a reverse trend as it by the initial T_{g0} : the higher the particle concentration, the lower the final $T_{g\infty}$, indicating a decreased network density of the particle-filled suspension compared to that by the reference system.

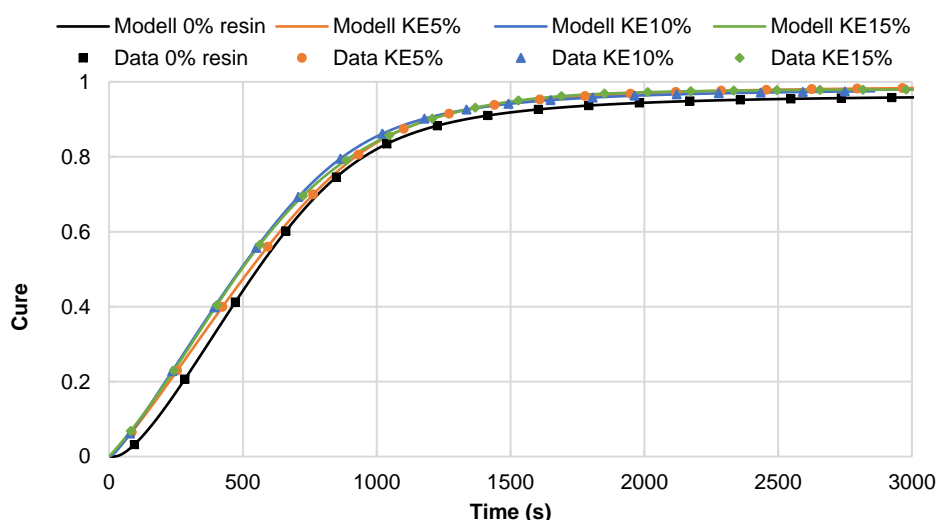


Figure 4.18: Comparison of the curing behavior depending on boehmite concentration (isotherm 120 °C)

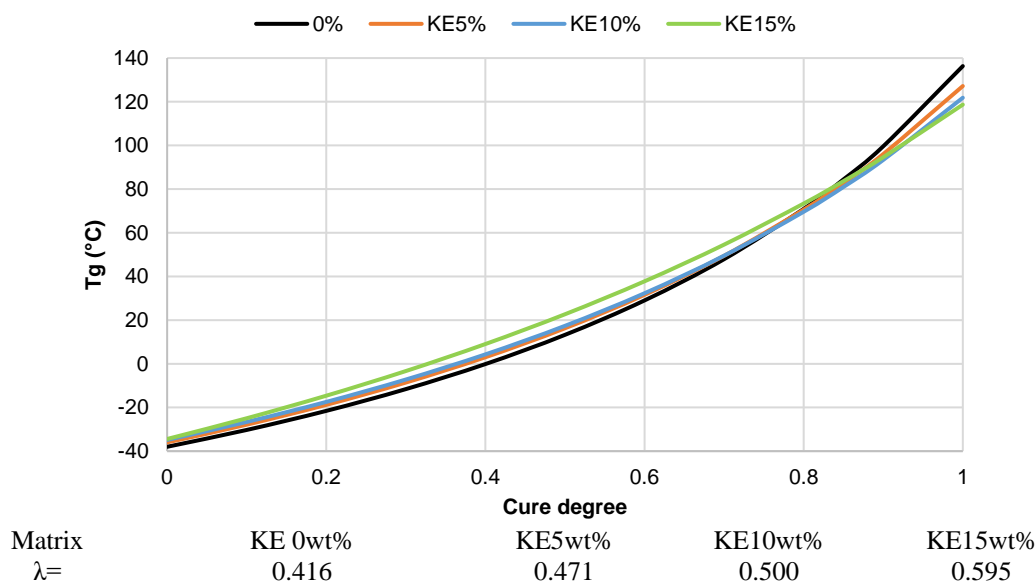


Figure 4.19: T_g versus cure depending on boehmite concentration

Some studies [49, 51] relating alumina and silica NPs reported an almost inert behavior of these particles – no big influence on the epoxy network formation and T_g , yet some others reporting an remarkable increase – up to 15 °C – in the T_g by an alumina-epoxy matrix [175]. The influence of the NPs to the T_g is closely related to the specific surface of the particles and surface functionality – the reactivity with the epoxy matrix. If the particles play a catalytic role participating in the epoxy reaction resulting a larger portion of immobilized polymer chain, an increase in the T_g is to be expected, or vice versa. **The boehmite NP that is used in the study is proven by dynamic DSC studies to be reactive to the epoxy groups, presumably due to the excessive hydroxyl groups on the surface, which inevitably influences the reaction kinetics of the matrix. In addition, it could be shown a slight accelerating effect at the beginning until a certain cure degree that presumably due to the reactivity of the boehmite NPs with the epoxy, but after that an inhibiting effect on the cure reaction – probably due to the spatial hindrance by the NPs. Finally, the boehmite NPs lead to a decreased polymerization network density of the matrix.** This assumption could be further validated later in Chapter 6 by the dynamic thermal-mechanical analysis of the NP modified FRP structures.

Moreover, it is also found that the boehmite-epoxy suspension contains some little number of coarse particles or agglomerates with size of several microns, which also lead to a dramatic decreased specific surface and decreased crosslinking density. The coarse particles will be further discussed in the Chapter 5 combining the flow studies.

4.1.2 Rheology characterization and modeling

4.1.2.1 Rheology characterization

According to the viscosity development versus temperature, as shown in the Figure 4.20, it could be seen that the optimal processing temperature for the suspensions are from 80 °C to 120°C where the viscosity is below 0.1 Pa·s. As most of the LCM processes are based on isothermal process, 80 °C is selected to be more optimal considering the ideal viscosity and the processing time for the target matrix system. If the viscosity limit is considered to be 1 Pa·s – typical for standard LCM processes, the isothermal processing time for the pure resin system without particle is about 72 min, it decreased to about 52 min with 10 wt% and 42 min with 15 wt% of the boehmite NPs. It is obvious that, with the increase of the NP concentration, the effective processing time is inevitably decreased by about 28 % by 10 wt% (4.5 vol%) and 40 % by 15 wt% (6.9 vol%) boehmite concentration. Similarly, Mahrholz et al [16] studied silica NPs with the same anhydride hardener and accelerator systems (100:90:0.5) and reported a decrease of about 15 % process time by 15 wt% (8.76 vol%). This decrease in the processing time exerts extra requirements and restrictions on the processing strategies and parameters

4 Key aspect I: Material characterization and modeling

considering the decreased impregnation length, which would be further handled in the next chapter.

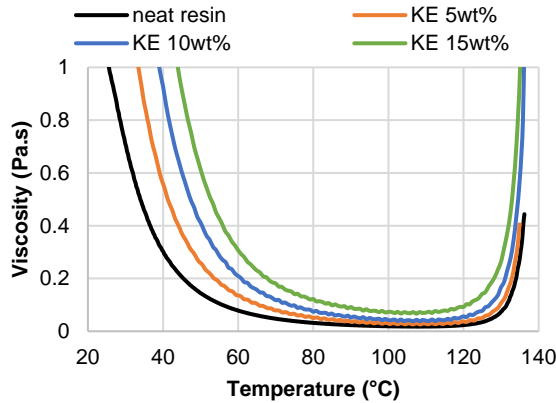


Figure 4.20: Viscosity vs. Temperature (dynamic process)

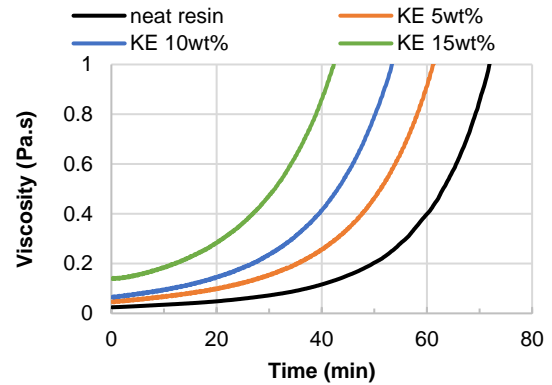


Figure 4.21: Viscosity vs. time (isotherm process, 80 °C)

4.1.2.2 Estimation of rheological model parameters

Similar to the modeling of cure kinetics, the start values for the parameters of the viscosity model need to be firstly determined. As described in Chapter 3, initial values of E_η (activation energy for flow) and η_∞ (viscosity at T_∞) could be obtained from dynamic viscosity plots of $\ln\eta$ versus $1/RT$. As the equation only holds when the curing degree is zero, therefore, only viscosity data in the temperature range from 20 °C to 50 °C is considered, where the curing rate is very low to be presumed to be zero. This assumption could be also verified by the linear development of the curve as in Figure 4.22:

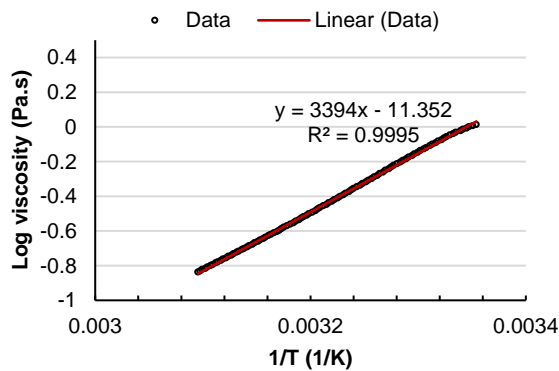


Figure 4.22: Log viscosity vs. Temperature plot (pure resin)

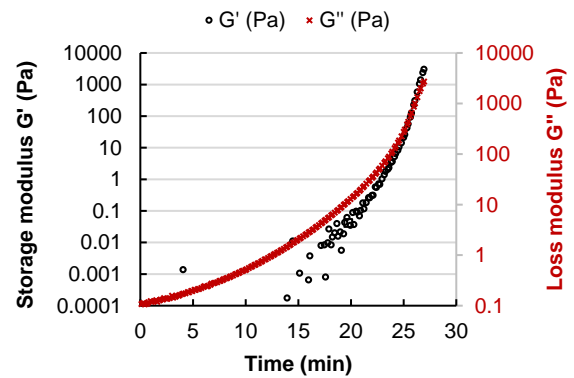


Figure 4.23: Oscillation viscosity test (isothermal 100 °C, pure resin)

Based on the fitting curve, the start values for the rheology model can be calculated. Besides these two parameters, the critical curing degree at the gel point is needed for the rheological model. The gel point is measured by oscillation method in rheometer, and is determined by the time where the storage modulus (G') exceeds the loss modulus (G''), as shown in the Figure 4.23. Based on the cure kinetics and gel time, the gel conversion can be calculated. Similarly,

the start values and cure degree at gel point for the boehmite particle-filled reactive suspensions are calculated as follow:

Table 4.9 : Estimated start kinetic parameters for rheological modeling by Castro-Macosko model

Kinetic parameter Mixture	η_{∞} (Pa.s)	E_{η} (J/mol)	Gel conversion
0% (neat resin)	1.1746E-05	28219.3	0.44
KE 5wt%	7.89722E-06	29949.5	0.48
KE 10wt%	5.38443E-06	31514.3	0.51
KE 15wt%	3.29864E-06	33291.8	0.52

4.1.2.3 Rheological modeling

As indicated in the Castro-Macosko model, the development of the viscosity is dominated by the cure kinetics – the increased molecular size due to the curing. Therefore, the modeling of cure kinetics is necessary to predict the change of the curing degree regarding the temperature and time during the viscosity measurements, which is essential for the viscosity modeling. Furthermore, as it was shown by the modeling of cure kinetics, the multi-target regression algorithm delivers better model values with higher prediction quality. Therefore, the rheological modeling is conducted by multi-target regression analysis with the determined start parameter, based on four isothermal measurements.

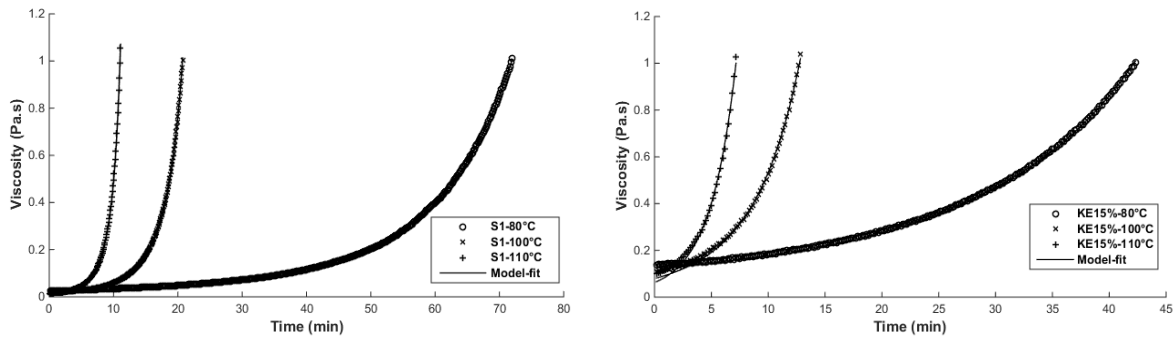


Figure 4.24: Rheological modeling with Castro-Macosko model
(Left: neat epoxy matrix; Right: 15wt% boehmite –epoxy matrix)

It can be seen that the rheological behavior of the system could be described by the model quite well. The boehmite NP-filled epoxy suspensions are also modeled with the same model, and the model parameters are provided in the following Table 4.10.

Table 4.10 : Castro-Macosko model parameters for different mixtures

Model parameter Mixture	η_{∞} (Pa.s)	E_{η} (J/mol)	A	B	Gel conversion	R ²
0% (Pure resin)	5.87E-06	24294.76	-0.0758T+33.31	0.1029T-43.61	0.44	0.99
KE 5wt%	3.95E-06	27679.17	-0.1042T+45.06	0.2801T-109.98	0.48	0.99
KE 10wt%	2.69E-06	29698.02	-0.1385T+57.42	0.3102T-120.56	0.51	0.99
KE 15wt%	4.95E-06	30055.32	0.0352T-6.32	-0.3942T+141.28	0.52	0.99

4 Key aspect I: Material characterization and modeling

If the model parameters are plotted against the NP concentration, although there is an apparent influence of the boehmite NPs on the model parameters, but it is not possible to determine a clear correlation of the model parameters with respect to the NP concentration. **This is presumably due to the ill-posed characteristics of the Castro-Macosko model, similar to the Kamal-Sourour model as described earlier. Therefore, further parameter analysis is carried out regarding the model parameters.**

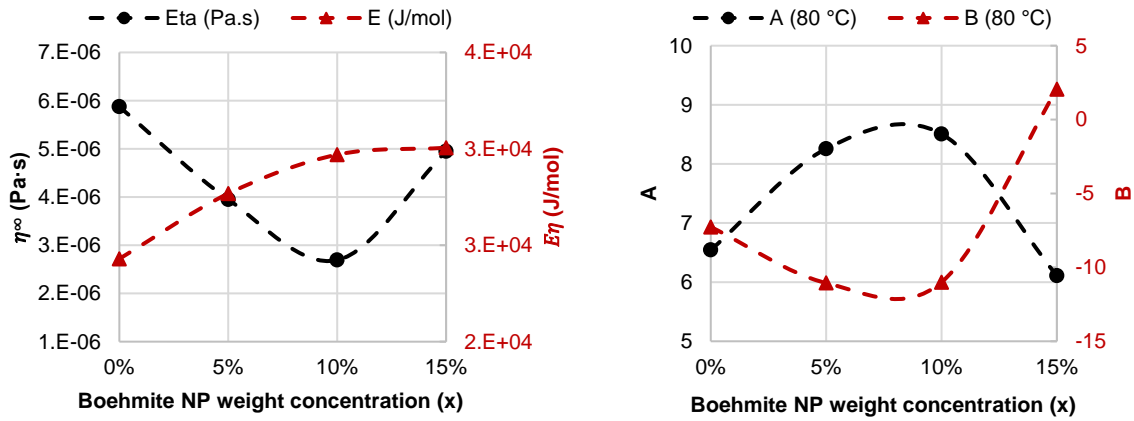


Figure 4.25: Change of rheological model parameters regarding the NP concentration

As already discussed earlier by the start parameter determination in Eq. 3.12, the start viscosity by zero cure degree is determined by the two parameters η_{∞} and E_{η} . Therefore, by the regression analysis for the rheological modeling, the E_{η} is controlled around the start parameter, so that only η_{∞} can be determined as a variable. Moreover, the influence of the parameter A , B and gel conversion on the curve development is shown in the Figure 4.26. It is obvious that, with the increase of A and B , the curve is steeper – indicating an increased viscosity development. In comparison, the gel conversion has the opposite influence – the smaller the gel conversion, the steeper the curve development. It is can be also noted that the curve development is more sensitive to the parameter A at the beginning, thereafter the parameters A and B affect similar on the curve development. Therefore, the parameter B is assumed to be zero, keeping only parameter A as a variable.

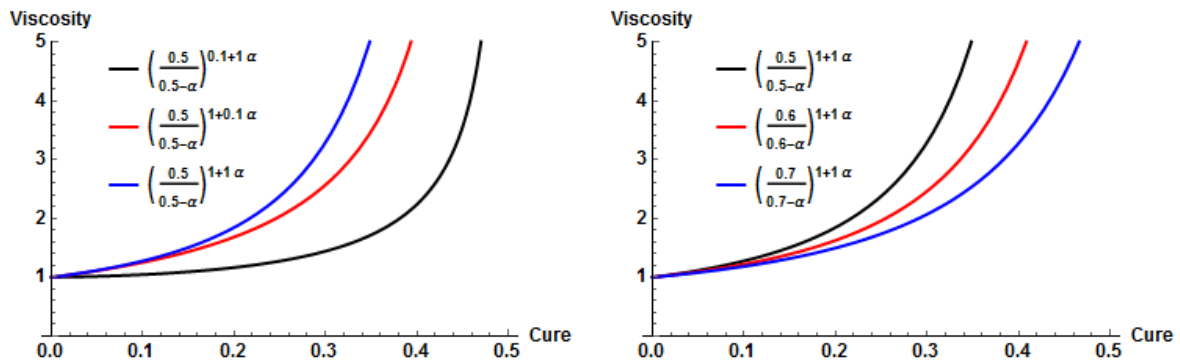


Figure 4.26: Influence of model parameters on the curve development in Castro-Macosko model.

Left: influence of A and B ; Right: influence of gel conversion

The new modeling based on the parameter analysis also shows good prediction of the viscosity, as shown in the Figure 4.27. The small deviation by KE 15 wt% at higher temperatures is presumably due to the experimental error from the heating and stabilization phase by isothermal measurement at the beginning.

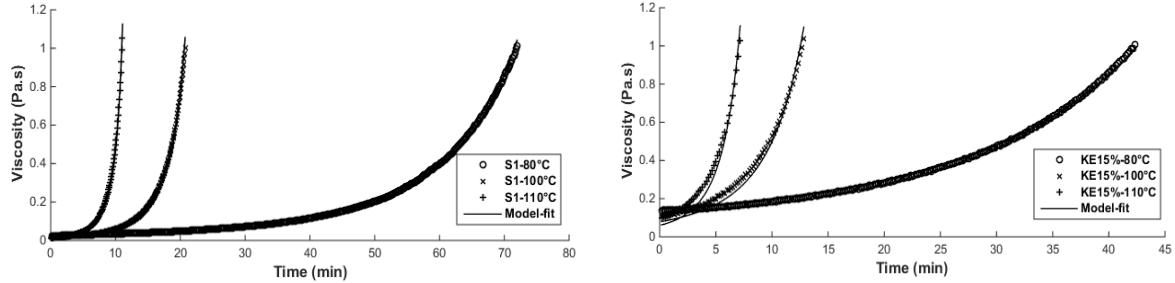


Figure 4.27: New rheological modeling with Castro-Macosko model
(Left: neat epoxy; Right: 15wt% boehmite –epoxy suspension)

Moreover, by the new analysis, the activation energy for flow E_η shows a linear increase and the η_∞ shows an exponential decrease with respect the NP concentration. By an isothermal temperature of 80 °C, the parameter A shows almost the same changing trend as to the gel conversion with respect to the NP concentration, Figure 4.28. The new model parameters are provided in Table 4.11.

Table 4.11 : New Castro-Macosko model parameters for different mixtures

Model parameter Mixture	η_∞ (Pa.s)	E_η (J/mol)	A	B	Gel conversion	R ²
0% (Pure resin)	1.18E-05	23759.97	$-0.0578T+24.61$	0	0.44	0.99
KE 5wt%	7.86E-06	26391.56	$-0.0525T+24.25$	0	0.48	0.99
KE 10wt%	5.36E-06	28391.56	$-0.0907T+38.15$	0	0.51	0.99
KE 15wt%	3.32E-06	31308.58	$-0.0287T+16.40$	0	0.52	0.99

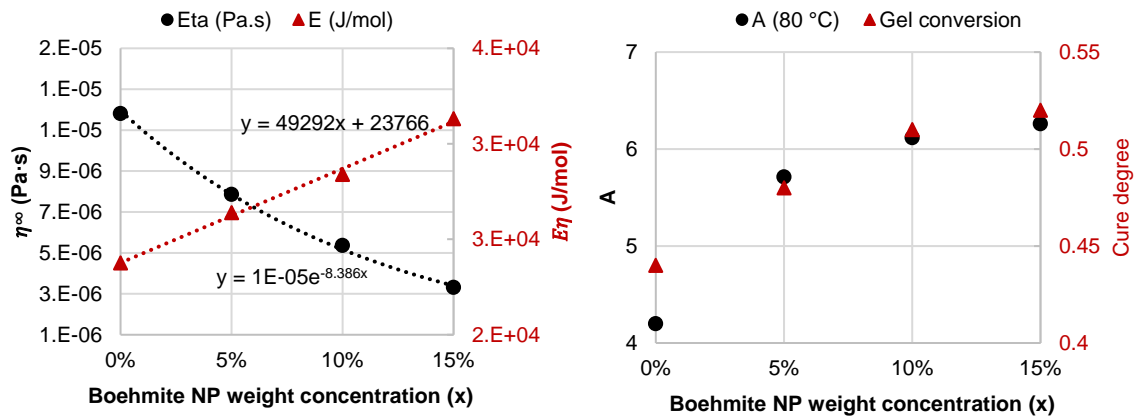


Figure 4.28: Change of rheological model parameters regarding the NP concentration

Based on the new analysis and modeling, it is now also possible to generalize the Castro-Macosko model to predict the rheological behavior depending on the NP concentration, with the model parameters as shown in the following Table 4.12.

4 Key aspect I: Material characterization and modeling

Table 4.12 : Generalized Castro-Macosko model parameters against NP concentration

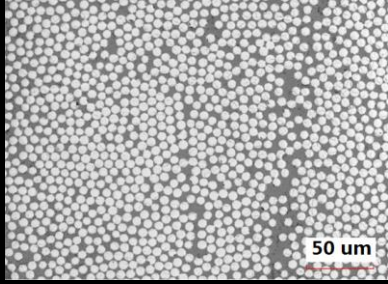
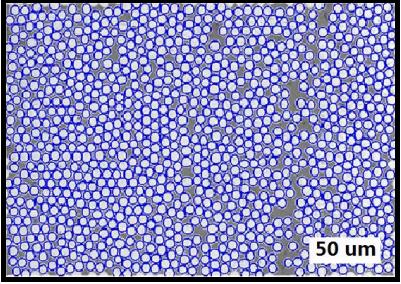
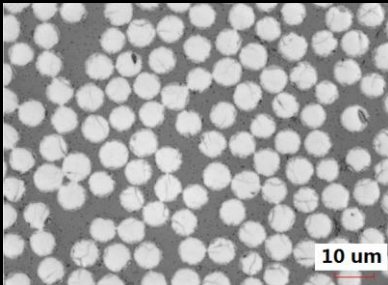
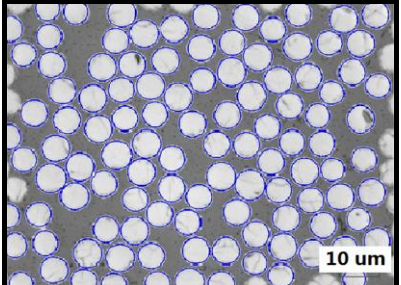
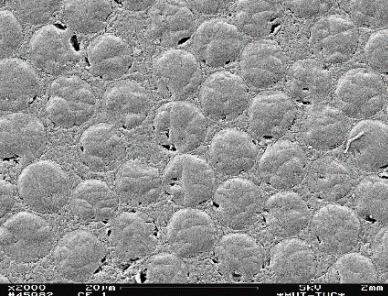
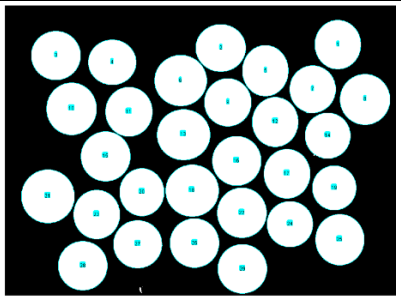
Model parameters	Model parameters regarding NP concentration wt% (x)
η_{∞} (Pa.s)	$1E-5\exp(-8.386x)$
E_{η} (J/mol)	$49292x+23766$
A (80 °C)	$-2.0999\exp(-25.3165x)+6.2980$
Gel conversion	$-0.1021\exp(-10.7991x)+0.5416$

4.2 Fiber preform

4.2.1 Filament diameter distribution

Three kinds of images with different resolutions are compared, in order to compare and find out the influence of resolution on filament recognition and statistic error due to sample size. With the increase of magnification factor, the filament profile is clearer, but the number of observable filaments, sample size, could also decrease remarkably, as shown in Table 4.13.

Table 4.13: Laminated cross section images by different methods and resolutions.

Method	Magnification	Original image	Processed image
OM	1000x		
OM	3000x		
SEM	5000x		

In Figure 4.29, the filament diameter distribution from the three different images are provided. For each characterization, at least three images are analyzed from each types, to get a systematic information. According to the data the average value of filament diameter is found to be 6.35 μm , 6.6 μm and 7.08 μm corresponding to the different magnifications: OM 1000x, OM 3000x and SEM 5000x. It's obvious that SEM images provides the most accurate result,

whereas data from OM images are inaccurate because the boundary of CF by lower resolutions (OM images above) could not be clearly recognized and analyzed. Therefore, only the diameter from the SEM images are considered in the following calculations for local FVF and filament distance distribution.

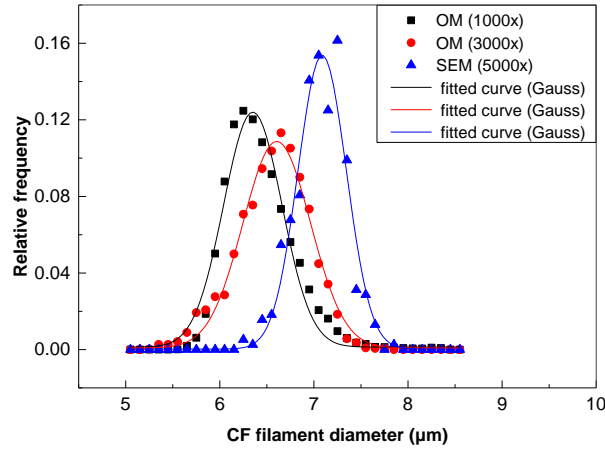


Figure 4.29: CF diameter distribution based on OM (1000x and 3000x) and SEM (5000x)

4.2.2 Global/local fiber volume fraction

Fiber volume fraction (FVF) is one of the dominating factors for the permeability of the fiber preform and the flow behavior of the fluid – especially for particle-filled systems. Therefore, it is quite important and critical to precisely determine the FVF. The theoretical FVF and measured FVF of epoxy/CF or GF textiles hybrid composites (fabricated by RTM process) are shown in Table 4.14. The change of global and local FVF is shown in the following Figure 4.30 and Figure 4.31.

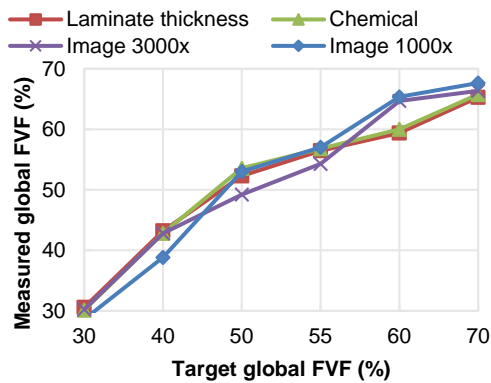


Figure 4.30: Global FVF measured by different methods

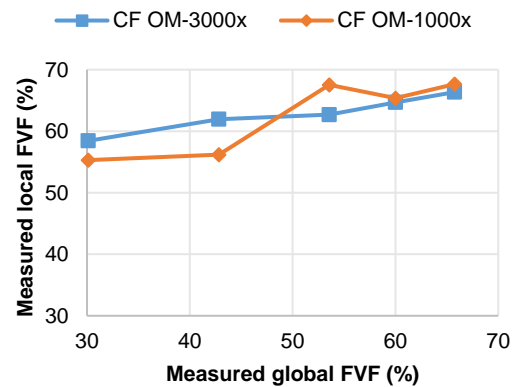


Figure 4.31: Local FVF measured by image processing method

According to Figure 4.30, the global FVF value from the laminate thickness method fits well with the result from chemical method. In comparison, the global FVF value that is calculated by image processing method showed some deviations in certain laminate samples. This deviation is presumably because that the outline of CF roving could be hardly detected correctly due to the irregularities by image processing software as shown in Figure 3.10.

4 Key aspect I: Material characterization and modeling

Nevertheless, the determination of the local FVF is only possible by the image processing method, as shown in the Figure 4.31.

Table 4.14: Theoretical FVF vs. measured FVF in CF laminate

Theor. FVF (%)	Global-FVF in laminate (%)				Local-FVF in roving (%)		Roving volume fraction (%)
	Method				Method		Method
	Laminate thickness	Chemical	Image		Image		Image
	CFRP	CFRP	CFRP (3000x)	CFRP (1000x)	CFRP (3000x)	CFRP (1000x)	CFRP (1000x)
30	30.58	30.12	30.23	28.61	58.43	55.30	51.74
40	43.21	42.83	42.82	38.84	61.94	56.18	69.13
50	52.3	53.56	49.22	53.02	62.68	67.52	78.53
55	56.46	56.79	54.28	57.02	57.14	60.01	95.02
60	59.38	60.00	64.68	65.37	64.68	65.37	100
70	65.28	65.76	66.35	67.65	66.35	67.65	100

Interestingly, according to the result of local FVF, the local FVF is relative high even the global FVF is low: 58.43% (OM 3000x) by a global FVF of 30%. With the increase of compaction, until a global FVF of about 68%, the local FVF increased almost linearly to 67.65%. This comparatively much higher local FVF in the rovings indicate a high local compaction of the fibers within the roving and a much lower local permeability compared to that between the rovings. This difference in the local compaction of the fibers and permeability is expected to have a considerable influence on the dual-scale flow behavior and especially particle flow behavior with increased filtration within the rovings, which will be investigated later in more detail combining the permeability of the preform.

4.2.3 Filament/Roving distance distribution

To characterize the filament distance, nearest neighbour center distance (NNCD), neighbour distance (ND) and Ripley's K function are combined with the filament diameter to get a full understanding and systematically distribution. It is clear that, similar to the filament diameter, the NNCD distribution also show a Gaussian distribution pattern, as shown in Figure 4.32. The mean value and standard deviation of the NNCD and filament diameter that are obtained from the Gaussian fitting are plotted in the Figure 4.33. As both the NNCD and filament diameter are not constant values but Gaussian distributed data, the NNCD is not directly subtracted with the mean value of the filament diameter considering the possible loss of systematical information. Both the NNCD and filament diameter distribution values with the standard deviation are illustrated. The distance between the NNCD and the filament lines can be considered as the smallest distance between the filaments.

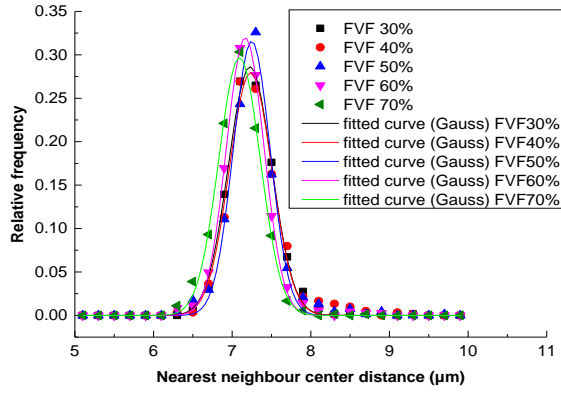


Figure 4.32: NNCD distribution vs. FVF

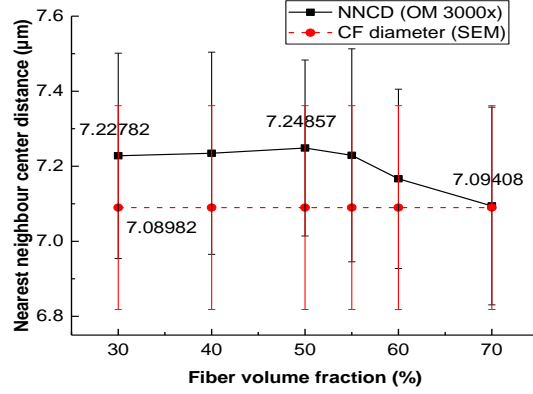


Figure 4.33: Change of NNCD vs. FVF

According to the results, the average value NNCD is around 7.23 μm at FVF of 30%. It stays almost constant until FVF 50%, and begins to decrease remarkably until 7.09 μm by FVF 70%. Correspondingly, the smallest distance between the filaments (NNCD-diameter) decreased from 138 nm at FVF 30% to 4.26 nm by FVF 70%. **Therefore, considering the change of smallest distance, the retention of the NPs could be quite critical after certain threshold compaction state, so that it is not to be underestimated.**

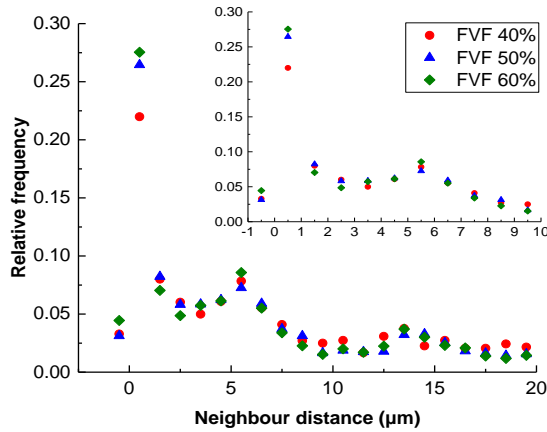


Figure 4.34: ND distribution vs. FVF

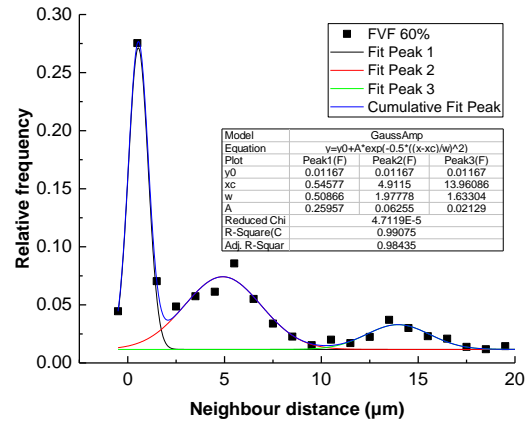
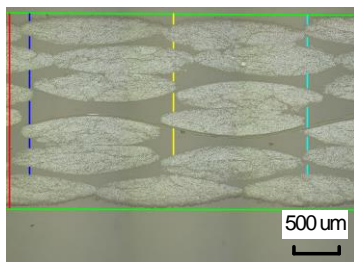
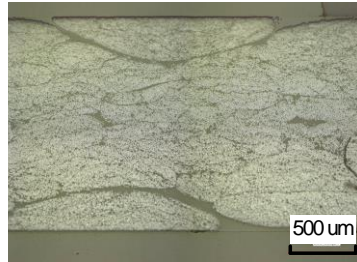


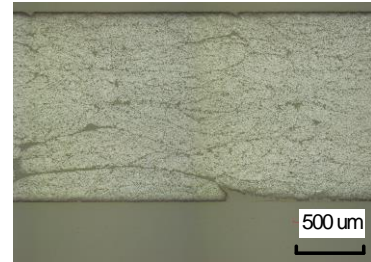
Figure 4.35: Fitting of ND distribution with three-peak Gaussian function



FVF 40%



FVF 55%



FVF 70%

Figure 4.36: Textile compression behavior and change in porous structure

In contrast to the distribution pattern of the NNCD and filament diameter, the ND show a multimodal distribution characteristics, as shown in the Figure 4.34. Similar fluctuations in the fiber distribution density are also reported by Vaughan et al [83]. Interestingly, with the

4 Key aspect I: Material characterization and modeling

increase of the FVF, the peak positions stay almost constant– showing only change in the relative frequency value. The distribution data is further fitted with a three-peak Gaussian equation, as shown in the Figure 4.35. The data analysis based on FVF 60% shows that the peaks lie around 0.55 μm , 4.91 μm and 13.96 μm , separately. With the increase of FVF, the relative frequency within the range of up to 5 μm showed a clear tendency to increase, while after that it begins to decrease. It is important here to note that, the filament distance considered here is just within the roving – regarding the local FVF. It seems that the distribution pattern of the filaments within the roving is dominated mostly by the pre-compaction during the roving/textile fabrication process, so the compaction during the impregnation process mostly influences the relative frequency of the peaks but not necessarily the pattern.

The change of the NNCD with the increase of FVF can be better understood combining the compaction behavior of the textiles, as shown in the Figure 4.36. It can be seen that, at the beginning of the compaction, mostly textile layers and rovings are compressed. Therefore, in this case, the compression mostly affects the macro-pores between the layers and rovings. However, as the compaction force increases above a certain threshold, corresponding to about FVF 55% in this case, the macro-pores disappear and the filaments within the rovings are also stronger compressed to each other. **This phenomenon could provide a valuable information indicating the critical phase transition of the porous structure in the textiles: by lower compaction and FVF, the textiles show a dual-scale porous structure, as shown in Figure 4.36 (FVF 40%). With the increase of the compaction until FVF 55%, the macro-pores begin to decrease, so the porous structure of the textiles becomes more homogenous, resulting a quasi-single-scale porous structure, as shown in Figure 4.36 (FVF 55%). With further compression, the macro-pores totally vanish resulting at the end in a single-scale porous structure, as shown in Figure 4.36 (FVF 70%).**

This critical change could be further quantified by the changing of roving distance vs. FVF. Roving distances in thickness direction are determined as follows: the roving distance in thickness direction is measured at three evenly distributed locations (cross-section image of FVF 40% in the Figure 4.36 left); finally, the sum length of segments

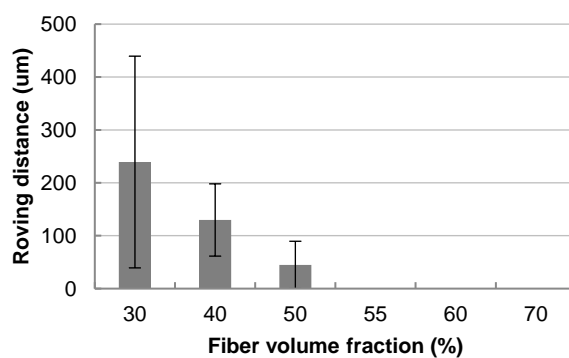


Figure 4.37: The sum of roving distance vs. FVF

at each location is correlated to the average fiber roving distance. According to the result as shown in Figure 4.37, the roving distance totally tends to zero by the FVF 55%.

It can be shown in the later study that the critical phase change in the textile porous structure has a significant influence on the flow and retention behavior of NP, which will be further investigated later in the chapter 5.

4.2.4 Permeability: DoE studies

4.2.4.1 Permeability based on silicon oil

Oil is mostly used as the standard fluid for permeability measurements. It could be seen from the Figure 4.38 that the change of permeability versus FVF could be well described by an exponential function. However, the development of the permeability shows a remarkable change by FVF 55%: after the critical FVF, the permeability showed larger drop.

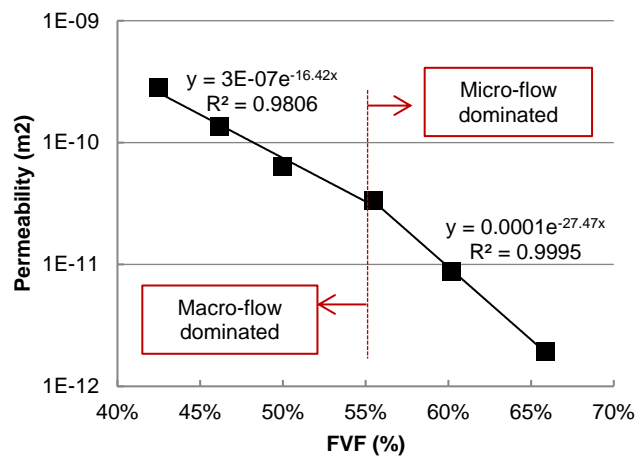


Figure 4.38: Permeability vs. FVF (Silicone oil)

Combining the filament distance distribution results, as discussed earlier, the change in the changing trend may be assumed to be from the phase change in the textile structure: up to FVF 55% the flow is macro flow dominated – due to the dual-scale porous structure, after then is micro-flow dominated due to the quasi-single-scale porous structure.

4.2.4.2 Permeability based on pure epoxy: DoE studies

Considering the dominating macro or micro flow during the impregnation, there could be some slight discrepancy between the real and apparent – to be measurable – flow front which leads to a deviation of the measured permeability from the real value. As could be seen earlier, there is a remarkable phase change in the porous structure of the textile structure depending on the compaction, which might lead to different dominating macro or micro flow impregnation mechanisms. In real applications where the textile will be injected with resin, the parameters, including FVF, temperature and pressure can have different influences on the flow behavior and the measured permeability values. Therefore, the influences of these parameters are investigated by the DoE method by the table shown as in Table 4.15. To prevent the evaluation errors due to the deviation in the parameters, the actual measured average values of FVF, temperature and pressure are used for the evaluations.

4 Key aspect I: Material characterization and modeling

Table 4.15: DoE table for permeability studies by pure resin

Exp. No.	FVF	Temperature (°C)	Pressure (bar)	Response (Permeability m ²)
1	0.45	61.09	0.44	1.89E-10
2	0.46	65.57	0.74	1.56E-10
3	0.46	62.58	1.65	1.37E-10
4	0.46	103.27	0.49	2.17E-10
5	0.45	88.74	0.95	1.53E-10
6	0.45	83.52	2.46	1.75E-10
7	0.56	106.64	2.67	3.67E-11
8	0.55	61.46	0.84	2.03E-11
9	0.56	65.58	0.89	2.38E-11
10	0.65	109.82	1.62	1.79E-12
11	0.67	60.95	2.95	7.20E-12
12	0.65	81.72	0.75	5.87E-12
13	0.65	85.19	0.69	5.72E-12
14	0.49	100.72	0.59	1.01E-10
15	0.55	101.11	2.42	9.56E-11
16	0.60	101.86	1.77	1.84E-11
17	0.49	61.96	1.79	7.44E-11
18	0.55	62.30	0.76	6.04E-11
19	0.60	62.49	2.67	1.32E-11
20	0.49	83.53	2.38	9.22E-11
21	0.60	83.48	0.77	2.55E-11

If the permeability values are shown just versus FVF, it could be seen that the average value of the permeability shows an exponential decrease depending on the increase of FVF, as shown in Figure 4.39 and Figure 4.40. Nevertheless, there are quite big deviations in the test data which makes it suspicious that the deviations may come from the dual-scale effects by different injection parameters. However, it also needs to be kept in mind that these deviations might be due to the influence the parameters – temperature and pressure – but also might due to the test deviation. In order to further investigate and differentiate these effect, the average absolute and relative deviations are calculated, which can be seen in Figure 4.41 and Figure 4.42. It can be seen that, both absolute and relative deviations didn't show any clear trends to follow, by which it is assumable that the scattering of the data is probably from test deviation. Nevertheless, the test deviation with resin seems to be much higher than that from the standard permeability measurements with oil. This might be due to the deformation of the test rig because of the influence of heating elements and temperature, which needs to be critically investigated in future more in detail.

4 Key aspect I: Material characterization and modeling

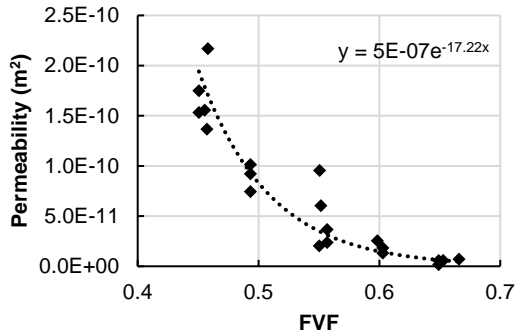


Figure 4.39: Permeability vs. FVF (DoE study, resin)

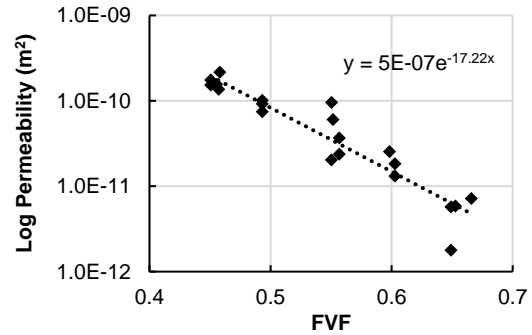


Figure 4.40: Log permeability vs. FVF (DoE study, resin)

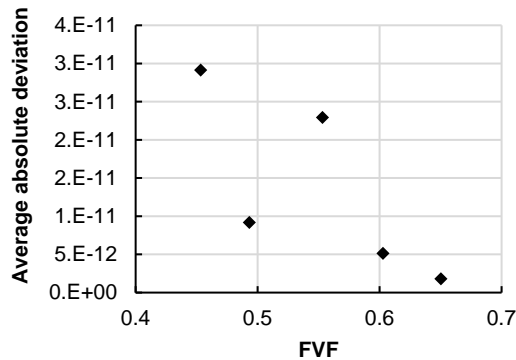


Figure 4.41: Average absolute deviation

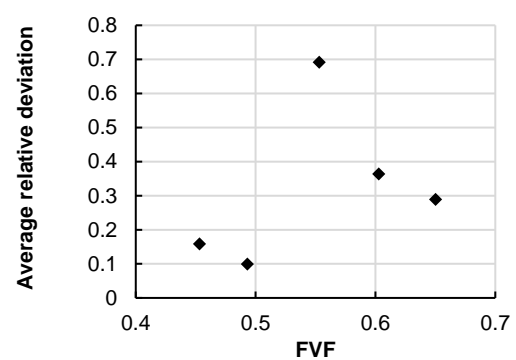


Figure 4.42: Average relative deviation

To investigate the influence of the parameters, for the first step, a parameter screening evaluation is carried out. The results are provided as in the Figure 4.43 and Figure 4.44 below. According to the probability value – p-value, as shown in the Figure 4.43, a low p-value (a value less than 0.05) indicates that results are statistically significant, which are identified by the color and asterisks. It is also obvious that only the parameter FVF is significant for the permeability results, with quadratic effect. This can be further verified by the half normal probability plot of effects as shown in the Figure 4.44—all the effects that lie along the line are negligible, whereas the larger effects deflect away from the line (FVF% and FVF%*FVF%).

Screening for Permeability					
Contrasts					
Term	Contrast	Lenth	Individual t-Ratio	p-Value	Simultaneous p-Value
FVF %	-6.16e-11		-9.81	<.0001*	0.0011*
Temperature	8.094e-12		1.29	0.1927	0.9864
Pressure	-3.48e-12		-0.55	0.6053	1.0000
FVF %*FVF %	1.953e-11 *		3.11	0.0128*	0.1573
FVF %*Temperature	-6.52e-12 *		-1.04	0.2844	0.9986
Temperature*Temperature	3.495e-12 *		0.56	0.6037	1.0000
FVF %*Pressure	2.122e-12 *		0.34	0.7476	1.0000
Temperature*Pressure	4.434e-12 *		0.71	0.4730	1.0000
Pressure*Pressure	5.29e-12 *		0.84	0.3823	1.0000
FVF %*FVF %*FVF %	-5.47e-12 *		-0.87	0.3665	1.0000
FVF %*FVF %*Temperature	0 *		0.00	1.0000	1.0000
FVF %*Temperature*Temperature	-5.32e-12 *		-0.85	0.3797	1.0000
Temperature*Temperature*Temperature	-3.04e-12 *		-0.48	0.6487	1.0000
FVF %*FVF %*Pressure	7.527e-12 *		1.20	0.2200	0.9859
FVF %*Temperature*Pressure	0 *		0.00	1.0000	1.0000
Temperature*Temperature*Pressure	-3.53e-12 *		-0.56	0.6010	1.0000
FVF %*Pressure*Pressure	3.942e-12 *		0.63	0.5580	1.0000
Temperature*Pressure*Pressure	-7.46e-12 *		-1.19	0.2240	0.9875
Pressure*Pressure*Pressure	0 *		0.00	1.0000	1.0000
Null21	7.343e-12		1.17	0.2302	0.9903

Figure 4.43: ANOVA analysis for the parameters screening by DoE studies for pure resin

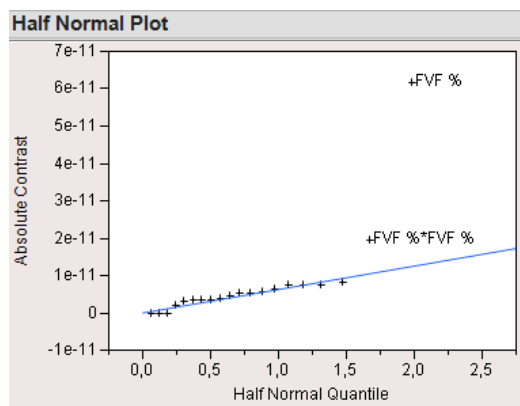


Figure 4.44: Half normal probability plot of effects by DoE studies for pure resin

4 Key aspect I: Material characterization and modeling

4.2.4.3 Permeability based on NP-epoxy suspension: DoE studies

Further measurements as shown in the Table 4.16 are carried out for boehmite nanosuspension as shown in the Table 4.16. The influence of FVF, NP concentration, temperature and pressure are evaluated by the DoE table as shown in these parameters are investigated by the DoE method by the table shown as in Table 4.16. In order to prevent the evaluation errors due to the deviation in the parameters, the actual measured average values of FVF, temperature and pressure are used for the evaluations.

Table 4.16: DoE table for permeability studies by boehmite-epoxy suspension

Exp. No.	FVF	NP (Wt%)	Temperature (°C)	Pressure (bar)	Maximum flow length (m)	Filtration factor (Exdecay factor_b)
1	0.49	0	100.72	0.59	230.64	-1.34E-08
2	0.60	0	101.86	1.77	210.97	-1.19E-08
5	0.55	0	62.30	0.76	140.44	-5.77E-09
6	0.60	0	62.49	2.67	127.21	-5.58E-09
7	0.49	0	83.53	2.38	196.25	-3.66E-08
8	0.60	0	83.48	0.77	140.90	-8.20E-09
9	0.55	2.5	84.30	1.88	154.95	-1.00E-08
10	0.50	5	106.65	0.70	0.41	-0.00346
11	0.50	5	94.57	2.53	0.56	-0.00592
12	0.60	5	98.35	0.87	0.29	-0.00215
13	0.60	5	106.66	2.94	0.30	-0.00448
14	0.50	5	61.52	0.83	0.83	-0.00012
15	0.50	5	61.52	2.84	0.30	-0.00812
16	0.60	5	61.34	0.84	0.27	-0.00018
17	0.60	5	61.66	2.97	0.41	-0.00044

It can be seen from the results that the maximum flow length (root of parameter a in Eq. 3.18) for permeability tests without particle is rather large while the decay factor is quite small. This may be considered to be as infinite large flow length with infinite small decay factors. In comparison, the maximum flow length value is remarkably decreased for injections with particle-filled suspensions, dependent on the injection parameters, with much higher decay factor values. As the permeability value from the particle filled-injection is not a constant value – dependent on the flow length, in this study the maximum flow length and decay factors are selected as a response, and DoE evaluations are conducted.

For the first step, a parameter screening evaluation is carried out. The results are provided as in the Figure 4.45 and Figure 4.46 below. According to the probability value— P value as shown in the Figure 4.43, a low p-value (a value less than 0.05) indicates that results are statistically significant, which are identified by the color and asterisks. It is also obvious that NP-concentration, FVF, temperature and their interactions all have a significant influence for the response value (maximal flow length). This could be further verified by the half-normal

probability plot of effects as shown in the Figure 4.46—all the effects that lie along the line are negligible, whereas the larger effects deflect away from the line.

Screening for Flow length (Exdecay_a*1/2)

Contrasts

Term	Contrast	Lenth	Individual t-Ratio	p-Value	Simultaneous p-Value
NP Wt%	-83,4632		-20,78	<,0001*	0,0001*
Temperature	11,7276		2,92	0,0204*	0,1806
FVF %	-6,8855		-1,71	0,0983	0,6619
Pressure	2,7659		0,69	0,4713	1,0000
NP Wt%*NP Wt%	-16,0547 *		-4,00	0,0081*	0,0615
NP Wt%*Temperature	-17,7760 *		-4,43	0,0053*	0,0402*
Temperature*Temperature	3,3529 *		0,83	0,3808	1,0000
NP Wt%*FVF %	7,4418 *		1,85	0,0795	0,5728
Temperature*FVF %	0,4853 *		0,12	0,9125	1,0000
FVF %*FVF %	-0,0165 *		-0,00	0,9963	1,0000
NP Wt%*Pressure	-4,0101 *		-1,00	0,2971	0,9946
Temperature*Pressure	-0,7467 *		-0,19	0,8661	1,0000
FVF %*Pressure	-0,9640 *		-0,24	0,8268	1,0000
Pressure*Pressure	-2,5889 *		-0,64	0,5577	1,0000
NP Wt%*Temperature*Temperature	-1,2882 *		-0,32	0,7701	1,0000

Figure 4.45: ANOVA analysis for the parameters screening by DoE studies for NP-epoxy suspension

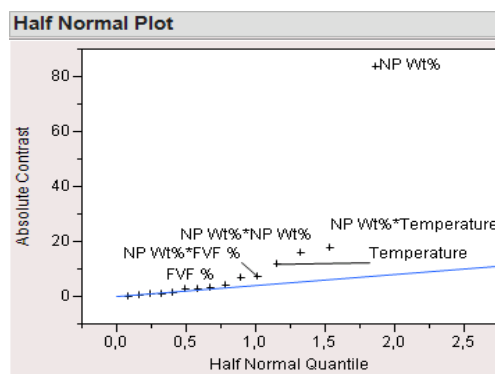


Figure 4.46: Half normal probability plot of effects for NP-epoxy suspension

The DoE studies from the NP-epoxy suspension show that, compared to permeability study with pure resin, the flow behavior of the particle-filled matrix system is dependent on many factors, and are correspondingly much more complex. Theoretically, by the DoE study, an experimental model for flow length and decay factor could be developed, with the critical parameters and their interactions, with a possibility of application for designing impregnation strategies and other parameters. Nevertheless, the semi-experimental models that are based on DoE studies are strongly based on statistic data distribution – regarding the maximum flow front and decay factors. Due to the fact that these two parameters differ quite remarkably – infinite big and small by the case without NP but decreases dramatically by the NP-epoxy suspension, the fit model is susceptible, as it is strongly influenced from the bigger values that under consideration. This is an interesting aspect to be critically evaluated and further optimized, therefore, there are no further investigations regarding the DoE model is carried out.

4.3 Short summary

In this chapter, the basic material components – NP, epoxy matrix and fiber reinforcement – and their interactions and correlations regarding to the process parameters are studied. Regarding the NP-epoxy matrix, the cure kinetics and rheological behaviors are investigated and modeled as a critical aspect with custom-developed software tools. By the modeling, the influence of different model-free and model-fitting methods and regression algorithms on the model quality and prediction accuracy is investigated. After that, the cure kinetics and rheology of the boehmite-epoxy suspensions are modeled based on the optimized model parameter estimation and regression algorithm. Finally, the influence of boehmite NPs on the cure kinetics and rheology of an epoxy resin system is systematically investigated. It can be shown that the boehmite NPs are reactive to the epoxy, which inevitably influences the reaction kinetics of the matrix. The boehmite NPs can slightly accelerate the reaction at the beginning until a certain

4 Key aspect I: Material characterization and modeling

cure degree, which presumably due to the reactivity of the boehmite NPs with the epoxy, but thereafter they inhibit the cure reaction – probably due to the spatial hindrance by the NPs. Finally, the boehmite NPs lead to a decreased polymerization network density of the matrix.

The standard Kamal-Sourour and Castro-Macosko models showed an ill-posed characteristic resulting that it is not possible to determine a clear correlation of the model parameters against the NP concentration. However, by the model parameter analysis combined with optimal regression algorithm, it is possible to develop a good correlation between the model parameters with respect to NP concentration. At the end, generalized models for describing the cure kinetics and rheology of the NP modified epoxy resin system are proposed, which enables to describe and predict the cure and rheological behavior depending on the time, temperature and the concentration of NPs. The generalized model can be also possibly transferred to other filler modified resin systems.

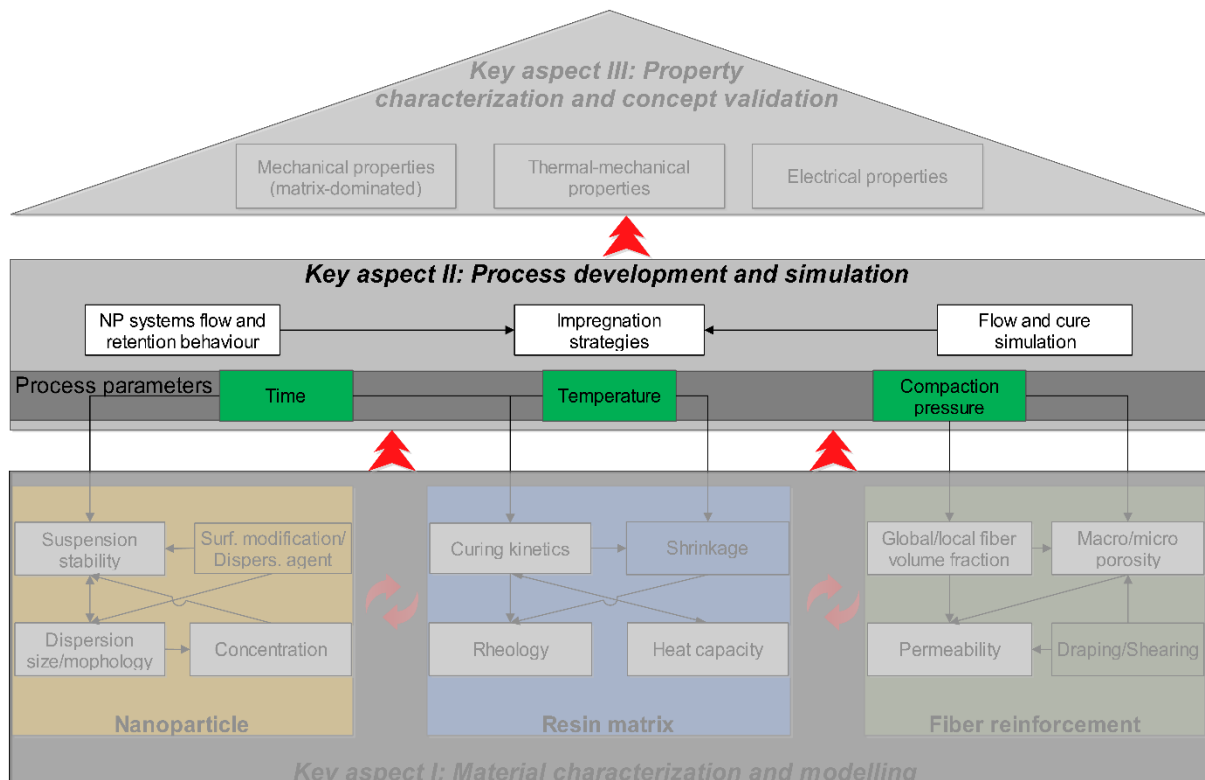
Regarding the fiber preform, the compaction behavior (global/local FVF, filament distance distribution) and permeability of the fiber preform considering the effects of NPs are also systematically investigated. The investigations regarding the compaction behavior of the textile – global/local FVF and filament distance – showed a critical phase transition of the porous structure in the textiles: from a dual-scale porous structure to a single-scale micro-porous structure with the increase of FVF. Correspondingly, the average value of the smallest distance between the filaments is around $0.138\ \mu\text{m}$ at FVF of 30%. It stays almost constant until FVF 50 -55%, and begins to decrease remarkably from FVF 55%, until $0.00426\ \mu\text{m}$ by FVF 70%. In contrast to the distribution pattern of the NNCD, the ND show a multimodal distribution characteristics with three peaks around $0.55\ \mu\text{m}$, $4.91\ \mu\text{m}$ and $13.96\ \mu\text{m}$, separately. It seems that the distribution pattern of the filaments within the roving is dominated mostly by the pre-compaction during the roving/textile fabrication process, so the compaction during the impregnation process mostly influences the relative frequency of the peaks but not necessarily the pattern.

Considering the influence of NP retention on the permeability, the influences of the critical material and process parameters – FVF, NP concentration, and temperature and injection pressures – are investigated by DoE studies with respect to the maximum flow front and decay factor.

5 Key aspect II: Process development and simulation

In this chapter, the focus lies in the second key aspect – process development and simulation. The particular flow and retention characteristic of the NP-filled epoxy matrix in the textile structure requires development of special impregnation strategies. The design of the impregnation strategy is supported by two main aspects: NP flow and retention study as well as flow and cure simulation.

By the flow and retention studies with different NPs – boehmite, silica and CNT – the NP gradient is quantified. At the same time, flow and cure simulations are necessary regarding the complex flow and cure behavior that is dependent on the NP gradient. Flow simulation assists to anticipate the flow front development during the impregnation by which a full impregnation without dry spots or air bubble inclusions can be guaranteed. In parallel, by cure simulation, the cure and temperature development within the laminates can be anticipated to improve the curing process, by which the cure efficiency can be enhanced as well as avoiding the critical temperature overshoot within the laminate. The flow and cure simulations support the evaluation and optimization of the impregnation strategies.



5.1 Nanoparticle systems flow and retention behavior

The flow and retention behavior of the quasi-spherical boehmite and silica NPs is investigated by the custom developed RTM-tool as described in Chapter 3. According to the results in the following Figure 5.1 and Figure 5.2, it can be found that at FVF 40% and 50%, the concentrations of both NPs decreases very slightly along the flow length – in both impregnations parallel and transverse to the fiber direction. This indicates a slight deep-bed retention behavior. The same trend applies also to silica NP even at high FVF of 60%. In comparison, at FVF 60%, boehmite NP showed a remarkable retention phenomenon – about 78% of the particles are filtered at a flow length of 100 mm by injection parallel to fiber direction and 57% by a flow length of 150 mm by injection transverse to fiber direction. The severe filtration of the boehmite NPs at the FVF 60% indicates a different filtration mechanism – cake filtration, with a large influence on the flow speed and maximum flow length so that the flow speed tends to zero at the flow length of 100 mm and 150 mm, respectively.

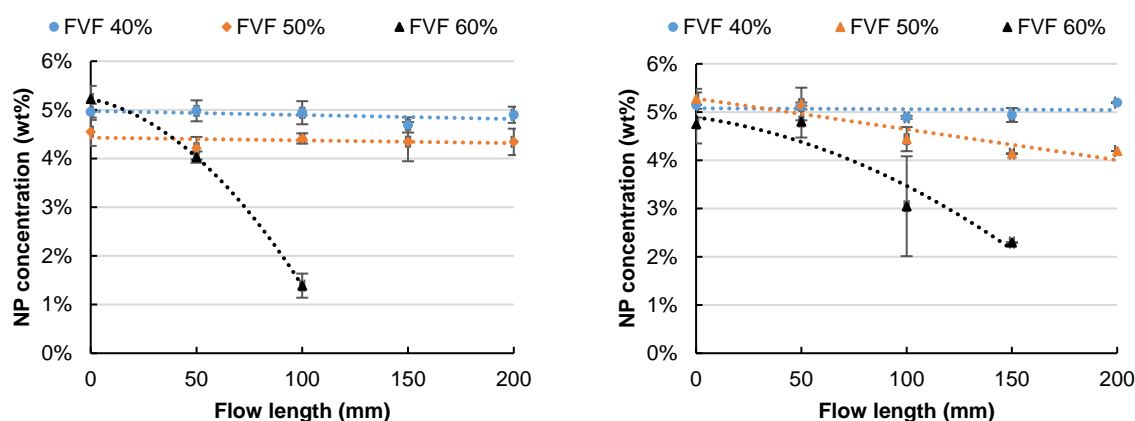


Figure 5.1: **Boehmite** NP concentration along flow length by different FVF.
Parallel to fiber (left) and transverse to fiber direction (right)

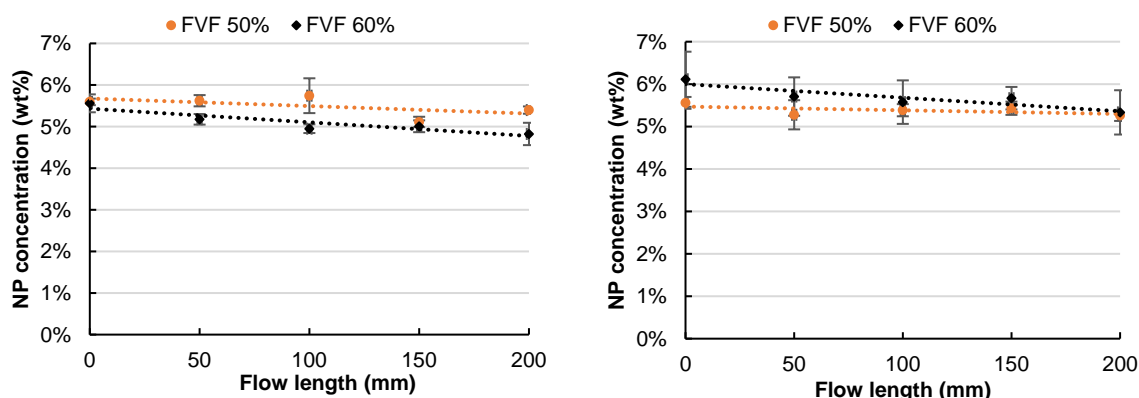


Figure 5.2: **Silica** NP concentration along flow length by different FVF.
Parallel to fiber (left) and transverse to fiber direction (right)

It is interesting to notice that the boehmite NPs showed a dramatic change in the retention behavior from FVF 50% to FVF 60%, where silica NPs do not. The dramatic change in the retention behavior of the boehmite NPs at FVF 60% can be explained combining the particle size distributions and filament distance distribution. According to the microscopic investigations as shown in the following Figure 5.4, by the high magnification – the figures on the left – there are plenty of fine dispersed NPs in both samples – boehmite and silica – to be observed. **Nevertheless, by the boehmite-epoxy samples, some amounts of coarse-particles at the micro-range can be observed – more obvious by the lower magnification. In comparison, by the silica-epoxy sample, the NPs seem to be better dispersed – without any observable coarse particles.** The similar observations regarding the coarse particles in the boehmite-epoxy sample can be further verified by different magnifications, as shown in Figure 5.4. In parallel, based on the reports in the literature, silica NPs showed some slight agglomeration only at high concentrations, but hardly any big coarse particles in the micro range, as shown in Figure 5.5.

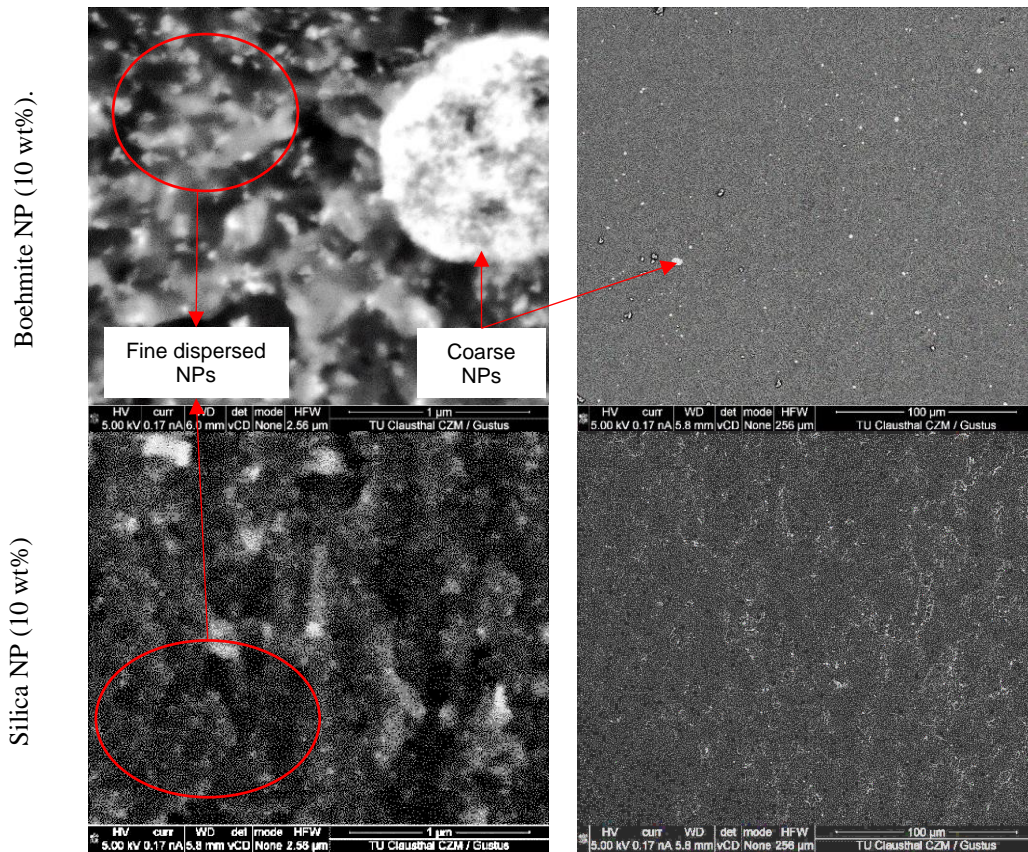


Figure 5.3: Particle size distribution in the cure sample
Magnification from left: 1 μm; right: 100 μm

Combining the results of NNCD in the Chapter 4 and the change of the dominating filtration mechanism of boehmite NP regarding the FVF, **it can be assumed that the significant change in the filtration mechanism of boehmite NPs is directly related to the phase transition in the textile microstructure depending on the critical FVF as described earlier.** Below the

5 Key aspect II: Process development and simulation

critical FVF, in this case about 55%, the preform showed a dual-scale porous structure with both macro and micro pores where the impregnation is dominated by dual-scale flow, the retention seems much smaller –even to be negligible, as particles can mainly flow between the macro-channels between the rovings. However, above this critical FVF by which the macro-channels disappear with just micro-channels are left, a remarkable filtration that is dominated by cake filtration is observed which could severely influence the impregnation.

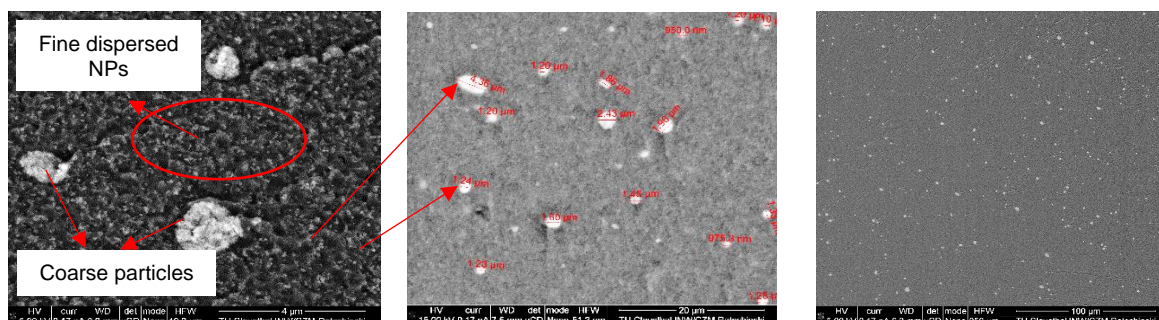


Figure 5.4: Bohemite NP distribution in the cured sample (10 wt%).
Magnification from left to right: 4 μm , 20 μm , 100 μm

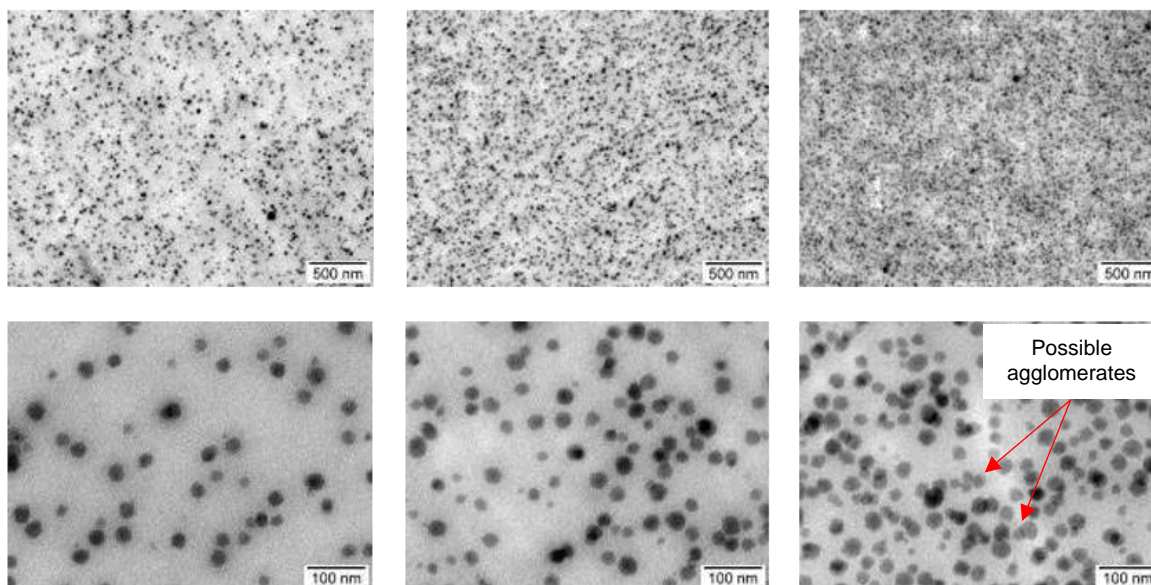


Figure 5.5: Silica NP distribution in the cured sample.
From left to right: 7 wt%, 11.8 wt%, 20 wt% [176, 177]

There are several possible assumptions regarding the origin of coarse species in the boehmite-epoxy samples. They could be the residual particle aggregates that are not well dispersed during the dispersion process. The dispersion of the particles in a kneader is achieved by the shear stress acting on the particles, which is dependent on the local shear rate within the kneader chamber. Since the local shear rate differs considerably within the kneader chamber due to varying gap widths and relative velocities of neighboring kneader blades, the kneader chamber shows a broad distribution of stress intensity. The final size of a particle is determined by the maximum stress intensity it experienced. A uniform dispersion state is therefore a matter of the

residence time of the particles within the kneader. A complete dispersion will therefore only be achieved at rather long dispersion times that is technically not practical.

The other possibility is the possible reaction between the boehmite NP with the epoxy. It is found that the boehmite NPs are slightly reactive to the epoxy resin where the excessive amount of hydroxyl groups on the boehmite surface could initiate a slight polymerization of the epoxy. It is already shown in the previous chapter by DSC measurements where the boehmite NP-epoxy mixture showed slight exothermic reaction enthalpy beginning at around 120 °C – indicating certain reaction between the NP and epoxy. Although the temperature during the dispersion process is strictly monitored and controlled, nevertheless it cannot be fully excluded that some local temperature overheating could occur, which might be critical to initiate the reaction between the NP and epoxy. If there is a reaction between the NP and epoxy before or during effective dispersion, they could build up local high-viscous or even gel-state coagulate with higher solid concentrations. The gel-state coagulates are difficult to be further dispersed or diluted with the hardener before the injection. Such gel-state coagulates are observed after some dilution processes and or after injection.

Of course, a third possible explanation is the possibly reagglomeration of the boehmite particles during the processing due to the different chemical composition or surface modifications as compared to silica. The elevated temperatures, the dilution and the addition of hardener to the suspension dramatically change the physico-chemical conditions in the system. It is quite important to differentiate these two aspects and find out the main reason considering the severe influence of these coarse particles on the impregnation by higher FVF.

If the morphology of the coarse particles in the boehmite-epoxy suspension is compared to the possible agglomerate structures from silica-epoxy, it is obvious that the coarse particles showed a solid-state morphology while the agglomerate structures in the silica-epoxy suspension showed more a loosened affinity of the primary particles where the primary particles are still to be recognized and differentiated. Based on this principal difference in the morphology, it is reasonable to assume that the coarse particles can be residuals that directly come from the masterbatch.

It is important to note that the silica-epoxy masterbatch for the experiments is produced by a modified sol-gel process. The silica NPs are synthesized in-situ in an aqueous sodium silicate solution. Odegard et al [178] reported the molecular models of such NPs and the huge amount of hydroxyl groups on the particle surface. In order to prevent agglomeration and to compatibilize the particles with the resin, the hydroxyl groups are reacted with silanes to achieve certain surface coating [49]. Conversely, the production of the boehmite-epoxy suspensions is based on dispersing of the dry powders directly in the epoxy. As the boehmite NPs are fabricated by spray-drying process, it might tend to build some aggregate/agglomerates

5 Key aspect II: Process development and simulation

during the drying process. **It seems that due to the processing characteristics by dry powder-particle-dispersion in kneader for preparation of the NP-epoxy suspensions and the reactivity of the particles with the epoxy, some amount of coarse particles might inevitably remain not well dispersed.** The argument could be also enhanced by the observation of Louis et al [51] on alumina-epoxy suspension. Based on the observations in the thin-film through-light microscopy, it was also found that remarkable amount of coarse particles exists in the nanoalumina-epoxy suspensions.

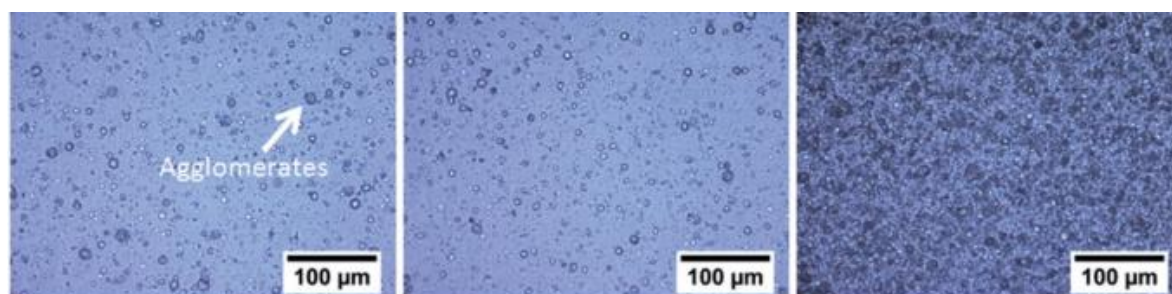


Figure 5.6: Alumina NP distribution in the cured sample.
Weight content from left to right: 5 wt%, 10 wt%, 25 wt% [51]

Based on the preliminary investigations together with the project partner – IPAT, TU Braunschweig, it is also found that due to the little amount and quite different size distribution of these coarse particles – several microns compared to the well dispersed particles in just dozens of nanometer, it is quite challenging to obtain a quantitative information regarding the amount of the coarse particles. It seems that the information from the big particles cannot be well captured due to the limit of the measurement spectrum of standard test instruments for NP size distribution characterization, or vice versa. There is also a similar issue by analyzing the images by SEM: due to the quite big size difference, the coarse particles can only be better quantified by lower magnifications, where the information about the fine-dispersed NPs might be inevitably lost, or vice versa. Nevertheless, considering that the coarse particles are mostly problematic by the impregnation of high FVF laminates (single-scale porous structure), image processing methods are applied for detecting the coarse particles to get some qualitative information for comparing the agglomeration behaviors, as shown in the following Figure 5.7.

It can be seen from the Figure 5.8 that, there are still remarkable amount of the particles with a diameter of up to 3-4 μm with an apparent average size of around 1 μm . However, it must be kept in mind that, the average particle size and absolute value of the differential and integral distribution based on the image recognition process is not accurate, as the fine dispersed NPs are not considered due to the image resolution limit. Nevertheless, it provides still important qualitative information about the coarse particles and the agglomeration behavior. Therefore, **it seems that it might be a general problem in the dry-particle dispersion process: due to the process characteristic, a little amount of residual coarse particles might remain not well dispersed, and these coarse particles are quite critical in the impregnation process,**

especially at high FVF where the structure shows a micro-porous structure. The average value of the coarse particle size will be inverse calculated and discussed later in the 5.2: Flow simulation.

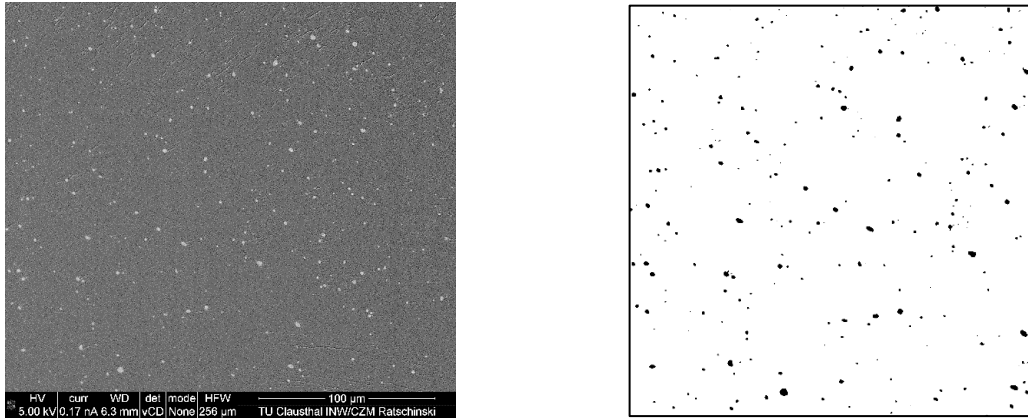


Figure 5.7: Coarse particles in the boehmite-epoxy matrix.
Left: original SEM image; Right: processed image with ImageJ

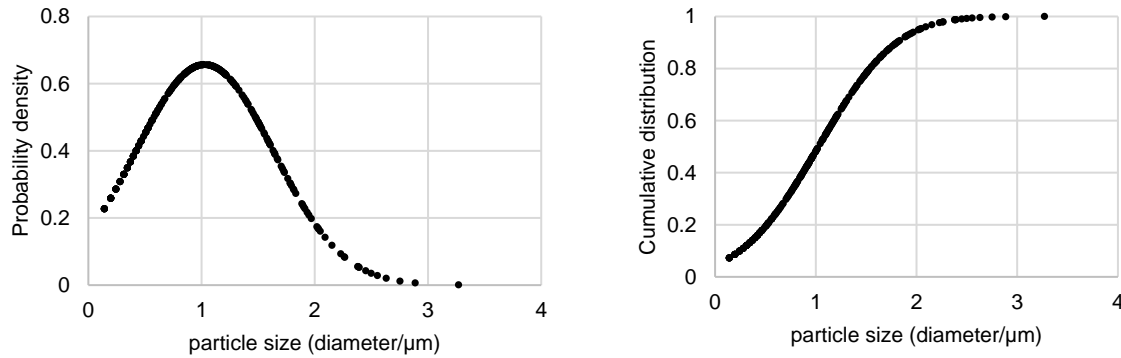


Figure 5.8: Coarse-particles distribution in the cured boehmite-epoxy matrix (10 wt%)

Besides the quasi-spherical NPs – boehmite and silica – that are described above, the flow and retention behavior of fibrous CNT NPs are also investigated. The comparative GF textiles are used to be able to visualize the filtration behavior. Laminates with FVFs of 30%, 40% and 50% are impregnated with CNT-epoxy suspensions using an RTM process with a CNT 0.1 wt%, as shown Figure 5.9. By FVF 30%, it seems that the CNT particles are well distributed along the flow length due to the low compaction of the textiles, with an impregnation time of about 30 min. However, at FVF of 40% and 50 %, the impregnation is strongly compromised due to the severe retention behavior of the CNT particles, without even being able to fully impregnate the plate until complete curing.

The main reasons that lead to the comparatively stronger retention behavior of the CNT NPs are ascribed to the rather big dimension of the CNTs in length direction with several microns. Moreover, the dispersion process of the CNTs is much more challenging compared to the quasi-spherical NP regarding the special fibrous morphology that tends to tangle each other. It can be seen in the Figure 5.10, that, even if the dispersion energy is rather high, there are still rather big observable agglomerates. The amounts of the agglomerates with size of bigger than 10 µm

5 Key aspect II: Process development and simulation

are quantified with image processing method as shown in the Figure 5.11 and Figure 5.12. Therefore, coarse particles or the big agglomerates of dozens of microns are inevitable in the suspension, which makes the impregnation quite challenging.

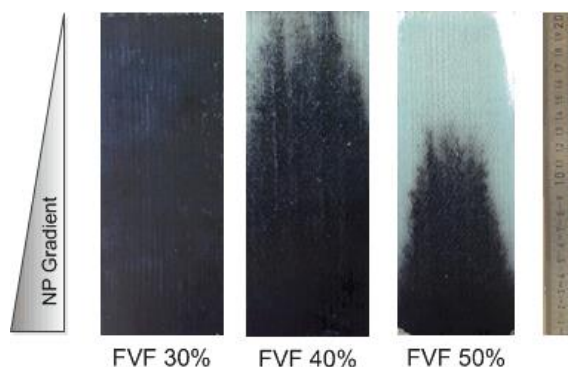


Figure 5.9: CNT retention by different FVF

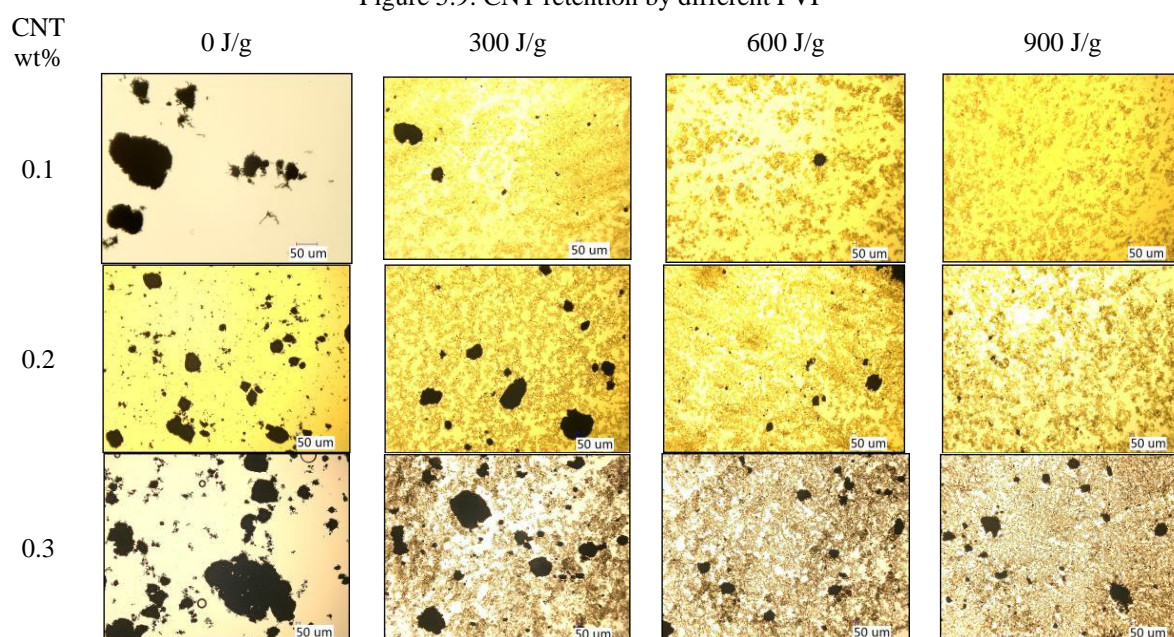


Figure 5.10: Dispersion state of the CNT NPs in epoxy depending on the concentration and ultrasonic dispersion energy (transmission optical microscopy)

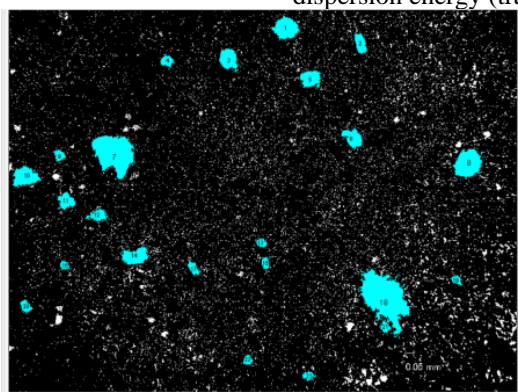


Figure 5.11: Agglomeration detection by CNT dispersion by image processing (original image: CNT 0.3 wt%, 900 J/g)

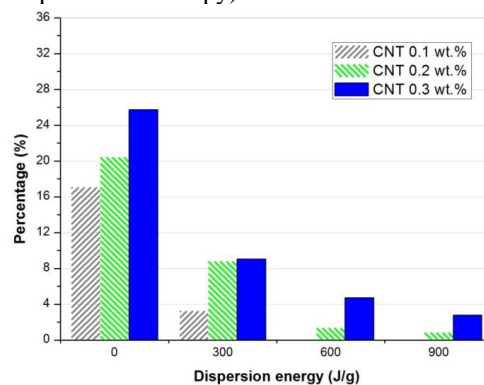


Figure 5.12: Quantification of the CNT agglomerates in the dispersion (particle size > 10 µm)

It is obvious that, depending on the particle type, NP-epoxy suspension preparation method, textile compaction state etc., the flow and retention behavior of the NPs show quite distinctive characteristics. It is therefore of big interest to develop and design optimal impregnation strategies depending on the particle size distribution characteristics, textile compaction behavior and structural complexity.

5.2 Flow simulation

In order to be able to design different in-plane or out-of-plane impregnation strategies with multiple inlet/outlet positions, it is indispensable to be able to describe and predict the flow behavior of different NP-modified resin systems during the impregnation. Therefore, flow simulations are carried out and validated by comparing the real (experimental) and the simulated flow front development versus injection time. The real flow front data and corresponding time are obtained by the permeability-measurement test rig as described earlier.

The following Figure 5.13 shows the flow simulation and validation results for a standard incompressible fluid (without NP) that used for the permeability measurements. It can be seen that, except from the experimental deviations by obtaining the flow front data at the beginning, the flow front development can be rather well predicted by the simulation.

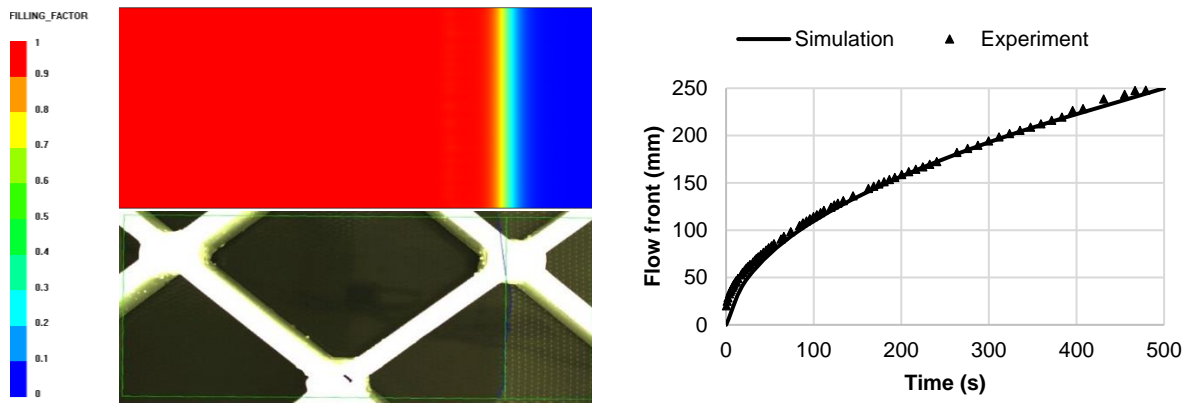


Figure 5.13: Flow simulation validation (FVF 55%, Oil)

Regarding the flow simulation with NP-filled epoxy matrix, as described in 3.3.2: Flow simulation, the average diameter of the filter medium is necessary to determine the permeability by the Kozeny-Carman equation, which nevertheless hard to be characterized by experiment. Therefore, an inverse calculation of the average filter medium diameter is carried out, as shown in the Figure 5.14. Among the diameters that are used as the filter diameter for the simulation, the 104 nm represents the average particle diameter in the boehmite-epoxy masterbatch, as shown in the Figure 3.5; the 1000 nm represents the average diameter of the coarse particles based on the image recognition process, as shown in Figure 5.8.

5 Key aspect II: Process development and simulation

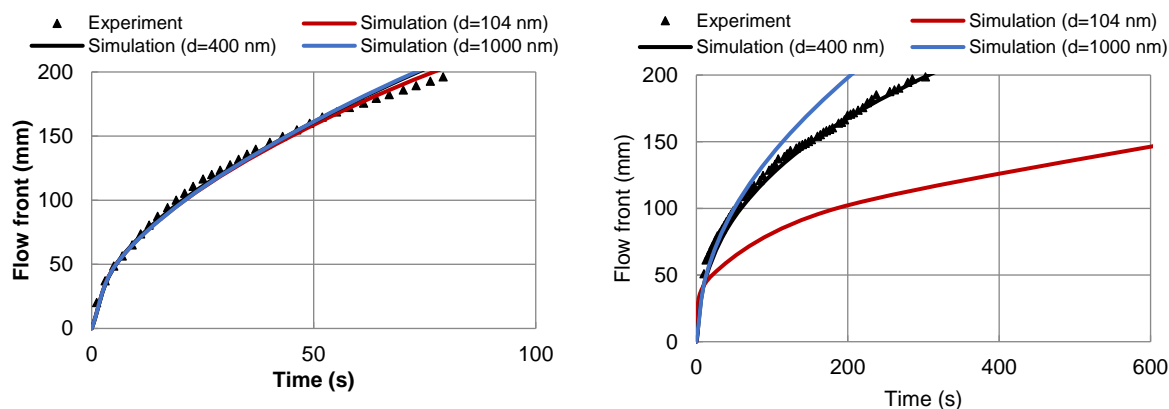


Figure 5.14: Inverse determination of the average filter-particle diameter
left: KE5%, 100 °C-FVF50%-1bar; right: KE5%, 100 °C-FVF60%-1bar

According to the results, by FVF 50%, the average filter diameter has a very slight influence on the simulation results regarding flow front development. In comparison by FVF of 60%, the results based on the filter-particle average diameter of 104 nm or 1000 nm deviate strongly from the experimental data. The difference can be explained by the different filtration mechanism of the NPs by the two different FVFs as discussed already in 5.1. By the FVF of 50%, the NPs showed a deep bed filtration with a very slight retention behavior, however, by FVF of 60% it showed a cake filtration with strong retention. **Therefore, by the FVF of 50%, the filter diameter is not critical as there is only a slight NP retention. In comparison, by the FVF of 60%, it is to be expected that there is a remarkable change in the filter diameter due to the strong cake filtration. So, it is also logical to believe that of these particle average sizes – 104 nm and 1000 nm – cannot fully represent the actual particle size in the process. By further calculation with an assumption of an average diameter of 400 nm, the simulation results fits well the experimental flow front data, indicating that the average particle size of the filter media lies around 400 nm.** This may represent a threshold particle size regarding the retention of the NPs in the fiber preform. Although it is so far not possible to determine the filter-cake particle diameter by experiment, so the inverse calculation is quite interesting and important.

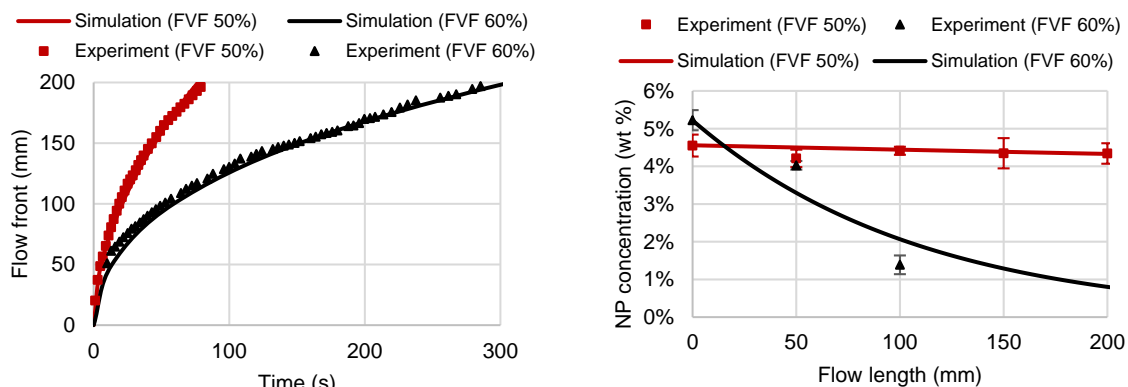


Figure 5.15: Flow simulation validation (KE5%, 100 °C-1bar)

Furthermore, the flow front development and NP retention behaviors by other scenarios are simulated and validated, as shown in the Figure 5.15. Regarding the NP retention behavior, the model can also well describe the NP retention behavior by FVF 50%, but it showed certain deviation by FVF 60%. The reason maybe because that the retention model that is selected to describe the NP retention behavior, as shown in Eq. 3.26, is mostly applied deep bed filtrations. It seems that it cannot necessarily good describe the retention behavior by a cake filtration – presumably the case by FVF 60% based on the analysis earlier.

Based on the simulation and validation result, it is clear that the model can be applied to predict the complex flow front development in the sequential and parallel injection strategies as put forward earlier, by which the inlet/outlet positions can be designed and the process robustness can be remarkably improved.

5.3 Cure simulation

Parallel to the flow simulation, cure simulation is also indispensable to predict the temperature/cure gradient and optimize the process. As described already in the Chapter 3, the curing process is dictated by the cure kinetics of the matrix, the heat capacity and the thermal conductivity of the composites. The curing kinetic modeling and the influence of the NPs on the cure kinetics are already investigated and analyzed in detail in the Chapter 4. Besides, the heat capacity and thermal conductivity is dependent on both cure degree and temperature.

Firstly, in order to investigate the dependency of the heat capacity on cure degree, the reference matrix system without any particle is investigated by quasi-isothermal MDSC at two different temperatures (100°C and 120 °C), by which the influence of the temperature can be neglected in each measurement. According to the results as shown in the following Figure 5.16 below, the heat capacity slightly decreases as the cure degree increases until a certain cure degree, and then shows a sudden step downwards and reaching a plateau. Combining the development of the heat capacity development and the heat flow curve, it can be determined that the “jump” in the heat capacity occurs where isothermal reaction tends to the stop. As discussed earlier in the Chapter 4 that, this is the critical curing degree where the vitrification occurs due to T_g exceeds T_{cure} . It seems that the heat capacity is much more influenced by the glass transition due to vitrification effect as from the cure degree.

Secondly, a dynamic MDSC process is applied to investigate the dependency of the heat capacity upon temperature. Considering that, the “jump” in the heat capacity is dependent on the vitrification effect that is dependent on T_g . Therefore, three different kind of samples are considered: the initial mixture (cure=0) is firstly measured until fully cure then the same sample is measured in a second heating cycle as fully cured sample (cure=1). Moreover, another sample is cured initially by an isothermal temperature at 100 °C by 25 min to achieve a certain

5 Key aspect II: Process development and simulation

initial cure degree (Cure neat resin=0.52; Cure KE 10% suspension=0.55) and T_g , and is measured in a second step with the dynamic MDSC.

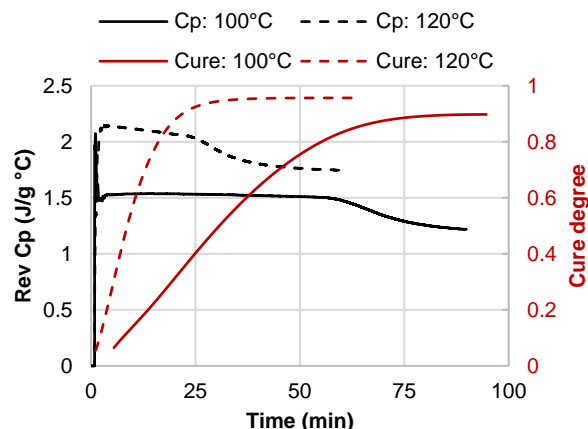


Figure 5.16: Change of neat epoxy matrix heat capacity depending on cure

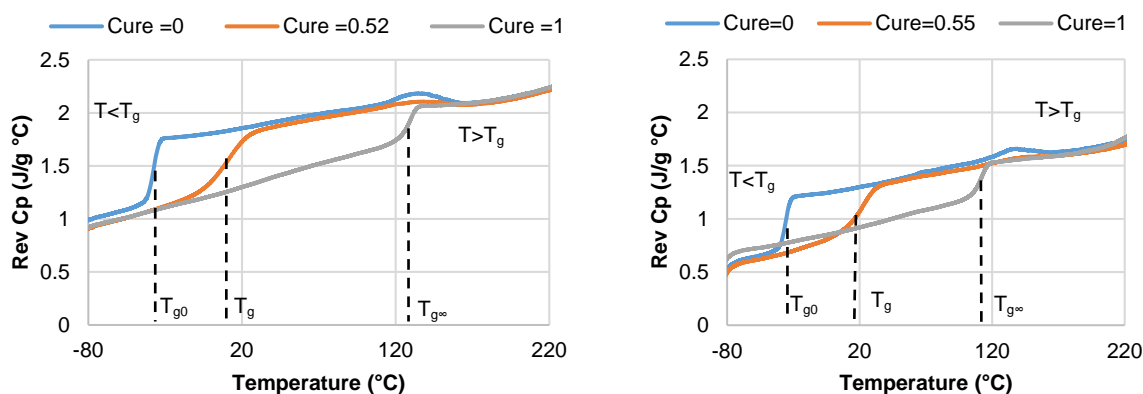


Figure 5.17: Change of heat capacity depending on temperature and cure.
Left: neat resin; Right: KE 10% suspension

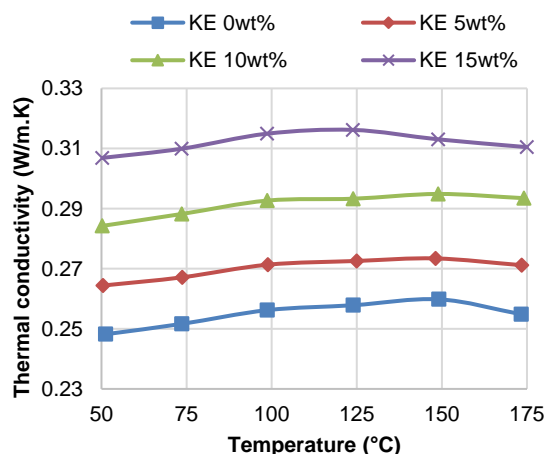


Figure 5.18: Thermal conductivity of NP-epoxy vs. NP concentration

As can be seen in the Figure 5.17, the heat capacity is almost a linear function of the temperature in the range $T > T_g$ or $T < T_g$. Nevertheless, the curve shows a remarkable “spring” by the transition of the fluid/rubbery state to the glass state depending on the T_g (alpha). Even if the slope of the linear function and transition zone (T_g) is rather reproducible in the repeating

tests, nevertheless the inception of the curves showed a remarkable deviation. It seems that the accuracy of the heat capacity test by the DSC is susceptible that might be due to the insufficient sensitivity of the device to small heat flow signals. The similar phenomenon with a deviation of up to $\pm 10\%$ was also reported in several other studies [132]. Considering that, the change of the heat capacity depending on cure degree is much smaller than that due to glass transition and test deviation; therefore, in this paper the heat capacity is modeled to be a function temperature and T_g . The curve development below and above the T_g transition can be well described by a linear function. The transition can be described by a $atan(T)$ function [132] or $tanh(T)$ function [179] as follows:

$$C_p(T, \alpha) = a_1 T + a_2 + a_3 \tanh(a_4(T - T_g))$$

a_1, a_2 : middle line to function $\tanh(T)$
 a_3 : vertical
 a_4 : width/slope of the transition zone

where distance between two linear parts
 Eq. 5.1

As the T_g is correlated to the cure degree (α) by the Dibenedetto equation which is characterized in the Chapter 4, so the start position of the transition zone is determined by the cure degree, as shown in the Figure 5.17. Except from the heat capacity, the thermal conductivity of the NP-modified epoxy samples is characterized as below in Figure 5.18. It can be seen there is a gradual increase in the thermal conductivity of the NP-epoxy matrix samples depending on the concentration of NPs. If the thermal conductivity by 50°C is to be compared, there is about 24% increase by modification with 15 wt% boehmite NPs.

For the simulation, a representative CFRP laminate cross section is considered, as shown in the figure below. As the boundary condition for curing, a typical curing cycle – 2 hours at 80°C and further 2 hours at 140°C – is applied.

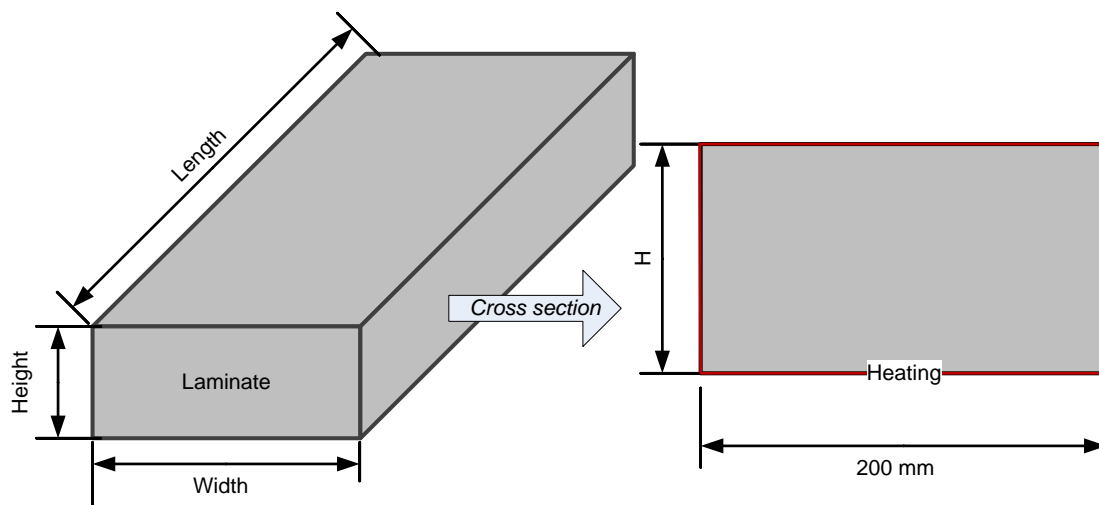


Figure 5.19: Physical model for curing simulation

5 Key aspect II: Process development and simulation

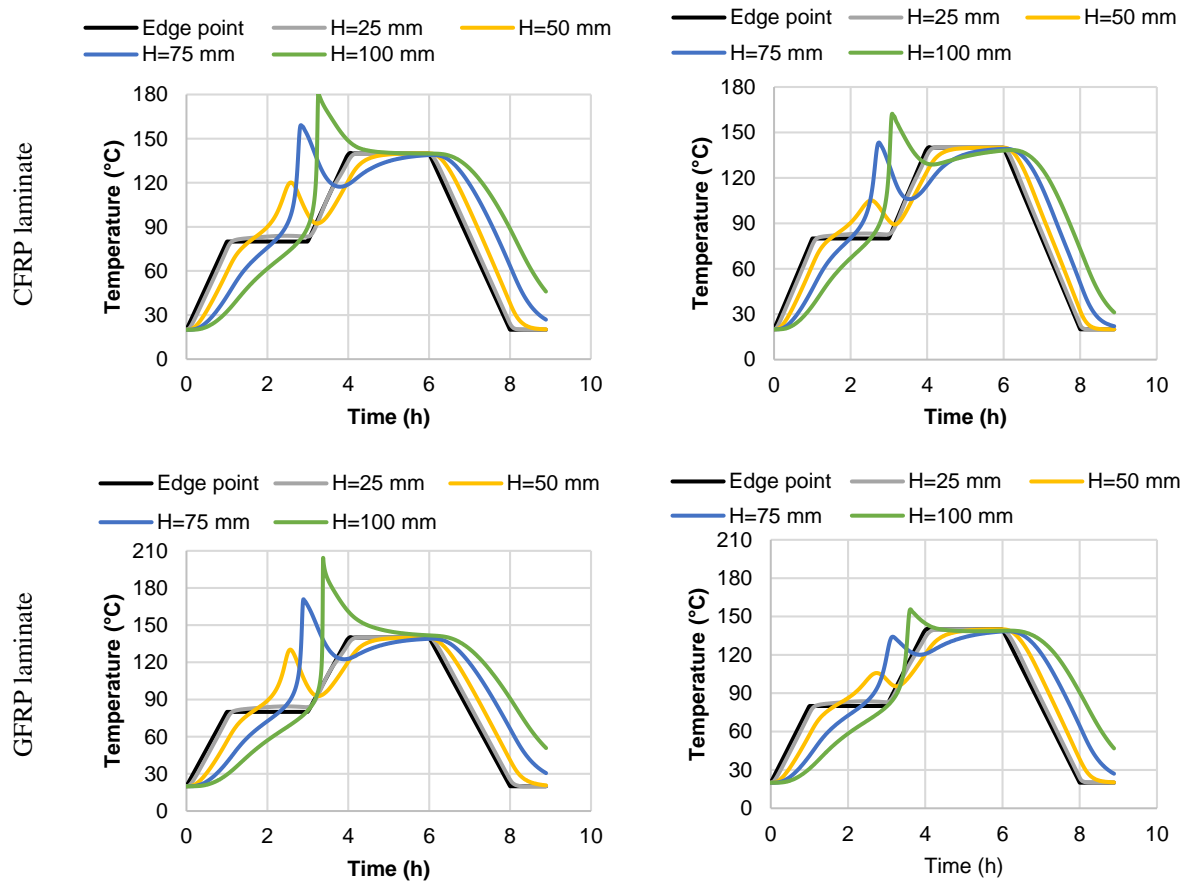


Figure 5.20: Evolution of FRP laminate temperature gradient depending on laminate thickness.
Left (neat resin matrix); Right (resin matrix with 10 wt% boehmite NP)

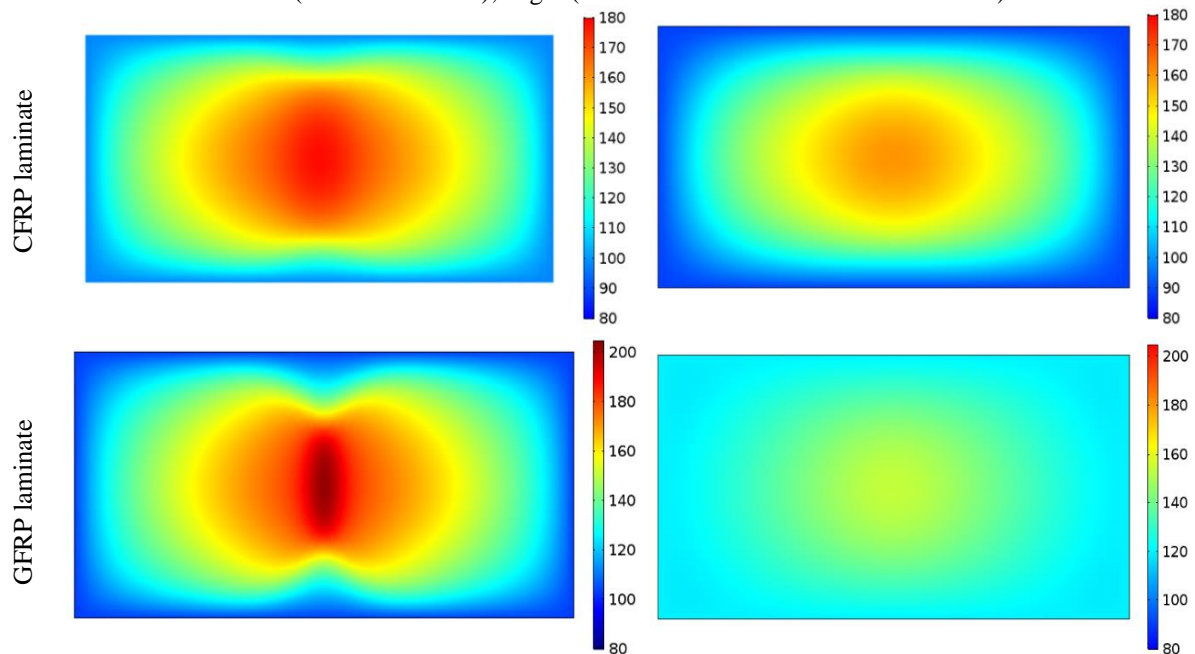


Figure 5.21: Maximum temperature gradient in FRP laminate during cure.
Left (neat resin matrix); Right (resin matrix with 10 wt% boehmite NP)

It can be shown from the results as shown in the Figure 5.20 that, with the increase in laminate thickness, there is a remarkable temperature increase in the middle of the laminate during the

curing process. If a laminate thickness of 100 mm is considered, the maximum temperature in the middle of the neat resin CFRP laminate arrives around 180 °C, as shown in the Figure 5.20 left. In comparison, by the 10 wt% boehmite NP- modified CFRP laminate the maximum temperature is just around 160 °C, as shown in the Figure 5.20 right. If a GFRP laminate is to be considered for comparison, by a similar laminate thickness of 100 mm, the maximum temperature in the middle of the neat resin GFRP laminate arrives around 200 °C, as shown in the Figure 5.20 left. In comparison, by the 10 wt% boehmite NP- modified GFRP laminate the maximum temperature is just around 155 °C, as shown in the Figure 5.20 right.

It is quite clear that by the introduction of the NPs the temperature gradient profile in the laminate can be remarkably decreased, so that the critical temperature overshooting can be reduced. Furthermore, it is to be expected that, by the modification of the matrix with NPs, the residual stress and resulted distortion due to the curing process can also be decreased.

5.4 Impregnation strategies

After determination of the design characteristics of a composite structure (geometry, applied fiber-preform, stacking sequence etc.), optimal impregnation strategies need to be designed depending on the structure geometry, maximum impregnation time/length of the matrix, as well as efficiency and complexity of the process. In a standard impregnation strategy design, the target function mostly would be impregnation time or impregnation quality (impregnation velocity, converging flow fronts etc.) with possibly small porosity. Correspondingly, the boundary conditions are the impregnation time/length of the matrix depending on the permeability. However, to fabricate gradient FRP structures with NP-filled matrix, comes additionally the required NP gradient – regarding the stress gradient – also as a target function, with the maximum flow length by different NP-epoxy matrix systems as a critical boundary condition to design optimal impregnation strategy.

As already discussed in the Figure 1.9, the main steps of the LCM process include draping/compaction, impregnation and curing. Considering the flow and retention behavior of the NPs, depending particle type, suspension preparation method, textile compaction state, fiber direction and flow length, it is possible to design proper process step sequences and impregnation strategies to optimally functionalize the structure.

First of all, two different impregnation methods, in-plane and out-of-plane, can be differentiated. By the in-plane impregnation process, as illustrated in Figure 5.22, the textiles are placed in a closed mold, and the matrix is injected from one side as linear (1D) or from the middle as radial flow (2D) form. The fluid flows in-plane homogenously within the textile to the outlet direction. In comparison, by the out-of-plane impregnation process (see Figure 5.23), a gap or a high permeable flow medium is adjusted above/under the textile, by which the fluid will quickly flow from the flow media and impregnate the laminate in the thickness direction

5 Key aspect II: Process development and simulation

due to the high permeability difference between the compacted textiles and the flow media. There are different variations of out-of-plane impregnation methods, including Compaction Resin Transfer Molding (CRTM) or Gap Impregnation etc. The out-of-plane impregnation methods are advantageous considering the very short impregnation length, especially considering particle-filled high-viscous suspensions. However, the out-of-plane impregnation processes are not as much flexible and robust as the in-plane impregnation methods for impregnation of complex geometrical structures.

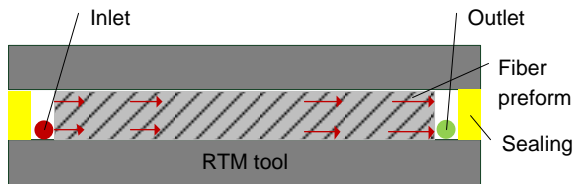


Figure 5.22: Illustration of in-plane impregnation process

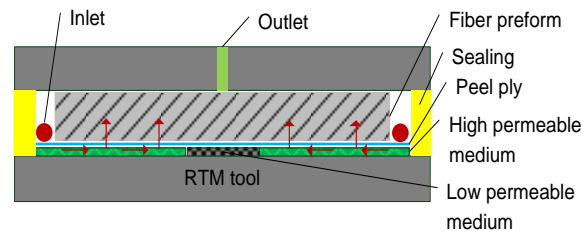


Figure 5.23: Illustration of out-of-plane impregnation process

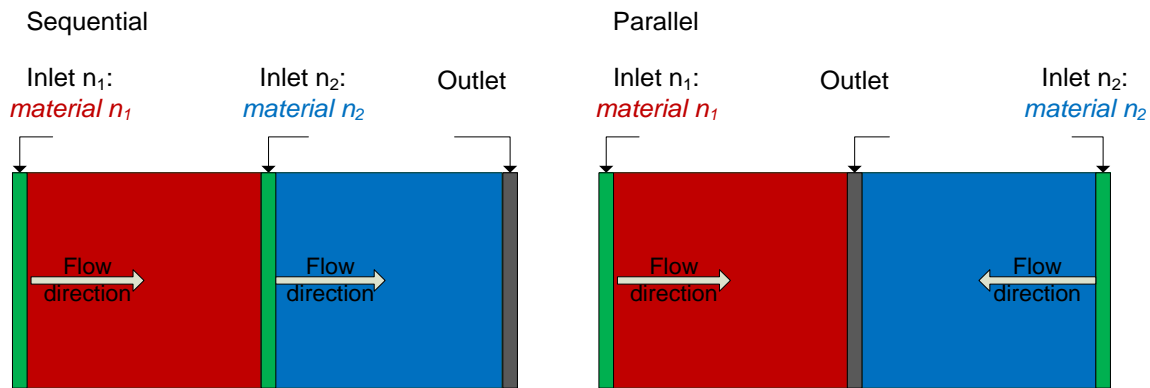


Figure 5.24: In-plane linear impregnation strategy. left: sequential injection; right: parallel injection

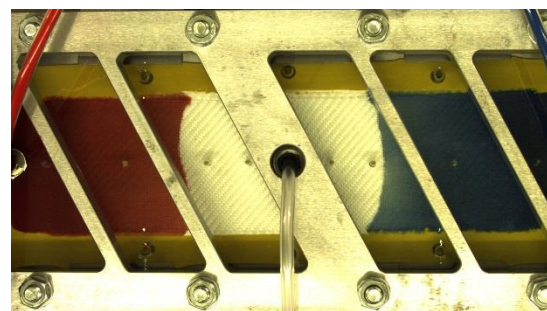


Figure 5.25: Visualization of in-plane impregnation strategies with different materials: parallel impregnation

For impregnation of complex geometries, in-plane impregnation is preferable, where the maximum flow length and retention factor are important for designing the inlet/outlet positions. Based on the maximum flow length and retention factor, optimal injection strategies regarding the desired NP gradient and structure complexity can be designed. The different in-plane injection strategies could be illustrated with the following two most representative injection strategies, as shown in Figure 5.24: sequential and parallel injection. By sequential injection,

multiple injection gates may be designed with the desired distance, according to the NP gradient degree and flow length. If the flow front reaches the nearby injection gate, the first gate closes, and the second gate opens. In comparison, by the parallel injection, all the injection gates simultaneously can be opened. **In both cases, NP-epoxy suspensions with different particle types or concentrations could be applied to adjust the optimal gradient profile in the structure, considering the maximum flow length and NP gradient factor.**

To investigate and validate the different in-plane injection strategies, different RTM tools, both 1D and 2D, with multiple inlet and outlet gates are designed. The impregnation concepts and particle gradient are firstly investigated by applying pigments with different colors in the epoxy to visualize the flow behavior and NP gradient. As shown in the Figure 5.25, two different kinds of materials are injected from both sides simultaneously (left: red, right: blue), representing different kinds of NPs or concentrations to locally modify the property profile of the structure.

Except from the in-plane impregnation strategies, different concepts and tools regarding the out-of-plane impregnation are developed and studied. Parallel to the concept which is illustrated in the above Figure 5.23 where the fiber preform is impregnated after the draping/compaction, a cost-effective and efficient out-of-plane impregnation process – Double Vacuum Assisted Resin Infusion (DVARI) – is applied where the fiber preform is impregnated before and draping/compaction. The advantage of this process is, as the impregnation occurs before the compaction of the preform, the textiles show quite large macro flow channels where the suspension rather quickly to impregnate the preform. Due to the rather small flow length in the thickness, and large filament/roving distance, such strategies can be used to achieve a uniform distribution of standard quasi-spherical NPs in the structures – even if the coarse particles exist. In addition, this also can be for effectively impregnating and generating functional gradient in the thickness direction with fibrous/sheet-form NP-epoxy suspensions.

The procedure of DVARI can be described in the following steps, as shown in Figure 5.26.

- Step 1: DVARI setup. Fiber textiles are placed on a flat mold and sealed. Besides, a perforated vacuum chamber is placed above the set-up. This chamber is also covered with vacuum bagging film to create a second vacuum.
- Step 2: Infusion of the NP-epoxy suspension. Vacuum is drawn in both inner and outer spaces. By adjusting the difference of the vacuum degree between the outer and inner spaces, the compaction of the textiles can be adjusted. When the vacuum degree of the outer space is slightly higher than the inner space, the first vacuum bag can be pulled up higher to generate an impregnation gap above the textiles, so that the fiber textiles under the inner vacuum bagging film will not undergo any pressure or compaction. Therefore, the matrix

5 Key aspect II: Process development and simulation

suspension would directly flow above the textile from the gap and impregnate the preform in the thickness direction due to the gravity and capillary effects.

- Step 3: Release of the second vacuum. The second vacuum is removed so that the suspension is pressed by the atmospheric pressure into the preform to get a better impregnation.
- Step 4: Hot press molding. Depending on the desired FVF, the impregnation can be further improved by a heat-press machine with higher pressure and temperature. For further information about the process and results regarding the process parameters, the readers are redirected to the following master thesis that is supervised by the author [180].

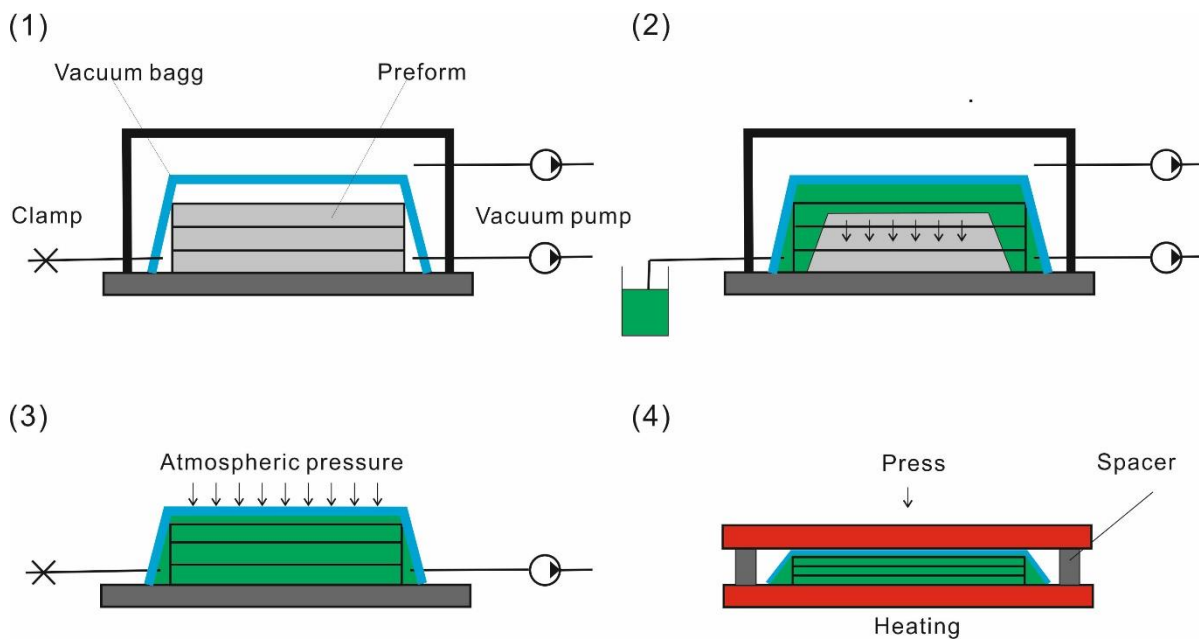


Figure 5.26: Schematic illustration of DVARI process

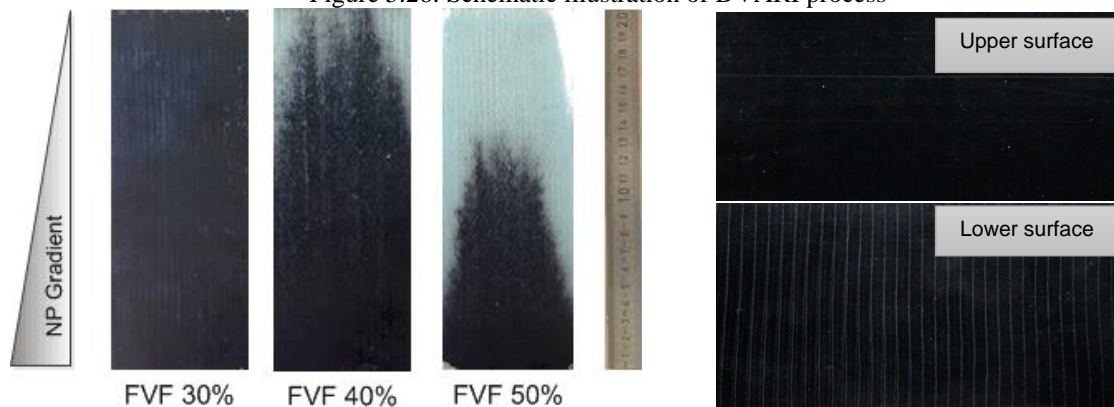


Figure 5.27: Comparison of the impregnation and CNT gradient between the in-plane (left: RTM) and out-of-plane (right: DVARI) impregnation strategies

As can be seen from the Figure 5.27, by applying suitable impregnation strategies, the impregnation quality can be remarkably improved. Moreover, the strong retention behavior of the CNTs that are already described earlier by in-plane impregnation can be effectively utilized to generate accumulation of the CNT particles on the surface to achieve a high surface electrical

conductivity of the composites, which will be further investigated and discussed in the next chapter.

Of course, the stress or property gradient in a structure is characterized not just by the direction, but also from the slope (gradient angle) and the evolution characteristics – linear, exponential decay, polynomial decay etc. – as illustrated in the following Figure 5.28.

It is already shown that depending on the particle type, dispersion state fiber direction and compaction state, the particles show different gradient behavior. Nevertheless, among them the fiber direction or stacking sequence is normally not a steerable parameter as it is mostly determined in design stage of a certain structure. Nevertheless, the fiber compaction state can be steered during processing – as discussed earlier regarding DVARI. In addition, it is also thinkable to prepare suspensions with different particle size so that the accurate adaption of the gradient slope and even the development can be realized. Nevertheless, in order to achieve the accurate adjustment of the gradient, the suspension preparation methods and the interactions of the particles with matrix and fibers needs to be further understood.

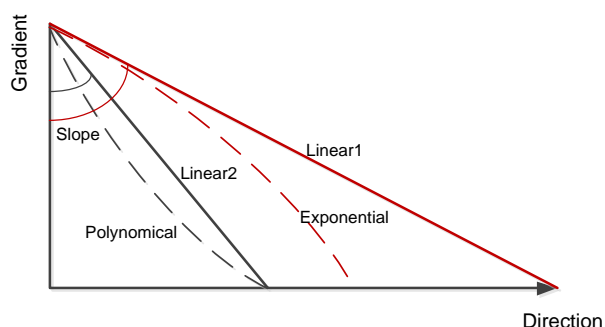


Figure 5.28: Typical gradient characteristics

5.5 Short summary

In this chapter, firstly NP flow and retention studies are carried out with different NPs – boehmite, silica and CNT, by which the NP gradient is quantified depending on the textile compaction, fiber direction and NP concentration. It is found out that the NP retention behavior is on one hand dependent on the dispersion quality of the NPs in the epoxy, which is closely dependent on the production method of the masterbatch, on the other hand the compaction status – filament distance distribution – of the fiber preform. It seems that, due to the process limit, a little amount of residual coarse particles might remain not well dispersed during the dry-particle dispersion process, and these coarse particles are quite critical in the impregnation process, especially at high FVF where the structure shows a micro-porous structure.

Flow and cure simulations are carried out to anticipate the complex impregnation and cure behavior with respect to the NP modified matrix systems and assist the design of the impregnation strategies and increase the process robustness and efficiency. The flow and retention coupled flow simulation showed good prediction compared to experiments. Moreover, the flow simulation is applied to inversely calculate the critical filter-particle diameter that is

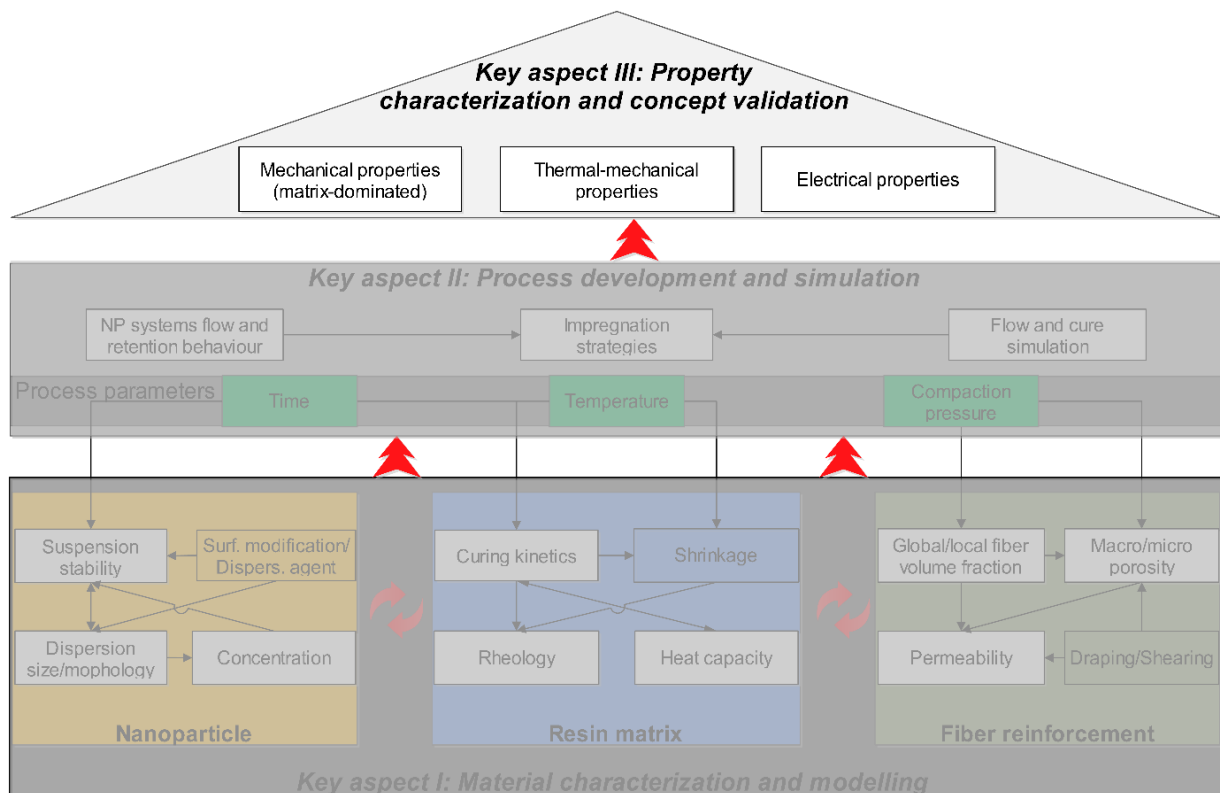
5 Key aspect II: Process development and simulation

determined to be around 400 nm. The cure simulations show a remarkable decrease in the cure/temperature gradient of the laminates with the modification of NPs. Finally, different in-plane (sequential, parallel) and out-of-plane impregnation strategies with single/multiple inlet/outlet positions are put. Different 1D and 2D RTM-tools are designed for the investigation of the impregnation strategies. The concepts and NP gradient are validated by visualization of multiple injected materials with different coloring agents.

6 Key aspect III: Property characterization and concept evaluation

In this chapter, the focus lies in the property characterization of the NP-gradient-functionalized FRP materials and structures. The goal is to investigate the critical properties regarding the NP gradient. By the coupon laminate, the critical mechanical, thermal-mechanical and electrical properties regarding the particle gradient are thoroughly characterized. Mechanical analysis is concentrated on the critical matrix dominated mechanical properties including interlaminar fracture toughness (G_{IC} , G_{IIC}), three-point-bending (transverse to fiber direction) and interlaminar shear strength (ILSS) tests.

As thermal-mechanical properties, thermal properties as well as dynamic thermal-mechanical analysis (DTMA) is studied. In addition, the surface and volume electrical properties of GFRP laminates that are modified by CNTs are investigated. Moreover, surface and volume electrical conductivities of the CNT-modified GFRP laminates are also investigated.



6.1 Mechanical properties

As discussed in Chapter 5, the particle gradient is strongly influenced by several material and process parameters. Considering that the influence of the NPs to the mechanical behavior of the composites is difficult to quantify since the coupons could show quite different behaviors depending on the gradient development (linear vs. non-linear) or even sample/test direction. Therefore, the out-of-plane impregnation strategy as illustrated in the Figure 5.23 is used to produce homogenously NP-distributed laminates with different particle concentrations, by which the influence of the NPs on the mechanical/thermal behavior can be well understood and described. It, nevertheless, enables the correlation of the property to the particle gradient. The correlations then could be transferred to in-plane impregnation, by which the particle gradient can be adjusted and optimized by designing different impregnation strategies.

The results of the G_{IC} , G_{IIC} , three-point bending and the ILSS properties are provided below separately in the Figure 6.1, Figure 6.2 and Figure 6.3. **It can be seen from the interlaminar fracture toughness and flexural properties that the influence of the boehmite NPs are quite remarkable: by modification with 15wt%, there are about 41.07 % and 45.91% increase in the G_{IC} and G_{IIC} fracture toughness properties, and about 38.14 % and 47.66% increase in the flexural modulus and strength.**

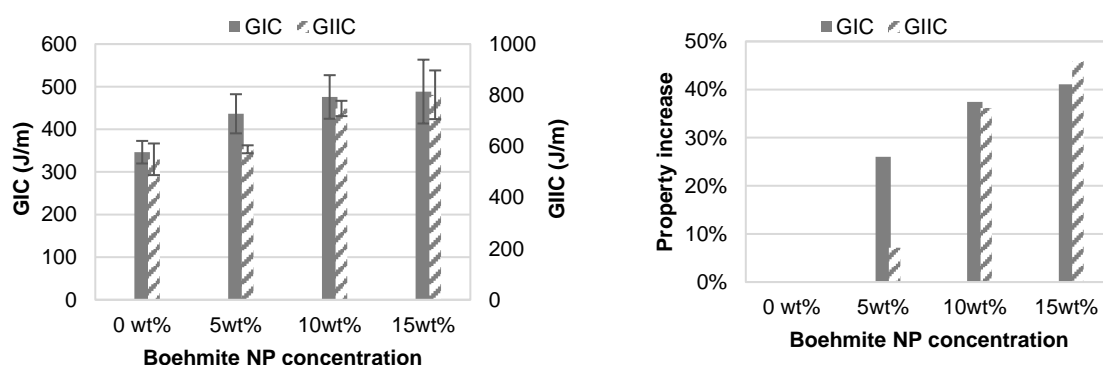


Figure 6.1: Interlaminar fracture toughness (G_{IC} , G_{IIC}) vs. boehmite NP concentration;

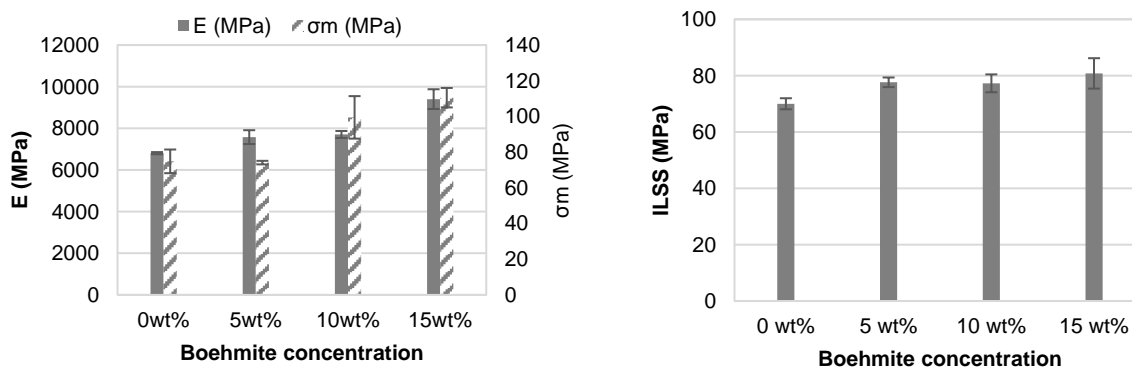


Figure 6.2: Flexural properties (fiber transverse direction) vs. boehmite NP concentration

Figure 6.3: Interlaminar shear strength vs. boehmite NP concentration

Regarding the ILSS properties, it needs to be pointed out here that, ILSS properties that are measured by short-beam test need to be quite critically checked, as it is only valid when there is a strict interlaminar shear failure. However, by the samples without much difference in the ILSS properties to other properties – compression, bending etc., it might happen that the samples could be broken earlier due to the local indentation or bending, indicating that results are not valid. This was also the case by the FRP samples that are tested in this work: **no samples were broken due to interlaminar shear, rather from local indentation and bending. Therefore, the results are supposed to be considered as apparent ILSS properties.** Nevertheless, the apparent ILSS properties showed an increase of about 15.4% with 15 wt% boehmite NPs.

There are several factors that may influence the fracture toughness of the particle-modified epoxy matrix [181]: deviation of the crack by the particle, which leads to an increased fracture surface; particle-matrix debonding with extra energy dissipation at the interphase; increase of the energy absorption through deformation of the particles; increase of the plastic ratio of the matrix. Of course, in the case of FRPs, comes the influence of fibers and their interaction into play.

The typical deformation mechanism of the NP-filled matrix can be illustrated by the following Figure 6.4. If the crack directly achieves a particle, depending on the stiffness of the particle, deviation (a) –by hard ceramic particle – or bridging (b) –by elastomeric particle – could be initiated. In parallel, depending on the particle-matrix interphase properties, micro crack around the NP (c) or deboning of the NP (d) from the matrix might occur. The voids that are generated from the debonding, plus the possible change in the matrix polymerization network density can lead to an increased plastic deformation by which the voids/cavitation further grow – known as “void/cavitation growth” as shown in (e). Furthermore, depending on the agglomeration state and the surface attraction of the NPs, if the crack front achieves an aggregate, crack branching might occur by splitting the agglomerates (f). In the extreme cases of agglomeration where the packing-density is quite high, it might also possible that the agglomerate structure cannot be fully impregnated with the matrix, which directly leads to enclose of air bubbles that enhances the void growth and crack branching (g). Of course, except from the NP, the chain segments of the epoxy matrix will be glided against each other which show a flow line on the fracture surface, which is known as shear banding. Furthermore, the matrix could also show some shear yielding characteristics.

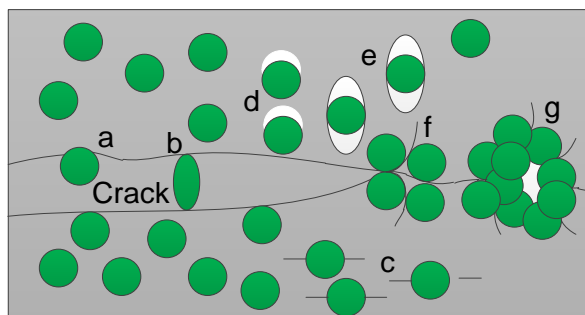


Figure 6.4: Illustration of the NP acting mechanisms in the matrix during crack propagation

The acting mechanism of the boehmite NPs can be revealed combining the microstructure of the fracture surfaces. The following Figure 6.6 shows the morphology of fracture surface from G_{IC} test by different magnifications in SEM. By the lower magnification ($10\ \mu\text{m}$) as in row *i*, the matrix in the unmodified CFRP samples showed large propagated fracture surfaces with a lot of river-line structures near the fibers, showing high interfacial loading and brittle failure at the interphase between the matrix and fiber. Most filaments are exposed without any matrix stuck on the surface. In comparison, by the boehmite NP modified sample, the matrix is much rougher but with much smaller irregularities. At the same time, there are also less directly exposed fiber filaments – still rest matrix on them. It seems that the main fracture mechanism by the unmodified CFRP sample is dominated by failure on the interface between the fibers and matrix. In comparison, by the modified CFRP sample, the fiber-matrix interface debonding seems to be a sub-dominating mechanism.

If the matrix surface is further magnified as shown in the row *ii* and *iii*, it can be observed that matrix fracture surface between the reference and modified samples are very different. The matrix by the unmodified CFRP system is rather smooth without much observable micro deformations or fractures. Nevertheless, the fracture surface of the boehmite NP modified CFRP structure showed an increasingly rough microstructure with quite remarkable debonding between the NP and matrix interface and void growth mechanism. Most interestingly, the microstructures of the matrix, especially by higher boehmite NP modification, show an extreme “porous” structure with large deformation and cavity buildings. This seems to be quite different compared to silica NPs even with much higher concentrations [182, 183].

According to the studies in Chapter 4 regarding the influence of boehmite NPs on the matrix curing behavior, it was found that the boehmite NPs can negatively influence the network density. The decreased network density results in an increased plastic ratio of the matrix that leads to increased ductile deformation under load. The extremely rough micro fracture surface and the cavity-buildings on the modified samples indicate an increased plastic deformation and possible air enclosures that can increase the void growth mechanism. **Therefore, it is reasonable to believe that main fracture mechanism by the boehmite NP modified CFRP structure is the debonding between the NP and epoxy interface, void growth and cavity**

building due to the plastic deformation of the matrix. In addition, it seems that it is also possible that some air bubbles might be enclosed in the agglomerate structures, which lead to increased cavity building, thus showing a porous structure in the matrix.

There are possibly two different mechanisms behind this phenomenon: firstly the boehmite NP may improve the fiber-matrix interfacial strength with possible fiber-matrix and fiber-NP interactions, or secondly it could be also possible that by the introduction of NP, the stress concentration is distributed and consumed more on the NP-matrix interface, reducing the stress concentration on the fiber-matrix interface, which may also likely to seem an increased fiber-matrix interfacial bonding strength.

One more aspect regarding the fracture behavior of the boehmite NP modified FRP laminates is the coarse particles that are already discussed earlier in Chapter 5. As shown at the G_{IC} fracture surface of the modified CFRP samples in Figure 6.5, clear debonding and crack deflection around the coarse particles can be observed. It was assumed in other studies that the agglomeration behavior of the alumina NPs can help to further improve the fracture toughness behavior, in a certain degree, by crack branching due to the splitting of the agglomerates [51]. Nevertheless, such effects are not observed or possible to be determined by the case of the boehmite NPs, as they seem to be quite firm with a stable geometry.

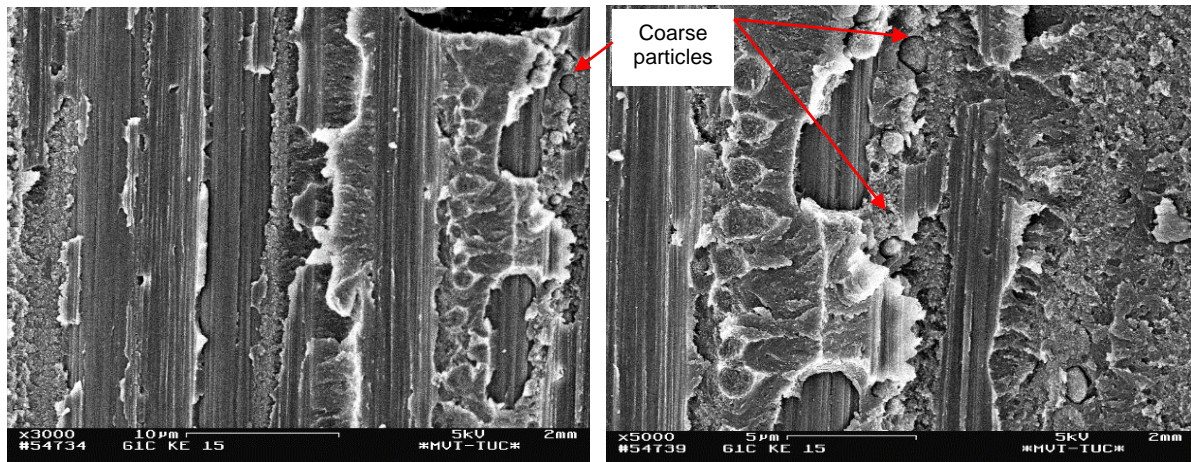


Figure 6.5: Coarse particles in CFRP modified with KE 15wt%

Of course, the different fracture mechanism and the acting principle of the boehmite NP are closely related to the matrix-fiber and matrix-NP interfacial properties. The difference and main mechanism can be further investigated and revealed by the dynamic mechanical analysis in the following chapter.

6 Key aspect III: Property characterization and concept evaluation

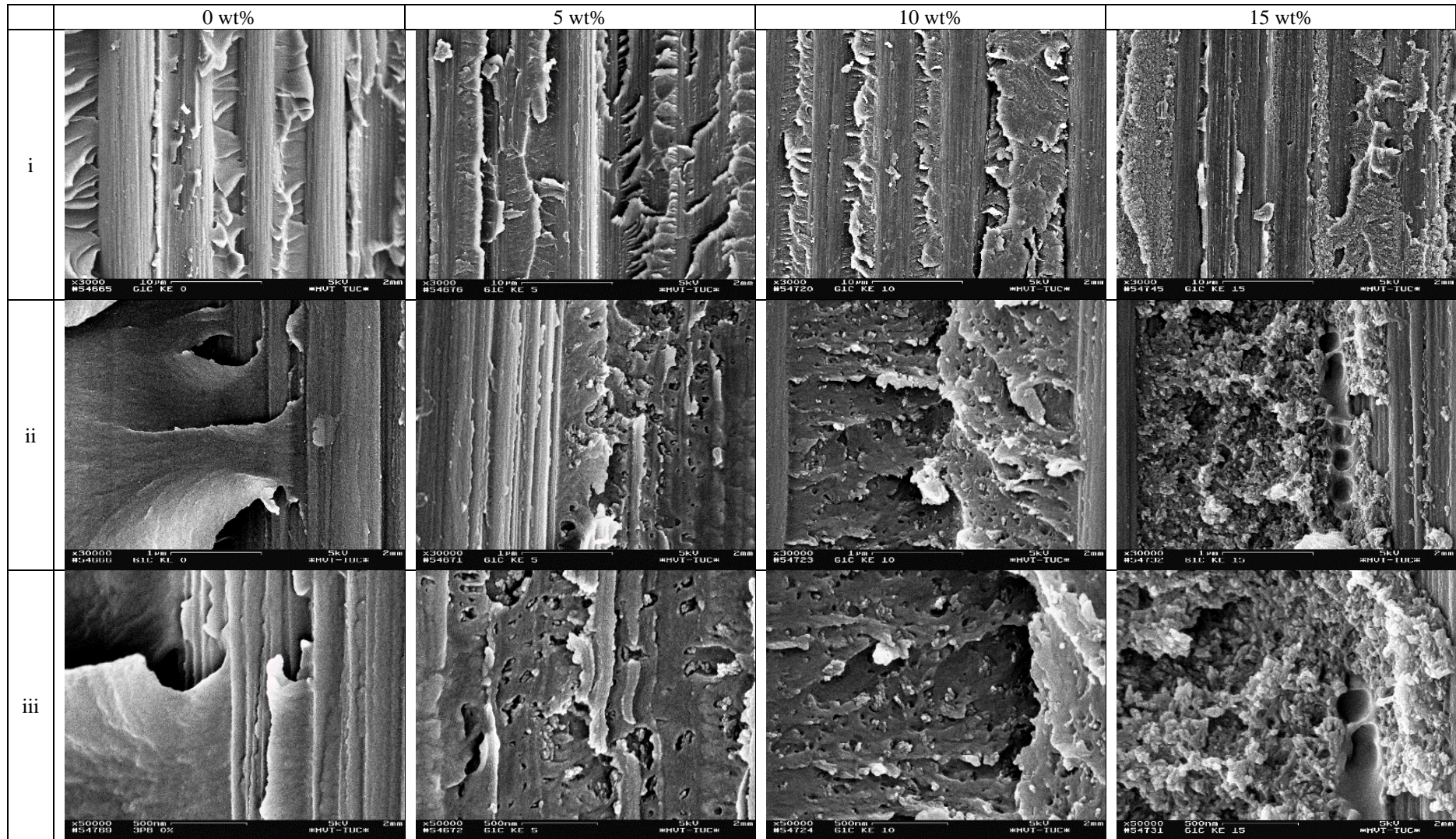


Figure 6.6: G_{IC} fracture surfaces of boehmite NP-modified CFRP

6.2 Thermal-mechanical properties

The influence of NP on the thermal conductivity and heat capacity properties are already provided and discussed combining 5.3: Cure simulation. So, here the focus lies in the DTMA analysis.

6.2.1 Dynamic thermal-mechanical analysis (DTMA)

Besides the static properties at room temperature, the dynamic thermal-mechanical properties under combined mechanical and thermal loading could provide further information about the NP-modified FRP structures under dynamic thermal and mechanical load conditions. It can be seen as an important property criterion for application in a structure level in complex load conditions. At the same time, it is also possible by the DTMA analysis to obtain some further information about the fiber-matrix, NP-matrix interfacial properties and temperature stability.

According to the dynamic mechanical properties (transverse to fiber direction), as shown in the following Figure 6.7, even if there is some test deviation regarding the storage modulus between the test samples, but generally the storage modulus of the FRP structures up to glass transition temperature are increased with the increase of boehmite concentration, similar to that of statistic mechanical properties.

In comparison, the peak position of Tangent Delta showed a consistent decreasing trend (Figure 6.7 right) – indicating a decrease in the T_g of the FRP structures. This indicates that the high-temperature stability of the FRP structure is decreasing with increased NP concentration, as also could be seen on Figure 6.7 left – with the increase of NP concentration; the storage modulus begins to drop earlier. The similar decreasing trend in T_g was also shown earlier in the cure kinetics investigation of the boehmite-epoxy suspensions.

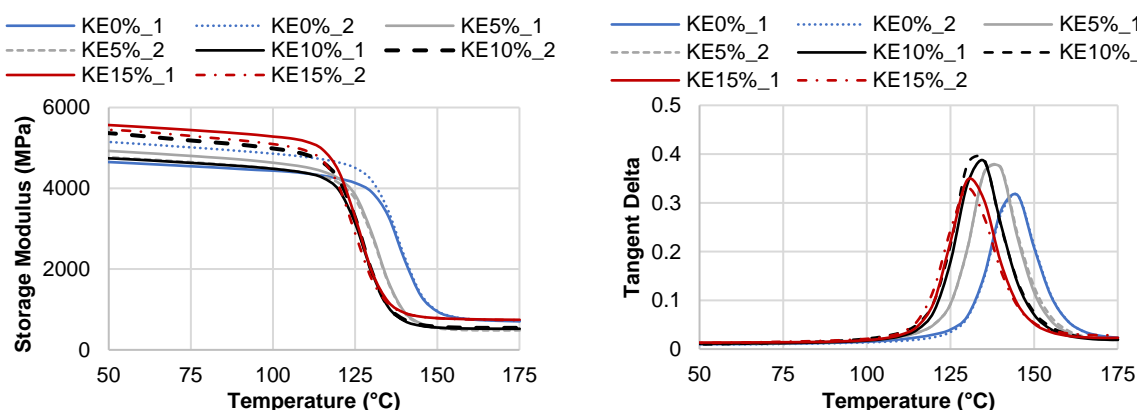


Figure 6.7: Dynamic mechanical properties of the boehmite-NP modified FRPs; left: storage modulus vs. temperature, right: Tangent delta vs. temperature

It was already shown earlier in Chapter 4 by the investigation of cure kinetics that the boehmite NPs could react with the epoxy to build covalent chemical connections. However, it needs to

be noticed that the high-temperature stability is decided by the intensity and density of the chemical connections after full cure. It seems that, even if the boehmite-NP can build covalent chemical connections with the epoxy, but the intensity and the density of the polymerization is weaker than that from the epoxy and anhydrite curing agent, which leads to a decreased stability at elevated temperatures. Of course, one more aspect with respect to the influence on T_g is the little number of coarse particles or agglomerates with size of several microns, which also lead to a dramatic decreased specific surface and decreased crosslinking density. The similar trends are also found in (-COOH) functionalized CNT NPs which increased the T_g by lower concentration due to the increased crosslinking density but decreased again by higher concentrations due to the agglomeration of the CNT NPs [184].

Nevertheless, combining the results on the static mechanical properties and observations on the fracture surface, the weak chemical bonding between the NP and the epoxy, in a certain degree, seems to provide positive influence on the fracture toughness and other similar mechanical properties of the FRP structures. As the introduced weak interphase provide potential path where the crack propagation could be very effectively initiated and deviated with increased plastic deformation, to transform the possible brittle failure to more ductile failure – higher fracture toughness. **Therefore, it is reasonable to believe that the main acting mechanism of the boehmite NPs in the CFRP is the energy distribution and consumption due to the weaker NP-epoxy interfacial strength where the cracks could be deviated and bridged due to the NP-epoxy debonding, micro-cracks etc. Therefore, the matrix showed an increased ductile behavior which could absorb and consume extra fracture energies.**

Moreover, by the addition of the boehmite NPs, the shrinkage and the coefficient of thermal expansion (CTE) of the matrix is expected to be decreased which helps to reduce the residual stresses between the fiber-matrix interphase. Therefore, due to these mechanisms, the stress concentration on the fiber-matrix interface is remarkably reduced, showing much lower fiber-matrix debonding failure. **The increase in the interlaminar fracture toughness could be well explained by these effects, as the increased interface and interphases with the NPs could provide potential path for crack propagation by pinning, bridging effects, showing a ductile fracture behavior with increased fracture toughness compared to the brittle failure in the neat matrix samples.**

6.3 Electrical properties

Besides the mechanical and thermal-mechanical properties of the NP-modified FRP structures, as described at the beginning, it is also of interest that in some applications, an increased electrical/thermal conductivity is expected, even in some cases preferably on the surface. Therefore, the electrical properties are investigated combining the gradient profile in the thickness direction by the CNT-modified GFRP laminates.

Due to the strong retention effect and restricted flow length of the CNT-epoxy matrix during impregnation of fiber preform, samples are fabricated by out-of-plane impregnation strategy based on the double-vacuum assisted resin infusion process (DVARI). In order to characterize the gradient functionality along the thickness direction, each sample is milled step-wise and the electrical conductivity – both surface and volume – is measured. The locations of the surfaces and residual volumes are shown in Figure 6.8.

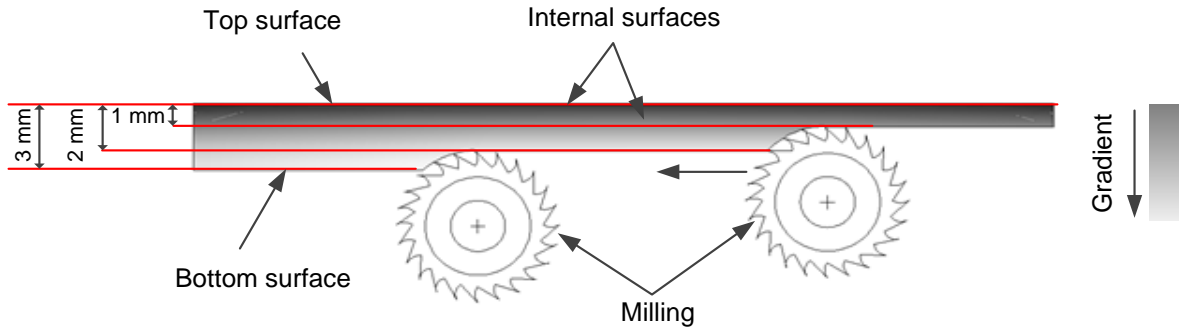


Figure 6.8: Illustration of sample preparation for EC conductivity gradient characterization

It can be seen from the Figure 6.9 (left) that, the electrical conductivity on the top surface reached saturation by just 0.1 wt% – indicating the critical percolation threshold concentration. This is presumably due to that, because of the strong retention effect, most of the CNTs are stocked on the top surface, resulting in the increased CNT concentration for percolation at lower concentration. This can be further validated by the Figure 6.10 (right), as by this critical CNT concentration, the electrical conductivity from the surface is almost the same until 1 mm thickness, but getting worse thereafter. This is due to the increased CNT accumulation of CNTs near top surface. With the increase of CNT concentrations, the electrical conductivity decreases as linear (0.1 wt%) or exponential (0.2 wt%, 0.3 wt%), Figure 6.9 (right). The decreased impregnation quality due to increased viscosity and retention of CNTs at higher concentrations, leads to negatively decrease of electrical conductivity and mechanical properties.

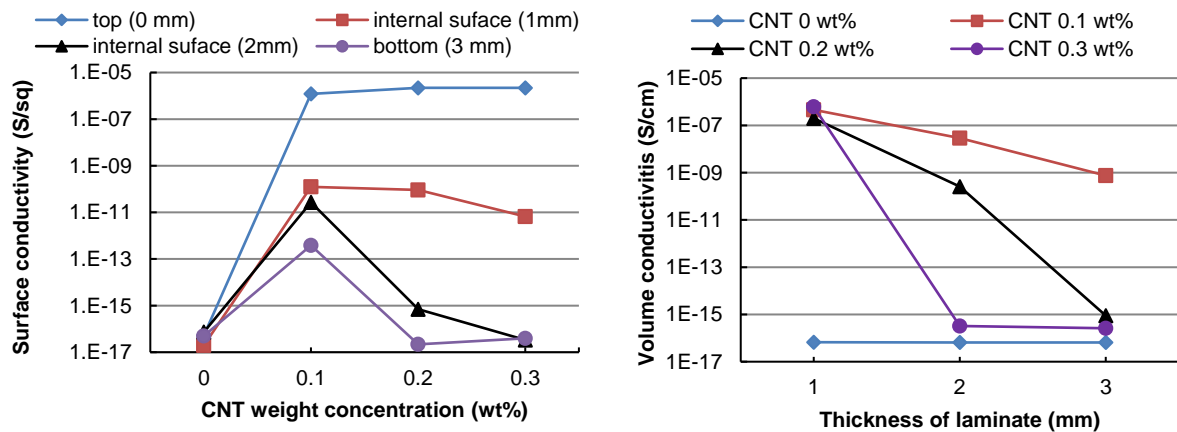


Figure 6.9: Electrical conductivity gradient vs. CNT concentration and impregnation thickness.

Left: surface conductivity; Right: volume conductivity

According to the typical applications of conducting composites, as shown in the Figure 6.10, the achieved electrical conductivity values on the surface can be used for antistatic protection.

6 Key aspect III: Property characterization and concept evaluation

To achieve higher electrical conductivity values, the concept could be transferred to more electrical conductive carbon-fiber textiles. Besides, studies also reported that by functionalization of CNT NPs, a rather high electrical conductivity can be achieved, as shown in Figure 6.11.

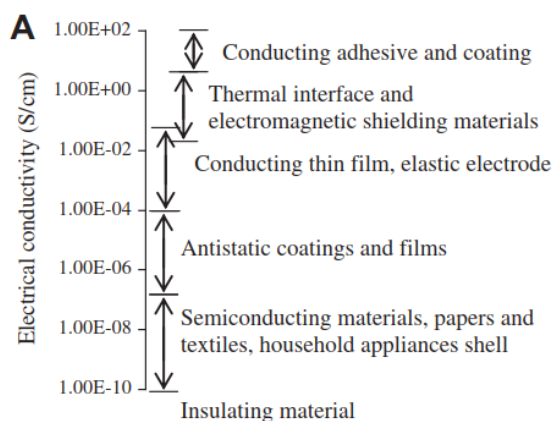


Figure 6.10: Typical applications of conducting composites [185]

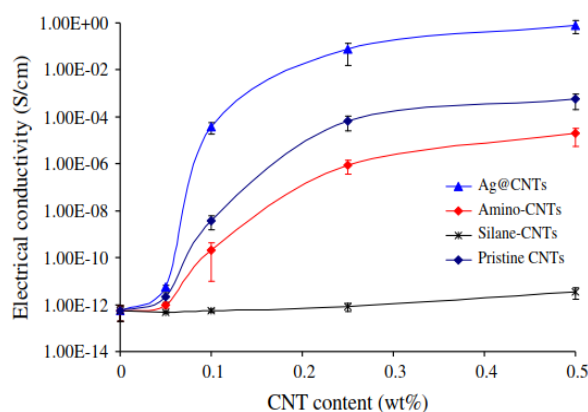


Figure 6.11: The effect of CNT functionalization on the electrical conductivities of CNT/epoxy nanocomposites [186, 187]

6.4 Short summary

In this chapter, the properties of the functional FRP materials are characterized. It is obvious that by the introduction of the boehmite NPs, the critical matrix-dominated mechanical properties are remarkably increased: by modification with 15wt%, there are about 41.07 % and 45.91% increase in the G_{IC} and G_{IIC} fracture toughness properties, and about 38.14 % and 47.66% increase in the flexural modulus and strength (transverse to fiber direction).

The DTMA analysis showed a certain decrease at the T_g – indicating a decreased network density – of the structure after modification with boehmite NPs. Nevertheless, combining the fracture surface analysis and the DTMA results, the main fracture mechanism by the boehmite NP modified CFRP structure is found to be the debonding between the NP and epoxy interface, void growth and cavity building due to the plastic deformation of the matrix. Therefore, the decrease in the network density is not necessarily always to be negative, as the poor connected particle-epoxy interfaces could provide extra paths for crack deviation and fracture energy dissipation.

Moreover, by the out-of-plane impregnation of CNT-filled epoxy suspension, the impregnation quality of the laminates is greatly improved. It is also applied to generate an electrical conductive gradient profile in the thickness direction with a highly conductive surface. Nevertheless, the results show an optimal concentration of the CNTs regarding the negative effects on the viscosity and impregnation quality, which negatively decreases the electrical and mechanical properties.

7 Summary and outlook

This chapter includes two main aspects. Firstly, important results and significant implications regarding the processing of NP-modified matrix by LCM processes and final properties of FRP structures are summarized and evaluated. Secondly, some important questions arising from the investigations that have not yet been fully understood or newly noticed are described, providing some future directions to be of interest and solution strategy recommendations.

7.1 Evaluation of the results

7.1.1 Key aspect I: Material characterization and modeling

The basic material components – NP, epoxy matrix and fiber reinforcement – and their interactions and correlations with process parameters are investigated. Regarding the NP-epoxy matrix, the cure kinetics/rheological behaviors are investigated and modeled as a critical aspect. By modeling, the influence of different model-free and model-fitting methods and regression algorithms on the model quality and prediction accuracy are investigated. After that, the cure kinetics and rheology of the boehmite-epoxy suspensions are modeled based on the optimized model parameter estimation and regression algorithm. Finally, the influence of boehmite NPs on the cure kinetics and rheology of an epoxy resin system is systematically investigated. It can be shown that the boehmite NPs are reactive to the epoxy, which inevitably influences the reaction kinetics of the matrix. The boehmite NPs can slightly accelerate the reaction at the beginning until a certain cure degree, which presumably due to the reactivity of the boehmite NPs with the epoxy, but after they inhibit the cure reaction – probably due to the spatial hindrance by the NPs. Finally, the boehmite NPs lead to a decreased polymerization network density of the matrix.

The standard Kamal-Sourour and Castro-Macosko models show an ill-posed characteristic, so that it is not possible to determine a clear correlation of the model parameters against the NP concentration. However, by optimization of the regression method combined with model parameter analysis, a good correlation between the model parameters and NP concentration is determined. Finally, generalized models are put forward to describe and predict the cure kinetics and rheology depending on time, temperature, and concentration of NPs. The generalization concept can also be possibly transferred to other filler-modified resin systems.

Regarding the fiber preform, the compaction behavior (global/local FVF, filament distance distribution) and permeability of the fiber preform considering the effects of NPs are also systematically investigated. The investigations regarding the compaction behavior of the textile – global/local FVF and filament distance – showed a critical phase transition of the porous

7 Summary and outlook

structure in the textiles: from a dual-scale porous structure to a single-scale micro-porous structure with the increase of FVF. Correspondingly, the average value of the smallest distance between the filaments at FVF of 30% is around 138 nm. It stays almost constant until FVF 50-55%, and begins to decrease remarkably from FVF 55%, until 4.26 nm by FVF 70%. Therefore, considering the change of smallest distance, the retention of the NPs could be quite critical after certain threshold compaction state, which is not to be underestimated.

In contrast to the single-modal Gaussian distribution pattern of the smallest distance, the neighbor distance shows a multimodal distribution characteristics with three peaks around 0.55 μm , 4.91 μm and 13.96 μm , separately. It seems that the distribution pattern of the filaments within the roving is dominated mostly by the pre-compaction during the roving/textile fabrication process, so the compaction during the impregnation process mostly influences the relative frequency of the peaks but not necessarily the pattern.

Considering the influence of NP retention on the permeability, the influences of the critical material and process parameters – FVF, NP concentration, and temperature and injection pressures – are investigated by DoE studies with respect to the maximum flow front and decay factor.

7.1.2 Key aspect II: Process development and simulation.

Firstly, NP flow and retention studies are carried out with different NPs – boehmite, silica and CNT, by which the NP gradient is quantified. It is found out that the NP retention behavior is dependent on the dispersion quality of the NPs in the epoxy that is closely dependent on the production method of the masterbatch, and the compaction status – porosity characteristics – of the fiber preform. The results showed that the impregnation of fibrous or sheet-structural NPs (CNT, GNP etc.) by standard in-plane impregnation processes is quite critical, due to the extremely limited impregnation length. In comparison, quasi-spherical NPs (boehmite, silica and so on) are better suited for in-plane impregnation. Nevertheless, even by the quasi-spherical NPs, the little amount of residual coarse particles that might remain not well dispersed during the dry-particle dispersion process are quite critical in the impregnation process, especially at high FVF where the structure shows a micro-porous structure.

In parallel, flow and cure simulations are carried out to anticipate the complex impregnation and cure behavior with respect to the NP modified matrix systems and assist the design of the impregnation strategies and increase the process robustness and efficiency. The flow and retention coupled impregnation simulation shows good prediction compared to experiments. Moreover, the flow simulation is applied to inversely calculate the critical threshold filter-particle diameter that is determined to be around 400 nm. Moreover, the cure simulations show a remarkable decrease in the cure/temperature gradient of the laminates with the modification

of matrix with NPs. Finally, different in-plane (sequential, parallel) and out-of-plane impregnation strategies with single/multiple inlet/outlet positions are put. Different 1D and 2D RTM-tools are designed for the investigation of the impregnation strategies. The concepts and NP gradient are validated by visualization of multiple injected materials with different coloring agents.

7.1.3 Key aspect III: Property characterization and concept evaluation

The properties of the functional gradient FRP materials are characterized. It is obvious that by the introduction of the boehmite NPs, the critical matrix-dominated mechanical properties are remarkably increased: by modification with 15wt%, there are about 41.07 % and 45.91% increase in the G_{IC} and G_{IIC} fracture toughness properties, and about 38.14 % and 47.66% increase in the flexural modulus and strength (transverse to fiber direction).

The DTMA analysis showed a certain decrease at the T_g – indicating a decreased network density – of the structure after modification with boehmite NPs. Nevertheless, combining the fracture surface analysis and the DTMA results, the main fracture mechanism by the boehmite NP modified CFRP structure is found to be the debonding between the NP and epoxy interface, void growth and cavity building due to the plastic deformation of the matrix. Therefore, the decrease in the network density is not necessarily always to be negative, as the poor connected particle-epoxy interfaces could provide extra paths for crack deviation and fracture energy dissipation.

Moreover, by the out-of-plane impregnation of CNT-filled epoxy suspension, the impregnation quality of the laminates is greatly improved. It is also applied to generate an electrical conductive gradient profile in the thickness direction with a highly conductive surface. Nevertheless, the results show an optimal concentration of the CNTs regarding the negative effects on the viscosity and impregnation quality, which negatively decreases the electrical and mechanical properties.

7.2 Conclusion

An overall evaluation of different NP-modified epoxy resin systems regarding the influence on the process and final properties is necessary, so that the optimal NP-modified epoxy system can be selected for functionalization of FRP structures by which an optimal balance between the processing and properties can be achieved. Therefore, the investigated NP-modified epoxy matrix systems are evaluated with the most important aspects regarding the process and final properties.

The evaluation of the reference boehmite NP-modified epoxy resin systems regarding the critical aspect on process and final properties are shown in the following column chart as shown in Figure 7.1 and Table 7.1. Depending on the concentration, boehmite NPs can positively

7 Summary and outlook

influence the critical matrix-dominated FRP properties. Nevertheless, optimized impregnation strategies are needed considering the negatively influence on the process time due to the increased viscosity and retention behavior.

In addition, it is also possible to compare different NPs so that the application of different NPs can be synergistically evaluated. If the different NPs (boehmite, silica and CNT) to be considered, the influence factors based the results in the thesis and from related literatures are normalized to unit volume of the particles and shown in the following column chart as shown in Figure 7.2 and Table 7.2. It seems that the CNTs are quite effective on enhancing the mechanical properties, compared to two other quasi-spherical NPs – boehmite and silica. Besides, if the thermal and electrical properties are to be considered, which are not provided in the figures, the influence of the CNT NPs is much more obvious than the other particles due to the high aspect ratio of the CNT so that a conductive network (percolation threshold) can be achieved much easier at lower concentrations. Nevertheless, the negative aspects of the CNT regarding the dispersion cost, process time, retention are also relative high so that it can directly endanger the processability by impregnation processes without carefully considering the preform permeability or impregnation strategy.

If the quasi-spherical boehmite and silica NPs to be considered, the reference boehmite nanosuspension – prepared by dry-particle dispersion – seems to show higher influence on the flexural modulus, strength, and G_{IC} properties. In comparison, the negative effects of the silica nanosuspension on the processing – process time, retention behavior, etc. – are much smaller than that from boehmite, which makes it quite attractive for LCM processing. Nevertheless, it is important to note by comparing the different NPs is that, the effects of the NPs on the comparing aspects may not always be linear – especially by CNTs, which means that the comparison based volume normalization is to be considered quite critically

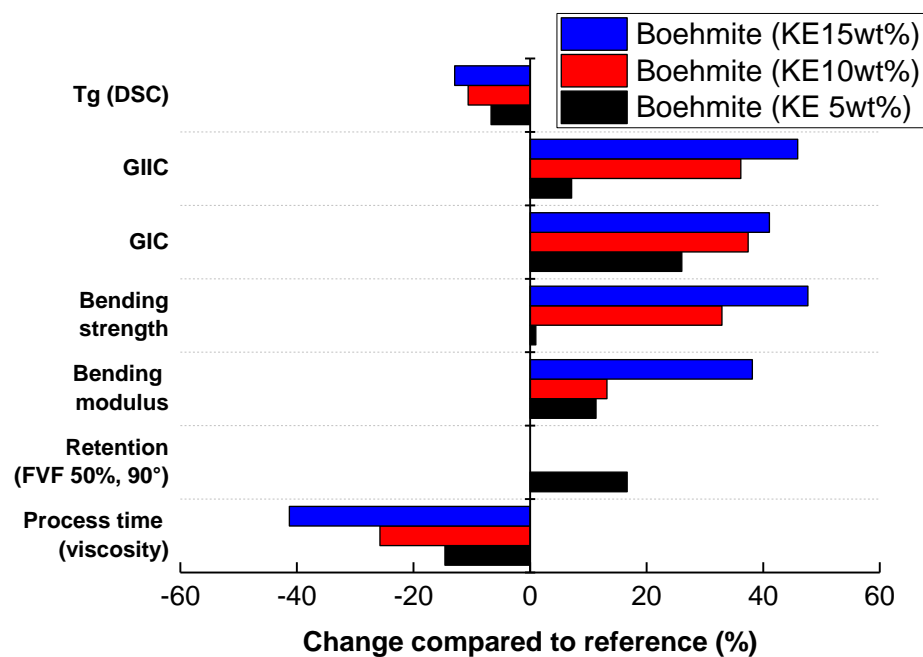


Figure 7.1: Evaluation the influence of the reference boehmite NPs regarding the critical aspect on process and final properties

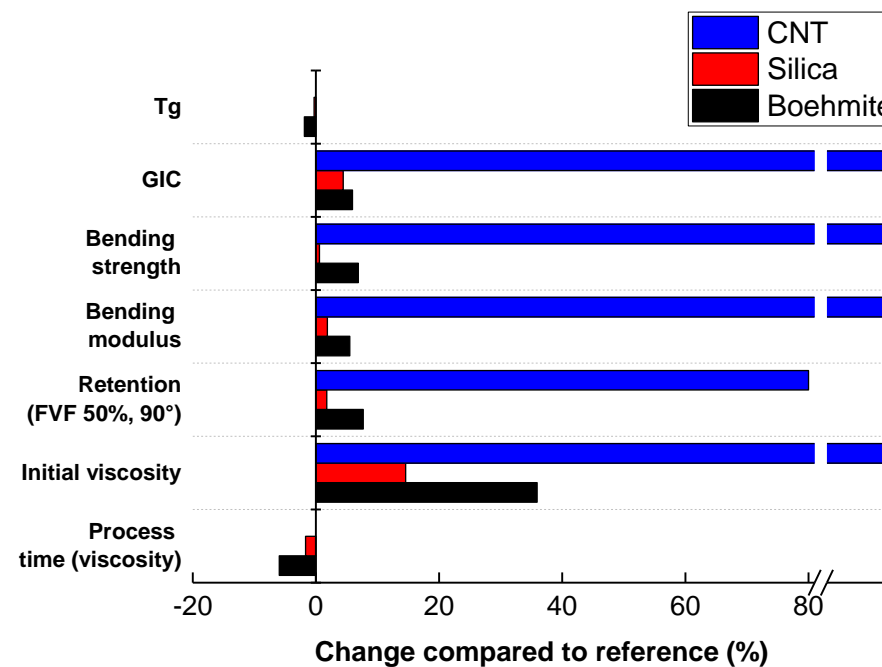


Figure 7.2: Evaluation the influence of the different NPs regarding the critical aspect on process and final properties (normalized to unit NP volume)

7 Summary and outlook

Table 7.1: Evaluation the influence of the reference boehmite NPs regarding the critical aspect on process and final properties

Boehmite	Volume fraction	Initial viscosity	Process time	Retention (FVF 50%)		Bending modulus	Bending strength	G _{IC}	G _{IIC}	T _g (DSC)
				0°	90°					
Reference	0.00%	0.00%	0.00%	0	0	0.00%	0.00%	0.00%	0.00%	0.00%
KE 5wt %	2.17%	84.61%	-14.62%	10.80%	16.66%	11.32%	-0.95%	26.03%	7.12%	-6.70%
KE 10wt %	4.48%	161.59%	-25.76%	-	-	13.18%	32.91%	36.17%	36.17%	-10.63%
KE 15wt %	6.93%	462.32%	-41.29%	-	-	38.14%	47.66%	41.07%	45.91%	-12.94%

Table 7.2: Evaluation the influence of the different NPs regarding the critical aspect on process and final properties (normalized to unit NP volume)

Particle type	Normalized volume fraction	Initial viscosity	Process time	Retention (FVF 50%)		Bending modulus	Bending strength	G _{IC}	T _g (DSC)
				0°	90°				
Reference	0.00%	0.00%	0.00%	0.00%	0.00%	0.00%	0.00%	0.00%	0.00%
Boehmite	1.00%	35.91%	-5.96%	4.97%	7.67%	5.50%	6.88%	4.71%	-1.87%
Silica	1.00%	14.57% [16]	-1.69% [16]	1.34%	1.77%	1.85% [16]	0.58% [16]	4.44% [17]	-0.30% [16]
CNT	1.00%	2523.92%	- [188]	80%	-	301.61%	726.77%	132.74% [23]	- [188]

7.3 Outlook

While critical aspects regarding the material, process and properties of the FRP materials and their interactions/correlations are systematically investigated, there are still some new aspects with potential interest for future investigation.

7.3.1 Material characterization and modeling

It is obvious that the dispersion quality of the NPs, particularly the coarse-particle concentration, in the masterbatch is critical for the impregnation process, especially by the high FVF. It is therefore important to focus on the particle dispersion process, especially by the dry-particle dispersion process. Nevertheless, the dispersion quality of the NPs is almost exponentially correlated to the dispersion time and energy: the smaller the average dispersion size is, the more time and energy is needed to further disperse the NPs and improve the masterbatch quality. That's presumably why some of the coarse particle might left inevitably regarding the exponentially increased process cost. Here comes an interesting question: how the dispersion process can be optimized to achieve the best dispersion of the NPs with an acceptable dispersion cost.

In parallel, the agglomeration during the dilution, mixing and injection processes is still an aspect which is not yet fully understood. Considering that the flow and retention behavior of some NPs can be quite critical above a certain FVF where the textile shows a single-scale porous structure, it is feasible to design and prepare the textile structures with targeted macro flow channels or “runners” so that the impregnation robustness and efficiency of the impregnation process with a NP-filled matrix can be greatly improved.

At the same time, the influence of different surface modifications on the process and final properties is surely an interesting and important aspect for further investigation, as it is shown by the boehmite NP that it has a remarkable influence on the process and final properties. It would be quite interesting in the future if the surface functional groups of the NPs could be target-oriented designed with respect to the influence on the process and final properties.

Additionally, to transfer the concept of “functional gradient” to complex FRP structures, the draping/shearing effect comes into play. The draping/shearing effects have direct influence on the macro/micro-porosity of the textile and on permeability which directly influences the flow and retention behavior of the NPs. Moreover, in this investigation, primarily in-plane permeability of the textiles and influence of the NPs are investigated. For flow simulation in complex structures, the z-permeability also plays also a critical role. Therefore, characterization of the z-permeability is important. It needs to be pointed out that, the measurement of the transient unsaturated permeability in the thickness direction is more

7 Summary and outlook

challenging than that of the 1D/2D permeability, as the detection of the flow front development is only possible by cost-intensive methods (such as ultrasonic, etc.) due to the very short flow length within closed tools. Therefore, the permeability is preferably determined by volume or mass flow of the fluid after the textile is fully impregnated (saturated permeability). Parallel to this investigation, currently an international permeability measurement benchmarking activity with a focus on the z-permeability is being carried out. More details about the test methods and results will be published soon. Moreover, an integrated simultaneous 3D permeability measurement concept would be very interesting where all the three major permeability values could be determined simultaneously.

7.3.2 Process development and simulation

The impregnation process with NP-modified resin systems would be quite complex regarding the three-dimensional flow and retention behavior of the NPs. Therefore, the modeling and simulation of the flow and cure process is indispensable to account for the process design complexity and enhance the robustness. Regarding the complex influence of the reaction on the flow and filtration behavior with the increased agglomeration effects during the injection, the flow simulation in this paper is concentrated on non-reactive NP-epoxy matrix so that firstly only the interaction between the flow and retention can be considered, to be able to evaluate the model quality and numerical methods by a simpler case. The coupling of the reaction in the real impregnation simulations would be surely of further interest.

According to the investigations by the author in the thesis, the standard flow/cure simulation software doesn't provide the possibility for the required complex flow and cure simulation regarding the time and location dependent material parameters that are mostly considered to be constant in the standard software solvers. Therefore, it is recommended that a more open-source software to be considered where the complex material properties and boundary conditions regarding the flow and cure process could be fundamentally described and simulated. Considering the extra effects of draping/shearing on the flow and filtration, as well as cure behavior in the 3D curved-structure, the results and methodology that are developed in this thesis need to be further extended and improved for optimized impregnation strategies regarding complex 3D FRP structures.

7.3.3 Visualization of the particle-particle and particle-fiber interactions

New possibilities for further understanding the possible interactions between the particle-particle and particle-fiber could be provided by applying fluorescent NPs for the impregnation process. The earlier investigations regarding this topic showed that the standard commercially available fluorescent particles are, on one hand, quite expensive, and on the other hand normally have particle size of several microns, which is not representative for the investigation

and visualization of the interactions regarding NPs. Moreover, some studies also show that many fluorescent coloring agents/pigments would bleach out after curing at elevated temperature, which makes it not possible to track the particles [189]. Therefore, two possible approaches are recommended: the first possible approach is to functionalize the surface of the NP directly with anchor fluorescent molecules so that the NPs could be directly tracked. The second possible method is ball milling of the commercially available bigger but cheaper luminous NPs into nanosize and dispersing them in the epoxy matrix to prepare a new masterbatch. Nevertheless, the possibility of these approaches needs to be further evaluated and proved.

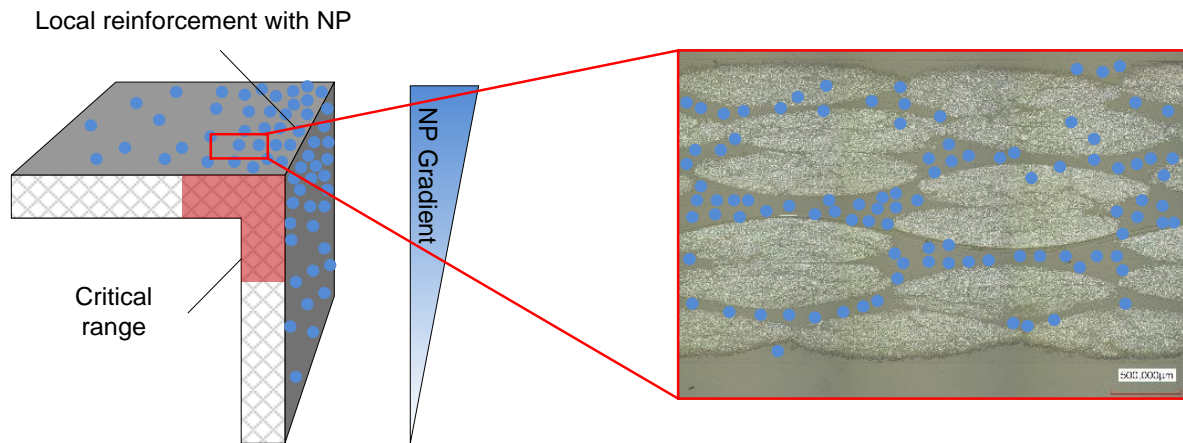


Figure 7.3: Visualization of the NP-fiber, NP-particle interactions with fluorescence particle

7.3.4 Nano-carrier-fiber: simultaneously binding and functionalization

With respect to manufacturing the complex FRP structure, mostly a binder system is required to drape and fix the textile on the complex geometry. In addition, the complex flow and retention behavior of some special NPs, especially considering the draping/shearing effects make the impregnation process quite complex, with a potential challenge on the process robustness. Therefore, a totally new concept which is based on a new epoxy-solvable, thermoplastic, nanoparticle-carrier-fiber (Nano-carrier-fiber) can be recommend which can be used as a binder to fix the textiles, and also as local reinforcement in the critical zones of the structures. Nevertheless, the production of the Nano-carrier-fibers, the solving behavior in the epoxy and the flow behavior of the NPs and their influences on the permeability and final properties of the structures are interesting aspects to be further investigated.

Furthermore, it is of great interest to investigate the macro and micro-mechanical behavior regarding the gradient property profile based on different NP types and concentrations. The interphases where the different NPs and concentration meet each other would be of particular interest, as they might show quite different acting mechanism of the NPs and failure behaviors.

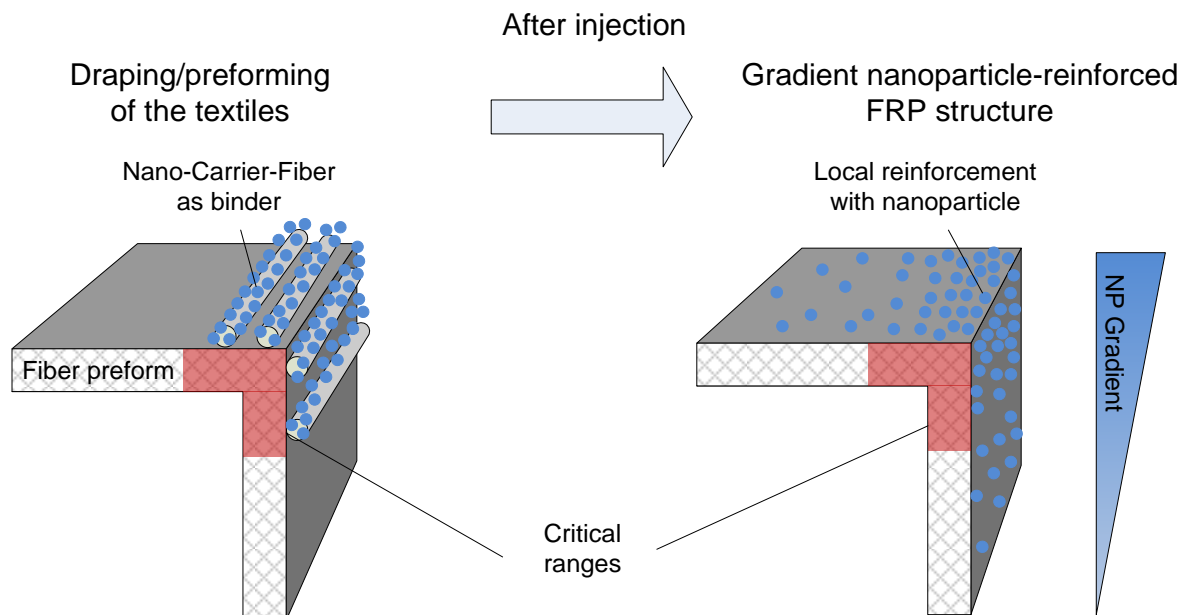


Figure 7.4: Locally modifying the FRP structures with the Nano-carrier-fiber

References:

- [1]. R. Lässig, et al., Series production of high-strength composites: Perspectives for the German engineering industry. 2012, Roland Berger Strategy Consultants.
- [2]. G. Ziegmann, M. Weinmann and D. Meiners, Trend report (Part 1): Fiber composite systems for lightweight construction. Zeitschrift Kunststofftechnik/ Journal of Plastics Technology, 2014. 2: p. 24-27.
- [3]. G. Ziegmann, M. Weinmann and D. Meiners, Trend report (Part 2): Fiber composite systems for lightweight construction. Zeitschrift Kunststofftechnik/ Journal of Plastics Technology, 2014. 4: p. 53-59.
- [4]. EADS Deutschland GmbH, The research requirements of the transport sectors to facilitate an increased usage of composite materials, part i: The composite material research requirements of the aerospace industry. 2004.
- [5]. E. Witten, T. Kraus and M. Kühnel, Composites Market Report 2015-Market developments, trends, outlook and challenges. 2015, Federation of Reinforced Plastics e.V. & Carbon Composites e.V.
- [6]. M. Onishi, Toray's business strategy for carbon fiber composite materials. 2012, Toray Industries, Inc.
- [7]. M. Kamiura, Toray's strategy for carbon fiber composite materials. 2008.
- [8]. M. G. Bader, Selection of composite materials and manufacturing routes for cost-effective performance. Composites Part a: Applied Science and Manufacturing, 2002. 33(7): p. 913-934.
- [9]. X. Chen, L. W. Taylor and L. J. Tsai, An overview on fabrication of three-dimensional woven textile preforms for composites, in Handbook of Technical Textiles (Second Edition). 2016, Woodhead Publishing: London. p. 285-304.
- [10]. V. Ogale and R. Alagirusamy, Textile preforms for advanced composites. Indian Journal of Fibre & Textile Research, 2004. 29(3): p. 366-375.
- [11]. G. A. Bibo and P. J. Hogg, The role of reinforcement architecture on impact damage mechanisms and post-impact compression behaviour. Journal of Materials Science, 1996. 31(5): p. 1115-1137.
- [12]. M. Wiedemann, CFK – Status der Anwendung und Produktionstechnik im Flugzeugbau, in Faszination Karosserie. 2009: Braunschweig. p. 12.
- [13]. M. Gagné and D. Theriault, Lightning strike protection of composites. Progress in Aerospace Sciences, 2014. 64: p. 1-16.
- [14]. A. Katunin, et al., Synthesis and characterization of the electrically conductive polymeric composite for lightning strike protection of aircraft structures. Composite Structures, 2017. 159: p. 773-783.
- [15]. D. Corporation, Lightning strike protection for carbon fiber aircraft. 2007.

- [16]. T. Mahrholz, J. Stangle and M. Sinapius, Quantitation of the reinforcement effect of silica nanoparticles in epoxy resins used in liquid composite moulding processes. *Composites Part a: Applied Science and Manufacturing*, 2009. 40(3): p. 235-243.
- [17]. S. Sprenger, Improving mechanical properties of fiber-reinforced composites based on epoxy resins containing industrial surface-modified silica nanoparticles: Review and outlook. *Journal of Composite Materials*, 2014. 49(1): p. 53-63.
- [18]. C. M. Manjunatha, A. Chandra and N. Jagannathan, Fracture and fatigue behavior of polymer Nanocomposites-A review. *Journal of the Indian Institute of Science*, 2015. 95(3): p. 249-266.
- [19]. J. Baur and E. Silverman, Challenges and opportunities in multifunctional nanocomposite structures for aerospace applications. *Mrs Bulletin*, 2007. 32(4): p. 328-334.
- [20]. L. Ye, et al., Functionalized composite structures for new generation airframes: A review. *Composites Science and Technology*, 2005. 65(9): p. 1436-1446.
- [21]. L. Sun, et al., Energy absorption capability of nanocomposites: A review. *Composites Science and Technology*, 2009. 69(14): p. 2392-2409.
- [22]. R. F. Gibson, A review of recent research on mechanics of multifunctional composite materials and structures. *Composite Structures*, 2010. 92(12): p. 2793-2810.
- [23]. Y. Tang, et al., Interlaminar fracture toughness and CAI strength of fibre-reinforced composites with nanoparticles – a review. *Composites Science and Technology*, 2013. 86: p. 26-37.
- [24]. G. Udupa, S. S. Rao and K. V. Gangadharan, Functionally graded composite materials: An overview. *Procedia Materials Science*, 2014. 5: p. 1291-1299.
- [25]. F. Tarlochan, Functionally graded material: A new breed of engineered material. *Journal of Applied Mechanical Engineering*, 2013. 02(02).
- [26]. R. M. Mahamood and E. T. A. Member. Functionally graded material: An overview. in *Proceedings of the World Congress on Engineering*. 2012. London, UK.
- [27]. K. Ghavami, C. de Souza Rodrigues and S. Paciornik, Bamboo: Functionally graded composite material. *Asian Journal of Civil Engineering (Building and Housing)*, 2003. 4(1): p. 1-10.
- [28]. A. K. Ray, et al., Bamboo—a functionally graded composite-correlation between microstructure and mechanical strength. *Journal of Materials Science*, 2005. 40(19): p. 5249-5253.
- [29]. T. Tan, et al., Mechanical properties of functionally graded hierarchical bamboo structures. *Acta Biomaterialia*, 2011. 7(10): p. 3796-3803.
- [30]. K. Ghavami, Bamboo as reinforcement in structural concrete elements. *Cement and Concrete Composites*, 2005. 27(6): p. 637-649.
- [31]. M. Koizumi and M. Niino, Overview of FGM research in japan. *Mrs Bulletin*, 1995. 20(1): p. 19-21.
- [32]. Intelligent production machines and systems : 2Nd I*PROMS Virtual Conference 3 - 14 July 2006. 2006. Amsterdam: Elsevier Science.
- [33]. B. Kieback, A. Neubrand and H. Riedel, Processing techniques for functionally graded materials. *Materials Science and Engineering: A*, 2003. 362(1-2): p. 81-106.
- [34]. J. J. Sobczak and L. Drenchev, Metallic functionally graded materials: A specific class of advanced composites. *Journal of Materials Science & Technology*, 2013. 29(4): p. 297-316.
- [35]. ASTM E2456 - 06(2012) Standard Terminology Relating to Nanotechnology. 2012.
- [36]. ISO/TS 27687:2008 Nanotechnologies -- Terminology and definitions for nano-objects -- Nanoparticle, nanofibre and nanoplate.
- [37]. European Commission: Recommendation on the definition of a nanomaterial. 2011.
- [38]. A. Maroudas and P. Eisenkla., Clarification of suspensions - a study of particle deposition in granular media .ii. A theory of clarification. *Chemical Engineering Science*, 1965. 20(10): p. 875-&.
- [39]. A. Maroudas and P. Eisenkla., Clarification of suspensions - a study of particle deposition in granular media .i. Some observations on particle deposition. *Chemical Engineering Science*, 1965. 20(10): p. 867-&.
- [40]. R. Sakthivadivel, Clogging of a granular porous medium by sediment. 1969, Berkeley: Hydraulic Engineering Laboratory, College of Engineering, University of California.
- [41]. E. F. Reia Da Costa, et al., RTM processing and electrical performance of carbon nanotube modified epoxy/fibre composites. *Composites Part a: Applied Science and Manufacturing*, 2012. 43(4): p. 593-602.
- [42]. J. J. Qiu, et al., Carbon nanotube integrated multifunctional multiscale composites. *Nanotechnology*, 2007. 18(27570827).
- [43]. F. H. Gojny, et al., Influence of nano-modification on the mechanical and electrical properties of conventional fibre-reinforced composites. *Composites Part a: Applied Science and Manufacturing*, 2005. 36(11): p. 1525-1535.
- [44]. S. S. Wicks, R. G. de Villoria and B. L. Wardle, Interlaminar and intralaminar reinforcement of composite laminates with aligned carbon nanotubes. *Composites Science and Technology*, 2010. 70(1): p. 20-28.

- [45]. H. Qian, et al., Carbon nanotube-based hierarchical composites: A review. *Journal of Materials Chemistry*, 2010. 20(23): p. 4751-4762.
- [46]. Y. Rachmadini, V. Tan and T. E. Tay, Enhancement of mechanical properties of composites through incorporation of CNT in VARTM - a review. *Journal of Reinforced Plastics and Composites*, 2010. 29(18): p. 2782-2807.
- [47]. M. Guo, et al., Simultaneously increasing the electrical conductivity and fracture toughness of carbon - fiber composites by using silver nanowires-loaded interleaves. *Composites Science and Technology*, 2014. 97: p. 27-33.
- [48]. M. Guo and X. Yi, The production of tough, electrically conductive carbon fiber composite laminates for use in airframes. *Carbon*, 2013. 58: p. 241-244.
- [49]. S. Sprenger, Epoxy resin composites with surface-modified silicon dioxide nanoparticles: A review. *Journal of Applied Polymer Science*, 2013. 130(3): p. 1421-1428.
- [50]. D. Pinto, et al., Mechanical properties of epoxy nanocomposites using alumina as reinforcement - a review. *Journal of Nano Research*, 2015. 30: p. 9-38.
- [51]. B. M. Louis, F. Klunker and P. A. Ermanni, Evaluation of nanoalumina and nanosilica particle toughened high glass-transition temperature epoxy for liquid composite molding processes. *Journal of Composite Materials*, 2016. 50(11): p. 1533-1545.
- [52]. Z. J. Wu, et al., Mechanical properties of epoxy resins reinforced with synthetic boehmite (AlOOH) nanosheets. *Journal of Applied Polymer Science*, 2015. 132(414095).
- [53]. W. Exner, et al., Nanoparticles with various surface modifications as functionalized cross-linking agents for composite resin materials. *Composites Science and Technology*, 2012. 72(10): p. 1153-1159.
- [54]. M. Jux, et al., Effects of Al(OH)O nanoparticle agglomerate size in epoxy resin on tension, bending, and fracture properties. *Journal of Nanoparticle Research*, 2017. 19(4).
- [55]. M. Ivankovic, et al., Curing kinetics and chemorheology of epoxy/anhydride system. *Journal of Applied Polymer Science*, 2003. 90(11): p. 3012-3019.
- [56]. C. Garschke, et al., Cure kinetics and viscosity modelling of a high-performance epoxy resin film. *Polymer Testing*, 2013. 32(1): p. 150-157.
- [57]. R. Hardis, et al., Cure kinetics characterization and monitoring of an epoxy resin using DSC, raman spectroscopy, and DEA. *Composites Part a: Applied Science and Manufacturing*, 2013. 49: p. 100-108.
- [58]. N. Rabearison, C. Jochum and J. C. Grandidier, A cure kinetics, diffusion controlled and temperature dependent, identification of the araldite LY556 epoxy. *Journal of Materials Science*, 2011. 46(3): p. 787-796.
- [59]. X. Huang and B. Patham, Experimental characterization of a curing thermoset Epoxy-Anhydride system—isothermal and nonisothermal cure kinetics. *Journal of Applied Polymer Science*, 2013. 127(3): p. 1959-1966.
- [60]. J. R. Baller, et al., Interactions between silica nanoparticles and an epoxy resin before and during network formation. *Polymer*, 2009. 50(14): p. 3211-3219.
- [61]. M. Harsch, J. Karger-Kocsis and M. Holst, Influence of fillers and additives on the cure kinetics of an Epoxy/Anhydride resin. *European Polymer Journal*, 2007. 43(4): p. 1168-1178.
- [62]. R. Sanctuary, et al., Influence of Al₂O₃ nanoparticles on the isothermal cure of an epoxy resin. *Journal of Physics-Condensed Matter*, 2009. 21(0351183).
- [63]. J. Baller, et al., The catalytic influence of alumina nanoparticles on epoxy curing. *Thermochimica Acta*, 2011. 517(1-2): p. 34-39.
- [64]. G. C. Huang and J. K. Lee, Isothermal cure characterization of fumed Silica/Epoxy nanocomposites: The glass transition temperature and conversion. *Composites Part a: Applied Science and Manufacturing*, 2010. 41(4): p. 473-479.
- [65]. A. Yousefi, P. G. Lafleur and R. Gauvin, Kinetic studies of thermoset cure reactions: A review. *Polymer Composites*, 1997. 18(2): p. 157-168.
- [66]. S. Vyazovkin, et al., ICTAC Kinetics Committee recommendations for performing kinetic computations on thermal analysis data. *Thermochimica Acta*, 2011. 520(1-2): p. 1-19.
- [67]. M. Yousefi, et al., Polymeric nanocomposite materials: Preparation and characterization of star-shaped PbS nanocrystals and their influence on the thermal stability of acrylonitrile - butadiene - styrene (ABS) copolymer. *Polyhedron*, 2011. 30(6): p. 1055-1060.
- [68]. M. Javdanitehran, et al., An iterative approach for isothermal curing kinetics modelling of an epoxy resin system. *Thermochimica Acta*, 2016. 623: p. 72-79.
- [69]. Ta-Instruments, A review of DSC kinetics methods. *Thermal Analysis & Rheology*, 2015(TA-073).
- [70]. ASTM E2070-13, Standard Test Method for Kinetic Parameters by Differential Scanning Calorimetry Using Isothermal Methods, ASTM International, West Conshohocken, PA, 2013, www.astm.org.

- [71]. J. Fournier, et al., Changes in molecular dynamics during bulk polymerization of an epoxide-amine system as studied by dielectric relaxation spectroscopy. *Macromolecules*, 1996. 29(22): p. 7097-7107.
- [72]. K. C. Cole, A new approach to modeling the cure kinetics of epoxy amine thermosetting resins .1. Mathematical development. *Macromolecules*, 1991. 24(11): p. 3093-3097.
- [73]. E. Rabinowitch, Collision, co-ordination, diffusion and reaction velocity in condensed systems. *Transactions of the Faraday Society*, 1937. 33(2): p. 1225-1232.
- [74]. P. J. Halley and M. E. Mackay, Chemorheology of thermosets—an overview. *Polymer Engineering & Science*, 1996. 36(5): p. 593-609.
- [75]. M. L. Williams, R. F. Landel and J. D. Ferry, Mechanical properties of substances of high molecular weight .19. The temperature dependence of relaxation mechanisms in amorphous polymers and other glass-forming liquids. *Journal of the American Chemical Society*, 1955. 77(14): p. 3701-3707.
- [76]. J. Mijovic and C. H. Lee, A comparison of chemorheological models for thermoset cure. *Journal of Applied Polymer Science*, 1989. 38(12): p. 2155-2170.
- [77]. J. M. Castro and C. W. Macosko, Studies of mold filling and curing in the reaction injection-molding process. *Aiche Journal*, 1982. 28(2): p. 250-260.
- [78]. H. Faria, F. M. A. Pires and A. T. Marques, Modeling the rheology of SR1500 and LY556 epoxies under manufacturer's recommended cure cycles after viscosimetry and rheometry characterization. *Polymer Engineering & Science*, 2014. 54(4): p. 831-839.
- [79]. A. Vanaerschot, et al., Experimentally validated stochastic geometry description for textile composite reinforcements. *Composites Science and Technology*, 2016. 122: p. 122-129.
- [80]. A. Vanaerschot, et al., Stochastic framework for quantifying the geometrical variability of laminated textile composites using micro-computed tomography. *Composites Part a: Applied Science and Manufacturing*, 2013. 44: p. 122-131.
- [81]. N. Vernet and F. Trochu, Analysis of mesoscopic pore size in 3D-interlock fabrics and validation of a predictive permeability model. *Journal of Reinforced Plastics and Composites*, 2016. 35(6): p. 471-486.
- [82]. M. Dickert, Einfluss von Binder auf die Herstellung von Faserkunststoffverbunden. 2015, Clausthal-Zellerfeld: Papierflieger Verlag GmbH.
- [83]. T. J. Vaughan and C. T. McCarthy, A combined experimental - numerical approach for generating statistically equivalent fibre distributions for high strength laminated composite materials. *Composites Science and Technology*, 2010. 70(2): p. 291-297.
- [84]. S. E. Wilding and D. T. Fullwood, Clustering metrics for two-phase composites. *Computational Materials Science*, 2011. 50(7): p. 2262-2272.
- [85]. S. Yang, A. Tewari and A. Gokhale, Modeling of non-uniform spatial arrangement of fibers in a ceramic matrix composite. *Acta Materialia*, 1997. 45(7): p. 3059-3069.
- [86]. B. Bonnard, P. Causse and F. Trochu, Experimental investigation of capillary flow porometry for characterization of dual scale porosity in fibrous reinforcements, in 13th International Conference on Flow Processing in Composite Materials (FPCM 13). 2016: Kyoto, Japan.
- [87]. B. Miller and I. Tyomkin, Liquid porosimetry - new methodology and applications. *Journal of Colloid and Interface Science*, 1994. 162(1): p. 163-170.
- [88]. H. Darcy, Les Fontaines publiques de la ville de Dijon ; Exposition et application des principes a suivre et des formules a employer dans les questions de distribution d'eau... 1856, Paris: V. Dalmont.
- [89]. S. Shahsavari and G. H. McKinley, Mobility and pore-scale fluid dynamics of rate-dependent yield-stress fluids flowing through fibrous porous media. *Journal of Non-Newtonian Fluid Mechanics*, 2016. 235: p. 76-82.
- [90]. V. Michaud, A review of non-saturated resin flow in liquid composite moulding processes. *Transport in Porous Media*, 2016. 115(3): p. 581-601.
- [91]. K. M. Pillai, Modeling the unsaturated flow in liquid composite molding processes: A review and some thoughts. *Journal of Composite Materials*, 2004. 38(23): p. 2097-2118.
- [92]. P. Ferland, D. Guittard and F. Trochu, Concurrent methods for permeability measurement in resin transfer molding. *Polymer Composites*, 1996. 17(1): p. 149-158.
- [93]. N. Vernet, et al., Experimental determination of the permeability of engineering textiles: Benchmark II. *Composites Part a: Applied Science and Manufacturing*, 2014. 61: p. 172-184.
- [94]. J. R. Weitzenb Ck, R. A. Shenoi and P. A. Wilson, Radial flow permeability measurement. Part a: Theory. *Composites Part a: Applied Science and Manufacturing*, 1999. 30(6): p. 781-796.
- [95]. A. W. Chan and S. Hwang, Anisotropic in-plane permeability of fabric media. *Polymer Engineering & Science*, 1991. 31(16): p. 1233-1239.
- [96]. K. L. Adams, W. B. Russel and L. Rebenfeld, Radial penetration of a viscous liquid into a planar anisotropic porous medium. *International Journal of Multiphase Flow*, 1988. 14(2): p. 203-215.

- [97]. E. Fauster, et al., Image processing and data evaluation algorithms for reproducible optical in-plane permeability characterization by radial flow experiments. *Journal of Composite Materials*, 2018(In revision).
- [98]. J. R. Weitzenboeck, R. A. Sheno and P. A. Wilson, Measurement of three-dimensional permeability. *Composites Part a: Applied Science and Manufacturing*, 1998. 29(1-2): p. 159-169.
- [99]. P. C. Carman, Fluid flow through granular beds. *Chemical Engineering Research & Design*, 1997. 75S: p. S32-S48.
- [100]. J. Dvorkin, Kozeny-Carman equation revisited. 2009.
- [101]. B. R. Gebart, Permeability of unidirectional reinforcements for RTM. *Journal of Composite Materials*, 1992. 26(8): p. 1100-1133.
- [102]. S. Sharma and D. A. Siginer, Permeability measurement methods in porous media of fiber reinforced composites. *Applied Mechanics Reviews*, 2010. 63.
- [103]. A. Szymkiewicz, Modelling water flow in unsaturated porous media accounting for nonlinear permeability and material heterogeneity. 2013, Springer: Berlin.
- [104]. P. Knabner and L. Angermann, Numerik partieller differentialgleichungen : Eine anwendungsorientierte einfu"hrung. 2000, Berlin [u.a.]: Springer.
- [105]. G. Dagan, U. Hornung and P. Knabner, Mathematical modeling for flow and transport through porous media. 1991.
- [106]. L. A. Richards, Capillary conduction of liquids through porous mediums. *Physics-A Journal of General and Applied Physics*, 1931. 1(1): p. 318-333.
- [107]. M. T. Vangenuchten, A closed-form equation for predicting the hydraulic conductivity of unsaturated soils. *Soil Science Society of America Journal*, 1980. 44(5): p. 892-898.
- [108]. R. H. Brooks and A. T. Corey, Properties of porous media affecting fluid flow. 1965, <Colo.: Colorado Agricultural Experiment Station.
- [109]. F. Klunker, et al., Modelling the resin infusion process. Part I: Flow modelling and numerical investigation for constant geometries. *Journal of Plastics Technology*, 2011. 5(7): p. 179-201.
- [110]. F. Klunker, et al., Modelling the resin infusion process. Part II: Accounting for deformation of textiles by analogy to thermomechanical models. *Journal of Plastics Technology*, 2011. 2(8): p. 179-205.
- [111]. F. Klunker, Aspekte zur Modellierung und Simulation des Vacuum Assisted Resin Infusion. 2008, Clausthal-Zellerfeld: Papierflieger Verlag GmbH.
- [112]. L. Gasc N, et al., Numerical prediction of saturation in dual scale fibrous reinforcements during liquid composite molding. *Composites Part a: Applied Science and Manufacturing*, 2015. 77: p. 275-284.
- [113]. H. Grössing, et al., Flow front advancement during composite processing: Predictions from numerical filling simulation tools in comparison with real-world experiments. *Polymer Composites*, 2016. 37(9): p. 2782-2793.
- [114]. C. H. Park and W. I. Lee, Modeling void formation and unsaturated flow in liquid composite molding processes: A survey and review. *Journal of Reinforced Plastics and Composites*, 2011. 30(11SI): p. 957-977.
- [115]. M. V. Bruschke and S. G. Advani, A finite element/control volume approach to mold filling in anisotropic porous media. *Polymer Composites*, 1990. 11(6): p. 398-405.
- [116]. A. Shojaei and S. R. Ghaffarian, Modeling and simulation approaches in the resin transfer molding process: A review. *Polymer Composites*, 2003. 24(4): p. 525-544.
- [117]. M. Erdal, S. I. Guceri and S. C. Danforth, Impregnation molding of Particle-Filled preceramic polymers: Process modeling. *Journal of the American Ceramic Society*, 1999. 82(8): p. 2017-2028.
- [118]. D. Lefevre, et al., Modelling the flow of Particle-Filled resin through a fibrous preform in liquid composite molding technologies. *Composites Part a: Applied Science and Manufacturing*, 2007. 38(10): p. 2154-2163.
- [119]. D. Lefevre, et al., Coupling filtration and flow during liquid composite molding: Experimental investigation and simulation. *Composites Science and Technology*, 2009. 69(13): p. 2127-2134.
- [120]. E. F. Reia Da Costa and A. A. Skordos, Modelling flow and filtration in liquid composite moulding of nanoparticle loaded thermosets. *Composites Science and Technology*, 2012. 72(7): p. 799-805.
- [121]. H. Haji, A. Saouab and Y. Nawab, Simulation of coupling filtration and flow in a dual scale fibrous media. *Composites Part a: Applied Science and Manufacturing*, 2015. 76: p. 272-280.
- [122]. D. Abliz, et al., Low-energy electron beam cured tape placement for out-of-autoclave fabrication of advanced polymer composites. *Composites Part a: Applied Science and Manufacturing*, 2014. 65: p. 73-82.
- [123]. Y. G. Duan, et al., Effects of compaction and UV exposure on performance of acrylate/glass-fiber composites cured layer by layer. *Journal of Applied Polymer Science*, 2012. 123(6): p. 3799-3805.
- [124]. Y. Duan, et al., Fabrication and mechanical properties of UV-curable glass fiber-reinforced polymer-matrix composite. *Journal of Composite Materials*, 2010. 45: p. 565.
- [125]. A. Endruweit, M. S. Johnson and A. C. Long, Curing of composite components by ultraviolet radiation: A review. *Polymer Composites*, 2006. 27(2): p. 119-128.

- [126]. D. Abliz, et al., Curing Methods for Advanced Polymer Composites - a Review. *Polymers & Polymer Composites*, 2013. 21(6): p. 341-348.
- [127]. A. Keller, et al., Fast-Curing epoxy polymers with silica nanoparticles: Properties and Rheo-Kinetic modelling. *Journal of Materials Science*, 2016. 51(1): p. 236-251.
- [128]. S. Duwe, et al., A detailed thermal analysis of nanocomposites filled with SiO₂, AlN or boehmite at varied contents and a review of selected rules of mixture. *Composites Science and Technology*, 2012. 72(12): p. 1324-1330.
- [129]. S. Nakouzi, et al., Curing simulation of composites coupled with infrared heating. *International Journal of Material Forming*, 2010. 3(0): p. 587-590.
- [130]. A. Shojaei, S. Reza Ghaffarian and S. Mohammad Hossein Karimian, Three-dimensional process cycle simulation of composite parts manufactured by resin transfer molding. *Composite Structures*, 2004. 65(3 - 4): p. 381-390.
- [131]. J. H. Oh and D. G. Lee, Cure cycle for thick glass/epoxy composite laminates. *Journal of Composite Materials*, 2002. 36(1): p. 19-45.
- [132]. F. Klunker, M. Voigt and W. Wu, Composites in automotive applications: Simulation of leaf spring processing, in SAMPE. 2010: Seattle, WA.
- [133]. T. H. Hsieh, et al., The mechanisms and mechanics of the toughening of epoxy polymers modified with silica nanoparticles. *Polymer*, 2010. 51(26): p. 6284-6294.
- [134]. M. Jux, T. Mahrholz and M. Sinapius, Effect of agglomerate size, mass fraction and surface modification on the mechanical properties of epoxy/nano-boehmite carbon fiber composites, in 20th International Conference on Composite Structures (ICCS20). 2017: Paris, France.
- [135]. F. Inam, et al., Effects of dispersion surfactants on the properties of ceramic-carbon nanotube (CNT) nanocomposites. *Ceramics International*, 2014. 40(1A): p. 511-516.
- [136]. M. Shaffer and A. H. Windle, Fabrication and characterization of carbon nanotube/poly(vinyl alcohol) composites. *Advanced Materials*, 1999. 11(11): p. 937-+.
- [137]. D. Abliz, et al., Effect of CNT concentration on mechanical properties of composites manufactured by compression resin transfer molding (CRTM), in ECCM16 - 16th European Conference on Composite Materials. 2014: Seville, Spain.
- [138]. L. Mao, Investigation of Carbon Nanotube (CNT) filtering effect by in-plane and out-of-plane impregnation Liquid Composite Molding (LCM) process. 2016, TU Clausthal.
- [139]. S. Cheng, Handbook of thermal analysis and calorimetry: Vol. 3, applications to polymers and plastics. Vol. 407. 2002, Amsterdam; London: Elsevier. 121-123.
- [140]. P. I. Karkanis, I. K. Partridge and D. Attwood, Modelling the cure of a commercial epoxy resin for applications in resin transfer moulding. *Polymer International*, 1996. 41(2): p. 183-191.
- [141]. ASTM E2041-13e1, Standard Test Method for Estimating Kinetic Parameters by Differential Scanning Calorimeter Using the Borchardt and Daniels Method, ASTM International, West Conshohocken, PA, 2013, www.astm.org.
- [142]. ASTM E2890-12, Standard Test Method for Kinetic Parameters for Thermally Unstable Materials by Differential Scanning Calorimetry Using the Kissinger Method, ASTM International, West Conshohocken, PA, 2012, www.astm.org.
- [143]. ASTM E698-16, Standard Test Method for Kinetic Parameters for Thermally Unstable Materials Using Differential Scanning Calorimetry and the Flynn/Wall/Ozawa Method, ASTM International, West Conshohocken, PA, 2016, www.astm.org.
- [144]. H. L. Friedman, Kinetics of thermal degradation of char-forming plastics from thermogravimetry. Application to a phenolic plastic. *Journal of Polymer Science Part C: Polymer Symposia*, 1964. 6(1): p. 183-195.
- [145]. T. Ozawa, A new method of analyzing thermogravimetric data. *Bulletin of the Chemical Society of Japan*, 1965. 38(11): p. 1881-1886.
- [146]. E. Duemichen, et al., Analyzing the network formation and curing kinetics of epoxy resins by in situ near-infrared measurements with variable heating rates. *Thermochimica Acta*, 2015. 616: p. 49-60.
- [147]. A. T. Dibenedetto, Prediction of the glass-transition temperature of polymers - a model based on the principle of corresponding states. *Journal of Polymer Science Part B-Polymer Physics*, 1987. 25(9): p. 1949-1969.
- [148]. O. Georjon, J. Galy and J. P. Pascault, Isothermal curing of an uncatalyzed dicyanate ester monomer - kinetics and modeling. *Journal of Applied Polymer Science*, 1993. 49(8): p. 1441-1452.
- [149]. J. P. Pascault and R. Williams, Glass-Transition temperature versus conversion relationships for thermosetting polymers. *Journal of Polymer Science Part B-Polymer Physics*, 1990. 28(1): p. 85-95.
- [150]. C. M. D. Hickey and S. Bickerton, Cure kinetics and rheology characterisation and modelling of ambient temperature curing epoxy resins for resin infusion/VARTM and wet layup applications. *Journal of Materials Science*, 2013. 48(2): p. 690-701.

- [151]. DIN EN 2564:1998, Aerospace series - Carbon fibre laminates - Determination of the fibre-, resin- and void contents.
- [152]. DIN EN ISO 1172 -1998: Textile-glass-reinforced plastics -- Prepregs, moulding compounds and laminates -- Determination of the textile-glass and mineral-filler content -- Calcination methods.
- [153]. N. Sematech, E-Handbook of Statistical Methods (<http://www.itl.nist.gov/div898/handbook/>). 2015.
- [154]. A. Santos and P. H. L. Barros, Multiple particle retention mechanisms during filtration in porous media. *Environmental Science & Technology*, 2010. 44(7): p. 2515-2521.
- [155]. H. Fallah, H. B. Fathi and H. Mohammadi, The mathematical model for particle suspension flow through porous medium. *Geomaterials*, 2012. 02(03): p. 57-62.
- [156]. P. Xu and B. Yu, Developing a new form of permeability and Kozeny-Carman constant for homogeneous porous media by means of fractal geometry. *Advances in Water Resources*, 2008. 31(1): p. 74-81.
- [157]. H. S. Sas and M. Erdal, Modeling of particle - resin suspension impregnation in compression resin transfer molding of Particle-Filled, continuous fiber reinforced composites. *Heat and Mass Transfer*, 2014. 50(3): p. 397-414.
- [158]. E. Olsson and G. Kreiss, A conservative level set method for two phase flow. *Journal of Computational Physics*, 2005. 210(1): p. 225-246.
- [159]. E. Olsson, G. Kreiss and S. Zahedi, A conservative level set method for two phase flow II. *Journal of Computational Physics*, 2007. 225(1): p. 785-807.
- [160]. Y. C. Changa, et al., A level set formulation of eulerian interface capturing methods for incompressible fluid flows. *Journal of Computational Physics*, 1996. 124(2): p. 449-464.
- [161]. R. Gantois, et al., Mold filling simulation of resin transfer molding combining BEM and level set method. *Applied Mechanics and Materials*, 2011. 62: p. 57-65.
- [162]. M. Ismail, Level set and phase field methods: Application to moving interfaces and two-phase fluid flows.
- [163]. RTM-Worx FEM/CV flow simulation software.
- [164]. OpenFOAM: The open source CFD toolbox.
- [165]. MyRTM - Software for simulating the RTM process.
- [166]. G. Barandun, M. Henne and E. Giger, MyRTM: An Approach for the simulation of resin transfer moulding (RTM) processes based on cellular automata, in 6th European Congress on Computational Methods in Applied Sciences and Engineering (ECCOMAS 2012). 2012: Vienna, Austria.
- [167]. AITM 1-0005 / EN 6033 Fibre reinforced plastics - Determination of interlaminar fracture toughness energy - Mode I - Gic.
- [168]. AITM 1-0006 / EN 6034 Fibre reinforced plastics - Determination of interlaminar fracture toughness energy - Mode II - GIIC.
- [169]. DIN EN ISO 14125 Fibre-reinforced plastic composites: Determination of flexural properties.
- [170]. DIN EN ISO 14130 Fibre-reinforced plastic composites -- Determination of apparent interlaminar shear strength by short-beam method.
- [171]. ASTM D257-14, Standard Test Methods for DC Resistance or Conductance of Insulating Materials, ASTM International, West Conshohocken, PA, 2014, www.astm.org.
- [172]. S. Krämer, S. Rothe and S. Hartmann, Homogeneous stress - strain states computed by 3D-stress algorithms of FE-codes: Application to material parameter identification. *Engineering with Computers*, 2015. 31(1): p. 141-159.
- [173]. P. Spitzer, C. Zierhofer and E. Hochmair, Algorithm for multi-curve-fitting with shared parameters and a possible application in evoked compound action potential measurements. *Biomedical Engineering Online*, 2006. 5(13): p. 13-13.
- [174]. G. Hülster, Reaktionskinetik von Verbundmörtelsystemen für tragende Anwendungen im Bauwesen. *Journal of Plastics Technology*, 2010. 3(6).
- [175]. B. Wetzels, et al., Epoxy nanocomposites - fracture and toughening mechanisms. *Engineering Fracture Mechanics*, 2006. 73(16): p. 2375-2398.
- [176]. A. Jumahat, et al., Effect of silica nanoparticles on compressive properties of an epoxy polymer. *Journal of Materials Science*, 2010. 45(21): p. 5973-5983.
- [177]. S. Liu, et al., Epoxy resin filled with high volume content Nano-SiO₂ particles. *Journal of Nanoscience and Nanotechnology*, 2009. 9(2SI): p. 1412-1417.
- [178]. G. M. Odegard, T. C. Clancy and T. S. Gates, Modeling of the mechanical properties of nanoparticle/polymer composites. *Polymer*, 2005. 46(2): p. 553-562.
- [179]. J. M. Balvers, Determination of cure dependent properties for curing simulation of Thick-Walled composites. 2008: p. 1.
- [180]. Y. Zhang, Fabrication of carbon nanoparticle/epoxy/fiber textile hybrid composites by double vacuum assisted resin infusion (DVARI) process. 2014, TU Clausthal.

- [181]. H. Walter, Morphologie-Zähigkeits-Korrelationen von modifizierten Epoxidharzsystemen mittels bruchmechanischer Prüfmethoden an Miniaturprüfkörpern. 2003, Martin-Luther-Universität Halle-Wittenberg: Halle.
- [182]. Y. L. Liang and R. A. Pearson, Toughening mechanisms in epoxy – silica nanocomposites (ESNs). *Polymer*, 2009. 50(20): p. 4895-4905.
- [183]. B. B. Johnsen, et al., Toughening mechanisms of nanoparticle-modified epoxy polymers. *Polymer*, 2007. 48(2): p. 530-541.
- [184]. B. Wang, X. Zhou and K. Ma, Fabrication and properties of CNTs/carbon fabric hybrid multiscale composites processed via resin transfer molding technique. *Composites Part B: Engineering*, 2013. 46: p. 123-129.
- [185]. P. C. Ma, et al., Dispersion and functionalization of carbon nanotubes for polymer-based nanocomposites: A review. *Composites Part a: Applied Science and Manufacturing*, 2010. 41(10): p. 1345-1367.
- [186]. P. C. Ma, B. Z. Tang and J. K. Kim, Effect of CNT decoration with silver nanoparticles on electrical conductivity of CNT-polymer composites. *Carbon*, 2008. 46(11): p. 1497-1505.
- [187]. P. C. Ma, J. K. Kim and B. Z. Tang, Effects of silane functionalization on the properties of carbon nanotube/epoxy nanocomposites. *Composites Science and Technology*, 2007. 67(14): p. 2965-2972.
- [188]. A. Allaoui and N. El Bounia, How carbon nanotubes affect the cure kinetics and glass transition temperature of their epoxy composites? – a review. *Express Polymer Letters*, 2009. 3(9): p. 588-594.
- [189]. R. Kaps, Kombinierte Prepreg- und Infusionstechnologie für integrale Faserverbundstrukturen. 2010, Braunschweig: Deutsches Zentrum für Luft- und Raumfahrt e.V.

Appendix: Material datasheets

TECHNISCHES DATENBLATT



Artikel: Style 796
Einstellung [Fd./cm]: 6,5/3,0
Bindung: Leinwand
Ausrüstung: stuhrohr

Konstruktion:	Kette	Schuss
Material:	Carbon	Glas
Feinheit:	400 tex	34 tex

Technische Daten		Einheit	Sollwert	+/-	Toleranz
Dichte ^{1) 3)}	Kette	g/cm³	n.G.	+/-	n.G.
	Schuss	g/cm³	n.G.	+/-	n.G.
Feinheit ¹⁾	Kette	tex	400	+/-	20
	Schuss	tex	34	+/-	2
Drehung ¹⁾	Kette	T/m		+/-	
	Schuss	T/m		+/-	
Einstellung	Kette	Fd./10cm	6,5	+/-	0,3
	Schuss	Fd./10cm	3,0	+/-	0,2
Flächengewicht		g/m²	270	+/-	10
Trockengewicht		g/m²		+/-	
Feuchtegehalt		%			
Dicke ²⁾		mm	0,35	+/-	0,05
Breite		cm	nach Bestellung	+/-	1

1) oder n.G.: nach Bestellung und jeweiliger Garnspezifikation

2) Richtwert, nicht freigaberelevant

3) wird nicht geprüft, Angabe des Garnherstellers

Bemerkung:

Die aufgeführten Werte beschreiben den Ausfall des Gewebes aus einem begrenzten Produktionszeitraum.

Datum 01.04.2014	QM Sybille Büscher	Dieses Datenblatt unterliegt nicht dem Änderungsdienst
----------------------------	------------------------------	---

Technisches Datenblatt
HP-U400E



Produktkennung

Artikelnummer:	HP-U400E
Bezeichnung:	Unidirektional-Glas-Gelege
Faserausrichtung:	0°

Technische Spezifikation

Konstruktion	Flächengewicht [g/m²]	Toleranz [± %]	Material
0°	402	5	E-Glas
-45°		5	E-Glas
90°	40	5	E-Glas
+45°		5	E-Glas
CSM		5	E-Glas
Nähfaden	15	5	PES
Gesamtflächengewicht	457	5	g/m²
Nähbindung	Trikot		
Nähfeinheit	10		

Aufmachung

Länge:	50	lfm	± 2%
Breite:	127	cm	± 2%

Verpackung

Hülsendurchmesser:	76	mm	innen
Folie:	LDPE	transparent	

Die Angaben in diesem Produktdatenblatt wurden nach bestem Wissen zusammengestellt und entsprechen unserem derzeitigen Erkenntnisstand. Eine Verbindlichkeit kann hieraus jedoch nicht abgeleitet werden.

Advanced Materials

Araldite® LY 556* / Aradur® 917* / Accelerator DY 070*

HOT CURING EPOXY MATRIX SYSTEM

Araldite® LY 556 is an epoxy resin
 Aradur® 917 is an anhydride hardener
 Accelerator DY 070 is an imidazole accelerator

APPLICATIONS	High performance composite parts		
PROPERTIES	Anhydride-cured, low-viscosity standard matrix system with extremely long pot life. The reactivity of the system is adjustable by variation of the accelerator content. The system is easy to process, has good fibre impregnation properties and exhibits excellent mechanical, dynamic and thermal properties. It has an excellent chemical resistance especially to acids at temperatures up to 80 °C. This epoxy system fulfills MIL specifications R 9300.		
PROCESSING	Filament Winding Pultrusion Pressure Moulding		
KEY DATA	Araldite® LY 556		
	Aspect (visual)	clear, pale yellow liquid	
	Colour (Gardner, ISO 4630)	≤ 2	
	Epoxy content (ISO 3000)	5.30 - 5.45	[eq/kg]
	Viscosity at 25 °C (ISO 12058-1)	10000 - 12000	[mPa s]
	Density at 25 °C (ISO 1675)	1.15 - 1.20	[g/cm ³]
	Flash point (ISO 2719)	> 200	[°C]
	Aradur® 917		
	Aspect (visual)	clear liquid	
	Colour (Gardner, ISO 4630)	≤ 2	
	Viscosity at 25 °C (ISO 12058-1)	50 - 100	[mPa s]
	Density at 25 °C (ISO 1675)	1.20 - 1.25	[g/cm ³]
	Flash point (ISO 2719)	195	[°C]
	Accelerator DY 070		
	Aspect (visual)	clear liquid	
	Colour (Gardner, ISO 4630)	≤ 9	
	Viscosity at 25 °C (ISO 12058-1)	≤ 50	[mPa s]
	Density at 25 °C (ISO 1675)	0.95 - 1.05	[g/cm ³]
	Flash point (ISO 2719)	92	[°C]
	Storage temperature (see expiry date on original container)	2 - 40 °C	[°C]

* In addition to the brand name product denomination may show different appendices, which allows us to differentiate between our production sites: e.g., BD = Germany, US = United States, IN = India, CI = China, etc.. These appendices are in use on packaging, transport and invoicing documents. Generally the same specifications apply for all versions. Please address any additional need for clarification to the appropriate Huntsman contact

STORAGE	<p>Provided that Araldite® LY 556, Aradur® 917 and Accelerator DY 070 are stored in a dry place in their original, properly closed containers at the above mentioned storage temperatures they will have the shelf lives indicated on the labels. Partly emptied containers should be closed immediately after use. Because Aradur® 917 is sensitive to moisture, storage containers should be ventilated with dry air only. Araldite® LY 556 which has crystallized and looks cloudy can be restored to its original state by heating to 60 - 80 °C.</p>
----------------	---

PROCESSING DATA

MIX RATIO	<i>Components</i>	<i>Parts by weight</i>	<i>Parts by volume</i>
	Araldite® LY 556	100	100
	Aradur® 917	90	86
	Accelerator DY 070	0.5 - 2	0.6 - 2.4

We recommend that the components are weighed with an accurate balance to prevent mixing inaccuracies which can affect the properties of the matrix system. The components should be mixed thoroughly to ensure homogeneity. It is important that the side and the bottom of the vessel are incorporated into the mixing process. When processing large quantities of mixture the pot life will decrease due to exothermic reaction. It is advisable to divide large mixes into several smaller containers.

PROCESSING RECOMMENDATIONS	<p>To simplify the mixing process the resin can be preheated to about 30 °C to 50 °C before adding the cold hardener. Hardener and accelerator can be premixed, thus allowing the use of two component mixing/metering equipment. The mix of hardener and accelerator has a shelf life of several days.</p> <p>The processing of the system at elevated temperatures of 30 °C to 40 °C shows the best results. The gelation temperature should not be higher than absolutely necessary. A high gelation temperature induces high shrinkage and generates internal stresses.</p>
-----------------------------------	---

INITIAL MIX VISCOSITY (HOEPPLER, ISO 12058-1B)	[°C]	[mPa s]
	at 25	600 - 900
	at 40	200 - 300
	at 60	< 75

VISCOSITY BUILD-UP (HOEPPLER, ISO 12058-1B)	<i>Components [pbw]</i>	<i>System 1</i>	<i>System 2</i>	<i>System 3</i>
	Araldite® LY 556	100	100	100
	Aradur® 917	90	90	90
	Accelerator DY 070	0.5	1	2

	[°C]	[mPa s]			
	at 25	to 1500	[h]	10 - 12	3.5 - 4.5
		to 3000	[h]	33 - 37	16 - 18
	at 40	to 1500	[h]	19 - 21	7 - 8
		to 3000	[h]	23 - 26	9 - 10
	at 80	to 1500	[min]	95 - 105	52 - 57
		to 3000	[min]	105 - 115	60 - 65
	at 90	to 1500	[min]		32 - 35
		to 3000	[min]		35 - 38
					14 - 16
					15 - 17

POT LIFE	[°C]		<i>System 1</i>	<i>System 2</i>	<i>System 3</i>
(TECAM, 65 % RH, 100 G)	at 23	[h]	165 - 175	95 - 105	48 - 54
10 KG METAL CONTAINER	at 40	[h]	5 - 7	4 - 5	-

GEL TIME (HOT PLATE)	[°C]		<i>System 1</i>	<i>System 2</i>	<i>System 3</i>
	at 80	[min]	230 - 270	140 - 160	65 - 75
	at 100	[min]	65 - 75	35 - 45	18 - 22
	at 120	[min]	21 - 25	10 - 12	5 - 7
	at 140	[min]	7 - 9	3 - 5	1 - 3
	at 160	[min]	2 - 4	1 - 2	-

The values shown are for small amounts of pure resin/hardener mix. In composite structures the gel time can differ significantly from the given values depending on the fibre content and the laminate thickness.

TYPICAL CURE CYCLES	Gelation either	2 - 4 h at 80 °C
	or	1 - 3 h at 90 °C
	Post-cure either	4 - 8 h at 120 °C
	or	2 - 8 h at 140 °C
	or	2 - 8 h at 160 °C

Cure temperatures in excess of about 130 °C cause brown discolouration but do not impair the properties of the product.

PROPERTIES OF THE CURED, NEAT FORMULATION

Unless otherwise stated, the processing schedule for the samples tested was gelation for 4 hours at 80 °C and post-cured for 8 hours at 140 °C.

GLASS TRANSITION TEMPERATURE (T_g) (IEC 1006, 10 K/MIN)	<i>Cure:</i>	T_g DSC [°C]	T_g TMA [°C]
	4 h 80 °C + 4 h 120 °C	140 - 144	125 - 128
	4 h 80 °C + 8 h 120 °C	144 - 148	125 - 128
	4 h 80 °C + 4 h 140 °C	145 - 150	130 - 135
	4 h 80 °C + 8 h 140 °C	148 - 153	135 - 145
	4 h 80 °C + 4 h 160 °C	150 - 155	140 - 145
	4 h 80 °C + 8 h 160 °C	150 - 155	140 - 145

TENSILE TEST (ISO 527)	Tensile strength	[MPa]	83 - 93
	Elongation at tensile strength	[%]	4.2 - 5.6
	Ultimate strength	[MPa]	80 - 90
	Ultimate elongation	[%]	5.0 - 7.0
	Tensile modulus	[MPa]	3100 - 3300

FLEXURAL TEST (ISO 178)	Flexural strength	[MPa]	125 - 135
	Deflection at maximum load	[mm]	10 - 18
	10 days in H ₂ O 23 °C	[MPa]	110 - 120
	Flexural strength	[mm]	8 - 18
	Deflection at maximum load		
	60 min in H ₂ O/100 °C		
	Flexural strength	[MPa]	125 - 135
	Deflection at maximum load	[mm]	10 - 18

FRACTURE PROPERTIES BEND NOTCH TEST (PM 258-0/90)	Fracture toughness K _{1C}	[MPa√m]	0.56 - 0.6
	Fracture energy G _{1C}	[J/m ²]	88 - 96

WATER ABSORPTION (ISO 62)	<i>Immersion:</i>		
	1 day H ₂ O 23 °C	[%]	0.10 - 0.15
	10 days H ₂ O 23 °C	[%]	0.30 - 0.40
	30 min H ₂ O 100 °C	[%]	0.10 - 0.15
	60 min H ₂ O 100 °C	[%]	0.15 - 0.20

COEFFICIENT OF LINEAR THERMAL EXPANSION (DIN 53 752)	<i>Mean value:</i>		
	α from 20 - 100 °C	[10 ⁻⁶ /K]	55 - 57
	α from 100 - 130 °C	[10 ⁻⁶ /K]	67 - 70

POISSON'S RATIO		[μ]	0.35
------------------------	--	-----------	------

PROPERTIES OF THE CURED, REINFORCED FORMULATION

Unless otherwise stated, the figures given are for pressed laminate samples comprising 16 layers (4 mm) of E-glass fabric 1:1, 280 - 300 g/m ² , fibre volume content 42 - 47 %.			
FLEXURAL TEST (ISO 178)	Flexural strength	[MPa]	520 - 550
	Deflection at maximum load	[mm]	5 - 6
	Flexural modulus	[MPa]	16500 - 16700
	10 days in H ₂ O 23 °C		
	Flexural strength	[MPa]	390 - 410
	Deflection at maximum load	[mm]	4 - 5
	60 min in H ₂ O/100 °C		
	Flexural strength	[MPa]	460 - 480
TENSILE TEST (ISO 3268 - 1978)	Deflection at maximum load	[mm]	5 - 6
	Tensile strength	[MPa]	345 - 375
	Ultimate elongation	[%]	1 - 2
INTERLAMINAR SHEAR STRENGTH (ASTM D 2344)	Tensile modulus	[MPa]	25500 - 26000
	Short beam: E-glass unidirectional specimen Laminate thickness t = 6.4 mm Fibre volume content: 60 %		
	Shear strength:	[MPa]	75 - 77
WATER ABSORPTION (ISO 62)	<i>Immersion:</i>		
	1 day H ₂ O 23 °C	[%]	0.15 - 0.20
	10 days H ₂ O 23 °C	[%]	0.25 - 0.30
	30 min H ₂ O 100 °C	[%]	0.01 - 0.05
	60 min H ₂ O 100 °C	[%]	0.03 - 0.07
TENSILE, COMPRESSIVE AND TORSIONAL TEST (TCT)	E-glass	Roving	E-glass roving, 1200 tex, silane finish
		Fibre volume content	67 %
		Gelation temperature	90 °C
		Post-cure	8 h at 140 °C
	Carbon HT	Roving	Carbon fibre high tensile, Torayca T 300 B - 6000 - 50 B
		Fibre volume content	64 %
		Gelation temperature	90 °C
		Post-cure	8 h at 140 °C
	Transverse tensile test		
			<i>E-Glass</i> <i>Carbon HT</i>
	Tensile strength	[MPa]	48 - 55 77 - 85
	Tensile strain	[%]	0.25 - 0.33 0.9 - 1.0
	Elastic modulus	[MPa]	18000 - 20000 9300 - 9900
	Transverse compressive test		
	Compressive strength	[MPa]	165 - 175 190 - 206
	Compressive strain at brak	[%]	1.2 - 1.4 2.7 - 3.4
	Elastic modulus	[MPa]	20000 - 22000 9700 - 9900
	Torsional test		
	Shear strength	[MPa]	77 - 82 76 - 80
	Shear angle	[%]	2.7 - 3.1 3.3 - 4.0
	Shear modulus	[MPa]	6100 - 7100 6000 - 6300

**HANDLING
PRECAUTIONS**

Personal hygiene

Safety precautions at workplace

protective clothing	yes
gloves	essential
arm protectors	recommended when skin contact likely
goggles/safety glasses	yes

Skin protection

before starting work	Apply barrier cream to exposed skin
after washing	Apply barrier or nourishing cream

Cleansing of contaminated skin

Dab off with absorbent paper, wash with warm water and alkali-free soap, then dry with disposable towels. Do not use solvents

Disposal of spillage

Soak up with sawdust or cotton waste and deposit in plastic-lined bin

Ventilation

of workshop	Renew air 3 to 5 times an hour
of workplaces	Exhaust fans. Operatives should avoid inhaling vapours

FIRST AID

Contamination of the eyes by resin, hardener or mix should be treated immediately by flushing with clean, running water for 10 to 15 minutes. A doctor should then be consulted.

Material smeared or splashed on the skin should be dabbed off, and the contaminated area then washed and treated with a cleansing cream (see above). A doctor should be consulted in the event of severe irritation or burns. Contaminated clothing should be changed immediately.

Anyone taken ill after *inhaling* vapours should be moved out of doors immediately.

In all cases of doubt call for medical assistance.

IMPORTANT LEGAL NOTICE

Huntsman Advanced Materials warrants only that its products meet the specifications agreed with the user. Typical properties, where stated, are to be considered as representative of current production and should not be treated as specifications.

The manufacture of materials is the subject of granted patents and patent applications; freedom to operate patented processes is not implied by this publication.

While all the information and recommendations in this publication are, to the best of Huntsman Advanced Material's knowledge, information and belief, accurate at the date of publication, NOTHING HEREIN IS TO BE CONSTRUED AS A WARRANTY, WHETHER EXPRESS OR IMPLIED, INCLUDING BUT WITHOUT LIMITATION, AS TO MERCHANTABILITY OR FITNESS FOR A PARTICULAR PURPOSE. IN ALL CASES, IT IS THE RESPONSIBILITY OF THE USER TO DETERMINE THE APPLICABILITY OF SUCH INFORMATION AND RECOMMENDATIONS AND THE SUITABILITY OF ANY PRODUCT FOR ITS OWN PARTICULAR PURPOSE.

The behaviour of the products referred to in this publication in manufacturing processes and their suitability in any given end-use environment are dependent upon various conditions such as chemical compatibility,

temperature, and other variables, which are not known to Huntsman Advanced Materials. It is the responsibility of the user to evaluate the manufacturing circumstances and the final product under actual end-use requirements and to adequately advise and warn purchasers and users thereof.

Products may be toxic and require special precautions in handling. The user should obtain Safety Data Sheets from Huntsman Advanced Materials containing detailed information on toxicity, together with proper shipping, handling and storage procedures, and should comply with all applicable safety and environmental standards.

Hazards, toxicity and behaviour of the products may differ when used with other materials and are dependent on manufacturing circumstances or other processes. Such hazards, toxicity and behaviour should be determined by the user and made known to handlers, processors and end users.

Except where explicitly agreed otherwise, the sale of products referred to in this publication is subject to the general terms and conditions of sale of Huntsman Advanced Materials LLC or of its affiliated companies including without limitation, Huntsman Advanced Materials (Europe) BVBA, Huntsman Advanced Materials Americas Inc., and Huntsman Advanced Materials (Hong Kong) Ltd.

Huntsman Advanced Materials is an international business unit of Huntsman Corporation. Huntsman Advanced Materials trades through Huntsman affiliated companies in different countries including but not limited to Huntsman Advanced Materials LLC in the USA and Huntsman Advanced Materials (Europe) BVBA in Europe.

Aradur and Araldite are registered trademarks of Huntsman Corporation or an affiliate thereof.

Copyright © 2007 Huntsman Corporation or an affiliate thereof. All rights reserved.

Main Office :
Huntsman Advanced Materials (Switzerland) GmbH
Klybeckstrasse 200
4057 BASEL
Switzerland
+41 61 966 3333

SASOL
reaching new frontiers



PRODUCTNAME	DISPERAL HP14
PRODUCTCODE	535120

NO TDS AVAILABLE

Chemical Marketing Concepts
coa@chemicalmarketing.nl
Waalkijk
Netherlands
coa@chemicalmarketing.nl

Brunsbüttel, 19.03.2014

CERTIFICATE OF ANALYSIS

**** INSPECTION CERTIFICATE DIN 50049-3.1 -- EN 10204-3.1 ****

Product: DISPERAL HP 14
Shipping advice on: 21,5 kg
Lot: 78774
Order-/Release-no: 25000, 25107
Delivery note: 1888569 from 18.03.2014 (Chemical Marketing Concepts Europe)

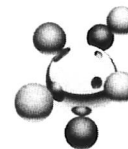
Analysis	Results
Surface area (550°C/3h) [m ² /g]	152
Solid-content [%]	79.0
Loose bulk density [g/ml]	0.40
Dispersibility (10%, 0.46%ige HNO ₃) [%]	98.4
Crystallite size (021) [Å]	142
Pore volume total (Hg) [ml/g]	1.080
Particle size: < 25 µm [%]	42.7
Particle size: < 45 µm [%]	78.6
Particle size: < 90 µm [%]	100.0

Sasol Germany GmbH
P.O. Box 1160
D-25534 Brunsbüttel
Phone: 0049(0)4852/392-0 Fax: 0049(0)4852/3285

Best regards
Works inspector
Michael Claußen

This document has been prepared by electronic data-processing and does not require a signature.

This certificate of analysis is for information only and does not guarantee any particular product properties. It does not free the recipient of the obligation to carry out a product receiving inspection. This certificate of analysis does not create claims of third parties to which it is passed on. All transactions are subject to our general Business Conditions as amended up to the time concerned.

**DISPERAL HP 14**

Version: 4.05

Revision Date 2011/11/21

1. IDENTIFICATION OF THE SUBSTANCE/MIXTURE AND OF THE COMPANY/UNDERTAKING

1.1 Product identifier

Trade name	DISPERAL HP 14
REACH No.	01-2119555298-28-0002
Substance name (REACH / CLP)	Boehmite (Al(OH)O)

1.2 Relevant identified uses of the substance or mixture and uses advised against

Use	industrial use base material for catalytic converters additive for viscosity adjustment flame retardant
Uses advised against	

1.3 Details of the supplier of the safety data sheet

Company	SASOL Germany GmbH Anckelmannsplatz 1 20537 Hamburg Telephone: +49 40 63684-1000 Telefax: +49 40 63684-3700
Information (Product safety):	Telephone: + 49 (0) 23 65 - 49 47 05 Telefax: + 49 (0) 23 65 - 49 92 40
E-mail:	msds-info.germany@de.sasol.com

1.4 Emergency telephone number

Emergency telephone number	+ 49 (0) 5 51 - 1 92 40
----------------------------	-------------------------

2. HAZARDS IDENTIFICATION

2.1 Classification of the substance or mixture**Classification (REGULATION (EC) No 1272/2008)**

Not a hazardous substance or mixture according to Regulation (EC) No. 1272/2008.

Classification (67/548/EEC, 1999/45/EC)

Not a hazardous substance or mixture according to EC-directives 67/548/EEC or 1999/45/EC.

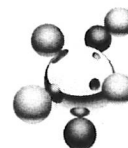
2.2 Label elements

Not a hazardous substance or mixture according to Regulation (EC) No. 1272/2008.

2.3 Other hazards

No hazards to be specially mentioned.

3. COMPOSITION/INFORMATION ON INGREDIENTS



DISPERAL HP 14

Version: 4.05

Revision Date 2011/11/21

This product is a substance in the meaning of regulation (EC) 1907/2006.

CHEMICAL CHARACTERIZATION

Boehmite (Al(OH)O)

component type: Active ingredient

EC-No.: 215-284-3

Index-No.:

CAS-No.: 1318-23-6

REACH No.: 01-2119555298-28-0002

Substance name (REACH / CLP): Boehmite (Al(OH)O)

COMPONENTS TO BE NAMED IN ACCORDANCE WITH REGULATION (EC) 1907/2006 AS WELL AS OTHER HAZARDOUS INGREDIENTS AND CONTAINED SUBSTANCES WITH WORK PLACE LIMIT VALUES

No dangerous ingredients according to Regulation (EC) No. 1907/2006

Other data

Synonyms: Aluminium hydroxide oxide; CAS-No.: 24623-77-6

4. FIRST AID MEASURES

4.1 Description of first aid measures

General advice	No hazards which require special first aid measures. If you feel unwell, seek medical advice (show the label where possible).
If inhaled	Provide fresh air.
In case of skin contact	Wash off with plenty of water. If skin irritation persists, call a physician.
In case of eye contact	Immediately flush eye(s) with plenty of water. If eye irritation persists, consult a specialist.
If swallowed	Consult a physician. Do not induce vomiting without medical advice. Never give anything by mouth to an unconscious person.

4.2 Most important symptoms and effects, both acute and delayed

Most important symptoms and effects, both acute and delayed	Symptoms: No information available. Risks: No information available.
---	---

4.3 Indication of any immediate medical attention and special treatment needed

Indication of any immediate medical attention and special treatment needed	Treatment: No information available.
--	--------------------------------------

5. FIREFIGHTING MEASURES

5.1 Extinguishing media

Suitable extinguishing media	Use extinguishing measures that are appropriate to local circumstances and the surrounding environment. Use extinguishing measures that are appropriate to local circumstances and the surrounding environment.
------------------------------	--

5.2 Special hazards arising from the substance or mixture

Specific hazards during firefighting	Not applicable.
--------------------------------------	-----------------

**DISPERAL HP 14**

Version: 4.05

Revision Date 2011/11/21

5.3 Advice for firefighters**Special protective equipment for firefighters**

Not applicable.

Further information

The product itself does not burn. Use extinguishing measures that are appropriate to local circumstances and the surrounding environment.

6. ACCIDENTAL RELEASE MEASURES**6.1 Personal precautions, protective equipment and emergency procedures****Personal precautions**

Avoid dust formation.

6.2 Environmental precautions**Environmental precautions**

Do not flush into surface water or sanitary sewer system.

6.3 Methods and materials for containment and cleaning up**Methods for cleaning up**

Use mechanical handling equipment. The material taken up must be disposed of in accordance with regulations.

6.4 Reference to other sections

Treat recovered material as described in the section "Disposal considerations".

7. HANDLING AND STORAGE**7.1 Precautions for safe handling****Advice on safe handling**

Avoid dust formation. Provide appropriate exhaust ventilation at places where dust is formed. Do not breathe vapours/dust.

Advice on protection against fire and explosion

Normal measures for preventive fire protection. The product is not flammable.

Temperature class

not applicable

Fire-fighting class

not applicable

Dust explosion class

no data available

7.2 Conditions for safe storage, including any incompatibilities**Requirements for storage areas and containers**

Keep tightly closed. Keep in a dry place.

Further information on storage conditions

none

Advice on common storage

No materials to be especially mentioned.

Storage classification (VCI system/Germany):

13; Non Combustible Solids

Other data

Stable under normal conditions.

7.3 Specific end uses**Specific use(s)**

This information is not available.

**DISPERAL HP 14**

Version: 4.05

Revision Date 2011/11/21

8. EXPOSURE CONTROLS/PERSONAL PROTECTION**8.1 Control parameters****COMPONENTS WITH WORKPLACE CONTROL PARAMETERS****NATIONAL OCCUPATIONAL EXPOSURE LIMITS**

Components	Typ	Control parameters	Update	Basis
ALUMINUM METAL AND INSOLUBLE COMPOUNDS, RESPIRABLE FRACTION	TWA	1 mg/m ³	2009	ACGIH

The maximum allowable workplace concentrations for respirable and inhalable dusts are to be observed.

no data available

The maximum allowable workplace concentrations for respirable and inhalable dusts are to be observed.

EUROPEAN OCCUPATIONAL EXPOSURE LIMITS

no data available The maximum allowable workplace concentrations for respirable and inhalable dusts are to be observed.

DERIVED NO EFFECT LEVEL (DNEL)**Boehmite (Al(OH)O)**

Workers, dermal, Acute/short-term exposure - systemic effects:

Not relevant / not applicable

Workers, Inhalation, Acute/short-term exposure - systemic effects:

Not relevant / not applicable

Workers, dermal, Acute/short-term exposure - local effects:

Not relevant / not applicable

Workers, Inhalation, Acute/short-term exposure - local effects:

Not relevant / not applicable

Workers, dermal, long-term exposure - systemic effects:

Not relevant / not applicable

Workers, Inhalation, long-term exposure - systemic effects:

Not relevant / not applicable

Workers, dermal, long-term exposure - local effects:

Not relevant / not applicable

Workers, Inhalation, long-term exposure - local effects:

Not relevant / not applicable

Consumers, dermal, Acute/short-term exposure - systemic effects:

Not relevant / not applicable

Consumers, Inhalation, Acute/short-term exposure - systemic effects:

Not relevant / not applicable

Consumers, Oral, Acute/short-term exposure - systemic effects:

Not relevant / not applicable

Consumers, dermal, Acute/short-term exposure - local effects:

Not relevant / not applicable

Consumers, Inhalation, Acute/short-term exposure - local effects:

Not relevant / not applicable

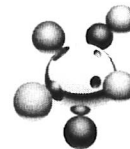
Consumers, dermal, long-term exposure - systemic effects:

Not relevant / not applicable

Consumers, Inhalation, long-term exposure - systemic effects:

Not relevant / not applicable

Consumers, Oral, long-term exposure - systemic effects:

**DISPERAL HP 14**

Version: 4.05

Revision Date 2011/11/21

Not relevant / not applicable

Consumers, dermal, long-term exposure - local effects:
Not relevant / not applicableConsumers, Inhalation, long-term exposure - local effects:
Not relevant / not applicable**PREDICTED NO EFFECT CONCENTRATION (PNEC)****Boehmite (Al(OH)O)**Fresh water:
Not relevant / not applicableMarine water:
Not relevant / not applicableintermittent release:
Not relevant / not applicabletreatment plant:
Not relevant / not applicableFresh water sediment:
Not relevant / not applicableMarine sediment:
Not relevant / not applicableSoil:
Not relevant / not applicablefood:
Not relevant / not applicable**8.2 Exposure controls****ENGINEERING MEASURES**

In case of dust being formed, provide for adequate extraction.

Provide sufficient air exchange and/or exhaust in work rooms.

PERSONAL PROTECTIVE EQUIPMENT**Respiratory protection**

No personal respiratory protective equipment normally required. In inadequately ventilated areas, where workplace limits are exceeded, where unpleasant odours exist or where dust, fibres and smoke occur, use self-contained breathing apparatus or breathing apparatus with a type P2 or P3 filter, in compliance with EN 143.

Hand protection

Coordinate hand protection with other chemicals used. Preventive hand protection is recommended. Use barrier cream regularly.

Eye protection

Safety glasses

Hygiene measures

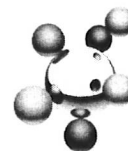
Handle in accordance with good industrial hygiene and safety practice.

Protective measures

Avoid contact with the skin and the eyes.

ENVIRONMENTAL EXPOSURE CONTROLS**General advice**

Do not flush into surface water or sanitary sewer system.



DISPERAL HP 14

Version: 4.05

Revision Date 2011/11/21

9. PHYSICAL AND CHEMICAL PROPERTIES

9.1 Information on basic physical and chemical properties

Physical state	solid; 20 °C; 1,013 hPa
Form	powder
Colour	white
Odour	odourless
Odour Threshold	no data available
pH	ca. 6 - 9; 100 g/l
Melting point/range	2,054 °C
Boiling point/boiling range	Not relevant / not applicable Justification: Solid
Flash point	Not relevant / not applicable Justification: Solid
Evaporation rate	Not relevant / not applicable Justification: Solid
Flammability (solid, gas)	The product is not flammable.
Lower explosion limit	Not relevant / not applicable Justification: Solid
Upper explosion limit	Not relevant / not applicable Justification: Solid
Vapour pressure	Not relevant / not applicable, Justification: Solid
Relative vapour density	Not relevant / not applicable, Justification: Solid
Density	2.837 g/cm ³
Water solubility	< 0.00005 g/l30 °C
Partition coefficient: n-octanol/water	not applicable
Ignition temperature	not applicable
Autoignition temperature	not auto-flammable
Viscosity, dynamic	not applicable
Viscosity, kinematic	not applicable
Explosive properties	not applicable
Oxidizing properties	The substance or mixture is not classified as oxidizing.
Burning number	not applicable
Solubility(ies)	; immiscible

9.2 Other data

Additional advice	This sheet describes a group of products. It only contains safety-relevant data. For specific data, see Product Information sheet.
-------------------	--

**DISPERAL HP 14**

Version: 4.05

Revision Date 2011/11/21

10. STABILITY AND REACTIVITY**10.1 Reactivity**

Note No hazards to be specially mentioned.
No hazards to be specially mentioned.

10.2 Chemical stability

Note Stable

10.3 Possibility of hazardous reactions

Hazardous reactions No dangerous reaction known under conditions of normal use.

10.4 Conditions to avoid

Conditions to avoid Avoid dust formation.

10.5 Incompatible materials to avoid

Materials to avoid fluorine, chlorine, hydrogen chloride;

10.6 Hazardous decomposition products

Hazardous decomposition products No decomposition if used as directed.

Thermal decomposition Stable under normal conditions.

11. TOXICOLOGICAL INFORMATION**11.1 Information on toxicological effects****Acute toxicity**

Acute oral toxicity LD50 rat: > 2,000 mg/kg; OECD Test Guideline 401
(literature value)
Category approach
Based on available data, the classification criteria are not met.

Acute inhalation toxicity LC50 rat: > 2.3 mg/l; ; 4 h; OECD Test Guideline 403
(literature value)
Category approach
Based on available data, the classification criteria are not met.

Acute dermal toxicity The study is not necessary.
Justification:
The substance is poorly absorbed via skin.

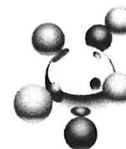
Skin corrosion/irritation

Skin irritation rabbit: not irritating
(literature value)
Category approach
Based on available data, the classification criteria are not met.

Serious eye damage/eye irritation

Eye irritation rabbit: not irritating
(literature value)
Category approach
Based on available data, the classification criteria are not met.

Respiratory or skin sensitization

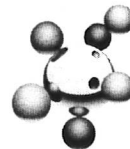


DISPERAL HP 14

Version: 4.05

Revision Date 2011/11/21

Sensitisation	guinea pig: not sensitizing (literature value) Category approach Based on available data, the classification criteria are not met.
Germ cell mutagenicity	
Genotoxicity in vitro	In vitro tests did not show mutagenic effects (literature value) Category approach
Genotoxicity in vivo	In vitro tests did not show mutagenic effects (literature value) Category approach
Remarks	Based on available data, the classification criteria are not met.
Carcinogenicity	
Carcinogenicity	Animal testing did not show any carcinogenic effects. (literature value) Category approach
Remarks	Based on available data, the classification criteria are not met.
Reproductive toxicity	
Reproductive toxicity	; OECD Test Guideline 422 Fertility and developmental toxicity tests did not reveal any effect on reproduction. (literature value) Category approach
RemarksReproductive toxicity	Based on available data, the classification criteria are not met.
Teratogenicity	rat; Oral; OECD Test Guideline 414 Did not show teratogenic effects in animal experiments. (literature value) Category approach
Remarks-Teratogenicity	Based on available data, the classification criteria are not met.
STOT - single exposure	
Remarks	The substance or mixture is not classified as specific target organ toxicant, single exposure.
STOT - repeated exposure	
Remarks	The substance or mixture is not classified as specific target organ toxicant, repeated exposure.
Repeated dose toxicity	rat; drinking water; 1 year Symptoms: Neuromuscular effects (literature value) Category approach rat; Inhalation; 6 months; OECD Test Guideline 413 (literature value) Category approach
Aspiration hazard	
Aspiration toxicity	not applicable
Further information	
Human experience	Prolonged skin contact may cause skin irritation.
Toxicological information	Based on the available structural data, phys-chem properties and toxicology data, it is likely that the substance is very poorly absorbed.

**DISPERAL HP 14**

Version: 4.05

Revision Date 2011/11/21

The substance is excreted unmetabolised.

12. ECOLOGICAL INFORMATION**12.1 Toxicity**

Toxicity to fish	In the range of water solubility not toxic under test conditions. (literature value) Category approach
Toxicity to fish - Chronic toxicity	In the range of water solubility not toxic under test conditions. (literature value) Category approach
Toxicity to daphnia and other aquatic invertebrates.	In the range of water solubility not toxic under test conditions. (literature value) Category approach
Toxicity to daphnia and other aquatic invertebrates. - Chronic toxicity	In the range of water solubility not toxic under test conditions. (literature value) Category approach
Toxicity to aquatic plants	(72 h) <i>Selenastrum capricornutum</i> (green algae); OECD Test Guideline 201; In the range of water solubility not toxic under test conditions. (literature value)
Toxicity to bacteria	The substance is not to be considered to be inhibitory to bacteria. (literature value) Category approach
Toxicity to soil dwelling organisms	The study is not necessary. Justification: exposure considerations
Toxicity to terrestrial flora	The study is not necessary. Justification: exposure considerations
Toxicity for other terrestrial non-mammalian fauna	The study is not necessary. Justification: Accumulation in terrestrial organisms is unlikely.

12.2 Persistence and degradability

Biodegradability	The methods for determining biodegradability are not applicable to inorganic substances.
-------------------------	--

12.3 Bioaccumulative potential

Bioaccumulation	Does not bioaccumulate.
------------------------	-------------------------

12.4 Mobility in soil

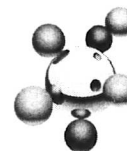
Mobility	The mobility depends on the pH value.
-----------------	---------------------------------------

12.5 Results of PBT and vPvB assessment

Results of PBT assessment	This substance is not considered to be persistent, bioaccumulating nor toxic (PBT). Based on available data, the classification criteria are not met.
----------------------------------	---

12.6 Other adverse effects

General advice	None known.
-----------------------	-------------

**DISPERAL HP 14**

Version: 4.05

Revision Date 2011/11/21

13. DISPOSAL CONSIDERATIONS**13.1 Waste treatment methods**

Product	Can be landfilled, when in compliance with local regulations.
Contaminated packaging	Store containers and offer for recycling of material when in accordance with the local regulations.
waste code of the European Union: EWC	A waste code in accordance with the European Waste Catalogue (EWC) may not be assigned to this product since it admits of a classification only when the consumer uses it for some purpose. The waste code must be determined in agreement with the regional waste disposal authority or company.

14. TRANSPORT INFORMATION**14.1 UN number**

ADR	Not dangerous goods
RID	Not dangerous goods
ADN	Not dangerous goods
IMDG	Not dangerous goods
ICAO/IATA	Not dangerous goods

14.2 Proper shipping name

ADR	Not dangerous goods
RID	Not dangerous goods
ADN	Not dangerous goods
IMDG	Not dangerous goods
ICAO/IATA	Not dangerous goods

14.3 Transport hazard class

ADR	Not dangerous goods
RID	Not dangerous goods
ADN	Not dangerous goods
IMDG	Not dangerous goods
ICAO/IATA	Not dangerous goods

14.4 Packing group

ADR	Not dangerous goods
RID	Not dangerous goods
ADN	Not dangerous goods
IMDG	Not dangerous goods
ICAO/IATA	Not dangerous goods

14.5 Environmental hazards

ADR	Environmentally hazardous	no
RID	Environmentally hazardous	no
ADN	Environmentally hazardous	no
IMDG	Marine pollutant	no
ICAO/IATA	Environmentally hazardous	no

14.6 Special precautions for user

**DISPERAL HP 14**

Version: 4.05

Revision Date 2011/11/21

Not classified as dangerous in the meaning of transport regulations.

14.7 Transport in bulk according to Annex II of MARPOL 73/78 and the IBC Code

Remarks No information available.

15. Regulatory information**15.1 Safety, health and environmental regulations/legislation specific for the substance or mixture****NOTIFICATION STATUS**

US. Toxic Substances Control Act	TSCA	y (positive listing)
Canada. Canadian Environmental Protection Act (CEPA). Domestic Substances List (DSL). (Can. Gaz. Part II, Vol. 144)	DSL	y (positive listing)
Australia. Industrial Chemical (Notification and Assessment) Act	AICS	y (positive listing)
New Zealand. Inventory of Chemicals (NZIOC), as published by ERMA New Zealand	NZIOC	y (positive listing)
Japan. Kashin-Hou Law List	ENCS (JP)	y (positive listing)
Japan. Industrial Safety & Health Law (ISHL) List	ISHL (JP)	y (positive listing)
Korea. Existing Chemicals Inventory (KECI)	KECI (KR)	y (positive listing)
Philippines. The Toxic Substances and Hazardous and Nuclear Waste Control Act	PICCS (PH)	y (positive listing)
China. Inventory of Existing Chemical Substances	INV (CN)	y (positive listing)
Switzerland. Consolidated Inventory	CH INV	y (positive listing)

Please note: the names and CAS numbers which are used for this product in the stated inventories may deviate from the information which is listed in chapter 3.

15.2 Chemical Safety Assessment**Boehmite (Al(OH)O)**

A Chemical Safety Assessment has been carried out for this substance.

16. Other information**Safety datasheet sections which have been updated:**

- 11. Toxicological information
- 12. Ecological information

Further information:

The information provided in this Safety Data Sheet is correct to the best of our knowledge, information and belief at the date of its publication. The information given is designed only as a guidance for safe handling, use, processing, storage, transportation, disposal and release and is not to be considered a warranty or quality specification. The information relates only to the specific material



DISPERAL HP 14

Version: 4.05

Revision Date 2011/11/21

designated and may not be valid for such material used in combination with any other materials or in any process, unless specified in the text. This safety datasheet only contains information relating to safety and does not replace any product information or product specification.

Annex

Attachments to the safety data sheet and/or lists of the identified uses for the listed substances can be downloaded using the internet links below.

Boehmite (Al(OH)O)

http://www.sasolgermany.de/fileadmin/doc/productsafety/Annex/CON000000018_EN_01.pdf

NANOPOX® F 400

NANOPOX® F 400 is a high performance, versatile, silica reinforced Bisphenol A based epoxy resin for the use in fibre composites. The silica phase consists of surface-modified synthetic SiO₂ nanospheres of very small size (average diameter of 20 nm) with a narrow particle size distribution (maximum diameter 50 nm). Despite the high SiO₂ content of 40 wt%, NANOPOX® F 400 has a comparatively low viscosity due to the agglomerate-free colloidal dispersion of the nanoparticles in the resin.

Technical data (no specification)

Property	Units	Typical Values
Base resin		Bisphenol A diglycidyl ether
Appearance		opaque liquid
SiO ₂ -content	[wt%]	40
Density @ 20 °C	[g/ml]	1.4
Viscosity @ 25 °C	[mPas]	60 000
Epoxy equivalent weight	[g/eq]	295
Shelf life	[months]	6*

*if stored in the original unopened container

Processing Instructions

NANOPOX® F 400 can be used as any other Bisphenol A diglycidyl ether. However, the colloidal silica in NANOPOX® products tends to agglomerate if the stabilisation is affected by inappropriate formulation components like hydrocarbon solvents (e. g. xylene). Therefore the compatibility between NANOPOX® F 400 and all other formulation components should be tested separately before starting formulation development.

Handling and Storage

NANOPOX® F 400 should be handled in accordance with good industrial practice. Detailed information is provided in the Material Safety Data Sheet.

Keep container(s) tightly closed when not in use!

NANOPOX® F 400 tends to crystallize at ambient temperatures. The product can be easily re-melted by heating it up to 70 °C for a short period of time.

11/2016

This information and all further technical advice are based on our present knowledge and experience. However, it implies no liability or other legal responsibility on our part, including with regard to existing third party intellectual property rights, especially patent rights. In particular, no warranty, whether express or implied, or guarantee of product properties in the legal sense is intended or implied. We reserve the right to make any changes according to technological progress or further developments. The customer is not released from the obligation to conduct careful inspection and testing of incoming goods. Performance of the product described herein should be verified by testing, which should be carried out only by qualified experts in the sole responsibility of a customer. Reference to trade names used by other companies is neither a recommendation, nor does it imply that similar products could not be used.

(Status: August 2014)

Evonik Nutrition & Care GmbH

Charlottenburger Str. 9, 21502 Geesthacht, Germany

Phone: +49 4152 8092-0, Fax: 49 4152 79156

nano-and-silicone-technology@evonik.com, www.evonik.com/nano-and-silicone-technology



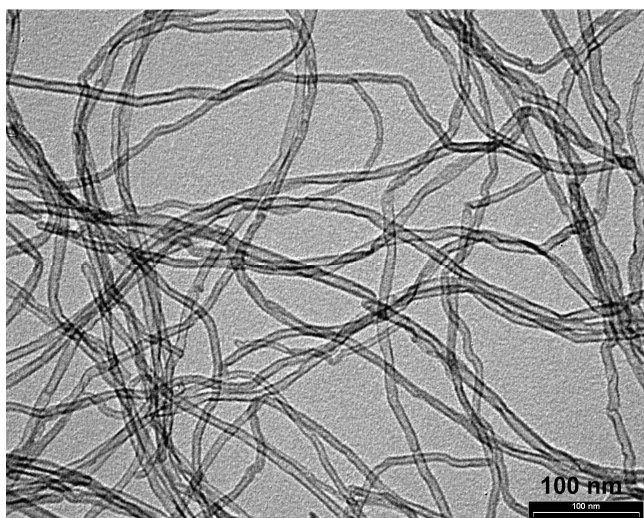
THE CARBON NANOTUBE SPECIALIST

NANO-ENGINEER YOUR FUTURE

Ref: NANOCYL™ NC7000 – 10 March 2009 - V05

NANOCYL™ NC7000 series - Product Datasheet – Thin Multi-Wall Carbon Nanotubes

General information



NANOCYL™ NC7000 series, thin multi-wall carbon nanotubes, are produced via the catalytic carbon vapor deposition (CCVD) process.

A primary interest is in applications requiring low electrical percolation threshold such as high-performance electrostatic dissipative plastics or coatings.

NC7000 is available in powder form in quantities starting at 2 kg to multi-tons.

Pre-dispersed forms are also available (PLASTICYL™, EPOCYL™, AQUACYL™).

Characterization NC7000

PROPERTY	UNIT	VALUE	METHOD OF MEASUREMENT
Average Diameter	nanometers	9.5	TEM
Average Length	microns	1.5	TEM
Carbon Purity	%	90	TGA
Metal Oxide	%	10	TGA
Amorphous Carbon	-	*	HRTEM
Surface Area	m ² /g	250-300	BET

* Pyrolytically deposited carbon on the surface of the NC7000

+ Further information is available upon request

The information contained on this datasheet is believed to be reliable— yet Nanocyl makes no warranties and assumes no liability in connection with any use of this information. Nothing herein is to be taken as a license to operate under or infringe any patent. While this information is accurate at the time of publication, please contact Nanocyl or check <http://www.nanocyl.com> for the most up-to-date information.

Nanocyl S.A.

Rue de l'Essor 4
B-5060 Sambreville
BELGIUM
Tel +32 71 750 380
Fax +32 71 750 390
sales@nanocyl.com

US contact

info-us@nanocyl.com

www.nanocyl.com

Curriculum Vitae



Personal

Name Dilmurat Abliz
Dilimulati Abulizi (Chinese)

Date of Birth 14th May, 1986

Nationality China

Profession

2012.02 – present Scientific employee
Institute of Polymer Materials and Plastics Engineering,
Clausthal University of Technology, Clausthal-Zellerfeld, Germany

Education

2012.02 – 2017.07 PhD: Materials Engineering
Institute of Polymer Materials and Plastics Engineering
Clausthal University of Technology, Clausthal-Zellerfeld, Germany

2008.09 – 2011.12 M.Sc.: Mechanical Engineering
School of Mechanical Engineering
State Key Laboratory for Manufacturing Systems Engineering,
Xi'an Jiaotong University, Xi'an, China

2004.09 – 2008.06 B.E.: Mechanical Engineering & Automation
School of Mechanical Engineering
Jiangnan University, Wuxi, China

Profession

2012.02 – present Scientific employee
Institute of Polymer Materials and Plastics Engineering,
Clausthal University of Technology, Clausthal-Zellerfeld, Germany

Language

Uyghur Mother tongue
Chinese Native language (bilingual)
English Fluent
German Fluent

Hobby

Basketball; Swimming; Skiing; Jogging; Music; Reading